

OREGON HEALTH & SCIENCE UNIVERSITY  
SCHOOL OF MEDICINE – GRADUATE STUDIES

CHARACTERIZATION OF A NOVEL GOT2-PPAR $\delta$  AXIS IN PANCREATIC  
DUCTAL ADENOCARCINOMA.

By

Hannah S. Sanford-Crane

A DISSERTATION

Presented to the Cancer Biology Program  
and the Oregon Health & Science University

School of Medicine

in partial fulfillment of

the requirements for the degree of

Doctor of Philosophy

January 2021

School of Medicine  
Oregon Health & Science University

CERTIFICATE OF APPROVAL

---

This is to certify that the PhD dissertation of

Hannah S. Sanford-Crane

has been approved

---

Mara H. Sherman, Ph.D., Mentor/Advisor

---

Sara A. Courtneidge, Ph.D., Co-mentor/Advisor

---

Melissa H. Wong, Ph.D., Committee Chair

---

Aaron Grossberg, M.D. Ph.D. Member \_

---

Elie Traer, M.D. Ph.D., Member \_

---

Jonathan Brody, Ph.D. Member \_

i) Table of Contents:

<b><u>I) TABLE OF CONTENTS:</u></b>	<b>1</b>
<b><u>II) LIST OF FIGURES</u></b>	<b>3</b>
<b><u>IV) LIST OF ABBREVIATIONS</u></b>	<b>4</b>
<b><u>V) ACKNOWLEDGMENT.</u></b>	<b>7</b>
<b><u>VI) ABSTRACT</u></b>	<b>8</b>
<b><u>CHAPTER 2: INTRODUCTION</u></b>	<b>10</b>
<b>RATIONALE AND HYPOTHESIS:</b>	<b>47</b>
<b><u>CHAPTER 2: NOVEL NUCLEAR LOCATION FOR GOT2 IN PDAC AND ARACHIDONIC ACID BINDING AND FATTY ACID TRANSPORT CAPABILITIES MAY HAVE A ROLE IN PDAC <i>IN VIVO</i> DEVELOPMENT.</u></b>	<b>48</b>
<b>ABSTRACT:</b>	<b>49</b>
<b>PERSONAL CONTRIBUTION:</b>	<b>50</b>
<b>INTRODUCTION:</b>	<b>51</b>
<b>MATERIALS AND METHODS:</b>	<b>57</b>
<b>RESULTS:</b>	<b>62</b>
<b>DISCUSSION:</b>	<b>73</b>
<b>ACKNOWLEDGEMENTS:</b>	<b>76</b>
<b><u>CHAPTER 3: THE TUMOR CELL INTRINSIC GOT2-PPARA AXIS HELPS CREATE THE IMMUNE-SUPPRESSIVE TME OF PDAC.</u></b>	<b>77</b>
<b>ABSTRACT:</b>	<b>78</b>
<b>PERSONAL CONTRIBUTION:</b>	<b>79</b>
<b>INTRODUCTION:</b>	<b>80</b>
<b>MATERIALS AND METHODS:</b>	<b>82</b>
<b>RESULTS:</b>	<b>88</b>
<b>DISCUSSION:</b>	<b>98</b>
<b>ACKNOWLEDGEMENTS:</b>	<b>101</b>
<b><u>CHAPTER 4: THE FATTY ACID BINDING ROLE OF GOT2 PRESENTS AN OPPORTUNITY FOR A UNIQUE DRUG TARGET IN PDAC.</u></b>	<b>102</b>

<b>ABSTRACT:</b>	<b>103</b>
<b>PERSONAL CONTRIBUTION:</b>	<b>104</b>
<b>INTRODUCTION:</b>	<b>105</b>
<b>MATERIALS AND METHODS:</b>	<b>108</b>
<b>RESULTS:</b>	<b>115</b>
<b>DISCUSSION:</b>	<b>120</b>
<b>ACKNOWLEDGEMENTS:</b>	<b>122</b>

---

**CHAPTER 5: CONCLUSIONS, LIMITATIONS, AND FUTURE DIRECTIONS. 123**

---

**REFERENCES: 133**

---

**APPENDICES: 155**

HANNAH SANFORD-CRANE, JAIME ABREGO, MARA SHERMAN. *FIBROBLASTS AS MODULATORS OF LOCAL AND SYSTEMIC CANCER METABOLISM*. *CANCERS* 11(5), 619, 2019. 155

J. MATTHEW MEINIG, SKYLAR J. FERRARA, TAPASREE BANERJI, TANIA BANERJI, HANNAH S. SANFORD-CRANE, DENNIS BOURDETTE, THOMAS S. SCANLAN. *STRUCTURE-ACTIVITY RELATIONSHIPS OF CENTRAL NERVOUS SYSTEM PENETRATION BY FATTY ACID AMIDE HYDROLASE (FAAH)-TARGETED THYROMIMETIC PRODRUGS*. *ACS MED. CHEM. LETT*, 10(1) 111-116, 2019. 176

HANNAH S. SANFORD-CRANE, TANJA PEJOVIC, XIANGSHU XIAO. *DRUGGING HOMOLOGOUS RECOMBINATION: BACK TO THE FUTURE*. *FUTURE MEDICINAL CHEMISTRY*, 10(11), 2018. 188

J. MATTHEW MEINIG, SKYLAR J. FERRARA, TANIA BANERJI, TAPASREE BANERJI, HANNAH S. SANFORD-CRANE, DENNIS BOURDETTE, AND THOMAS S. SCANLAN. *TARGETING FATTY-ACID AMIDE HYDROLASE WITH PRODRUGS FOR CNS-SELECTIVE THERAPY*. *ACS CHEMICAL NEUROSCIENCE*, 8(11), 2468-2476, 2017. 192

FERRARA, S. J., MEINIG J. M., PLACZEK, A. T., BANERJI T., MCTIGUE P., HARTLEY M.D., SANFORD-CRANE H. S., BANERJI T., BOURDETTE D., SCANLAN T. S. *ESTER-TO-AMIDE REARRANGEMENT OF ETHANOLAMINE-DERIVED PRODRUGS OF SOBETIROME WITH INCREASED BLOOD-BRAIN BARRIER PENETRATION*. *BIOORGANIC & MEDICINAL CHEMISTRY* 25, 2743-2753, 2017. 213

PLACZEK, A. T., FERRARA, S. J., HARTLEY M. D., SANFORD-CRANE H. S., MEINING J. M., & SCANLAN, T. S. *SOBETIROME PRODRUG ESTERS WITH ENHANCED BLOOD-BRAIN BARRIER PERMEABILITY*. *BIOORGANIC & MEDICINAL CHEMISTRY*, 24(22), 5842-5854, 2016. 235

---

**BIOGRAPHICAL SKETCH: 262**

## ii) List of Figures

<b>Figure 1 Graphical abstract: cancer cell-intrinsic GOT2-PPAR<math>\delta</math> axis suppresses antitumor immunity.....</b>	<b>9</b>
<b>Figure 1.1 The pancreas. ....</b>	<b>11</b>
<b>Figure 1.2 a dense desmoplasia characterizes PDAC.....</b>	<b>16</b>
<b>Figure 1.3 the hallmarks of cancer.....</b>	<b>37</b>
<b>Figure 1.4 the Warburg Effect and cancer cell metabolism.....</b>	<b>38</b>
<b>Figure 2.1: Summary of GOT1 &amp; GOT2 canonical enzymatic activity. ....</b>	<b>53</b>
<b>Figure 2.2: Summary of GOT2 metabolic roles and their relationship to the Krebs Cycle. ....</b>	<b>54</b>
<b>Figure 2.3 GOT2 is upregulated in PDAC.....</b>	<b>62</b>
<b>Figure 2.4 metabolic compensation makes GOT2 unessential for in vitro proliferation. ....</b>	<b>63</b>
<b>Figure 2.5 GOT2 loss results in morphological change and potential EMT switch. ....</b>	<b>64</b>
<b>Figure 2.6 GOT2 localizes to the mitochondria, membrane, and nucleus of PDAC cells and in tumor tissue. ....</b>	<b>66</b>
<b>Figure 2.7 GOT2 binds directly to fatty acids and affects FFA levels in the nucleus.....</b>	<b>67</b>
<b>Figure 2.8 Loss of GOT2 results in significant reduction in tumor size in vivo. ....</b>	<b>71</b>
<b>Figure 2.2 PDAC cell-intrinsic GOT2 suppresses tumor growth in a nude mouse model.....</b>	<b>90</b>
<b>Figure 3.1 PDAC cell-intrinsic GOT2 suppresses T cell-dependent immunologic control of tumor growth.....</b>	<b>90</b>
<b>Figure 3.3 Flow cytometry reveals changes to immune cell infiltration following loss of GOT2. ....</b>	<b>92</b>
<b>Figure 3.4 GOT2 positively regulates PPAR<math>\delta</math> activity and target gene expression. ....</b>	<b>95</b>
<b>Figure 3.5 genetic activation of PPAR<math>\delta</math> restores tumor growth in the absence of GOT2.....</b>	<b>96</b>
<b>Figure 4.1 Pharmacological activation of PPAR<math>\delta</math> restores tumor growth and T cell exclusion in a GOT2-null setting.....</b>	<b>115</b>
<b>Figure 4.2 tmGOT2 has reduced nuclear localization and PPAR<math>\delta</math> activity compared to wtGOT2. .</b>	<b>116</b>
<b>Figure 4.3 tmGOT2 has similar AST levels as wtGOT2 but fails to fully rescue tumor growth in the absence of Got2.....</b>	<b>118</b>

#### iv) List of Abbreviations

ANGPTL4	Angiopoietin Like 4
Arg1	Arginase 1
AST	Aspartate Aminotransferase
ATM	Ataxia telangiectasia mutated
ATR	ataxia telangiectasia and Rad3-related protein
BRCA1	Breast cancer type 1 susceptibility protein
BRCA2	Breast cancer type 2 susceptibility protein
CAF	Cancer associated fibroblast
Cas9	CRISPR associated protein 9
CAV-1	Caveolin 1
CCL1	Cancer cell line encyclopedia
CCL2	C-C motif chemokine ligand 2
CD3	Cluster of differentiation 3
CD4	Cluster of differentiation 4
CD8	Cluster of differentiation 8
CD36	Cluster of differentiation 36
CD44	Cluster of differentiation 44
CHK2	Checkpoint kinase 2
C-Myc	cellular MYC proto-oncogene
COX-2	Cyclooxygenase-2
CRISPR	Clustered regularly interspaced short palindromic repeats
CXCL1	C-X-C motif chemokine ligand 1
CXCL2	C-X-C motif chemokine ligand 2
CXCL9	C-X-C motif chemokine ligand 9
CXCL10	C-X-C motif chemokine ligand 10
DAPI	4',6-diamidino-2-phenylindole
DC	Dendritic Cell
DDR	DNA damage repair
DMEM	Dulbecco's modified eagle media
DNA	Deoxyribonucleic acid
DOX	Doxycycline
DSB	Double strand breaks
ECAD	Epithelial cadherin
ECM	Extra Cellular Matrix
EGF	Epidermal growth factor
EGFR	Epidermal growth factor receptor
EMT	Epithelial-mesenchymal transition
EREG	Epiregulin
F4/80	EGF-like module-containing mucin-like hormone receptor-like 1
FA	Fanconi anemia
FABP-1	Fatty Acid Binding Protein-1 (GOT1)
FAPB-5	Fatty Acid Binding Protein-5
FABPpm	Fatty Acid Binding Protein Plasma Membrane (GOT2)
FAO	Fatty acid oxidation
FAP $\alpha$	Fibroblast activation protein alpha
FBS	Fetal Bovine Serum
FFA	Free fatty acid
FFAR	Free fatty acid receptor
FFPE	Formalin-fixed paraffin-embedded

FOXO1	Forkhead box protein O1
GLUD1	Glutamate dehydrogenase 1
GLUT1	Glucose transporter 1
GOT1	Glutamic-oxaloacetic transaminase
GOT2	Glutamic-oxaloacetic transaminase 2
GPX	Glutathione peroxidase
GRZB	Granzyme B
GSH	Glutathione
H3K9 <sup>ac</sup>	Acetyl-histone H3 Lysine 9
H&E	Hematoxylin and eosin
HA	Hyaluronan
HAS	Hyaluronan Synthase
HIF	Hypoxia-inducible factor
HK2	hexokinase 2
HMGCS2	3-Hydroxy-3-Methylglutaryl-CoA Synthase 2
HR	Homologous recombination
HSC	Hematopoietic stem cell
HYALS	Hyaluronidases
IDH1	Isocitrate dehydrogenase isozyme 1
IFN $\gamma$	Interferon gamma
IHC	Immunohistochemistry
IL-2	Interleukin 2
IL-4	Interleukin 4
IL-6	Interleukin 6
JAK/STAT	Janus kinase/signal transducer and activator of transcription
KRAS	V-Ki-ras2 Kirsten rat sarcoma viral oncogene homolog
KD	Knock down
KO	Knock out
LDHA	Lactate dehydrogenase A
LLC	Lewis lung carcinoma
LXR	Liver X receptor
MAPK	Mitogen-activated protein kinase
MDSC	Myeloid-derived suppressor cell
MEK	Methyl ethyl ketone
MHC-II	Major histocompatibility complex class II
miRNA	MicroRNA
MMP-9	Matrix metalloproteinase 9
MMR	Mismatch repair
MRE11	Meiotic recombination 11
MS	Mass spectrometry
NAD(H)	Nicotinamide adenine dinucleotide
NADP(H)	Nicotinamide adenine dinucleotide phosphate
NBS1	Nibrin
NCAD	Cadherin 2
NER	Nucleotide excision repair
NF- $\kappa$ B	Nuclear factor kappa B
NHEJ	Non-homologous end joining
NK cell	Natural killer cell
NKp30	Natural killer protein 30
NKp44	Natural killer protein 44
NLS	Nuclear localization sequence

OXPHOS	Oxidative phosphorylation
PanCK	Pan-cytokeratin
PALB2	Partner and localizer of the BRCA2 gene
PARP	Poly (ADP-ribose) polymerase
PD-1	Programmed cell death protein 1
PDAC	Pancreatic ductal adenocarcinoma
PDGF	Platelet-derived growth factor
PDK4	Pyruvate dehydrogenase kinase 4
PFKL	6-phosphofructokinase, liver type
PG	Prostaglandin
PPAR $\alpha$	Peroxisome proliferator-activated receptor alpha
PPAR $\delta$	Peroxisome proliferator-activated receptor delta
PPAR $\gamma$	Peroxisome proliferator-activated receptor gamma
PTGS2	Prostaglandin-endoperoxide synthase 2
PTHRP	Parathyroid hormone-related peptide
P53	tumor protein p53
PanIN	Pancreatic intraepithelial neoplasia
PBS	Phosphate-buffered saline
PCR	Polymerase chain reaction
PDAC	Pancreatic ductal adenocarcinoma
RAD3	ATR checkpoint kinase Rad3
RAD50	RAD50 double strand break repair protein
RAD51	RAD51 recombinase
RNA	Ribonucleic acid
ROS	Reactive oxygen species
RXR	Retinoid X receptor
shRNA	Short hairpin RNA
sgRNA	Single guide RNA
SLC27a1-6	Solute carrier family 27 member 1-6
SSB	Single strand break
STAT3	Signal transducer and activator of transcription 3
TAM	Tumor associated macrophage
TAN	Tumor associated neutrophils
TCA	Tricarboxylic acid cycle
TGF $\beta$	Transforming growth factor beta
T <sub>H</sub> 1	T helper type 1
T <sub>H</sub> 17	T helper type 17
T <sub>H</sub> 2	T helper type 2
TNF $\alpha$	Tumor necrosis factor alpha
VEGF	Vascular endothelial growth factor
$\alpha$ -KG	alpha-ketoglutarate
$\alpha$ -SMA	alpha smooth muscle actin
$\beta$ -gal	beta-galactosidase

## v) Acknowledgment.

Throughout the planning, execution, and writing of this dissertation I have received a great deal of support and assistance.

I would first like to thank my supervisor, Professor Mara H. Sherman, for her unwavering support and invaluable expertise in formulating research questions and methodology. She continuously provided encouragement and was consistently enthusiastic about the research project even when data was at its most confusing. I would also like to thank my co-mentor, Professor Sara Courtneidge, for the thoughtful comments and recommendations on my research.

I would like to thank the Cancer Biology (CANB) graduate program for the fellowship which funded my stipend for the last year of my graduate research, and in general for creating a supportive and collaborative atmosphere at OHSU.

I would also like to thank the following people, without whom, completing this degree would have been much more challenging and much less fun. My fellow Sherman lab mates Erin Helms, M. Kathrina Onate, Chet Oon, Dr. Jaime Abrego (who assisted in this project), Mark Berry, and Dr. Sohinee Bhattacharyya. I would also like to thank the CANB graduate students who were always willing to offer a listening ear and coffee.

My husband for his patience with me sitting for hours, weeks on end, writing this dissertation and reading it out loud to him on and off. I would also like to thank my family for their encouragement and support in pursuing my PhD dreams and for letting me practice giving my talks to them, even though they have no idea or interest in the majority of my work. Thank you to everyone whom I have used as a sounding board over the last few years.

## vi) Abstract

The worldwide incidence of pancreatic ductal adenocarcinoma (PDAC) is expected to increase by nearly 80% by 2040[7]. While the incidence of PDAC has increased, most-likely due to increasing population prevalence of PDAC risk factors – obesity and diabetes - the mortality rate has remained fairly consistent as conventional therapies are ineffective in this disease[8, 9].

Novel immune-modulatory therapies hold promise to meaningfully improve outcomes for PDAC patients. However, development of such therapies will require an improved understanding of the immune evasion mechanisms that characterize the PDAC microenvironment, including frequent exclusion of antineoplastic T cells and abundance of immune-suppressive myeloid cells[10-13].

This dissertation will focus on how cancer cell-intrinsic glutamic-oxaloacetic transaminase 2 (GOT2) shapes the immune microenvironment to suppress antitumor immunity in PDAC. In our work we identified a novel location for GOT2 at the nucleus, along with its canonical locations at the mitochondria and plasma membrane. We found that mechanistically, GOT2 functions beyond its established role in the malate-aspartate shuttle[14-16] and promotes the transcriptional activity of nuclear receptor peroxisome proliferator-activated receptor delta (PPAR $\delta$ ), facilitated by direct fatty acid binding. This novel GOT2-PPAR $\delta$  axis results in a tumor supportive, immune-suppressive Tumor Microenvironment (TME) which is typical in PDAC patients. While we found that GOT2 in PDAC cells is dispensable for cancer cell proliferation both *in vitro* and *in vivo*, GOT2 loss *in vivo* results in T cell-dependent suppression of tumor growth, which is rescuable by genetic or pharmacologic activation of PPAR $\delta$ .

This cancer cell-intrinsic GOT2-PPAR $\delta$  axis promotes spatial restriction of both CD4<sup>+</sup> and CD8<sup>+</sup> T cells from the tumor microenvironment, and fosters the immune-suppressive phenotype of tumor-infiltrating myeloid cells. The immune-suppressive pathophysiology of PDAC has been linked to poor patient prognosis and makes most PDAC patients unresponsive to immune-therapies which have proven highly effective in cancers with improved T cell penetrance. Our

results suggest that the GOT2-PPAR $\delta$  axis could be a key player in the development of this immunological hallmark of PDAC.

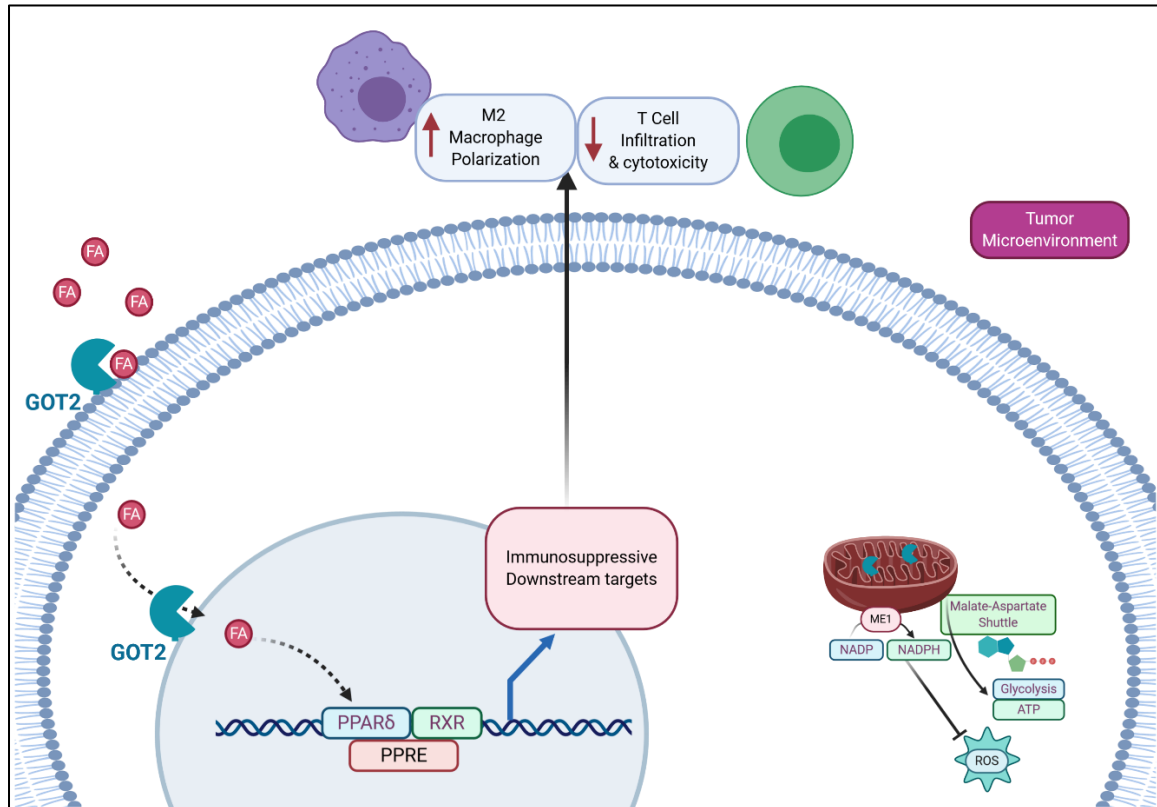


Figure 1 Graphical abstract: cancer cell-intrinsic GOT2-PPAR $\delta$  axis suppresses antitumor immunity.

GOT2 is found at a novel location at the nucleus. Here it functions by transporting long chain fatty acids to the nucleus, such as arachidonic acid, where they are released and interact as ligands for nuclear receptors, such as PPAR $\delta$ . Activation of PPAR $\delta$  causes downstream transcriptional changes resulting in an immunosuppressive TME with M2 macrophage polarization, decreased T cell infiltration, and decreased T cell cytotoxicity. Image created with BioRender.com

## Chapter 2: Introduction

*The tumor microenvironment section is an expanded version of what was published in a review.  
(Sanford-Crane H, Abrego J, Sherman MH. Fibroblasts as Modulators of Local and Systemic  
Cancer Metabolism. Cancers (Basel). 2019 May 3;11(5):619. doi: 10.3390/cancers11050619.  
PMID: 31058816; PMCID: PMC6562905.)*

## **The Pancreas: unique cells and metabolism.**

Normal pancreatic function is essential for maintaining health; as both exocrine – secretion of digestive enzymes and ions into the gastrointestinal tract – and endocrine – secretion of hormones into the blood – functions of the pancreas play important roles in metabolism and digestion[6].

Pancreatic cancer develops in the pancreas and an understanding of the unique physiology of this organ is important before researching the disease.

The pancreas is situated within the abdomen posterior to the stomach, colon, and omentum small intestinal loops and anterior to the portal vein, inferior vena cava, aorta, superior mesenteric artery, kidneys and vertebrae[6]. The distal common bile duct passes through the pancreatic head

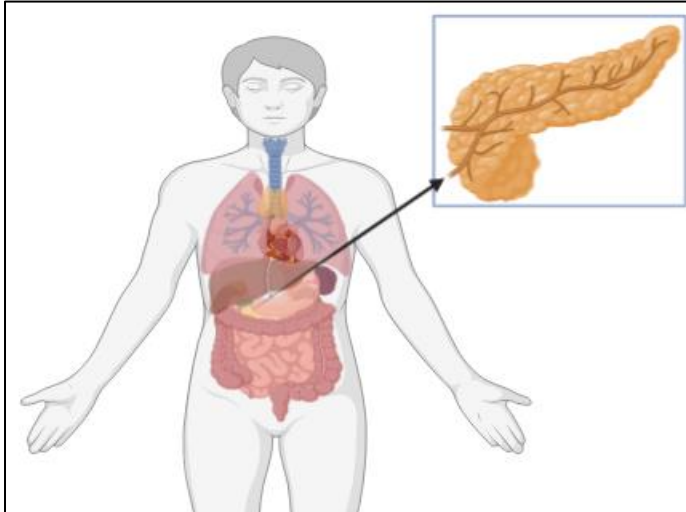


*Figure 1.1 The pancreas.*

The pancreas is within the abdomen. It is posterior to the stomach, colon, and omentum small intestinal loops and anterior to the portal vein, inferior vena cava, aorta, superior mesenteric artery, kidneys and vertebrae[6] Figure created with biorender.com

and can be occasionally blocked by pancreatic swelling or scarring providing one of the few symptoms of pancreatic cancer [6, 17]. The pancreas is supplied blood by two major arteries, the celiac and superior mesenteric arteries, which supply blood to the abdominal organs[17]. The dual artery supply of blood makes ischemia of the

pancreas via vascular obstruction rare, however, all blood is drained by the splenic vein which runs along the body of the pancreas to the superior mesenteric vein before draining to the portal vein, which makes obstruction of venous blood flow a concern[6]. Pancreatitis and pancreatic cancer frequently cause obstruction of the venous blood flow and cause thrombosis and vascular enlargement of the spleen, resulting in dangerous complications in these patients[17].

## **Pancreatic Ductal Adenocarcinoma.**

Pancreatic ductal adenocarcinoma (PDAC) is a devastating disease with a 5-year survival of less than 10% [7]. The worldwide incidence of PDAC is expected to increase, along with deaths, by nearly 80% by 2040 [7]. While the number of patients diagnosed yearly with PDAC has increased, the mortality rate has remained consistent, resulting in increasing numbers of people dying yearly from PDAC. This is reflected in the fact that while PDAC is currently the 3<sup>rd</sup> most frequent cause of cancer deaths in the United States, and is predicted to soon become the 2<sup>nd</sup> leading cause of cancer deaths [18], showing an important need to develop better treatment options to improve patient outcome.

There are several risk factors for PDAC, most often associated with western diets, helping to explain the high rate of PDAC in North America, Australia, and the UK compared with Asian and African countries [7]. These risk factors include age, obesity, diabetes, high fat diets, smoking, heavy alcohol consumption, low folate intake, and low fruit consumption [19]. Data from the World Health Organization Global Cancer Observatory (WHO GCO) shows that in the US around 11.3% of 2012 PDAC cases were attributed to excess body mass and that had population body mass stayed constant since 1982, around 3.7% of 2012 PDAC cases could have been prevented [7]. One of the largest risk factors caused by obesity is the increased risk of diabetes, which also confers elevated risk for PDAC development. Diabetic patients make up around 25% of diagnosed PDAC cases, although it should be noted that PDAC can cause diabetes as well and that screening patients who present with sudden-onset diabetes for PDAC has been proposed as a potential early screening technique to try and catch PDAC at earlier stages [18]. In total it is predicted that 36% of male and 39% of female PDAC cases are caused by preventable risk factors [18].

Chronic pancreatitis is another risk factor, with some suggesting a hazard ratio of 6.9 [1, 18]. Chronic pancreatitis can occur through diet, genetic predisposition, or through trauma, such as from an auto accident [6]. It is interesting to note, and supports the need for further research into

the cross-talk between PDAC and the tumor microenvironment (TME), that in chronic pancreatitis accumulation of desmoplastic stroma occurs similarly as in PDAC[20]. Current trends suggest that the world population of individuals with the greatest risk factors for PDAC – age, obesity, and diabetes – will continue to increase with each year, driving home the need to better understand and develop treatments for this devastating disease.

### **Diagnosis, grading, and treatment.**

PDAC makes up 90% of all pancreas malignancies and typically originates sporadically at an average age of onset of 70-71 years of age[1, 18, 21]. Like most cancers, stage of diagnosis is the best indicator for prognosis, however in PDAC only 10-20% of patients are diagnosed at an early resectable stage[1]. The vast majority of PDAC patients (80-90%) are diagnosed at locally advanced stages – which are not resectable – and with distant metastasis[1, 21]. Although there is a difference in classification between locally advanced PDAC and metastatic PDAC, it is understood that many cases of locally advanced PDAC also have distant sites of metastasis as well, regardless of if it is yet measurable or not[1, 18].

Early diagnosis of PDAC is the best prognosis marker, however, so far detection of early PDAC remains challenging. In fact, only around 3% of PDAC is diagnosed at stage T1a- the earliest stage with the best prognosis[22]. Most patients don't present symptoms until late stage PDAC and there are currently no definitive biomarkers. Although in use, carbohydrate antigen 19-9 (CA19-9) is considered unreliable[18, 19]. Symptoms of PDAC are generally mild and include fatigue, anorexia, weight loss, abdominal pain, and dark urine making it rare for PDAC patients to have unique symptoms which would indicate PDAC to a physician[19]. However, due to the location of the pancreas, occasionally swelling/scarring of the pancreatic head will block the bile duct, causing jaundice and allowing for diagnosis[6]. Recent onset of diabetes occurs in around 50% of diagnosed PDAC patients and may be a key screening factor in the future, and it has been suggested that screening all patients with recent onset of diabetes for PDAC could be a potential

way to increase early diagnosis of this disease[18]. PDAC is diagnosed through either endoscopic ultrasound (EUS), or magnetic resonance imaging (MRI), these imaging techniques allow tumors to be seen as long as they are above a certain size[18]. EUS is considered the superior method, as it also allows for fine-needle biopsies of the tumor and adjacent lymph nodes, without adding extra risk[23].

Early stage PDAC is operable with the best treatment options being either neoadjuvant clinical trials to try and shrink the tumor to a size where it can be easily resected, or immediate surgery[21]. After surgery the patient will also receive adjuvant chemotherapy. If the tumor does not respond to tumor control treatment options or is determined to no longer be resectable then it is considered to be progressed to a locally advanced stage and chemotherapy becomes the only viable remaining treatment option. Current adjuvant chemotherapy options are FOLFIRINOX, Gemcitabine, 5-FU, Gemcitabine-capecitabine, or Gemcitabine-paclitaxel[1, 21]. The combination therapies are most effective, however, they come with severe side effects that the elderly cannot tolerate and as the average age of PDAC onset is 70-71 this introduces a challenge for deciding on effective treatment in the majority of cases[1]. Once adjuvant therapies have failed, the only recourse is clinical trials or best supportive care. Most patients require intensive pain management and many develop intestinal blockage and malnutrition, requiring stents and gastric surgical operations[23]. Once metastasis is detected, 90% of PDAC patients will not survive for more than 5-years after diagnosis, mostly due to lack of effective treatment options[18, 23].

### **Progression to advanced PDAC**

PDAC develops from precursor lesions which show a ductal phenotype, and form as microscopic pancreatic intraepithelial neoplasia (PanIN); mucinous-papillary lesions which develop into invasive carcinoma[23]. PDAC develops from normal pancreatic tissue to PanIN-1A, PanIN-1B, PanIN-2, PanIN-3, invasive PDAC, and finally to metastatic PDAC[22, 24, 25]. PanIN-1

development is marked with mutation in *KRAS*, PanIN-2 with mutations in *CDKN2A*, PanIN-3/4 with mutations in *TP53* and *SMAD4*, these mutations are accompanied with epigenetic dysregulation[1, 18]. Other frequent mutations of PDAC include *AKT2* and *PI3K* which are key players in tumor cell survival and are typically upregulated in PDAC[1]. Epigenetic dysregulation of PDAC compromises chromatin-based mechanisms of DNA methylation, histone post-translational modification, and non-coding RNA regulation leading to repression of tumor suppressor genes and upregulation of oncogenes[1]. The impact of epigenetic reprogramming in PDAC tumor progression is influential enough that germline mutations of key DNA repair genes is not in itself enough to fully drive PDAC, and hence alterations of *BRCA1/2*, *PALB2*, *ATM*, are uncommon in most tumors; this is in contrast to several other types of cancers which are mainly driven by mutations of DNA repair genes[1].

These genetic and epigenetic variations in PDAC make it a highly heterogenic disease, and while attempts have been made to distinguish subtypes for personalized treatment there is still not a strong consensus on which subtyping method works the best[1]. Most classify PDAC by either epithelial-like gene expression (classic PDAC) or mesenchymal-like gene expression (poorer prognosis)[1]. These subtypes are then further stratified by markers *HNF1A* or *KRT81*, diagnosed through immunohistochemistry (IHC)[1]. Currently PDAC treatment does not rely on subtyping, but there is data suggesting that in the future, subtype-based stratification and genomics-driven personal medicine could make a difference in improving PDAC patient outcomes[1].

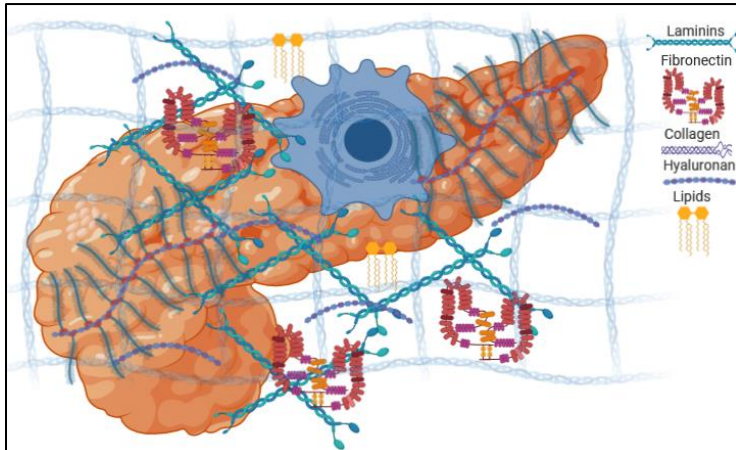


*Figure 1.2 a dense desmoplasia characterizes PDAC*  
 Activated stellate cells deposit extra cellular matrix components: laminins, fibronectins, collagens, hyaluronan, and lipids which help form the desmoplasia of PDAC[1-5]. Figure created with biorender.com

As mentioned earlier, a dense desmoplasia characterizes PDAC and can make up over 90% of the tumor volume[1, 18]. The majority of the desmoplasia is derived from cancer-associated fibroblasts (CAFs) from either a myofibroblastic (myCAF) or

inflammatory (iCAF) phenotype[1, 26-32]. It is believed that CAFs are formed from activated pancreatic stellate cells. These stellate cells undergo activation by microenvironment stresses, such as injury or chronic inflammation which typically occur along with the development of PDAC[1-5]. When activated, stellate cells deposit extra cellular matrix components, including; laminins, fibronectins, collagens, hyaluronan, and lipids[1-5]. Once formed, the dense desmoplasia limits infiltration into the tumor of oxygen, nutrients, and immune cells leading to hypoxia, hypovascularization, and reduction of T cell infiltration[1]. Interestingly, while T cell infiltration is reduced most PDAC tumors actually show an accumulation of myeloid cells, particularly of M2-like macrophages, which may be working in an immunosuppressive, pro-angiogenic, role to support PDAC progression[1, 33, 34]. New research in PDAC suggests that the *CXCL1/CXCR2*-axis maybe very important for intra-tumoral recruitment of myeloid-derived suppressor cells (MDSCs) and for their subsequent suppression of CD8+ T cell infiltration and function[1, 33, 35, 36].

**The tumor microenvironment.**

Pancreatic cancer is shown to be strongly affected by environmental factors, with chronic inflammation and obesity linked to increased risk more strongly than genetic factors[37-39]. It

has been shown that the stroma of PDAC co-evolves with tumor development with increased desmoplasia seen in pancreatitis and PanIN development throughout its formation[20].

While it was once thought that CAFs may simply provide metabolites to induce cell proliferation, evidence now suggests a wider arching role. CAFs appear to be the main component of the desmoplastic reaction, and are known to secrete components of the extracellular matrix which is essential for the creation of the fibrotic/hypovascular TME[20]. Crosstalk between CAFs and tumor cells support a co-evolution between the two that is simultaneously immunosuppressive and growth permissive. There is some controversy in the role of CAFs in PDAC development, as research has shown both protumor function and tumor-suppressive function[27, 30, 40], however this may be due to the fact that CAF populations are heterogenous and demonstrate a lack of understanding in subtypes of CAFs. While normal fibroblasts secrete factors supporting wound-healing, fibroblasts in the TME are activated into CAFs, which allows PDAC to co-opt the typical fibroblast cellular responses for wound-healing by activating CAFs to serve as paracrine regulators of cancer cell metabolism via ECM remodeling and creation of a tumor niche.

Metabolic reprogramming for the enhancement of glucose metabolism, the Warburg effect, is considered a hallmark of cancer and is the principle metabolic characteristic of cancer cells [41]. Recently, the reverse Warburg effect has been described in solid tumors using alternative carbon sources and complex metabolic interactions between tumor and stromal cells, suggesting that solid tumors are metabolically heterogeneous in energetic pathways and that the TME collaborates in their metabolism [41-43]. CAFs make up the majority of the tumor-associated stroma and also undergo a glycolysis switch following metabolic reprogramming upon interaction with tumor cells [44], suggesting that metabolic reprogramming of CAFs may play an important role in cancer development. As cancer cells proliferate, they consume oxygen at a higher rate while also increasing TME acidity through production of lactic acid as a by-product of glycolysis. This turns the tumor niche into a harsh hypoxic and hypo-nutrient environment and forces changes to

bioenergetics and biosynthesis, through metabolic reprogramming, of both cancer cells and CAFs [41, 45]. In normal tissue, cell checkpoints work to block proliferation under stressful conditions, such as found in hypoxic or hypo-nutrient environments. Factors released by CAFs including high energy metabolites such as lactate, pyruvate, and ketone bodies are used by adjacent cancer cells to overcome these checkpoints and to generate the energy required for them to continue proliferation [46, 47].

Reactive oxygen species (ROS) are one of the major regulators of metabolic reprogramming of CAFs and cancer cells [43]. Cancer cells produce large amounts of ROS from mitochondrial dysfunction, occurring from the switch to aerobic glycolysis in the “Warburg effect”, along with upregulation of NADPH oxidase 1, NADPH oxidase 4, and alterations in antioxidant enzymes [45]. This mitochondrial dysfunction triggers an increase in lactate and ROS levels while also decreasing antioxidant molecules leading to a cascade of intra and inter-cellular events within cancer cells and causing a metabolic switch [45].  $H_2O_2$  is one such trigger, once produced by cancer cells it induces oxidative stress in CAFs, decreasing their mitochondrial function and increasing glucose uptake and ROS levels, eventually leading to CAF differentiation when combined with TGF- $\beta$  [45]. Activated CAFs then secrete high levels of  $H_2O_2$  causing stromal remodeling due to impaired TGF- $\beta$  signaling and subsequent suppression of antioxidant enzyme glutathione peroxidase 1 [48]. TGF- $\beta$  is one of the key proteins involved in CAF differentiation because it allows for the increase in ROS which modulates  $\alpha$ -SMA - the most significant marker of fibroblast activation and CAF differentiation - expression through hypoxia-associated microRNA-210 [49, 50]. TGF- $\beta$  also triggers increased oxidative stress, autophagy/mitophagy, aerobic glycolysis, and downregulation of caveolin-1 (CAV-1) in CAF cells, but these alterations extend throughout the TME and work to support cancer cell growth [51]. TGF- $\beta$  is involved in an autocrine loop where its signaling downregulates isocitrate dehydrogenase 1 (IDH1) expression, which causes an increase in TGF- $\beta$  activated Smad signaling, while the decrease in IDH1 enzyme leads to impaired isocitrate to  $\alpha$ -

ketoglutarate conversion in a NADP<sup>+</sup> dependent manner, thus leading to increased cellular  $\alpha$ -KG levels which suppress Cav-1 expression, inhibiting TGFBR protein degradation and inducing higher levels of TGF- $\beta$  signaling to complete the autocrine loop [52]. Cav-1 levels are further decreased due to degradation following mitochondria disruption caused by autophagosomes-lysosomes fusion following high levels of oxidative stress, induced by ROS, in CAFs [46, 53]. Downregulation of Cav-1 leads to increased TGF- $\beta$  signaling and increased ROS production causing a positive feedback loop of increased oxidative stress in CAFs [46]. This positive feedback loop of increasing oxidative stress causes a shift in CAFs towards catabolic metabolism while also promoting mitochondrial activity in adjacent cancer cells [54]. The increased oxidative stress also results in proinflammatory transcriptional factor NF $\kappa$ B activity in CAFs and the surrounding TME, resulting in the upregulation of NF $\kappa$ B target gene cyclooxygenase-2 (COX-2) in both CAFs and cancer cells, while also taking part in the positive feedback loop by causing a defect in ROS detoxification through Gpx inhibition [55-57].

Once CAFs are activated through the hypoxic environment, they participate in a reverse Warburg effect with nearby cancer cells. During this effect anabolic cancer cells are metabolically coupled to catabolic CAFs, which generate high levels of energy-rich fuel for cancer cells through aerobic glycolysis [46]. Cancer cells then use mitochondrial oxidative phosphorylation (OXPHOS) to take advantage of the supporting metabolites released by CAFs. The differences in metabolic phenotype between CAFs and cancer cells allows them to co-exist in the TME and to support the growth and development of each other. Glycolytic enzyme hexokinase 2 (HK2) and 6-phosphofructokinase liver (PFKL) enzyme are upregulated in CAFs as well as in tumors undergoing glycolysis, suggesting that the metabolic pathway of cancer cells can be dynamic and change depending on TME nutrient conditions [58]. Oncogene cMyc further increases metabolic flux and glucose uptake in cancer cells by upregulating lactate dehydrogenase-A (LDH-A) and GLUT-1 expression [59]. Increased glycolysis in cancer cells and CAFs leads to an increase in lactic acid production and

subsequent increase in TME acidity. This increased acidity causes activation of matrix metalloproteinase-9 (MMP-9) which degrades nearby ECM and releases the reservoir of cytokines and growth factors bound within [60, 61]. Lactate is fluxed into cancer cells by monocarboxylate transporter 1 (MCT-1) which allows cancer cells to exploit lactate for enhanced anabolism and OXPHOS fuel [62]. Another metabolic remodeling in CAFs is downregulation of tricarboxylic acid (TCA) cycle through downregulation of isocitrate dehydrogenase 3 $\alpha$  (IDH3 $\alpha$ ), a critical marker for switching from OXPHOS to glycolysis in TGF- $\beta$ /PDGF-induced CAFs [58]. Downregulation of IDH3 $\alpha$  further decreases  $\alpha$ -KG levels by reducing the ratio of  $\alpha$ -KG to fumarate and succinate, which is required for prolyl hydroxylase domain-containing protein 2 (PHD2) activity, leading to a subsequent downregulation of HIF-1 and stabilization of HIF-1 $\alpha$  [63]. Once stabilized, HIF-1 $\alpha$  is transported to the nucleus where it is associated with the upregulation of over 100 genes, many of which are directly involved in the glycolytic pathway, particularly NADH dehydrogenase ubiquinone 1 alpha subcomplex, 4-like 2 (NDUFA4L2) [64]. NDUFA4L2 is a negative regulator of the mitochondrial complex 1 [58], so in summary, IDH3 $\alpha$  downregulation causes an upregulation of HIF-1 $\alpha$  and NDUFA4L2, resulting in a subsequent total effect of impaired OXPHOS and promotion of glycolysis in CAFs.

HIF-1 transcriptional activity is regulated by sirtuin1 (SIRT1) signaling, which deacetylates peroxisome proliferator activated receptor gamma coactivator 1 $\alpha$  (PGC1- $\alpha$ ) and by SIRT3, a mitochondrial deacetylase, which - upon downregulation - increases the level of inactive superoxide dismutase 2 (SOD2) acetylation [65]. The combination of these effects is increased mitochondrial function and hyper-production of ROS along with upregulation of pyruvate kinase M2 (PKM2), which triggers aerobic glycolysis [42]. When cancer cells interact with CAFs, PKM2 is oxidized by ROS and its tyrosine is phosphorylated by Src kinase, after which it is transported into the nucleus where it recruits HIF-1 and associated embryo-chondrocyte expressed gene-1

(DEC1); repressing miR-205 and driving a pleiotropic transcriptional metabolic reprogramming of cancer cells towards OXPHOS and EMT [66].

Cancer cells release factors which cause CAFs to enter metabolic overdrive to the detriment of their own survival, inducing autophagy and mitophagy to produce metabolic precursors – lactate, ketone bodies, glutamine, and pyruvate – through aerobic glycolysis and CAFs utilize microvesicles to transfer large amounts of these proteins and lipids to metabolically support cancer cell growth [67]. Many of these transferred proteins can act as metabolic enzymes and are one of the ways CAFs work to reprogram the metabolic state of cancer cells. Cancer cells are adaptive to their environment and switch between OXPHOS and glycolysis, depending on nutritional and oxygen status. CAFs behave in a self-destructive manner to provide the nutrients cancer cells require to continue using OXPHOS and proliferate quickly, regardless of the nutritional or oxygen status of the nearby TME. All of this suggests that it is possible the “Warburg effect” is not really a hallmark of PDAC, but rather a hallmark CAFs which act upon cancer cells to sustain their high proliferation rates in the dense desmoplasia typical of PDAC.

Recent investigations into the link between CAFs, TME, and metabolic status of cancer cells have suggested a more nuanced story behind metabolic regulation of cancer cells than previously realized. CAFs and cancer cells feature a positive feedback loop in which CAFs produce regulators important for cancer cell metabolism and cancer cells induce CAFs to produce these regulators through secretions. For example, CAFs produce hyaluronan (HA) which in turn regulates glucose metabolism in tumor cells [68]. HA released by CAFs also induces cancer cells to upregulate their own HA production, leading to higher levels in the TME and causing an overall increase in ECM stiffness [69]. The increased stiffness of the ECM results in downstream mechanosensing signaling in CAFs, causing them to release aspartate to support cancer cell proliferation, while also inducing cancer cells to secrete glutamate, helping to balance the redox state of CAFs, promoting further ECM remodeling and the formation of a tumor niche [69]. This is further evidenced by the fact that

cell-free extract from stromal cells alters survival of PDAC cell lines *in vitro* by causing a series of transcriptional changes in TCA cycle, anabolic metabolism, and cell growth [70]. These alterations in the TME suggest a causative effect in the cancer cell epigenome, and thus implicates the TME as a potential anticancer therapeutic target. Supporting this connection, many TME-induced transcriptional changes match oncogenic Kras - the major oncogenic driver of PDAC - transcriptional changes [70], suggesting a pro-tumorigenic synergy between the TME and Kras.

Cancer has long been considered a type of chronic injury to which fibroblasts support with a wound-healing response [71]. This response is initiated partially by the production and secretion of transforming growth factor- $\beta$  (TGF- $\beta$ ), platelet-derived growth factor (PDGF), epidermal growth factor (EGF), and fibroblast growth factor (FGF) by cancer cells, leading to the activation and transformation of fibroblasts into CAFs [72]. Upon activation CAFs release collagen, fibronectins, proteoglycans, glycosaminoglycans, matrix metallo-proteinases (MMPs), chemokines (ex. CXCL2, CXCL2/SDF1, CCL2/MCP-1, CCL5/Rantes), vascularization promoting factors (ex. VEGF), tenascin C, and other factors (ex. TGF- $\beta$ , EGF, FGF, and hepatocyte growth factor) [72, 73]. Released proteoglycans and glycosaminoglycans integrate into the ECM, and bind to growth factors and cytokines due to their negative charge, once in the ECM, they act as a storage site for these factors [74]. During cancer progression, cancer cells secrete MMPs to degrade nearby ECM, causing a release the reservoir of cytokines and growth factors [60]. These factors then act as part of a fibroinflammatory stromal response, which is known to influence initiation and progression of PDAC along with clinical outcome in patients [70]. This occurs through adaptive responses in PDAC by increasing transcriptional networks for growth and altering metabolome in response to stromal signals [70]. Stromal signals cause epigenetic changes in PDAC, driving histone acetylation and transcriptional enhancement of many genes, such as the bromodomain and extraterminal (BET) family of epigenetic readers and Bromodomain-containing protein 2 (BRD2) [70]. BET proteins regulate gene transcription through changes in epigenetic interactions via

bromodomains and acetylated histones and aberrant expression can be oncogenic through mediating hyperacetylation of the proliferation-promoting genes of the chromatin [75]. Further epigenetic changes on BET bromodomains can occur through c-MYC - a well-studied oncogene and “master regulator” - repression of BET bromodomain transcriptional network and its aberrant expression also contributes to carcinogenesis [75]. There is also evidence that tumor activation derives from the combination of Kras mutation and stromal cues, illustrating the importance of understanding the role of the tumor microenvironment during all stages of tumor initiation, development, and growth [70]. Normal tissue architecture provides barriers to tumorigenesis, which solid tumors overcome through disrupting tissue homeostatic mechanisms [60, 76]. In PDAC, the main architecture to overcome is the dense fibroinflammatory stroma produced by CAF secreted ECM components, although this same dense desmoplasia also provides tumor-supportive properties and so a balance of degradation and thickening stroma is required for cancer development [42, 70].

Dynamic changes in the TME occur throughout tumor progression and are observed to thicken the fibroinflammatory stroma and create aberrant immune response along with the continued accumulation of desmoplasia [77]. These responses are all aberrant variations of a normal wound-healing response [78] with an end result of co-opting the classical wound-healing response for a driving force towards tumorigenesis and oncogenic alterations [79, 80] and a suppression of immune response leading to reduced effects of cytotoxic and immune-target therapies in PDAC [81-84]. These dynamic changes also result in the activation of tissue resident stellate cells towards transdifferentiation into myofibroblast-like cells, changing stellate cell activity from basement membrane maintenance to driving fibroinflammatory response of ECM components, cytokines, and growth factors [85-87]. All of this evidence supports the idea that PDAC-associated stroma has both tumor-supportive [88, 89] and tumor-suppressive roles [90-92]. Understanding the molecular

basis for these roles may one day lead to the ability to modulate PDAC-associated stroma to be fully tumor-suppressive as a method of cancer treatment.

HA is a major component of the ECM and plays a role in cancer progression and aggression. It is expressed in 80% of PDAC tissues, in both tumor and stromal sections, and PDAC patients expressing low levels of HA have over 2.5 times the median survival time as patients expressing high levels [93]. In normal tissue, HA levels are maintained through a balance of synthesis, by hyaluronan synthase (HAS), and degradation, by hyaluronidases (HYALs). However, in the surrounding stroma and tumors of various cancers HA accumulates at high levels [93]. HA accumulates in PDAC metastatic sites and high HA levels are an independent prognostic factor for PDAC patients as well as a poor prognosis indicator in prostate, breast, and ovarian cancers [93]. HA binding to CD44 has been shown to downregulate tumor suppressor protein PDCD4, causing anti-apoptosis and chemotherapy resistance and activation of Ras-MAPK and PI3K-protein kinase B signaling pathways causing increased angiogenesis, cell migration and invasion, cell survival, proliferation, and drug resistance in cancer cells [93]. Furthermore, co-culture between CAFs and PDAC cells leads to an increase in the production of HA in the medium and increased *HAS2* mRNA in PDAC cells, leading to increased HA production [93]. In line with this, HA synthesis inhibitor 4-methylumbelliferone has been shown to have anticancer effects in several cancers including melanoma, breast, esophageal, and liver, as well as reducing PDAC growth and metastasis *in vivo* [93].

Along with direct action of HA binding to receptors on cancer cells, HA indirectly affects the TME through increased interstitial fluid pressure, causing vascular collapse, and decreased vascular permeability leading to chemoresistance by impairing drug delivery [93]. This causes an increase in ECM stiffness and downstream mechanosensing which induces CAFs to release aspartate, supporting cancer cell proliferation, while cancer cells in turn secrete glutamate and balance the redox state of CAFs to further promote ECM remodeling [69]. A stiff ECM also mechanoactivates

the YAP/TAZ pathway which plays a central role in cell proliferation, survival, and polarity, especially in tumor cells [69]. Mechanostimuli of the ECM is thus linked to tumor cell metabolism, while tumor cell metabolism is linked to responses by the CAFs to increase ECM stiffness, resulting in a positive feedback between CAFs and tumor cells leading to increased tumor growth and aggressivity. HA inhibitor, PEGPH20, depletes stromal HA and leads to a reduction of interstitial fluid pressure, improving permeability and reversing impaired drug delivery [93]. HA is a powerful oncogenic factor and is secreted by both CAFs and tumor cells, promoting tumor cell proliferation, migration, angiogenesis, and invasion through direct HA-receptor signaling with downstream pathway activation as well as through ECM remodeling creating a barrier to drug delivery and enhanced chemoresistance. On top of the stiffening of the ECM leading to reduced drug delivery, CAFs release glutathione and cysteine, which contribute to stroma-mediated chemoresistance [94]. Glutathione and cysteine are normally released to maintain intracellular GSH hemostasis, but the release of thiols by CAFs increases GSH levels, leading to a reduction of platinum accumulation in cells treated with platinum-based therapies [94]. CAFs also secrete sFRP2, causing loss of key redox effector APE1 in melanoma cells and making them resistant to targeted therapy [95]. CAFs can also secrete cytokines in response to p38 MAPK signaling, mobilizing glycogen in tumor cells to promote proliferation and metastasis [96].

CAF regulate the innate anti-tumor immune response through secretion of several immunomodulatory factors including: CXCL1, CXCL2, CXCL5, CXCL6/GCP-2, CXCL8, CXCL9, CXCL10, CXCL12/SDF1, CXCL2/MCP-1, CCL3, CCL5/Rantes, CCL7, CCL20, CCL26, IL-1b, IL-6, IL-10, VEGF, TGF- $\beta$ , indoleamine-2,3-dioxygenase, prostaglandin E2, tumor necrosis factor, and nitric oxide (as reviewed in [72]). Fibroblasts would secrete similar factors as part of the wound-healing response to recruit immune factors to an injury, but during cancer the CAF secreted factors have an immune suppressive function rather than supportive. During cancer, CAF secretion of CXCL12/SDF1, M-CSF/CSF-1, IL-6, and CCL2/MCP-1 recruits tumor-

associated macrophages to the TME and actively differentiates them into an M2 immunosuppressive phenotype (as reviewed in [72]). CAF secretion of CXCL1, CXCL2, CXCL5, CXCL6, CXCL8, and CCL2 recruits tumor-associated neutrophils (TAN) to the TME and polarize them to an N2 pro-tumoral phenotype, which are correlated with poor prognosis in patients due to TAN-derived factors which promote tumor cell proliferation, migration, and invasion along with inhibition of T cell function (as reviewed in [72]). TGF- $\beta$ , secreted by CAFs, induces miR-183 to inhibit DAP12 transcription resulting in reduced natural killer (NK) activating receptors (NKp30, NKp44, NKG2D) on the NK cell surface (as reviewed in [72]). Along with its impact on NK cells, TGF- $\beta$  also causes dendritic cells (DC) to downregulate MHC class II expression, CD40, CD80, and CD86 leading to decreased antigen presentation efficiency and decreased production of TNF- $\alpha$ , IFN- $\gamma$ , and IL-12, ultimately causing a reduction in T cell recruitment and survival in the TME. TGF- $\beta$  promotes cell death of CD8<sup>+</sup> T cells by inhibiting expression of genes involved in cytotoxic function, including perforin, granzymes A/B, Fas ligand, and IFN- $\gamma$  (as reviewed in [72]). IDO1 secretion further damages T cell response by catabolizing tryptophan degradation into Kyn, creating an immunosuppressive TME and causing T cell anergy and apoptosis through depletion of tryptophan combined with an accumulation of immunosuppressive tryptophan catabolites (as reviewed in [72]). CD4<sup>+</sup> Helper T lymphocytes react to CAF secretion of CCL2, CCL5, and CCL17 along with polarizing cytokines IL-1, IL-6, IL-13, and IL-26 by switching from an anti-tumor T<sub>H</sub>1 response to a pro-tumor T<sub>H</sub>2 and T<sub>H</sub>17 response (as reviewed in [72]). In summary, secretions by CAFs of several immunomodulatory factors regulate the immune response within the tumor niche by creating an immunosuppressive environment which decreases the antigen presenting capabilities of NKs and DCs while simultaneously decreasing cytotoxicity and survival of T cells.

CAF's promote extensive tissue remodeling to form a tumor niche through co-option of normal wound-healing mediators including; cytokines, chemokines, growth factors, and matrix remodeling

enzymes. Crosstalk between CAFs and tumor cells supports a co-evolution between the two that is both immunosuppressive and growth permissive, allowing cancer cells to proliferate rapidly. While much of previous research into cancer has focused on genetic modifications and oncogenes, such as Kras, it has become abundantly clear that a dynamic ECM and TME co-evolving with tumor cells may have a more profound effect on proliferation, immune evasion, and metastasis than the underlying gene mutations which initiated the cancer. There is a demonstrated complexity of CAF-tumor interactions, but many stroma-oncogenic effects are seen across cancer types, suggesting a potential avenue for stroma-directed anticancer therapies.

The increased reliance on glycolysis from the Warburg effect increases tumor growth but also provides several immune suppressive side-effects. It has been shown that highly glycolytic tumors are correlated with inhibition of T cell trafficking to the TME and with resistance to adoptive T cell therapy (as reviewed by [97]). This is most likely due to a side-effect of glycolysis; lactic acid production. Along with the effect on T cells, lactic acid also helps create an acidic environment around the tumor that promotes inflammation, angiogenesis, and tumor progression (as reviewed by [97]). The acidic microenvironment also increases MDSC generation in the TME (as reviewed by [97]) which have strong immunosuppressive properties rather than immunostimulatory through interactions with a variety of other immune cells. The acidic TME produced by high glycolysis levels similarly impairs cytotoxicity and cytokine capabilities of effector T cells and natural killer cells (as reviewed by [97]). While the original understanding of the Warburg effect was simply on proliferation and growth, it has now been shown to be a much more complex process where the by-products of rapidly reproducing tumor cells can have a direct impact on T cell, NK cell, DC cell, and macrophage immune responses creating an immune suppressive environment to promote tumor cell survival. The signaling goes both ways and  $\text{IFN}\gamma$ , released by T Cells, can control the release of glutathione and cysteine by CAFs through upregulating the JAK/STAT1 pathway and subsequently causing transcriptional repression of xc\_ cystine and glutamate antiporter [94], this

reduces the glutathione and cysteine released by CAFs and reduces the stromal-mediated chemotherapy resistance. As such it makes sense that the efficacy of chemotherapy is positively correlated with the amounts of tumor-infiltrating CD8<sup>+</sup> T cells and that suppression of CD8<sup>+</sup> T cells leads to chemotherapy resistance [94]. Cross-talk between CD8<sup>+</sup> T cells and fibroblasts normally support immune response in wound-healing, but in cancer this communication is co-opted to support tumor growth.

Along with glycolysis, the Warburg effect causes an increase in glutaminolysis, amino acid and lipid metabolism, pentose phosphate pathway flux, macromolecule biosynthesis, mitochondrial biogenesis, and maintenance of redox state (as reviewed by [69]) all of which are required to allow tumor cells to continue proliferating in the nutrient poor and hypoxic TME. The metabolic demands of the cells are too high to rely on glycolysis alone, and so cancer cells turn to glutaminolysis to create TCA cycle intermediates, including glutaminase to support aspartate production and induce cell proliferation (as reviewed by [69]). These metabolic changes may be linked to CAF metabolism and ECM stiffness which together provide the tumor niche which supports tumor progression.

Beyond metabolic dysregulation in its local tissue context, cancer is associated with metabolic alterations in the host [98]. Abnormal whole-body metabolic responses to cancer include cancer cachexia, a potentially lethal wasting syndrome driven by negative energy balance and associated with loss of adipose and muscle tissue [99]. Cachexia has been mechanistically linked to the inflammatory response to cancer, and particularly to elevated levels of systemic pro-inflammatory cytokines [100]. Cachexia is a common and early event in the pathogenesis of some cancer types, and evidence of tissue breakdown associated with cachexia may even be a biomarker of early tumorigenesis [101, 102]. Though mechanisms driving cancer cachexia are complex and remain to be elucidated, early evidence has emerged that CAFs may play a role in tissue wasting, in part by mediating an inflammatory response and in part through direct interactions with relevant host tissues. Fibroblast activation protein- $\alpha$  (FAP $\alpha$ ) marks activated fibroblastic cells in tumors [103]

and other pathologic inflammatory conditions, including atherosclerosis [104]. FAP $\alpha$ -positive cells in the primary tumor microenvironment have been associated with immune suppression, promoting T cell exclusion via secretion of CXCL12 [83]. However, recent work using a FAP $\alpha$  reporter in mice showed that these FAP $\alpha$ -expressing fibroblastic cells can be found in numerous tissues in the adult mouse, including skeletal muscle [105]. FAP $\alpha$ -positive cells across tissue contexts have similar transcriptomes, suggesting a common lineage. Depletion of FAP $\alpha$ -positive cells in healthy mice caused a cachexia-like syndrome, characterized by rapid weight loss and reduced muscle mass despite adequate food intake [31, 105]. FAP $\alpha$ -positive fibroblasts in skeletal muscle were shown to be the predominant source of Lama2 and Follistatin (Fst288 and Fst315), key regulators of myofiber thickness and muscle growth [105]. Significant loss of FAP $\alpha$ -positive cells from skeletal muscle in cachectic tumor models were found in the mouse model [105]. These findings implicate fibroblastic cells in maintenance of muscle mass, and raise the possibility that fibroblast loss from skeletal muscle promotes the muscle wasting observed in cancer cachexia, with major implications for systemic metabolism.

The host metabolic perturbations associated with cancer progression have been partly attributed to increased systemic levels of pro-inflammatory cytokines [100]. IL6 in particular has been functionally linked to cachexia [106-113], and is elevated in patients with cachexia-associated cancers [114-116]. Further, activation of STAT3 downstream of IL6 has been linked to muscle wasting in cancer [117]. In multiple cancer types, CAFs are reported as a significant source of IL6 in the tumor microenvironment [118-122], highlighting CAF-derived IL6 as a potential link to cancer cachexia. Shining light on the role of IL6 in cancer cachexia, recent work demonstrated that the elevated IL6 in cachexia-associated tumor models suppresses hepatic ketogenesis, by downregulating expression of master ketogenic regulator PPAR $\alpha$  in the liver [106]. IL6 promoted metabolic stress in response to caloric restriction, including elevated corticosterone levels, and recombinant IL6 lowered fasting ketone and glucose levels. Interestingly, the increase in systemic

glucocorticoids in response to IL6-mediated suppression of hepatic ketogenesis was associated with a suppression of anti-tumor immunity. Reduced food intake was a driver of the increase in glucocorticoids and immune suppression, and caloric deficiency is commonly seen among patients with cachexia-associated cancers. Notably, IL6 can also directly regulate the hypothalamic-pituitary-adrenal axis [123], and may further contribute to cachexia through its activity in the brain. While CAFs can function to locally suppress anti-tumor immunity, these findings raise the possibility that CAFs participate in a complex metabolic and inflammatory host response, leading to systemic elevation of glucocorticoids and immune suppression.

While studies of the metabolic, immune-modulatory, or paracrine signaling functions of CAFs in various solid tumors suggest tumor-supportive roles for these cells, three papers published in 2014 demonstrated a protective role for CAFs in pancreatic cancer with respect to survival outcome [90-92]. To probe the roles of the abundant CAF population in these tumors, the authors used genetic or pharmacologic approaches to ablate CAFs during pancreatic tumorigenesis, either ablating Shh-dependent CAFs [90, 92] or  $\alpha$ SMA-positive CAFs [91]. Though these different systems yielded somewhat different results, these studies together provide compelling evidence that CAF ablation causes mice to succumb significantly earlier to the disease compared to CAF-replete controls. Interestingly, in the study by Rhim et al. employing both genetic and pharmacologic inhibition of Shh to ablate CAFs, the authors report that mice succumb with very small tumors, but with severe cachexia, including wasting of adipose tissue and muscle exceeding that seen in controls. Data are shown from systemic Shh inhibition, but the authors report that the same phenotype was observed in their genetic model which specifically targets Shh in the pancreas, and therefore specifically inhibits Shh-dependent CAFs within the local tumor microenvironment. This raises the intriguing possibility that pancreatic CAFs promote improved survival outcomes in part by inhibiting pro-cachectic mechanisms within the primary tumor. A mechanistic connection between Shh-dependent CAF function and critical mediators of cancer cachexia has not been established.

However, further investigation into this axis may be warranted, as therapies targeting pancreatic CAFs would ideally leave any such cachexia-suppressive mechanisms intact.

Likely related to their evolutionary role in the wound-healing response, CAFs are important sources of growth factors in the tumor microenvironment, as discussed above. In multiple solid tumor types, CAFs have been described as significant sources of growth factor ligands for the epidermal growth factor receptor (EGFR), including high-affinity ligands betacellulin (BTC) [85] and heparin-binding EGF-like growth factor (HB-EGF) [124] as well as lower-affinity ligand epiregulin (EREG) [125]. CAFs and normal fibroblasts are also prominent producers of parathyroid hormone-related protein (PTHrP) [126, 127], a developmental regulatory molecule activated by EGFR signaling [128]. A recent study aimed to identify novel regulators of cancer cachexia, and found a novel connection between factors that promote adipose tissue browning and the onset of features of cachexia including weight loss and muscle atrophy [129]. Cachexia is characterized in part by increased resting energy expenditure, which has been linked to increased thermogenesis by brown adipose tissue [130-133] and to browning of white adipose tissue [134]. Kir et al. found that Lewis lung carcinoma (LLC) cells induce adipose tissue browning and cachexia. By comparing gene expression in more thermogenic versus less thermogenic clones, they identified candidate paracrine thermogenic regulators. By testing candidate recombinant proteins, the authors found that the 3 EGFR ligands discussed above—BTC, HB-EGF, and EREG—as well as PTHrP all stimulate thermogenic gene expression in primary adipocytes. Though the study focused on cancer cell-derived PTHrP as a key regulator of adipose tissue browning in the LLC system, a link between EGFR ligand production and cancer cachexia is intriguing and warrants further study. Activation of EGFR/MEK signaling in the primary tumor has been recently linked to MEK activation and wasting in host tissues [135], and while CAFs as a source for these ligands or for PTHrP have not been specifically addressed, EGFR signaling has been functionally linked to cachexia and/or energy expenditure in additional systems [136, 137].

Providing ligands which act either via tumor cells or directly on adipocytes to promote thermogenesis might suggest a deleterious role for CAFs as promoters of cancer cachexia, and such a role may indeed be tissue- and context-dependent.

Non-malignant cells of the tumor microenvironment, including but not limited to CAFs, exert an important influence on key metabolic pathways in cancer cells and on intratumoral metabolite levels. The significance of these paracrine interactions warrants further study *in vivo*, as cancer cells exhibit specific and complex metabolic requirements within host tissues [138-142] that are difficult to model using *in vitro* systems. CAFs present a limitation in this regard, as specific Cre lines to achieve genetic manipulation in these cells are presently lacking. Further, while studies of metabolite exchange *in vitro* have established important modes of cell-cell contact within the tumor microenvironment, validation and further investigation of these interactions will be bolstered by emerging means to study intercellular metabolic relationships within tissues [143]. In considering CAF-cancer cell interactions as potential therapeutic targets, it will be important to understand the critical and non-redundant metabolic functions of CAFs that enable cancer cells to maintain their proliferative capacity within a nutrient-poor tumor microenvironment. As cancer cells exhibit metabolic plasticity [144, 145], therapies targeting metabolism-modulating pathways will likely need to target parallel mechanisms fulfilling bioenergetic needs, or to combine metabolic inhibitors with therapeutic interventions that suppress cancer cell plasticity and thus the capacity for metabolic adaptation. Further, as suppression of anti-tumor immunity is increasingly linked to intratumoral metabolite levels and to activity of key metabolic pathways in immune cells [146], the consequence of the CAF secretome on the metabolism and function of immune cells in the tumor microenvironment warrants further investigation.

### **Mutations and pathways driving PDAC development.**

Although 5-year survival rates for PDAC have increased from 6% to 10% since 2015, the majority of these improvements are in neoadjuvant and adjuvant therapies which are effective in

the population of PDAC patients which have pre-existing deficiencies in DNA damage repair[147]. PDAC, like many cancers, is characterized by complex chromosomal rearrangement patterns and high genomic instability[148]. When combined with mutations in DNA double-strand break (DSB) repair or DNA damage repair (DDR) pathways, including non-homologous end joining (NHEJ) and homologous recombination (HR) pathways, the genomic instability of PDAC is further reduced. However, mutations in DDR pathways also represent a personalized medicine target in patients who express alterations in these repair pathways. Providing a weakness in PDAC tumors to accumulation of unresolved single-strand breaks (SSB) and DSB, leading to increased cell death. DNA damage must be repaired or failure of cellular division and cell death can occur. SSB DNA damage can be repaired through base excision mismatch repair (MMR) or nucleotide excision repair (NER), while DSB DNA damage can be repaired through NHEJ or HR (as reviewed by[148]). Mutations in *BRCA1*, *BRCA2*, *ATM*, and *PALB2* have been frequently described in PDAC[149, 150] and have been suggested to be predictive biomarkers for response to poly ADP-ribose polymerase (PARP) inhibitors, such as Olaparib, treatment[148, 151-153].

During HR repair BRCA1, BRCA2, PALB2 form a complex to activate RAD51 and allow sister chromatid homologous sequences to combine, an essential step for DNA repair through HR. Mutations in any of these three proteins can cause a HR-deficient phenotype, often referred to as “*BRCAness*” of the tumor, resulting in tumors more susceptible to classical DNA-damaging agents and therapeutics[148]. ATM is involved in the repair of DSBs when a complex of MRE11, RAD50, and NBS1 proteins activates the cell cycle regulatory serine/threonine kinases ataxia telangiectasia mutated and the ATM and RAD3-related (ATR) protein to start formation on the ends of the protruding 3’ sides of the break, which in turn recruits the BRCA1/PALB2/BRCA2 complex and activation of RAD51 for binding SSB DNA segments[148]. ATM also activates cell cycle progression arrest through activation of CHK2 and subsequent interaction with TP53[154].

Rather than just by being activated by ATM, ATR can be instead activated by phosphorylation of the Fanconi anemia (FA) core complex to repair the DNA crosslink adduct[148]. This redundancy in DNA repair mechanisms may help explain why despite being the most frequently mutated DNA repair gene found in sporadic PDAC (at 3.4%), ATM germline mutations are detected in patients lacking a family history of cancer[155]. This suggests that mutations in DDR genes have an incomplete penetrance in PDAC and that while mutations in these genes may suggest a patient would be more susceptible to platinum agents and other therapeutics which result in a buildup of DSBs, the mutations themselves do not necessarily fully explain the development of the cancer.

The majority of PDAC cases do not occur based on DNA damage repair deficiencies which makes them more difficult to treat and identification of high-risk families more complex[147, 156-159]. There are, however, several recurrent somatic mutations in PDAC which may be the main drivers for its development. These mutations include *KRAS*, *TP53*, *CDKN2A*, *SMAD4*, *RNF43*, *ARID1A*, *TGF $\beta$ 2*, *GNAS*, *RREB1*, *PBRM1*, *BRAF*, and *CTNNB1*, but only mutations of *KRAS*, *P16/CDKN2A*, *TP53*, and *SMAD4/DPCA4* genes are considered to be the main driver mutations of PDAC[147, 159, 160]. Mutations in *KRAS* are found in more than 90% of PDAC cases but mutations in RAS, WNT, NOTCH signaling, TGF $\beta$  pathway, cell cycle control, epigenetic regulation and DNA damage repair are also found and identified in PDAC patients[8, 147, 161]. Mutations in *KRAS* are also frequently found in PanINs, PDAC precursor lesions, while other mutations are not typically found until late stages of tumor development suggesting that *KRAS* mutations may be an initiating event in the formation of PDAC[20]. Indeed, genetically engineered mouse models with oncogenic pancreatic *Kras* recapitulate the progression of PanINs to pancreatic cancer, supporting the idea that *KRAS* may be an important precursor for PDAC development in patients with this mutation[162].

Mouse models of PDAC have allowed the research of early stages of pancreatic cancer to be explored, as most human PDAC cases are diagnosed too late for early-stage samples to be collected. There is some controversy with the accuracy of mouse models, as human PDAC is so poorly understood that it is difficult to say what cell of origin is most common in human disease[163], and therefore difficult to say if the same cell of origin is occurring in the mouse models. Mouse models of PDAC appear to occur from acinar cells which dedifferentiate through acinar-ductal metaplasia (ADM) or through ductal cells which transform into aggressive tumors with loss of *Trp53*[164] or inactivation of *Pten*[165] in addition to an underlying *Kras* mutation. The formation of ductal origin PDAC follows closely with that of human disease, where the *Kras* mutation is not sufficient alone to achieve PDAC development and mice develop lesions as they age with PDAC developing only at an advanced age and with low penetrance[162]. Mutational characterization of PDAC is made more difficult because PDAC is made of dense desmoplasia with only 5-20% of the tumor being comprised of PDAC cells[159]. This complicates single cell analysis and other methodologies, as actual PDAC cells make up such a small percentage of collected cell mass from a tumor.

PDAC develops from multiple PanIN sites, which can take decades to develop into invasive PDAC[166]. Inflammation is one of the key significant factors in development of PDAC with both hereditary and sporadic pancreatitis associated with increased risk. Combinations of genomic damage and cell proliferation from inflammation creates a favorable environment for malignant transformation of PDAC cells[167]. Mouse models for pancreatitis use caerulein treatment, a cholecystokinin agonist[168], to drive accumulation of a fibroinflammatory stroma which when combined with oncogenic *Kras* leads to ADM and PanIN formation[169, 170]. There is further evidence that inflammatory induction of PDAC relies on activation of MAPK signaling and that expression of oncogenic *Kras* is not enough to for carcinogenesis in adults, while chronic pancreatitis is[80, 122, 171]. Typically, cancers are subtyped for best treatment options, however

there have been no obvious genetic mutations underlying PDAC subtypes, aside from mutations in DDR as discussed above, making subtyping non-DDR PDAC for best treatment difficult[147]. *TP53* mutation may be linked to the squamous/basal-like subtype, but more research is needed for subtype classification of PDAC[147, 172]. It is possible that epigenetic changes, and non-coding mutations, may play the primary role in PDAC subtypes or changes to the TME could be controlling transcriptional changes of PDAC tumor cells[147, 173, 174].

Further research into somatic mutations of PDAC has suggested that there may be driver mutations in 15 genes or more including kinases, cell cycle proteins, and cell adhesion proteins[160]. *PIK3CG*, *DGKA*, *STK33*, *PRKCG* are kinases which may be driver genes in PDAC and could potentially cross-talk with Kras-signaling pathways, allowing for synergistic aberrant signaling networks for growth, survival, and metastasis of PDAC[160]. Several of these driver mutations may be the catalyst for inflammation which is known to be a significant factor in the development of PDAC, and allow KRAS-driven changes to take affect[167, 175]. Other KRAS-driven changes involve metabolic changes which may be crucial for the development of PDAC.

### **Metabolic changes driving PDAC development**

There are currently considered to be ten main hallmarks of cancer which, as research continues, will probably be expanded over the years. List adapted from the *Ten Hallmarks of Cancer* (Hanahan and Weinberg, 2000; Hanahan 2011)[176, 177].

1. Growth autonomy: cells no longer require normal signaling to undergo division.
2. Growth inhibition insensitivity: cells no longer respond to growth inhibitory signals, both external and internal.
3. Evasion of apoptosis: apoptosis is not induced even when DNA damage or abnormalities are detected.
4. Telomeres no longer regulate reproductive potential: cell cycle arrest no longer occurs with shortened telomeres, or cells maintain the length of their telomeres despite frequent replication.
5. Induced and sustained angiogenesis: signaling for stimulation of blood vessel development is no longer required for induction and sustainment of angiogenesis.

6. Invasion and metastasis: cancer cells invade other tissues, which normal cells do not do past embryo development.
7. Deregulation and reprogramming of metabolic pathways: high demand for energy and nutrients forces cancer cells to use abnormal metabolism to meet them.
8. Immune system suppression and evasion: tumors develop the ability to evade the immune system.
9. Chromosomal instability: lack of replicative arrest and response to apoptosis leads to increased chromosomal instability.
10. Inflammation: local chronic inflammation and associated immune effects are seen in most cancers.

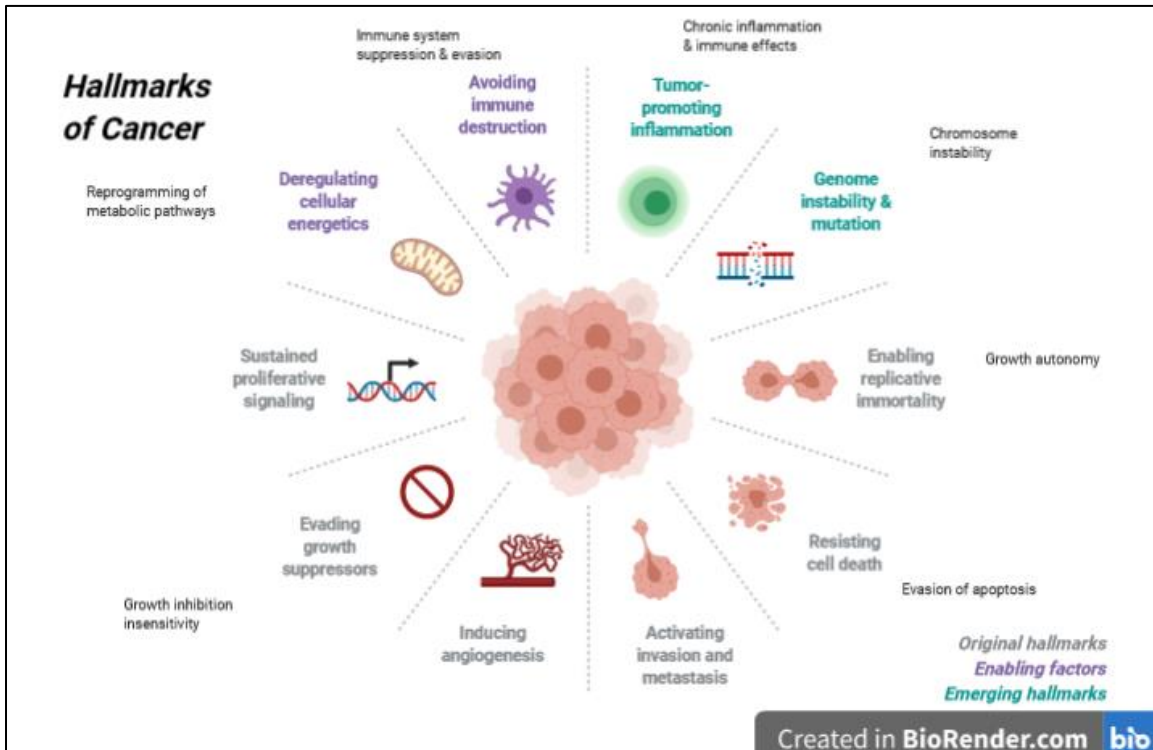


Figure 1.3 the hallmarks of cancer.

Graphical representation of the 10 hallmarks of cancer: avoiding immune destruction, tumor-promoting inflammation, genome instability, replicative immortality, resisting cell death, invasion and metastasis, angiogenesis, evasion of growth suppressors, sustained proliferative signaling, and deregulation of cellular energetics. Adapted from the Ten Hallmarks of Cancer (Hanahan and Weinberg, 2000; Hanahan 2011) and created with BioRender.com from an adapted existing template.

Metabolic alterations of cancer cells allow for rapid proliferation even in poor nutrient environments, with changes to cellular metabolism recognized as a hallmark of cancer since the increased glucose uptake and aerobic glycolysis of cancer cells was first observed by Otto Warburg in 1956[178]. His publication on the origin of cancer cells lead to the increased glucose uptake and aerobic glycolysis of cancer cells to be referred to as the “Warburg Effect”, a term still in general use today. In cancer, aerobic glycolysis is the most frequent type of glucose conversion

to lactate, creating only 2 moles ATP per 1 mole glucose, while in non-cancer cells 38 moles of ATP are synthesized per 1 mole glucose under aerobic conditions[178-180]. These changes also support an increase in lipogenic enzymes and increased glucose carbon incorporation into lipids, allowing more membrane formation and supporting rapid proliferation of cancer cells[179, 181-183]. Increase of fatty acid synthesis is linked to carcinogenesis and cancer cell survival, with

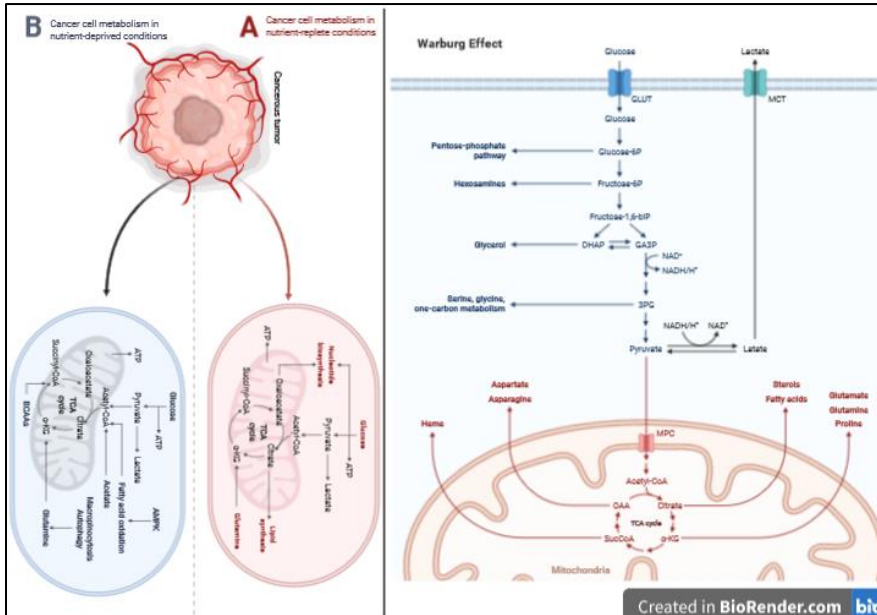


Figure 1.4 the Warburg Effect and cancer cell metabolism.

Cancer cells undergo different metabolic pathways depending on if they are in nutrient-deprived or nutrient-replete conditions [178-183]. The Warburg Effect is one of the earliest and best described metabolic changes that typically occur in cancer cells to allow for rapid proliferation in poor nutrient environments, by changing cellular metabolism to increase glucose uptake and aerobic glycolysis [178]. Figure created in BioRender.com from existing templates.

inhibition of lipogenic enzymes decreasing tumor growth[179]. High Fatty Acid Synthase (FASN) levels in serum of PDAC patients has been linked to high mortality[179].

Along with synthesizing fatty acids, cancer cells

can also use fatty acids from circulation whether from diet, synthesized in liver, or released from adipose tissue. Pyruvate is one of the key metabolic products for cells and is formed from glucose during aerobic glycolysis. Pyruvate is then converted to lactate by lactate-dehydrogenase (LDH) or is taken to the mitochondria where it is decarboxylated to pyruvate dehydrogenase (PDH) by acetyl-CoA[179]. Within the mitochondria, citrate synthase (CS) or in the cytosol, ATP citrate lyase (ACLY), acetyl-CoA is then formed, providing a key factor for lipid biosynthesis[179]. PDH-catalyzed reactions can also occur through PDH kinase activity in hypoxic conditions, or with certain oncogenic influences, allowing for non-glucose carbon sources to be used for lipid

synthesis[184, 185]. Upregulation of PDH kinase 1 (PDHK1)- phosphorylates mitochondrial PDH, causing inactivation of the pyruvate dehydrogenase complex- is linked to Myc and HIF-1 oncogene activity[185]. This allows tumor cells to transition to aerobic glycolysis rather than oxidative phosphorylation and tyrosine phosphorylation of PDHK1 is linked to decreased mitochondrial use of pyruvate and increased tumor growth in mice, showing another metabolic change in tumor cells that promotes the Warburg effect[185]. As research has progressed and a better, wider, understanding of cellular metabolism has occurred it has become apparent that the Warburg effect may be more complicated than originally proposed.

One thing that has become clear, is that cancer cells have a preference for glutamine uptake and resort to glycolysis and linked lactate secretion, rather than the more efficient ATP production through mitochondrial oxidative phosphorylation, in order to rapidly produce biomass[186]. Though it may seem to be counter-intuitive that rapidly reproducing cells would use less efficient ATP productive measures, it makes sense in the broader understanding that cellular metabolism relies on more than just ATP and cancer cells must either intake all required nutrients or produce them. In the hypoxic, nutrient-poor TME of PDAC cancer cells take in what nutrients they can and shunt excess metabolites to metabolic pathways for biosynthesis of those lacking in the TME[187].

Studies on *KRAS*, the main oncogenic driver associated with PDAC, suggests that oncogenic *Kras* results in remodeling of multiple metabolic pathways. It has been known that oncogenic *Kras* it is required for PDAC tumor maintenance and that it reprograms PDAC metabolism by increasing glucose uptake and glycolysis[188]. Recent research suggests that it does this through regulation of glucose transporters and rate-limiting enzymes at the transcriptional level, resulting in a shift in cellular metabolism away from glucose and towards anabolic pathways like the Hexosamine Biosynthetic Pathway (HBP) for protein glycosylation and the Pentose phosphate pathway (PPP) for ribose production[188]. The non-oxidative arm of PPP creates precursors for

DNA and RNA biosynthesis, which as cancer cells require both energy and biosynthetic precursors for cell growth, it makes sense that demand for cellular building blocks would increase as well. Work on oncogenic *Kras* has also shown that there may be changes to the TME metabolism to match that of tumor development. When tumors express oncogenic *Kras*, they begin to develop the prominent desmoplastic stroma of PDAC and stopping oncogenic *Kras* expression is capable of reducing the amount of SMA-positive pancreatic stellate cells in the TME, which are linked to development of the desmoplasia and poor prognosis[188]. The communication between tumor cells and the desmoplastic stroma is a developing research area, with the dense desmoplasia of PDAC present a particularly rich environment for study. It has been shown in the literature that metabolic reworking of PDAC results in metabolic reprogramming of nearby stellate cells[2]. In summary it can be concluded that cancer cells undergo metabolic reprogramming which is both plastic and responsive to changes in the TME, which is in turn capable of undergoing its own metabolic reprogramming. This crosstalk has been linked to nuclear receptor ligand-activated transcription and downstream inflammatory signaling of cancer cells.

#### **Inflammatory signaling of cancer cells:**

Nuclear receptor ligand-activated transcription regulates metabolism of lipids, drugs, energy, cellular differentiation, reproduction, and other key developmental pathways[189]. These receptors are a type of ligand-induced molecular switch activated by intracellular signals, including lipophilic hormones, dietary lipids, and vitamins[190]. Nuclear receptors have a variable NH<sub>3</sub>-terminal region which has an AF-1 ligand-independent activation domain and a central DNA-binding domain of two conserved zinc-finger motifs which are targeted to hormone response elements (HRE), specific DNA sequences consisting of two hexa-nucleotide motifs AGGTCA and variants[189]. They also contain an C-terminal ligand-binding domain responsible for receptor dimerization, ligand recognition, and cofactor interaction and a C-terminal AF-2

helix which changes conformation following ligand binding[189]. When un-bound to ligands nuclear receptors are either in the cytoplasm in complex with heat shock proteins or other chaperones or are constitutively bound to HRE acting as a repressive complex with SMRT/NCOR or HDAC corepressors[191, 192]. Because of the flexibility of the structure of nuclear receptors, they can have constitutive receptor activation, when AF-2 is in an active conformation, or be repressive when in complex with other corepressors, when AF-2 is not in an active conformation. When nuclear receptors are constitutively active their activity is regulated by amount of nuclear receptor or by signal-induced modifications to the receptor like phosphorylation or acetylation[189].

The peroxisome proliferator-activated receptor (PPAR) nuclear receptor superfamily is a specific type of nuclear receptor which is classified as “Adopted Orphan Receptors”, based on sequence homology to endocrine receptors, and act as lipid sensors for fatty acids[189]. PPAR $\gamma$  and PPAR $\alpha$  have been shown to be drug targets for reversing insulin resistance and dyslipidemia[193, 194]. PPAR $\delta$  is less well studied but is believed to be a ligand receptor for lipids and could prove important for inflammation[189]. All PPARs form a heterodimer with retinoid X receptor (RXR), a member of the steroid/thyroid hormone superfamily of nuclear receptors with roles in cell differentiation, development, and metabolism[195].

PPAR $\alpha$  was identified by fenofibrate, a fibrate-class of anti-hyperlipidemic drug, and is now known to bind to and act as an endogenous sensor for polyunsaturated fatty acids[194]. PPAR $\alpha$  is found mostly in liver, heart, muscle, and kidney cells where it regulates apolipoprotein synthesis, fatty acid oxidation, and hepatic peroxisomal fatty acid oxidation during fasting[189]. It is also found in human macrophage foam cells where it has anti-inflammatory and anti-atherogenic effects[196]. PPAR $\alpha$  agonists have been used in both rodent models and human clinical studies, where they have been shown to correct dyslipidemia and reduce cardiovascular mortality and

morbidity[194]. In mouse models PPAR $\alpha$  agonists appear to suppress satiety and improve insulin resistance, but these effects have not yet been recapitulated in human trials[189].

PPAR $\gamma$  is targeted by thiazolidinedione (TZD)-class of insulin sensitizers, majority of current oral anti-diabetic drugs, and is mainly expressed in adipose tissue where it acts as a regulator of adipogenesis[189, 193]. It is thought that TZDs work to increase insulin sensitivity by activating PPAR $\gamma$  in adipocytes causing an increase in fat storage and secretion of adipokines, like adiponectin[193]. The signaling of PPAR $\gamma$  in insulin sensitization appears to be more complicated than a direct agonist benefit. It appears to be paradoxical that PPAR $\gamma$  can promote insulin sensitivity while also promoting fat differentiation, a process which normally induces insulin resistance, yet studies in mice show that partial loss-of-function mutations of Pro12Ala in PPAR $\gamma$  improves insulin sensitivity while gain-of-function Pro115Gln mutations cause obesity and insulin resistance[193]. Human genetic studies also suggest that partial decrease in PPAR $\gamma$  activity could be more effective than complete agonists for increasing insulin sensitization, suggesting a complexity to PPAR $\gamma$  signaling and activity[189]. Cancer-associated inflammation has been linked to PPAR $\gamma$  with research showing that activation of PPAR $\gamma$  in dendritic cells decreases CD1a cell surface glycoproteins, which present self- and non-self-lipid and glycolipid antigens, and increases CD1d levels, promoting induction of invariant natural killer T cell expansion[197, 198].

PPAR $\delta$  has been studied the least of all the PPARs but is thought to be mainly involved in the promotion of mitochondrial fatty acid oxidation, energy expenditure, and thermogenesis -with PPAR $\delta$  knockout mice showing increased rates of obesity and insulin resistance[189]. Unlike PPAR $\gamma$  or PPAR $\alpha$ , PPAR $\delta$  is expressed ubiquitously and is a sensor for polyunsaturated fatty acids and VLDL lipoprotein particles[199]. It was noticed that PPAR $\delta$  plays a role in protecting cells from metabolic-syndrome-related diseases, including insulin resistance and type 2 diabetes, but when PPAR $\delta$  agonists (activating ligands specific for PPAR $\delta$ ) were tried as therapeutics there

was an increase in cancer progression[200]. This increase in cancer progression appeared to be from a defense mechanism to nutritional deprivation and energy stress, employed by cancer cells as a result of increased PPAR $\delta$  activity[200]. PPAR $\delta$  promotion of fatty acid oxidation could be the cause for increased cancer progression, though PPAR $\delta$  also appears to have anti-inflammatory functions in some situations and to increase inflammation in others (as reviewed in [200]). These contrasting roles of PPAR $\delta$  indicated how context specific its activity may be, especially in cancer where cross-talk between tumor cells and the TME could be affecting signaling and activity.

Signaling of the PPAR Nuclear receptor superfamily has been linked to tumor-associated inflammation, angiogenesis, and fibrosis, as well as to cancer initiation, progression, and treatment resistance[197]. Tumorigenesis is a multistep process which requires numerous components to develop. These components usually come from the surrounding TME and are indicative of a call and response interplay between cancer cells and tumor-associated cell types. PPAR nuclear receptors are believed to be one of the key signaling mechanisms within tumor cells which allow them to communicate to the TME to increase tumor-associated inflammation, angiogenesis, and fibrosis[197]. The release of secreted factors by cancer cells, for example transforming growth factor- $\beta$  (TGF- $\beta$ ) or stromal cell-derived factor 1 (SDF-1), have been shown to change the oncogenic and metastatic potential of tissue surrounding the tumor[201].

Complicated crosstalk between tumor cells and cells of the TME, including immune and stromal cells, results in changes to the factors secreted by both tumor cells and cells of the TME. This allows for the same immune or inflammatory cell subtypes to have protumorigenic functions in some situations and antitumorigenic functions in other contexts[197]. Along with their effect on supportive cells of the TME, secreted factors by cancer cells also have a complex crosstalk with infiltrating immune cells, and it is believed that PPAR nuclear receptor mediated transcriptional signaling could be playing a role in protumorigenic vs antitumorigenic responses of these

infiltrating immune cells[197]. Activity of PPAR signaling has been linked to inflammatory signaling in cancer, including to increased production of pro-inflammatory cyclooxygenase-2 (COX-2) production and downstream prostaglandin (PG) synthesis[202].

### **COX-2 signaling**

For years nonsteroidal anti-inflammatory drugs (NSAIDs) have seen broad use as potent anti-inflammatory agents that were understood to inhibit cyclooxygenase (COX) enzymes to inhibit downstream prostaglandins at sites of inflammation. Long-term use of NSAIDs has had unfortunate side effects which arise from inhibition of gastrointestinal and renal prostaglandins, leading to toxicities and limiting the usefulness of these cheap and effective drugs[203]. Research into NSAIDs and their function revealed the existence of two types of cyclooxygenase enzymes, COX-1 and COX-2, with different functions. The anti-inflammatory capabilities of general COX inhibitors appears to function through COX-2, while toxicities in the gastrointestinal tract appear to be related through inhibition of COX-1, leading to the development of selective inhibitors for COX-2[203]. This difference in activity appears to be linked to the idea that COX-1 is constitutively expressed across tissue types, but COX-2 is only expressed upon induction by proinflammatory cytokines[204]. Following activation, COX-2 produces prostaglandins which mediate inflammatory response and pain signaling transmission[204].

The EPHA2/TGF- $\beta$ /COX-2 axis has been indicated in pancreatic cancer as one of the major components of the immunosuppressive barrier that prevents T cells from infiltrating into PDAC[205, 206]. COX-2 is encoded by the gene prostaglandin endoperoxide synthase 2 (PTGS2), which is downstream of TGF- $\beta$  and EPHA2 signaling, and is believed to be involved in the exclusion of T cells in the PDAC TME[206]. Research into the EPHA2/TGF- $\beta$ /COX-2 axis has shown that deletion of *Epha2*, sensitized tumors to immunotherapy and reversed T cell exclusion and that *Ptgs2* deletion worked similarly[206]. The non-T cell-inflamed tumor

phenotype typical of PDAC has been linked to decreased sensitivity to immunotherapies and poor patient prognosis[207].

Along with the recently discovered EPHA2/TGF- $\beta$ /COX-2 axis, COX-2 has been shown to promote tumor growth and to suppress tumor immunity[208]. COX-2 appears to be involved in resistance to immunotherapy through its crucial role in innate and adaptive immune response through suppression of dendritic cells, natural killer, and T cells, through the COX-2-prostaglandin E<sub>2</sub> (PGE<sub>2</sub>) membrane receptor signal cascade which inhibits type-1 immunity while promoting tumor immune evasion[208]. PGE<sub>2</sub> is a modulator of activated macrophages and tumor-associated macrophages (TAMs) are a major subpopulation of infiltrating immune cells in PDAC. COX-2 is believed to hinder macrophage polarization to M1 subtype while promoting M2 macrophage differentiation and downstream macrophage-mediated immune suppression of regulatory T cell infiltration, leading to reduced CD8<sup>+</sup> cytotoxic T cell function[209-211]. PGE<sub>2</sub> inhibits natural killer cells, lymphocytes involved in innate immunity, by acting on their EP receptors (EP2 and EP4) and inhibiting their ability to migrate, secrete IFN $\gamma$ , and exert cytotoxic effects[212]. It has also been shown that regulatory T cells are significantly associated with COX-2 expression along with intra-tumoral localization of regulatory T cells, and that these regulatory T cells can contribute to the immunosuppressive TME in cancer by inhibiting effector T cells in a COX-2 dependent manner[213-215]. COX-2, through its activity with PGE<sub>2</sub> also affects the maturation of dendritic cells and the communication between the innate and adaptive immune responses. COX-2 decreases expression of MHC class II in dendritic cells, reducing their ability to present antigen to activate T cells, while PGE<sub>2</sub> increases IL-10 production further downregulating dendritic cellular functions[216].

Studies in a breast cancer murine model with genetic COX-2 knockout mice showed that loss of COX-2 disrupted M2-like tumor-associated macrophage function, enhanced T cell survival, and immune surveillance[217]. A study in breast cancer involving mice fed etodolac showed that

COX-2 inhibition leads to a reduction in regulatory T cells and myeloid derived suppressor cells within tumors, showing evidence of a shift in TME to favor Th1 immune responses rather than the tumor supportive Th2[218].

## **Rationale and Hypothesis:**

PDAC relies on metabolic and immunosuppressive changes to grow and thrive in the hypoxic, low-nutrient, stroma rich TME[16, 219-228]. As shown by our lab and other, in early stages of PDAC development, fibroblasts interact with neoplastic cells and secrete fatty acids into the TME[3, 4, 229-232]. The functional role of these released fatty acids is unknown, but we hypothesized that fatty acid transporters, which are known to be upregulated in PDAC, could be importing them to assist with neoplastic cell growth in the nutrient-poor PDAC TME. Of the fatty acid transporters in PDAC, GOT2/FABPpm is consistently upregulated and is a poorly studied protein in the context of cancer. GOT2 is an enzymatic protein known mostly for its mitochondrial and metabolic roles, but with additional known and suspected fatty acid binding activities. While current knowledge of GOT2 has been focused on its metabolic roles, with increased understanding on the importance of fatty acids as signaling molecules for both metabolic activity and immune response we were curious as to what additional roles GOT2 provided, especially in a PDAC context, through its fatty acid binding capabilities.

We hypothesize that GOT2 has roles beyond its canonical mitochondrial and plasma membrane fatty acid transport, and that GOT2 has specific functions related to its fatty acid transport roles that are separate from its mitochondrial enzymatic roles. Although the only known disease linked to GOT2 mutations is a treatable malate-aspartate shuttle-related encephalopathy[14], GOT2 is upregulated in PDAC and other cancers suggesting an importance in either the development or maintenance of this disease. We will investigate the role of GOT2 in PDAC through the creation of GOT2-null murine and human cell lines for *in vitro* and *in vivo* characterization.

Chapter 2: Novel nuclear location for GOT2 in PDAC and arachidonic acid binding and fatty acid transport capabilities may have a role in PDAC *in vivo* development.

Portions of this chapter were included in a publication submitted to Nature and is undergoing revisions as of Jan 25<sup>th</sup>, 2021.

“A cancer cell-intrinsic GOT2-PPAR $\delta$  axis suppresses antitumor immunity”

Hannah Sanford-Crane, Jaime Abrego, Chet Oon, Xu Xiao, Shanthi Nagarajan, Sohinee Bhattacharyya, Peter Tontonoz, Mara H. Sherman  
bioRxiv 2020.12.25.424393; doi: <https://doi.org/10.1101/2020.12.25.424393>

**Abstract:**

The majority of research into Glutamic-oxaloacetic transaminase 2 (GOT2) has been in its mitochondrial transaminase function and its impact on the malate-aspartate shuttle and cellular redox homeostasis[14, 233]. The fatty acid transport function of GOT2 has been less researched, and has typically been published under the alternative name for GOT2, plasma membrane fatty acid binding protein or FABPpm. GOT2 is often referred to as FABPpm due to being described at a membrane-proximal location in hepatocytes and the fact that GOT2/FABPpm antiserum disrupts fatty acid trafficking in hepatocytes and cardiomyocytes[234, 235]. Our work, and that of others, has shown that fatty acid trafficking can be important for solid tumor progression[230, 236, 237]. As GOT2 is consistently overexpressed in human PDAC[236], while other transmembrane fatty acid transporters were variably expressed, we decided to investigate if GOT2 is important for PDAC progression *in vivo* and to investigate if its mitochondrial role or its less characterized fatty acid transport role is more important in PDAC progression. Here we show GOT2 is found at an undescribed location in the nucleus of PDAC cells along with its described locations at the plasma membrane and within the mitochondria. We also show definitive binding of GOT2 with arachidonic acid and oleic acid, and demonstrate that GOT2 status affects nuclear lipid levels. This provides some interesting new characteristics of a poorly understood gene and suggests novel roles for GOT2 in the transport of nuclear receptor ligands.

## **Personal contribution:**

HSC's contribution to this chapter are as follows:

Figure 1: a. HSC created the CCLE database graph, b. JA created the TCGA database graph, c. HSC created the Gln metabolism CCLE database graph, d. HSC ran western blot and Ponceau for normal and PDAC cell lines.

Figure 2: a. CO ran these western blots, b & c. CO ran cell-titer glo assays.

Figure 3: a. HSC ran qPCR, b. HSC took cell images

Figure 4: a. JA stained tissue and HSC imaged z-stacks, b. JA stained & imaged DAB images, c. JA stained and imaged DAB images, d. HSC and CO ran western blots, e. HSC ran ICC-IF and imaged, f. HSC performed transient transfection and ICC-IF, g. HSC performed transient transfection and IP pulldown.

Figure 5: a-c. SN performed *in silico* modeling of GOT2, d. XX performed competition binding assays, e. HSC developed and performed NBD-aa assay, f. NYU core performed untargeted lipidomics, g. HSC performed nuclear bodipy uptake assay, h. HSC developed and performed PacFA localization assay, i. NYU core performed lipidomic MS analysis, j. HSC performed, imaged, and analyzed bodipy uptake ICC-IF, k. HSC developed and performed PacFA localization ICC-IF.

Figure 6: HSC and JA performed *in vivo* implantation & collection, JA performed IHC-IF and analyzed Ki67, b. HSC and JA performed *in vivo* implantations & collection, JA performed IHC-IF, c. HSC and JA performed *in vivo* implantations & collection.

688M sgGot2 cell lines and FC1245 shGot2 cell lines were created by JA. FC1245 sgGot2 cell lines were created by CO. All human shGOT2 cell lines were created by HSC, except DOX-inducible lines which were a gift. All lentiviruses for cell transduction were created by HSC from plasmids made by CO or purchased. Purchased plasmids were grown and purified by HSC and CO.

Western blots, ICC-IF, IHC-IF, and proliferation assays were done by HSC, JA, and CO. IHC-dab was performed by JA, as was quantification of dab images. Z-stack imaging of tumors and analysis was performed by HSC, IHC-IF quantification and analysis was done by HSC and JA.

NBD-aa assay was designed and implemented by HSC. Click chemistry protocol was created and implemented by HSC. Dual-luciferase assays were done by HSC. PPAR $\delta$  PPRE assay was done by HSC. Detergent free nuclear fractionation protocol was developed by HSC from an existing Rockland Antibody protocol.

*In silico* modeling was done by SN.

GOT2 binding and competition assays were performed by XX.

Figures for this manuscript were put together by HSC.

## **Introduction:**

Cross talk between PDAC tumor cells and the TME is a research area with increasing importance.

It has been described by our lab, and others, that both PDAC cells and cells of the TME undergo metabolic reprogramming upon coming into contact with each other[3, 4, 30, 41, 42, 51, 66, 229, 230, 238, 239]. When hepatic stellate cells (HSCs) become activated they transform into myofibroblasts and undergo a subsequent loss of internal lipid droplets in addition to metabolic reprogramming for the production of extracellular matrix (ECM)[240]. This caused us to ask the question of whether release of lipid droplets into the PDAC TME by HSCs could be having an impact on the metabolic reprogramming of PDAC through fatty acid transporters. Fatty acid transporters are known to be upregulated in PDAC[236] and Glutamic-Oxaloacetic Transaminase 2 (GOT2) also known as fatty acid binding protein plasma membrane (FABPpm) is one of the most consistently upregulated in this disease (Fig 4a.). This made us consider whether it would be a good candidate for further characterization in PDAC.

The majority of research into GOT2 has been in its mitochondrial transaminase function and its impact on the malate-aspartate shuttle and cellular redox homeostasis[14, 233]. The fatty acid transport function of GOT2 has been less researched, and has typically been published under the alternative name for GOT2, FABPpm. GOT2 is often referred to as FABPpm due to being described at a membrane-proximal location in hepatocytes and the fact that GOT2/FABPpm antiserum disrupts fatty acid trafficking in hepatocytes and cardiomyocytes[234, 235]. Our work, and that of others, has shown that fatty acid trafficking can be important for solid tumor progression[230, 236, 237]. As GOT2 is consistently overexpressed in human PDAC[236], while other transmembrane fatty acid transporters were variably expressed, we decided to investigate if GOT2 is important for PDAC progression *in vivo* and to investigate if the mitochondrial role is key or its less characterized fatty acid transport role.

Glutamate oxaloacetate transaminase 1 and 2 are pyridoxal 5'-phosphate (PLP)-dependent enzymes that are canonically cytosolic (GOT1) or mitochondrial (GOT2) and function to catalyze reversible interconversion of oxaloacetate and glutamate to aspartate and  $\alpha$ -ketoglutarate as key components of the malate-aspartate shuttle system[14-16]. The malate-aspartate shuttle system is important for intracellular NAD(H) redox homeostasis where NADH from cytosolic NAD-linked dehydrogenase reactions is re-oxidized to NAD<sup>+</sup> in the mitochondrial membrane[241]. The redox shuttle system is required to transport NAD<sup>+</sup> and NADH across the relatively impermeable inner mitochondrial membrane[142, 242].

Although GOT1 has been studied more extensively than GOT2, recent studies suggest that GOT2 supports PDAC development by inhibiting cellular senescence, which is a tumor-suppressive mechanism[16]. Metabolic regulation of cells is linked to proliferation and cell cycle arrest, so it is believed that GOT2 inhibition of cellular senescence is through metabolic reprogramming in PDAC[16]. PDAC cells use aspartate derived from glutamine to maintain redox state, rather than the typical use of glutamine derived from glutamate that most cancer cell types rely on[223, 224]. Knockout (KO) of GOT2 in PDAC cells decreases the amount of glutamine derived aspartate and oxaloacetate, which – as aspartate and oxaloacetate are essential for maintaining cellular redox- leads to a decrease in cellular redox homeostasis and increase in reactive oxygen species (ROS)[16]. GOT2 knockdown in PDAC also decreases the cellular NADPH/NADP<sup>+</sup> ratio and increases senescence-associated  $\beta$ -galactosidase (SA- $\beta$ ) both of which can be rescued by extracellular treatment by oxaloacetate or aspartate[16]. The ability of extracellular treatment of oxaloacetate or aspartate to rescue ROS increase, NADPH/NADP<sup>+</sup> ratio, and increased SA- $\beta$  in

GOT2 knockdown PDAC cells strongly supports the canonical role of GOT2 in the malate-aspartate shuttle system.

The oncogenic *Kras* mutation seen typically in PDAC patients may also push cells towards a stronger reliance on GOT1 and GOT2 activity. Typically, cells rely on use mitochondrial glutamate dehydrogenase (GLUD1) to convert glutamine-derived glutamate to  $\alpha$ -ketoglutarate ( $\alpha$ -

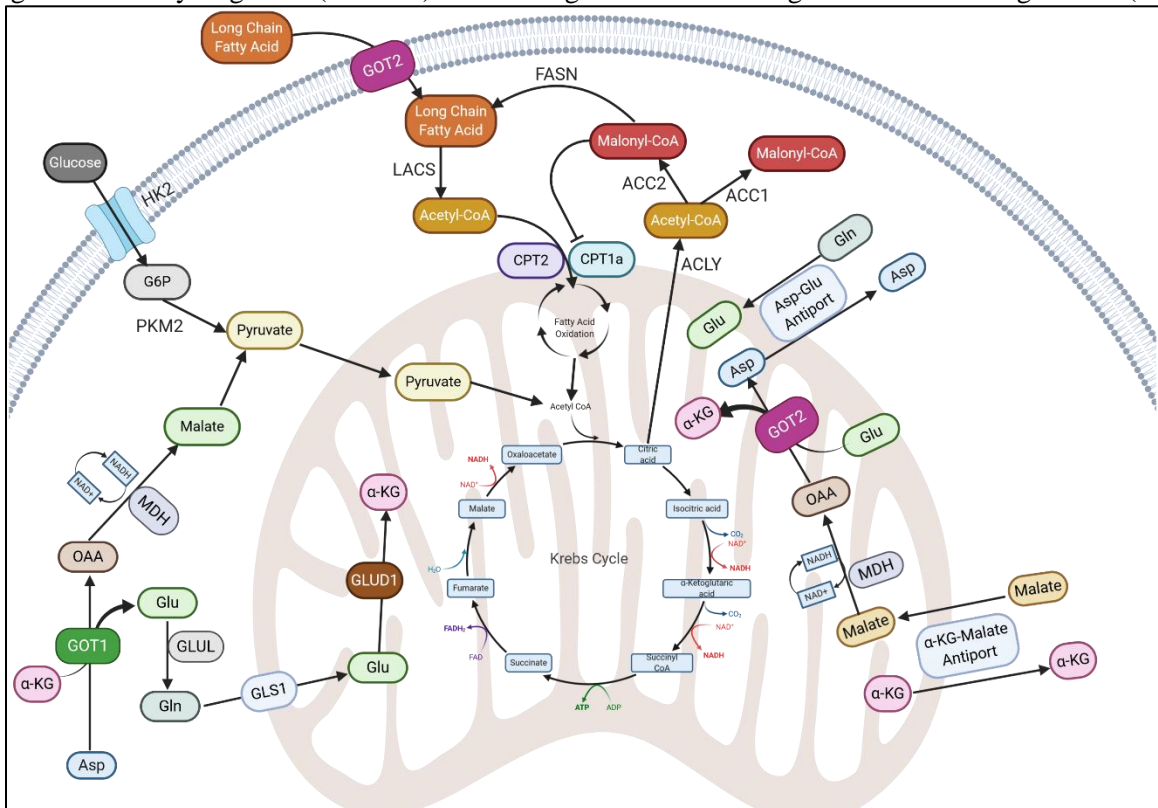


Figure 2.1: Summary of GOT1 & GOT2 canonical enzymatic activity.

Cytosolic GOT1 converts aspartate to oxaloacetate, which is further converted to malate and pyruvate [224]. At the membrane GOT2 functions to import long chain fatty acids into the cell, allowing them to be used in down stream metabolic and signaling processes. Within the mitochondria, GOT2 functions in the malate shuttle system where it converts oxaloacetate to aspartate [16]. Figure created using BioRender.com

KG) for TCA, but in PDAC cells seem to rely more heavily on cytosolic GOT1 to convert glutamine-derived aspartate to oxaloacetate, which is then subsequently converted to malate and then pyruvate[224]. This alternative pathway may allow PDAC cells to more easily maintain their cellular redox state and reduce ROS through increasing the NADPH/NADP<sup>+</sup> ratio with GOT1 generated pyruvate[224]. Supporting the importance of GOT1 in PDAC, suicide inhibitors of GOT1 have been identified to which KRAS mutant PDAC cells are selectively sensitive to and

cause a proliferative decrease[243]. It has also been shown that the creation of GOT1-null PDAC cells sensitizes them to glucose deprivation and decreases the cellular NADH/NAD<sup>+</sup> ratio, which can only be partially rescued with extracellular treatment of oxaloacetate and phosphoenol pyruvate (downstream metabolic intermediates of GOT1)[244]. Taken together, these studies suggest that GOT1 has an important role in regulating and coordinating glycolytic and oxidative phosphorylation pathways of KRAS mutant PDAC cells, particularly in low glucose levels when

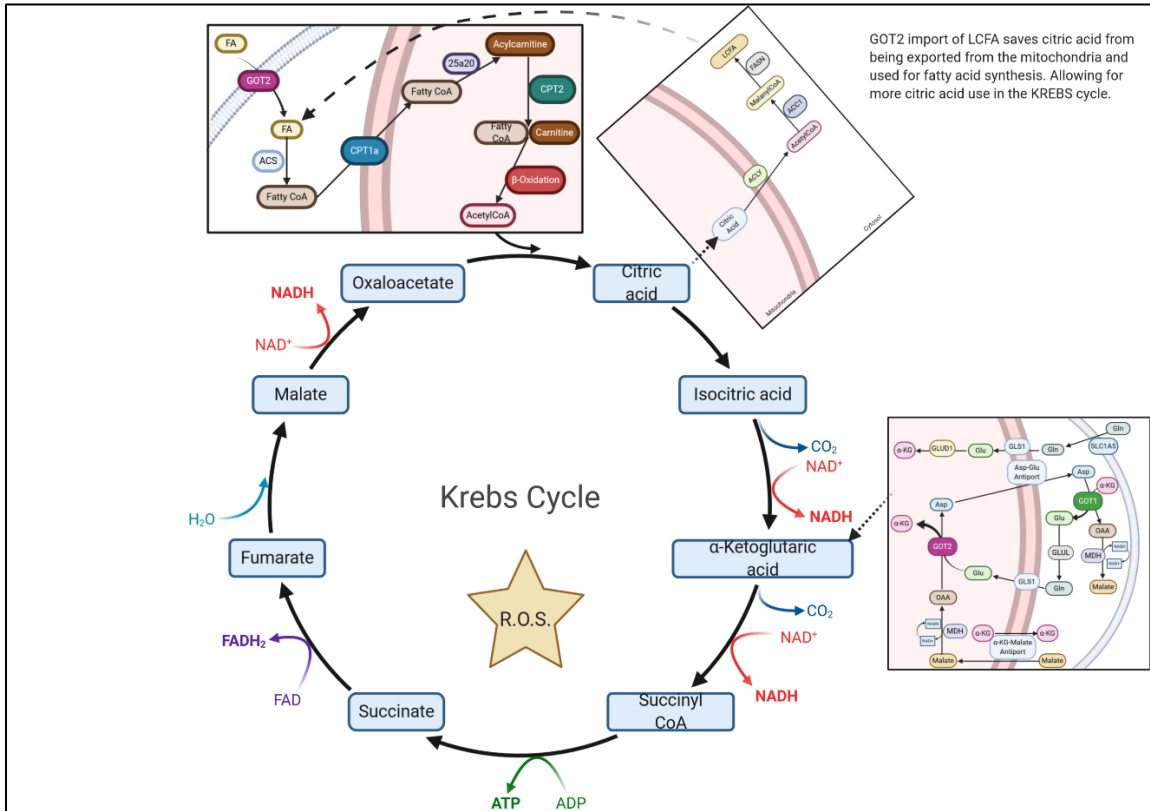


Figure 2.2: Summary of GOT2 metabolic roles and their relationship to the Krebs Cycle.

Both roles of GOT2, fatty acid import and α-KG malate antiport shuttle, provide important factors for continuation of the Krebs Cycle and improved cellular metabolism & redox state [16,224]. Figure created with BioRender.com

maintaining redox homeostasis is critical. The role of GOT2 in the α-ketoglutarate malate antiport shuttle could also explain why ROS levels rise when GOT2 is decreased in PDAC cells. It is clear that in PDAC GOT1 and GOT2 appear to function in a balanced manner from within the cytosol and within the mitochondria to support cellular metabolism and cellular redox state which is key for rapidly reproducing PDAC cells.

Along with its enzymatic mitochondrial roles, GOT2 is also known as plasma membrane-associated fatty acid binding protein (FABP<sub>pm</sub>) due to its functional role in transporting fatty acids into the cell. While GOT1 is known as fatty acid binding protein 1 (FABP-1) or fatty acid binding protein liver (FABPL) due to its own fatty acid binding roles described originally in the liver[245]. The over expression of GOT2 in muscle cells has been shown to increase palmitate transport and incorporation into phospholipids and palmitate oxidation, without similar increase in fatty acid translocase (FAT)/CD36 levels[246]. FAT/CD36 was the first mammalian plasma membrane fatty acid transporter to be discovered and is in the class B scavenger receptor family where it binds long-chain fatty acids, native and oxidized lipoproteins, thrombospondin-1, amyloid B, and other ligands[247]. It is believed that FAT/CD36 and GOT2 may work together to import fatty acids into the cell, as FAT/CD36 and GOT2 co-immunoprecipitate[248]. This supports the idea that GOT2 has a role in importing long chain fatty acids into the cell where they can be used for downstream metabolic activities. Further evidence for GOT2 playing a role in fatty acid metabolism includes the fact that in the heart AMP kinase activation or increased muscle contraction increases translocation and expression at the plasma membrane of both FAT/CD36 and GOT2[248]. Despite co-immunoprecipitating, there appears to be evidence that FAT/CD36 and GOT2 have different roles in fatty acid transport and are activated by different environmental factors. While insulin exposure has been shown to increase expression of FAT/CD36, causing FAT/CD36 to permanently relocate to the plasma membrane – contribution to insulin resistance by increasing influx of fatty acids into muscle cells – GOT2 expression does not appear to be linked to insulin exposure[248]. Along with their role in metabolic activity and as an important substrate for energy production, fatty acids can act to modify diverse proteins, regulating their activity and cellular localization. They are also known to act as signaling molecules capable of regulating immune responses through toll-like receptors and the synthesis of eicosanoids, as well as by acting as direct ligands of nuclear receptors[247]. In this work we

examine and further characterize the role of GOT2 fatty acid transport in the metabolic reprogramming of PDAC.

## **Materials and Methods:**

### ***Animals***

All experiments were reviewed and overseen by the institutional animal use and care committee at Oregon Health and Science University in accordance with NIH guidelines for the humane treatment of animals. C57BL/6J (000664, for models with FC1245[249]) or B6129SF1/J (101043, for models with 688M[250]) mice from Jackson Laboratory were used for orthotopic transplant experiments at 8-10 weeks of age. Tissues from 6- or 12-month-old *Kras<sup>LSL-G12D/+</sup>;Pdx1-Cre* (KC) mice were kindly provided by Dr. Ellen Langer (OHSU).

### ***Human Tissue Samples***

Human patient PDAC tissue samples donated to the Oregon Pancreas Tissue Registry program (OPTR) in accordance with full ethical approval were kindly shared by Dr. Jason Link and Dr. Rosalie Sears (OHSU).

### ***Plasmids***

pLenti wtGOT2 PCR product was generated using sense primer 5'-GGGGACAAGTTTGTACAAAAAAGCAGGCTTAATGGCCCTGCTGCACT-3' and antisense primer 5'-GGGGACCACTTTGTACAAGAAAGCTGGGTTTTTAGTGATGGTGGTGATGATGGTGG-3'. Triple mutant GOT2 was constructed using Q5 Site-Directed Mutagenesis Kit (New England E0552S) in two subsequent steps. Two sets of primers were used to generate three site mutations; primer set 1 for K234A mutation (F:5'-AACAGTGGTGCGCAAAGGAATCTC-3'; R:5'-GCTATTTCCCTTCCACTGTTC-3') and primer set 2 for K296A and R303 mutations (F:5'-GTCTGCGCAGATGCGGATGAAGCCAAAGCGGTAGAGTC-3'; R:5'-CATAGTGAAGGCTCCTACACGC-3'). pLenti tmGOT2 was then generated using the same approach and primers as pLenti wtGOT2.

### ***Cell Lines***

Human pancreatic cancer cell lines MIAPaCa-1, PA-TU-8988T, Panc1, HPAF-II, and Capan-2 were obtained from ATCC and grown in Dulbecco's modified Eagle's medium (DMEM) containing 10% fetal bovine serum. Non-transformed, TERT-immortalized human pancreatic ductal epithelial cells were kindly provided by Dr. Rosalie Sears (OHSU)[251]. FC1245 PDAC cells were generated from a primary tumor in *Kras<sup>LSL-G12D/+</sup>;Trp53<sup>LSL-R172H/+</sup>;Pdx1-Cre* mice and were kindly provided by Dr. David Tuveson (Cold Spring Harbor Laboratory)[249]. 688M PDAC cells were generated from a liver metastasis in *Kras<sup>LSL-G12D/+</sup>;Trp53<sup>LSL-R172H/+</sup>;Pdx1-Cre;Rosa26<sup>LSL-tdTomato/+</sup>* mice and were kindly provided by Dr. Monte Winslow (Stanford University School of Medicine)[250]. Cell lines were routinely tested for *Mycoplasma* at least monthly (MycoAlert Detection Kit, Lonza).

The pSpCas9(BB)-2A-Puro(PX459) v2.0 plasmid (Addgene #62988) was used to clone guide sequences targeting *Got2* per supplier's protocol; sgRNA A: GACGCGGGTCCACGCCGGT, sgRNA B: ACGCGGGTCCACGCCGGTG. The 688M or FC1245 cell line was transfected with control plasmid or plasmid containing either of the sgGot2 sequences and subject to selection with 2 µg/ml puromycin for 4 days. Single-cell clones were expanded and screened for GOT2 protein expression by Western blot.

Lentivirus preparation for stable cell line generation was done with pMD2.G envelope plasmid (Addgene #12259) and psPAX2 packaging plasmid (Addgene 12260) in 293T-LentiX cells. Briefly, 5ug pMD2.G, 5ug psPAX2 and 10ug of plasmid DNA (shGOT2 KD, VP16-PPARdelta, wtGOT2, tmGOT2, or scramble Ctrl) were combined with 600ul optimum and 20ul lipofectamine 2000 for 20 mins at room temp. 10cm dishes of 293T-LentiX were kept in 0% FBS DMEM and

the mixture was added in a dropwise manner. 12hrs later media was changed to 10% FBS DMEM. At 24hrs after transduction and 48hrs after transduction, media was collected and filtered through a 0.25um filter, aliquoted, and frozen at -80C. The shGOT2 plasmids were purchased from addgene. Human shGOT2 lot #04161910MN TRCN0000034824, TRCN0000034827, TRCN0000034826, TRCN0000034825. Mouse shGOT2 lot #04161910MN TRCN00000326018, TRCN00000325946, TRCN00000119800, TRCN00000119798, TRCN00000119801.

Lentiviral transduction of human and mouse cell lines: cells were plated to 6-well plates. 10ug/mL polybrene (EMD Millipore TR-1003-G) was added to 1mL 10% FBS DMEM and 300ul of filtered lentivirus media. 24hrs later media was changed to fresh 10% FBS DMEM. 48hrs after initial transduction, cells were treated with 2ug/mL puromycin (Thermo Fisher A1113803), or 4ug/mL puromycin depending on cell line. A control well of non-transduced cells was used as an indicator for proper selection.

### ***Western Blots***

PDAC cells were treated as described in the text, and whole cell lysates were prepared in RIPA buffer containing protease inhibitor cocktail (Sigma-Aldrich 11836170001). Alternatively, sub-cellular fractions were prepared by several different fractionation methods.

Detergent Free Fractionation protocol: Cells are scraped and collected from 10cm dishes. Washed with PBS (450g x 5mins) and 1/5 of the volume is separated for whole cell lysis in RIPA (Amresco N653-100mL) + cOmplete EDTA-free Protease inhibitor cocktail (Sigma-Aldrich 11836170001). Remain 4/5 of cell mass is centrifuged (450g x 5mins), PBS is removed and cells are lysed on ice for 15 mins in Lysis buffer (5x of cell pellet volume). Lysis Buffer: 10mM HEPES pH 7.9, 1.5mM MgCl<sub>2</sub>, 10mM KCl with 1mM DTT and EDTA-Free cOmplete mini protease inhibitor cocktail. Centrifuge (450g x 5mins), decant super, add lysis buffer (2x cell volume) and grind on ice with a plastic homogenizer 10x in 1.5mL Eppendorf tubes. Centrifuge (10,000g x 20mins) collect supernatant as cytosolic fraction. Wash with 200ul lysis buffer (10,000g x 5mins) decant super and add extraction buffer (2/3x cell pellet volume). Extraction buffer: 20mM HEPES pH 7.9, 1.5mM MgCl<sub>2</sub>, 0.42M NaCl, 0.2uM EDTA, 25% glycerol (V/V), 1mM DTT and cOmplete mini EDTA-free protease inhibitor cocktail. Grind nuclei with plastic homogenizer in 1.5mL Eppendorf tubes 20x. Incubate at 4C with gentle shaking for 10 mins. Centrifuge (20,000g x 5mins) and transfer supernatant to cold Eppendorf tube, label as Nuclear portion.

Cell Signaling Tech Cell Fractionation Kit (CST 9038S) was performed following the manufacturer's recommendations. Briefly cells were collected with scraping and washed in PBS (350g x 5mins). Resuspend in 500ul PBS and remove 100ul for whole cell lyses in RIPA buffer + cOmplete mini EDTA-free protease inhibitor cocktail. Remaining cell pellet was centrifuged (500g x 5 mins), PBS was decanted and 500ul CIB + 5ul Protease Inhibitor and 2.5ul PMSF was added. Vortex and store on ice 5 mins. Centrifuge (500g x 5mins) supernatant is cytosolic fraction. Wash with CIB. Decant supernatant. Add 500ul MIB + 5ul Protease Inhibitor and 2.5ul PMSF to the cell pellet. Vortex 15 seconds, incubate on ice 5 mins, and centrifuge (8000gx 5 mins). Supernatant is the membrane & organelle fraction. Wash in MIB. Decant supernatant. Add 250ul CyNIB + 2.5ul Protease Inhibitor + 1.25ul PMSF to the cell pellet. Sonicate for 5 sec at 20% power 3x. For western blot add 60ul 3X LDS loading buffer with 10X reducing agent for every 100ul of supernatant per fraction. Boil for 5 mins at 95C and centrifuge for 3 mins at 15,000g. Load 15ul of each fraction along with 15ul of whole cell lysate.

Protein concentration was quantitated using the BCA protein assay kit (Pierce). Equal amounts of protein were loaded in each lane and separated on a 4-12% Bis-Tris NuPAGE® gel (Invitrogen), then transferred onto a PVDF membrane. Membranes were probed with primary antibodies and

infrared secondary antibodies: anti-GOT2 (Thermo Fisher PA5-77990), anti-His-tag (R&D Systems MAB050-100), anti-PPAD (Abcam ab178866), anti-Lamin A/C (Cell Signaling Technology 4777S), anti-COX IV (Cell Signaling Technology 11967S), anti-rabbit Alexa Fluor Plus 680 (Thermo Fisher A32734) and anti-mouse Alexa Fluor Plus 800 (Invitrogen A32730). Protein bands were detected using the Odyssey CLx infrared imaging system (LICOR Biosciences).

### ***Nuclear Fatty Acid Uptake Assay***

MiaPaca2 ctrl and sh27 cells were plated at  $5 \times 10^5$  in a 6 well plate and allowed to adhere overnight. Media was changed to 0% FBS DMEM and the cells were incubated for 24hrs. The media was changed to 0.5% Fatty-Acid Free BSA DMEM with either chloroform (ctrl) or 2.5  $\mu$ M NBD-arachidonic acid (Avanti Polar Lipids 810106C). Media was made before being added to cells, heated to 37°C and vortexed until fatty acid was completely in solution. Cells were incubated at 37°C for durations indicated in the manuscript and collected and fractionated using the Detergent Free Method described above (PPAR $\delta$  transcription factor activity assay). Nuclear lysates were placed in a white-walled 96-well plate and fluorescence was measured at 480 nm excitation and 540 nm emission. Lysate concentration was measured using a BCA kit. FC1245 cells were plated  $5 \times 10^5$  per well and treated as described above, but treatment was reduced to 2  $\mu$ M NBD-arachidonic acid for 15 minutes due to lipid toxicity in this cell line.

### ***Free Fatty Acid Measurements***

Samples were subjected to an LCMS analysis to detect and quantify levels of free fatty acids in sample extracts. A fatty acid extraction was carried out on each sample using 100% methanol as the homogenization solvent. Whole cell pellets ( $1 \times 10^6$  cells/sample) were lysed with 1000  $\mu$ L of methanol and ~100  $\mu$ L of zircon beads (0.5 mm). Manual disruption with a p1000 pipette tip was performed to assist initial pellet suspension in extraction buffer. The methanol extracts were centrifuged (21,000g x 3 min) and transferred to glass LCMS inserts for analysis. The LC column was a Waters<sup>TM</sup> BEH-C18 (2.1  $\times$ 100 mm, 1.7  $\mu$ m) coupled to a Dionex Ultimate 3000<sup>TM</sup> system and the column oven temperature was set to 25°C for the gradient elution. The flow rate was 0.1 mL/min and used the following buffers; A) water with 0.1% formic acid and B) acetonitrile with 0.1% formic acid. The gradient profile was as follows; 60-99%B from 0-6 min, hold at 99%B from 6-10 min, 99-60%B from 10-11 min, hold at 60%B from 11-15 min. Injection volume was set to 1  $\mu$ l for all analyses (15 min total run time per injection).

MS analyses were carried out by coupling the LC system to a Thermo Q Exactive HFTM mass spectrometer operating in heated electrospray ionization mode (HESI). Data acquisition was 10 min with a negative mode full MS scan (profile mode) and one microscan, with an AGC target of 3e6 and a maximum IT of 100 ms at 120,000 resolution, with a scan range from 160-400 m/z. Spray voltage was 3.5kV and capillary temperature was set to 320°C with a sheath gas rate of 35, aux gas of 10, and max spray current of 100  $\mu$ A. The acquisition order of samples and standard curve points was randomized, with blank matrix controls before and after each standard curve point to assess carry over (none detected). The resulting free fatty acid peaks were quantified by measuring the relative intensities (peak heights) of the high resolution extracted ion chromatogram (XIC) for each fatty acid across the samples and external standard curve samples ranging from 10  $\mu$ g/mL to 100 ng/mL. All fatty acids were detected as the negative mode [M-H] ion and retention times of the fatty acids were defined using a cocktail of authentic standards. For each XIC, the theoretical m/z of each fatty acid ( $\pm$  5 ppm) was used to extract the peak height (24 sec retention time window, 12 sec retention time tolerance) as follows: Lauric acid (199.1704 m/z, 2.3 min), Myristic acid (227.2017 m/z, 3.1 min), Palmitoleic acid (253.2173 m/z, 3.4 min), Palmitic acid (255.2330 m/z, 4.1 min), Oleic acid (281.2486 m/z, 4.4 min), Stearic acid

(283.2643 m/z, 5.1 min), Arachidic acid (311.2956 m/z, 6.0 min), Nervonic acid (365.3425 m/z, 6.9 min), Lignoceric acid (367.3582 m/z, 7.5 min). The resulting standard curve points (in duplicate) were fit to a linear regression (GraphPad Prism8), and this equation was used to interpolate the concentration of fatty acids in the sample extracts, as prepared.

### ***Click Chemistry***

Briefly, for the fractionation plate reader results: cells were plated at  $1 \times 10^6$  per 10cm plate and allowed to adhere overnight. They were then treated with  $10 \mu\text{M}$  PacFA + 0.5% fatty-acid free BSA DMEM overnight. They were exposed to 350nm UV for 2 mins then collected with cell scrapers and fractionated using the NE-PER kit.

For IF; cells were plated at  $5 \times 10^4$  on 12mm coverslips and allowed to adhere overnight. They were then treated with  $20 \mu\text{M}$  PacFa + 0.5% fatty acid free BSA DMEM overnight. Exposed to 350nm UV for 2 mins then incubated in 10% NBF for 10 minutes, washed in PBS, incubated in TX-100 for 10 minutes, washed in PBS, incubated in PBS and actin-red for 30 minutes and mounted with DAPI-free prolong gold mounting media and allowed to dry for 24 hours. Coverslips were imaged by spinning disk.

### ***Immunofluorescence***

Cells plated on coverslips were fixed in 10% neutral buffered formalin for 10 minutes at room temperature, washed three times with PBS, and permeabilized with .1% Triton X-100 for 10 min at room temperature. When MitoTracker staining was performed, cells plated on coverslips were stained with 100 nM MitoTracker (Thermo Fisher M22462) at  $37^\circ\text{C}$  for 15 minutes prior to fixation. Following permeabilization, coverslips were blocked for one hour at room temperature in blocking solution (Aqua block buffer, Abcam ab166952) and then transferred to a carrier solution (Aqua block) containing diluted primary antibodies: GOT2 (Sigma-Aldrich HPA018139), GOT2 (Thermo Fisher PA5-77990), COX IV (Cell Signaling Technology 11967S), His (R&D Systems MAB050-100). Coverslips were incubated with the primary antibody at  $4^\circ\text{C}$  overnight and then washed five times for 5 minutes each in PBS following which, secondary Alexa-flour conjugated antibodies diluted in the same carrier solution (1:400) were added to the coverslips for one hour at room temperature. After the secondary antibody incubation, coverslips were washed five times for five minutes each in PBS and mounted with Vectashield mounting media containing DAPI (Vector Laboratories H-1500). Images were captured on a Zeiss LSM 880 laser-scanning inverted confocal microscope in the OHSU Advanced Light Microscopy Shared Resource, and a  $40\times/1.1$  NA water objective or  $63\times/1.4$  NA oil objective was used to image the samples.

### ***Proliferation Assays***

PDAC cells were seeded into 96-well plates at  $2 \times 10^3$  cells per well in DMEM containing 10% FBS. Cells were treated as indicated in the manuscript text with  $100\text{nM}$  GW501516 (Cayman Chemical 10004272) at the time of cell seed or  $5\text{mg/mL}$  doxycycline (Sigma-Aldrich D9891) 48 hours prior to cell seeding. GW501516 and doxycycline treatments were both replenished every 48 hours for extended time points. After 72 hours, cells were lysed with CellTiter-Glo<sup>®</sup> Luminescent Cell Viability Assay reagent (Promega) and luminescence was read using a GloMax plate reader.

### ***Orthotopic Implantation In Vivo model***

The orthotopic transplant method used here was described previously<sup>6</sup>. In brief, 8- to 10-week-old wild-type male C57BL/6J (for FC1245) or B6129SF1/J (for 688M) mice were orthotopically transplanted as described previously with  $5 \times 10^3$  FC1245 cells or  $8 \times 10^4$  688M cells in 50%

Matrigel (Corning 356231), 50% DMEM. Mice were euthanized when control animals were moribund, and tumors were excised, weighed, and immediately fixed in formalin.

### ***Immunohistochemistry of Tumor Tissue***

Mice were anesthetized and euthanized according to institutional guidelines. Pancreatic tumors were excised carefully and fixed overnight in 10% phosphate-buffered formalin. Tissue samples were paraffin embedded and sectioned by the OHSU Histopathology Shared Resource. Human PDAC tissue sections from formalin-fixed, paraffin-embedded blocks were obtained from the OPTR. In brief, tissue sections were de-paraffinized and rehydrated through an ethanol series and ultimately in PBS. Following antigen retrieval, tissue samples were blocked for 1 hour at room temperature in blocking solution (8% BSA solution) and then transferred to a carrier solution (8% BSA solution) containing diluted antibodies: GOT2 (Sigma-Aldrich HPA018139), GOT2 (Thermo Fisher PA5-77990), COX IV (Cell Signaling Technology 11967S), COX2 (Abcam ab15191). Sections were incubated overnight at 4°C and then washed five times for 5 minutes each in PBS. For fluorescence imaging, secondary Alexa-fluor conjugated antibodies diluted in the same carrier solution (1:400) were added to the sections for one hour at room temperature. Sections were then washed five times for five minutes each in PBS and were mounted with Vectashield mounting media containing DAPI. For DAB chromogen imaging, sections were stained with primary antibody as described above, then the samples were incubated in polymeric horseradish peroxidase (HRP) conjugated secondary antibody (Leica PV6121) for one hour followed by 5 five-minute 1xTBST washes. HRP was detected using DAB chromogen (3,3'-Diaminobenzidine) solution (BioCare Medical BDB2004) prepared per manufacturer instructions. Tissues were exposed to chromogen solution until a brown precipitate was detected produced from oxidized DAB where secondary poly-HRP antibody is located. As soon as DAB chromogen is detected the tissue-slides were washed in diH<sub>2</sub>O, counterstained in hematoxylin, dehydrated and cleared for mounting. Stained tissue sections were scanned on a Leica Biosystems Ariol digital fluorescence scanner or Leica Biosystems Aperio brightfield digital scanner.

### ***Fatty Acid Binding Assay***

Reactions were carried out in binding buffer (0.003% digitonin in 1X PBS) containing 1 µM of purified human GOT2 protein (AA30-430) and 0.5 µCi/ml [<sup>3</sup>H]-arachidonic Acid. After incubation for 1hr at 4°C, the mixture was incubated with pre-equilibrated of TALON Metal Affinity Resin (Takara, 635502) at 4°C for 1 h, then loaded onto a column and washed with binding buffer, then binding buffer with 0.01% BSA, and binding buffer again. The protein-bound [<sup>3</sup>H]-arachidonic was eluted with elution buffer (50 mM sodium phosphate, 300 mM sodium chloride, 150 mM imidazole; pH 7.4.) and quantified by scintillation counting. For competition experiments with unlabeled lipids, the assays were carried out in the presence of ethanol containing the indicated unlabeled sterol (0 –1 mM).

### ***Statistical Analysis***

GraphPad Prism software was used for all statistical analysis. Welches unpaired T-tests were used to compare two treatment groups to each other. One-Way Anova was used to compare multiple treatment groups for one variable. A P value of < 0.05 was considered significant.

## Results:

Two independent RNA-seq datasets of fatty acid transport mRNA levels in PDAC show that GOT2/FABPpm is consistently upregulated in PDAC while other fatty acid transporters have more variable expression (Fig 2.3a, b). In our hands, western blot analysis shows similar increases in GOT2 protein levels in these cell lines (Fig 2.3d). As GOT2 is consistently upregulated in PDAC cell lines, in contrast to some of the other fatty acid transporters, it is likely

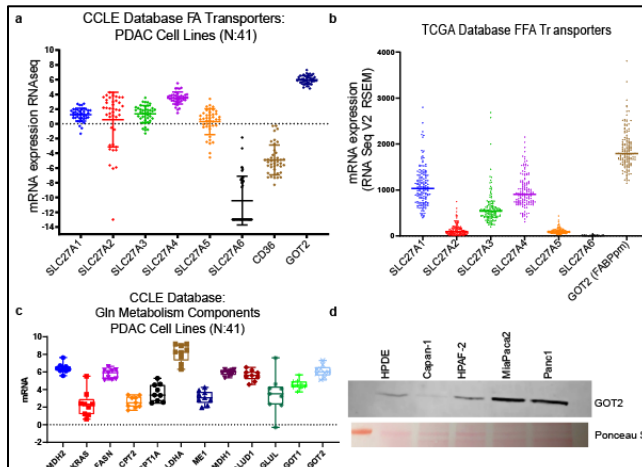


Figure 2.3 GOT2 is upregulated in PDAC

a. CCLL database shows GOT2 is consistently upregulated in PDAC, b. TCGA database shows GOT2 is consistently upregulated in PDAC, c. CCLL database shows components of glutamine metabolism are upregulated in PDAC, d. western blot shows upregulation of GOT2 protein levels in most PDAC lines compared to normal pancreas ductal cells (HPDE).

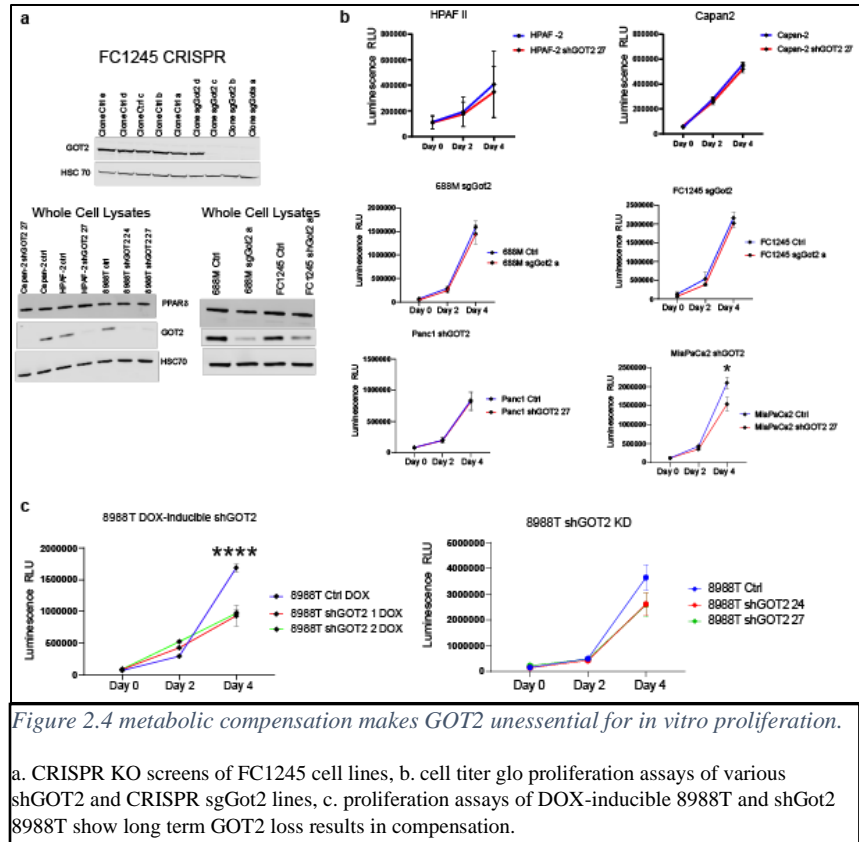
that the role of GOT2 could be more critical than that of other similar fatty acid transporters. However, since GOT2 plays a variety of roles in the cell - having mitochondrial function as well as a membrane fatty acid transport function - it is difficult to say whether the upregulation and importance of GOT2 is due to its fatty acid transport specific role. Indeed, when looking at other

genes involved in the malate-shuttle metabolic process it is clear that nearly every gene involved in this process are also upregulated in PDAC (Fig 2.3c). Aberrant GOT2 expression has been linked to aberrant Jak/STAT and NF- $\kappa$ B signaling in lymphoma, with high *GOT2* expression linked to prognostic outcome in large B-cell lymphoma[252]. Transcriptional regulation of GOT2 appears to occur through cooperative phosphorylation of STAT3 and joint binding of STAT3 and p65/NF- $\kappa$ B to the proximal promoter of *GOT2*[252]. Transcriptional regulation of GOT2 in PDAC could be occurring through similar mechanisms and drives the question of whether GOT2 is being upregulated in PDAC due to its function in mitochondrial metabolism or due to its function as a fatty acid transporter.

Looking at GOT2, one would expect that the loss of a mitochondrial protein would lead to impaired cellular growth, increased ROS, and decreased metabolic activity. To assess the significance of GOT2 for PDAC progression we used shRNA and CRISPR/Cas9 loss-of function systems to create human and murine PDAC cell-lines with reduced or missing GOT2. Cas9 and sgRNAs were

transiently transfected into murine cell lines, 688M and FC1245, and cas9 was no longer expressed by the time they were used for *in vivo* studies (Fig 2.4a). When analyzing our created cell lines, we were surprised to find that the loss of GOT2 had

no apparent effect on *in vitro* cell proliferation in the vast majority of PDAC cell lines tested (Fig 2.4b). We had expected the loss of GOT2 to have a decreased proliferation effect, so were initially puzzled by this result, especially as previous publications had shown loss of GOT2 in PDAC cells to show a proliferative defect *in vitro*. We gathered proliferation data in hypoxic, normoxic, low glutamine and low glucose, and low serum conditions and all failed to reduce proliferation between control and GOT2 KD cells, except for in MiaPaCa2 cell lines which showed a very minor decrease (Fig 2.4b). We also attempted to use colony formation assays to analyze the impact of GOT2 on seeding, but found that variations in morphology between GOT2 control and GOT2 KD cells made interpretation very difficult. In the majority of cell lines



created, GOT2 KD resulted in a shift from epithelial-like to mesenchymal-like (Fig 2.5b). Leading to different styles of growth (large clumps vs spread out cells) which made interpretation of colony formation assays difficult. Because the literature suggested that GOT2 KD should reduce proliferation *in vitro*, we hypothesized that the long-term stable KD of GOT2 was resulting in compensation and affecting our results. In support of this idea, when we investigated proliferation in GOT2 knockdown DOX-inducible 8988-T cell line we found that 8988-T dox-inducible GOT2 KD cell lines do show a reduction in proliferation as previously reported in the literature (Fig 2.3c)[253]. Yet, when we created a matching stable shGOT2 8988T cell line there was no longer a significant reduction in *in vitro* proliferation (Fig 2.3c). This suggests that the extreme metabolic plasticity found in PDAC cells allows for compensation for the loss of GOT2

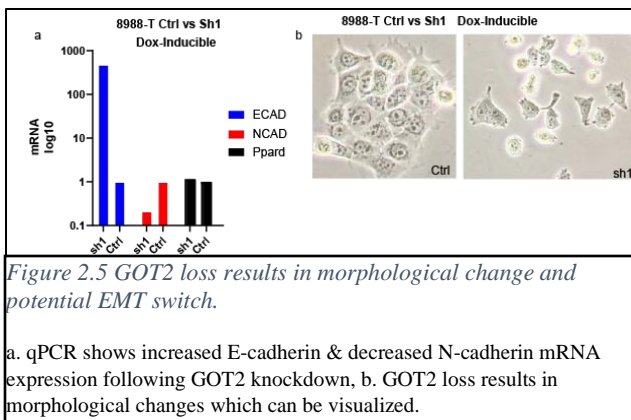


Figure 2.5 GOT2 loss results in morphological change and potential EMT switch.

a. qPCR shows increased E-cadherin & decreased N-cadherin mRNA expression following GOT2 knockdown, b. GOT2 loss results in morphological changes which can be visualized.

over time in a stable knockdown, but not when acute GOT2 loss is induced through DOX treatment in the DOX-inducible KD cell lines. Looking at other metabolic genes involved in glutamine metabolism (Fig 2.2c) it is clear that this pathway is greatly upregulated in PDAC.

It is certainly possible that GLUT1, GOT1, and MDH2 upregulation, among others, could be compensating for a loss of GOT2 in the stable knockdowns and that this compensation takes long enough to occur that it is not seen in the DOX-inducible model.

When we characterized the DOX-induced KD of GOT2 in 8988T cells, we saw that E-cadherin (ECAD) levels rose while N-cadherin (NCAD) levels decreased which matches the observed change in physical morphology of the cells (Fig 2.5a, b), turning them from a more mesenchymal-like phenotype to a more epithelial-like phenotype. This has some interesting implications as epithelial-mesenchymal transition (EMT) has been shown to be inhibited, along

with metastasis, by PPAR $\gamma$  activation which is thought to act by inhibiting TGF- $\beta$  and EMT through antagonizing Smad3 function[254]. Our data also suggests that GOT2 KD may affect cell

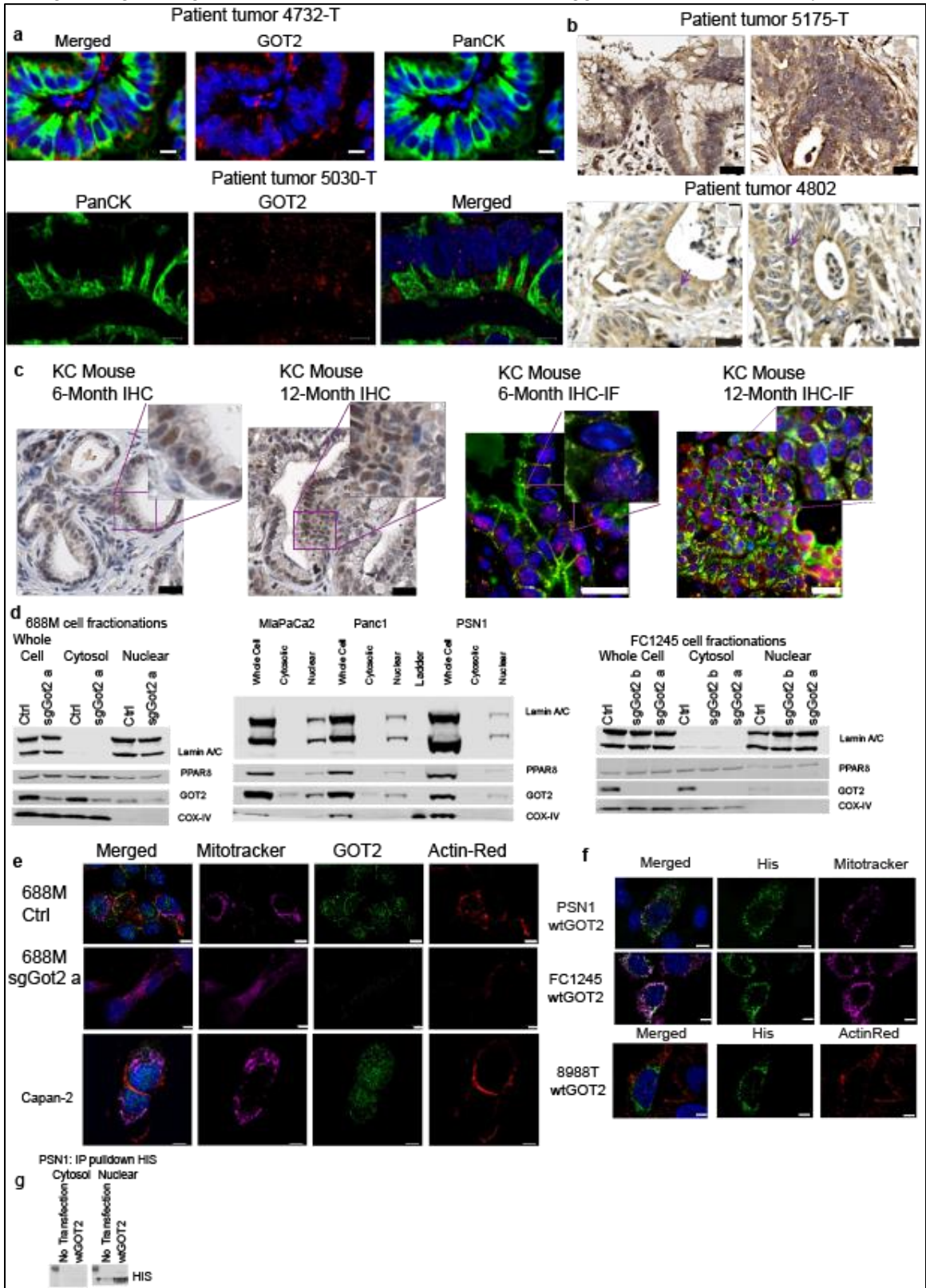


*Figure 2.6 GOT2 localizes to the mitochondria, membrane, and nucleus of PDAC cells and in tumor tissue.*

a-b. GOT2 localizes to the nucleus, mitochondria, and membrane in 4 different human patient samples, by IHC-IF and IHC-DAB. There is variation in the amount of nuclear GOT2 from patient to patient and within the same tumor. c. KC mouse tumors develop higher levels of GOT2 at the nucleus as they develop from 6 months, majority PanIN, to 12 months, some PDAC. d. Western blots show localization of GOT2 at the nucleus of both human and murine cell lines. e. ICC-IF shows GOT2 at the membrane, mitochondria, and nucleus of 688M and Capan-2 cells. f. exogenous His-tagged GOT2 localizes mostly to the mitochondria, with a few visible nuclear puncta. g. IP pulldown on exogenous His-tagged GOT2 purified nuclei shows wtGOT2 at the nucleus of PSN1 cells.

lines differently depending on their starting subtype. Separating PDAC cells by starting metabolic subtype shows a link between glycolytic subtype and mesenchymal-like phenotype and the lipogenic subtype and the epithelial-like phenotype [227]. The link between GOT2 status, metabolic subtype, and EMT is something that needs to be further elucidated in the future and could be an interesting project for the lab.

One of the things we noticed early on in the project was the GOT2 protein seemed to appear by western blot, and by IF, in the nucleus along with at its known locations of the outer cell membrane and the mitochondria. This was observed in murine pre-malignant lesions and PDAC and in human PDAC in vivo (Fig 2.6c). The human tumor IHC for GOT2 showed variation of how much GOT2 was located at the nuclear portion of the cell, but we observed GOT2 in pan-cytokeratin+ tumor cells at the mitochondrial, membrane-proximal regions, and nuclear regions of the majority of cells (Fig 2.6a, b). In vitro we were able to observe nuclear GOT2 whether through endogenous GOT2 expression or with exogenous, His-tagged GOT2 expression (Fig 2.6d-f). We saw this through western blot, IHC-DAB, IHC-IF, and ICC-IF leading us to speculate that GOT2 may be playing a novel role in this location (Fig 2.6d-f). We also observed that IP-pulldown using His beads to target His-tagged wtGOT2 pulled down wtGOT2 in nuclear extracts (Fig 2.6g), providing further support for the novel location of GOT2. Based on the fact that GOT2-null cells had no decrease in in vitro proliferation or in vivo proliferation, we hypothesized that metabolic adaptation mechanisms were in place to maintain redox balance, but a potentially yet undiscovered non-canonical function of GOT2 fatty acid binding capacity could be playing a role in nuclear transport of fatty acid which PDAC cells are not capable of adapting to maintain with the loss of GOT2.

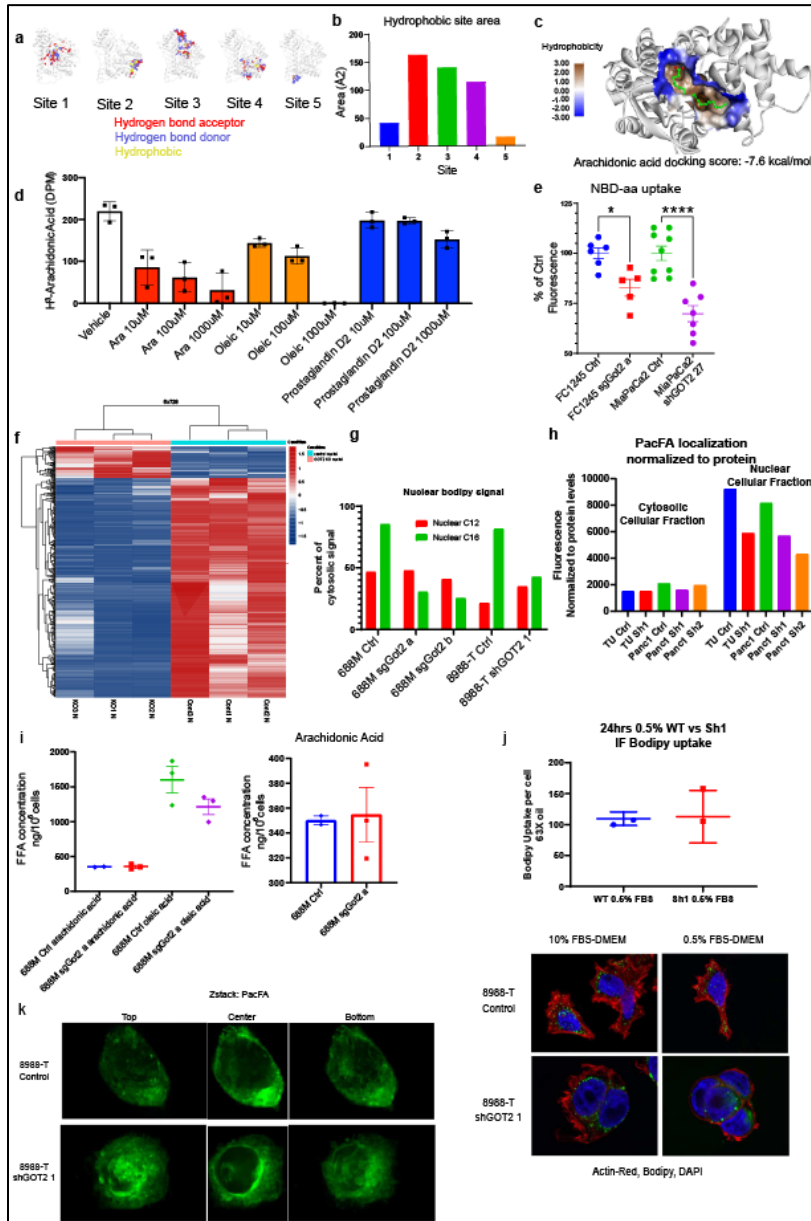


Figure 2.7 GOT2 binds directly to fatty acids and affects FFA levels in the nucleus.

a-b. *in silico* modeling predicts several FA binding sites in GOT2, c. *in silico* modeling predicts AA will bind at site #2 with a docking score of -7.6 kcal/mol, d. competition binding assay shows direct binding of GOT2 with AA and oleic acid, but no direct binding to PGD<sub>2</sub> e. NDA-aa assay shows loss of GOT2 reduces nuclear uptake of fluorescently tagged AA, f. untargeted lipidomics show differences between ctrl and sgGOT2 KD nuclei, g. nuclear uptake of C16 is reduced with GOT2 KD while C12 is unaffected, h. PacFA nuclear uptake is reduced with GOT2 KD, i. nuclear levels of AA are too low to accurately describe levels in control and GOT2 KD cells, oleic acid is reduced by not significantly, j. C12 bodipy uptake is not changed with GOT2 KD, but location may be affected, as seen by ICC-IF, k. PacFA localization appears to be affected by GOT2 KD, with more building up around the nucleus of GOT2 KD cells and control cells have a more even dispersal.

Tissue staining of human PDAC primary tumors shows high levels of GOT2 in the mitochondria and some puncta in the nucleus (Fig 2.6a, b) though it should be noted that there is a great deal of heterogeneity of GOT2 location between tumors and within tumor sections. IHC-DAB and IHC-IF of KC mouse tumors, generously provided by Dr. Ellen Langer, at 6-month and 12-months of age show that GOT2 levels increase as tumors develop (Fig 2.6c). As tumors develop a stronger GOT2 nuclear signal becomes clear, which is an unexpected

result as GOT2 is traditionally described as being localized to either the cell membrane or the mitochondria. With GOT2 playing an important role in both fatty acid transport and

mitochondrial metabolism, it seemed like a good target to look more into and characterize in PDAC. Our results showing GOT2 at a potential novel location also added to the interest to characterize it.

Based on the published crystal structure of human GOT2, we were able to identify 5 putative fatty acid binding sites (Fig 2.7a, b) based on hydrophobicity and size of the potential binding pocket[255]. We decided to focus on site 2 as the most-likely fatty acid binding site and performed *in silico* docking studies for arachidonic acid, a key ligand for nuclear receptors. We found a potential interaction between arachidonic acid and hydrophobic site 2 with a docking score of -7.6 kcal/mol (Fig 2.7c). This score strongly suggests binding could be occurring at site 2, as the known score for arachidonic acid binding to the ligand binding domain of PPAR $\gamma$  is -7.0 kcal/mol, an interaction which is known to be both direct and functionally significant, leading strong support that GOT2 may bind directly to arachidonic acid.

To investigate this potential interaction, we performed - with our collaborators at UCLA - competitive fatty acid binding assays with purified GOT2 protein and radiolabeled arachidonic acid, oleic acid- an acid previously described as binding to GOT2[256], or prostaglandin D2 (PGD<sub>2</sub>)- a downstream metabolite of arachidonic acid which was not predicted to bind to GOT2 based on computational modeling. In the competitive binding assay, increasing concentrations of cold arachidonic acid was able to displace radiolabeled ligand, but PGD<sub>2</sub> was unable to displace the radiolabeled ligand (Fig 2.7d). This matched our hypothesis that GOT2 was capable of binding arachidonic acid and unable to bind the downstream metabolite PGD<sub>2</sub>. Our results for Oleic acid, a fatty acid shown in the literature to be likely to bind to GOT2, was in between the binding for GOT2 to arachidonic acid and PGD<sub>2</sub>. To us this suggests that oleic acid may bind at the same site as arachidonic acid, but at a lower affinity, or at a different site entirely. Either way, our results were incredibly encouraging and suggest an important role for GOT2 in the import of ligands for PPAR members of the nuclear receptor superfamily of transcription factors.

To investigate if GOT2 status was able to cause whole cell and nuclear differences in PDAC cells, we sent whole cell lysates and nuclear extracts to the NYU metabolomics core for MS analysis (Fig 2.7f). The results showed there were significant differences in fatty acids of the nuclei's of 688M control and sgGot2 cells. These results, while untargeted, are extremely supportive of our hypothesis that GOT2 status affects nuclear fatty acid import and drove us to further characterize the impact of GOT2 status on nuclear fatty acid import. We also performed some in-house assays to investigate the effect of GOT2 status on nuclear levels of long chain fatty acids. We treated cells *in vitro* with either a C12 or C16-bodipy then fractionated the cells and measured the amount of fluorescence observed within the nucleus (Fig 2.7g). It was interesting to note that this preliminary data suggests GOT2 transport for nuclear fatty acids may be highly regulated and is potentially more specific for C16 than C12-bodipy. We followed this observations up with some click-chemistry for 9-(3-pent-4-ynyl-3-H-diazirin-3-yl)-nonanoic acid (PacFA) in 8988-T and Panc1 control and shGOT2 cells (Fig 2.7h, k). This click-chemistry technique uses photoreactive crosslinker chemistry to allow a fatty acid with an azide tail to be imported into the cells and then be locked in place following UV activation of the diazirine into a reactive carbene and subsequent binding to nearby proteins. A fluorescent azido is then introduced and a chemical reaction is induced to bind the fluorescent-azido to the locked-in-place PacFA. This causes a shift in nm fluorescence, making washing off excess dye less important than with other techniques. In our preliminary results, we were able to see that the cytosolic amounts of PacFA remained fairly unchanged between control and shGOT2 cells, however the level was lower than that detected in the nuclear extracts (Fig 2.7h). This was an unexpected result, but based on the functionality of the click-chemistry technique employed, it makes sense. The majority of PacFA within the cytosol will be near cytosolic structural proteins, such as actin, and so will be permanently attached to them following UV activation of their diazirine. When we perform fractionation on these cells, we end up removing the structural elements from both cytosol and nuclear fractions in our "waste" pellet. With this in mind it is no surprise that we

would lose the majority of PacFA signal from the cytosolic fraction and is a good reminder of the importance of understanding the mechanistic bases of protocols. IF imaging of 8988T control and shGOT2 1 cells treated with PacFA shows interesting results as it appears that shGOT2 cells, PacFA builds up around the nucleus, while it remains more diffuse in the control cells (Fig 2.7k). This agrees with some of our other data using the C16-bodipy and IF imaging which suggests that GOT2 status may affect the localization of fatty acids within the cells, even if total overall fatty acid import is unchanged (Fig 2.7j).

To try and analyze a potential relationship between GOT2 and arachidonic acid trafficking in cells, we used mass spectrometry to measure arachidonic acid in whole cells and in nuclei. At the whole cell level arachidonic acid was unchanged between 688M control and sgGot2 cells, and at the nuclei it was below the detectable limit (Fig 2.7i). We were able to detect oleic acid, which though decreased in the 688M sgGot2 a nucleus, was not significantly changed between sgGot2 and control (Fig 2.7i). The low amounts of arachidonic acid and oleic acid within the nuclei made measurements at the limit of detection, making getting usable data difficult. In the future we could attempt to spike the cells with arachidonic acid or oleic acid prior to nuclear fractionation to increase the amount of usable signal, or we could collect more cells for nuclear fractionation in the hopes of increasing signal. To overcome this limitation, we designed an assay to measure nuclear arachidonic acid accumulation using fluorescent-tagged arachidonic acid (NBD-aa). Cells were treated with NBD-aa containing media, collected and fractionated, and the amount of fluorescent signal was measured in isolated nuclear extracts. We observed significant reduction in NBD-aa uptake in the nuclei of GOT2 loss-of-function cell lines, MiaPaCa2 and FC1245 (Fig 2.7e). This information led us to the conclusion that GOT2 is playing a role in the import of nuclear fatty acids in PDAC and despite seeing no *in vitro* proliferation difference, we wanted to see if there would be *in vivo* tumor growth affects in a GOT2-null system. We hypothesized that loss of GOT2 could change communication between the tumor and the TME, as nuclear fatty

acids have been proposed as important signaling molecules for the communication between tumors and the TME[200, 257, 258].

Mouse cell lines derived from available mouse lines allow for the use of immunocompetent mice for *in vivo* tumor growth experiments, rather than xenograph models of human cells into immunodeficient nude mice. For this project we created CRISPR/Cas9 sgGot2 KD 688M cell lines, from the 688M cell line developed by the Winslow Lab[259], and shGOT2 KD FC1245 and CRISPR/Cas9 KO FC1245 cell lines for implantation in F1 aguti and Black 6 mice,

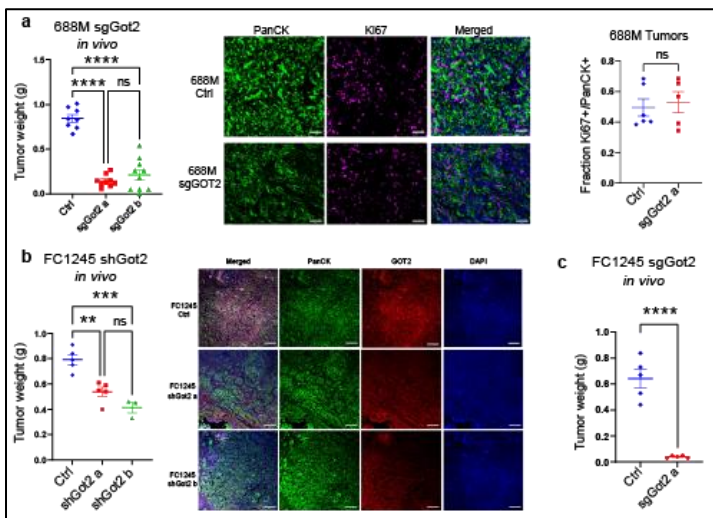


Figure 2.8 Loss of GOT2 results in significant reduction in tumor size *in vivo*.

a. Orthotopically implanted 688M sgGot2 cells grow much smaller tumors, but proliferation rates remain unchanged, b. Orthotopically implanted FC1245 shGOT2 cells grow smaller tumors, and show selective pressure towards cells that express GOT2, as GOT2 levels returned by the end of the experiment, c. Orthotopically implanted FC1245 sgGot2 tumors are significantly smaller than control.

respectively (Fig 2.4a). Cas9 and sgRNAs were introduced by transient transfection and Cas9 expression was lost before cells were used for *in vivo* studies. *In vitro* studies showed that none of the stable knockdown or knockout GOT2 cell lines had proliferation defects, supporting the idea of metabolic plasticity of PDAC to adapt to GOT2 loss (Fig

2.4b, c). However, when orthotopically implanted into the pancreata of immune-competent hosts sgGot2 KD in 688M, shGOT2 KD in FC1245, and sgGot2 KO in FC1245 cell lines showed significant reduction of tumor growth (Fig 2.8a-c). *In vivo* proliferation rates were not reduced in the tumor cells, as shown by IHC-IF staining and analysis of Ki67/PanCK levels remain similar between ctrl and KD tumors (Fig 2.8a), suggesting this *in vivo* growth reduction is independent of proliferation.

It is interesting to note that in the FC1245 shGOT2 KD *in vivo* implantation GOT2 levels began to return to the tumor (Fig 2.8b), resulting in larger tumors than in the sgGot2 KD CRISPR model of 688M (Fig 2.8a). To see if GOT2 levels are truly playing the key role to this effect, we created true CRISPR Got2 KO cells in the FC1245 cell line and implanted them orthotopically in immunocompetent B6 mice (Fig 2.8c). The CRISPR Got2 KO FC1245 tumors nearly completely failed to grow, while the control tumors grew rapidly. This strongly suggests that GOT2 levels are playing a key role in the tumor size reduction seen in our models and that even a small amount of GOT2 increases the size of the tumors.

## **Discussion:**

These results suggest that GOT2 plays a role in transporting fatty acids to the nucleus of PDAC cells and that this role could be having an effect on tumor growth. We demonstrate a novel location for GOT2 at the nucleus of PDAC cells and show that metabolic plasticity with long-term GOT2 removal results in metabolic compensation for the loss of GOT2. We also demonstrate that GOT2 is capable of binding to arachidonic acid, as well as oleic acid, and that loss of GOT2 causes a change in nuclear fatty acid composition. While we were unable to show significant decreases in arachidonic acid and oleic acid in the nuclei of Got2-null cells vs control, due to levels near the lowest detectable limit, we were able to see decreases in NBD-tagged arachidonic acid following *in vitro* treatment. Click-chemistry and bodipy results also suggest a change in both fatty acid storage and localization following loss of GOT2 in our systems.

Our *in vivo* results show a significant decrease in the growth of sgGot2 tumors compared to control in two separate models and that this decrease in growth is not due to a decrease in cell proliferation. Our observations of the return of GOT2 levels in the shRNA KD suggests that there is selective pressure *in vivo* for the expression of GOT2, supporting the hypothesis that GOT2 is playing an important role in the development and maintenance of PDAC. The observed change in fatty acid storage and localization may be linked to our observed *in vivo* growth defect of Got2-null PDAC tumors. It has become apparent that fatty acids, and the proteins that transport them, can be important nuclear signaling molecules for inflammation, tumorigenesis, and angiogenesis[237, 257, 258, 260-265].

The source of fatty acids could be interesting future research, especially with the link between obesity and pancreatic cancer risk. There are a few different conclusions one could take with this link, the main ones being; 1. Obesity increases inflammation and inflammatory signaling leading to improved physiological conditions for PDAC initiation and development or 2. Increased fatty acids in blood serum due to obesity and dietary choices affects signaling of fatty acid nuclear

receptors in cells, leading to conditions conducive to PDAC initiation and development. Although the most likely hypothesis would be a combination where increased fatty acids in blood serum and increased inflammatory signaling from obesity create an environment in the pancreas where supporting cells of the TME are primed to respond in an immune-suppressed way, once activated, setting up a response to PDAC that is both pro-tumorigenic and growth supportive. Metabolic reprogramming of both PDAC cells and supporting cells of the TME appears to be important for the initiation, development, and continued growth of PDAC[16, 188, 219-221, 223, 224, 226, 266-270].

Consequences of metabolic reprogramming could be increasing inflammation of the TME, changing immune response from immune-supportive to immune-suppressive, and simply increasing available nutrients and building materials crucial for PDAC development. We have shown here that the metabolic plasticity of PDAC cells allows for the recovery of AST activity and growth *in vitro* in GOT2-null cells, but that *in vivo* growth of these same cells is severely affected. We initially hypothesized that the difference between cells growing *in vitro* without defect but not growing *in vivo* was due to an inability to mimic the nutrient poor, hypoxic conditions of *in vivo* tumors. However, we were unable to reproduce a growth defect with our GOT2-null cells in hypoxic or nutrient poor conditions. This suggests the possibility that communication between cells of the TME and PDAC cells, reliant on GOT2 status, is the cause for the growth defect seen in our GOT2-null tumors. Literature suggests that fatty acid signaling can change inflammatory response to tumors and metabolic activity[16, 179, 188, 220, 223, 224, 226, 228, 269-272]. As we do not see a proliferation defect *in vivo* nor *in vitro*, and we have shown mitochondrial AST activity of GOT2 is not permanently reduced upon GOT2 loss, it makes sense to suspect that the decrease seen *in vivo* with GOT2-loss could be due to changes in fatty acid signaling from PDAC cells affecting response of the TME, and that this response of the TME is less conducive to PDAC development without GOT2 available for fatty acid transport to

the nucleus. Our results suggest the importance of further characterization of GOT2 in this novel nuclear location and the potential for interesting new insight into the function of fatty acid transporters in this deadly disease.

## **Acknowledgements:**

KC mouse tumor slides were generously provided by our collaborator Dr. Ellen Langer (OHSU).

GOT2 binding assays were performed by our collaborator Dr. Xu Xiao in Dr. Peter Tontonoz's lab (UCLA).

Dr. Drew Jones and Leonard Ash at the NYU Langone Health Metabolomics Laboratory performed lipidomic MS analysis of cell nuclear lysates.

This study was supported by a postdoctoral fellowship from the OHSU Fellowship for Diversity in Research (to JA), a graduate student fellowship from the Knight Cancer Institute Cancer Center Support Grant P30 CA069533 (to HSC), NIH grants R00 CA188259 and RO1 CA229580 (to MHS) including CA229580-S1 (awarded to MHS in support of JA), American Cancer Society grant RSG-18-142-01-CSM (to MHS), and an OHSU Faculty Innovation Fund Award (to MHS). Members of the OHSU histopathology shared resource, medicinal chemistry core, and advanced light microscopy shared resources provided support for this study as well.

## Chapter 3: The tumor cell intrinsic GOT2-PPAR $\delta$ axis helps create the immune-suppressive TME of PDAC.

Portions of this chapter were included in a publication submitted to Nature and undergoing revisions as of Jan 25<sup>th</sup>, 2021.

“A cancer cell-intrinsic GOT2-PPAR $\delta$  axis suppresses antitumor immunity”

Hannah Sanford-Crane, Jaime Abrego, Chet Oon, Xu Xiao, Shanthi Nagarajan, Sohinee Bhattacharyya, Peter Tontonoz, Mara H. Sherman  
bioRxiv 2020.12.25.424393; doi: <https://doi.org/10.1101/2020.12.25.424393>

**Abstract:**

While the incidence of PDAC has increased, the mortality rate has remained fairly constant due to conventional therapies being ineffective in this disease[8, 9], immune-modulatory therapies hold promise to meaningfully improve outcomes for PDAC patients. However, development of such therapies will require an improved understanding of the immune evasion mechanisms that characterize the PDAC microenvironment, including frequent exclusion of antineoplastic T cells and abundance of immune-suppressive myeloid cells[10-13]. Here we show that cancer cell-intrinsic glutamic-oxaloacetic transaminase 2 (GOT2) shapes the immune microenvironment to suppress antitumor immunity. We identified a novel location for GOT2 at the nucleus, along with its canonical locations at the mitochondria and plasma membrane. Mechanistically, we find that GOT2 functions beyond its established role in the malate-aspartate shuttle[14-16] and promotes the transcriptional activity of nuclear receptor peroxisome proliferator-activated receptor delta (PPAR $\delta$ ), facilitated by direct fatty acid binding. This GOT2-PPAR $\delta$  axis results in a tumor supportive, immune-suppressive Tumor Microenvironment (TME). While GOT2 in PDAC cells is dispensable for cancer cell proliferation *in vivo*, GOT2 loss results in T cell-dependent suppression of tumor growth, and genetic or pharmacologic activation of PPAR $\delta$  restores PDAC progression in the GOT2-null context. This cancer cell-intrinsic GOT2-PPAR $\delta$  axis promotes spatial restriction of both CD4<sup>+</sup> and CD8<sup>+</sup> T cells from the tumor microenvironment, and fosters the immune-suppressive phenotype of tumor-infiltrating myeloid cells. Our results demonstrate a non-canonical function for an established mitochondrial enzyme in transcriptional regulation of immune evasion, which may be exploitable to promote a productive antitumor immune response.

## **Personal contribution:**

HSC's contribution to this chapter are as follows:

Figure 3.1 Metascape analysis was done by JA. Immunofluorescence and analysis were performed by HSC and JA. Staining and quantification of Arg1 and F4/80 co-localization was done by HSC. T cell quantification was done by JA. IHC-dab was performed by JA.

Figure 3.2 *in vivo* implantations and collections were done by HSC and JA. Staining and quantification of CD68/Arg1 was done by HSC.

Figure 3.3 *in vivo* implantations and collections were done by HSC and JA. Flow cytometry was designed by HSC and implemented by the OHSU flow cytometry core. Analysis was done by the core and HSC.

Figure 3.4 ChIP-qPCR, dual-luciferase assay, and PPAR $\delta$  activity assay were performed by HSC. VP16-PPAR $\delta$  plasmids were made by CO and stable cell lines were created by HSC. Western blots were run by CO and HSC. qPCR with GW501516 was run by HSC, JA, and CO. COX-2 ICC-IF was stained and imaged by HSC.

Figure 3.5 cell titer glo assays were run by CO. qPCR was run by HSC. *In vivo* implantations and collections were done by HSC and JA.

## **Introduction:**

One of the key pathophysiological features of PDAC is an early infiltration of many immunosuppressive leukocytes into the tumor stroma, matched by low levels of intratumoral effector T cells[12]. Patient samples reveal similar results with the vast majority showing limited tumor-reactive T cell response and highly variable T cell infiltration in IHC imaging[13]. Tumors that showed increased CD8+ T cells, also showed increased markers for M2 macrophages, suggesting an immunosuppressive phenotype, suggesting that the majority of the CD8+ T cells were unlikely to be active[13]. Some of this immune suppression is believed to be driven by ras oncogenic function, leading to immunosuppressive tumors throughout development[12]. This potentially has some therapeutic benefit, as PDAC tumors would remain sensitive to T cell activity, if T cells were able to infiltrate into them. It has been shown that tumor cell-intrinsic factors are the main underlying cause of heterogeneity in immune cell infiltration and immunotherapy response across cancer types[11]. One of the strongest links was with the tumor cell-intrinsic production of CXCL1.

When tumor cells produce CXCL1 it was linked to a non-T-cell inflamed TME and blocking CXCL1 production leading to increased T cell infiltration and sensitivity to combinational immunotherapy treatment[11]. Taken together, this data suggests that the development of therapeutics which would reduce immunosuppressive mechanisms of PDAC and allow T cells into the tumor would be highly effective. *In Vivo* studies looking at spontaneous tumors in genetically engineered mouse models of PDAC have shown similar results, with host immune cells infiltrating the tumors at early stages of tumorigenesis and working in an immune suppressive way[273]. The early infiltration of these immunosuppressive cells effectively undermines lymphocytes that are recruited to the tumor and would otherwise have antitumor function, leading to highly aggressive tumors which, although inflammatory, lack functional immune response[273]. A full understanding of the immune evasion mechanisms that characterize the PDAC microenvironment, including frequent exclusion of antineoplastic T cells

and abundance of immune-suppressive myeloid cells[10-13] is part of the main hinderance holding back the development of immune-modulatory therapies that could meaningfully improve outcomes for PDAC patients.

Recent insight into a FABP5-PPAR $\delta$  axis suggests that fatty acid transporters could play a role in the development of the immune-suppressive TME of PDAC[264, 265]. We previously showed that GOT2 is capable of directly binding to arachidonic acid, a key ligand for several nuclear receptors, and that loss of GOT2 changes nuclear uptake of fatty acids. This suggests the potential for a GOT2-nuclear receptor axis playing a role in the immune-suppressive TME of PDAC, especially since GOT2 is so highly upregulated in this cancer.

## **Materials and methods:**

### ***Animals***

All experiments were reviewed and overseen by the institutional animal use and care committee at Oregon Health and Science University in accordance with NIH guidelines for the humane treatment of animals. C57BL/6J (000664, for models with FC1245[249]) or B6129SF1/J (101043, for models with 688M[250]) mice from Jackson Laboratory were used for orthotopic transplant experiments at 8-10 weeks of age. Tissues from 6- or 12-month-old *Kras<sup>LSL-G12D/+</sup>;Pdx1-Cre* (KC) mice were kindly provided by Dr. Ellen Langer (OHSU).

### ***Human Tissue Samples***

Human patient PDAC tissue samples donated to the Oregon Pancreas Tissue Registry program (OPTR) in accordance with full ethical approval were kindly shared by Dr. Jason Link and Dr. Rosalie Sears (OHSU).

### ***Plasmids***

The pCMX-VP16-PPARD plasmid was kindly provided by Dr. Vihang Narkar (University of Texas Health Science Center at Houston)[274]. To construct pLenti VP16 PPARD, the VP16-PPARD element was amplified by PCR using sense primer 5'-GGGGACAAGTTTGTACA AAAAAGCAGGCTTAATGGCCCCCGAC-3' and antisense primer 5'-GGGGACCACTTTGTACAAGAAAGCTGGGTTTTAGTACATGTCCTTGTAGATTTTCCTGG AGCAGG-3'. PCR product was inserted into pDONR 221 entry clone using Gateway BP Clonase II enzyme (Thermo Fisher 12535029). Entry clone VP16 PPARD element was swapped into expression region of pLenti CMV Puro DEST (Addgene #17452) using LR Clonase II enzyme (Thermo Fisher 11-791-020) to generate pLenti VP16 PPARD construct. The pCMV3 plasmid containing C-terminal His-tagged human GOT2 cDNA was purchased from Sino Biological (HG14463-CH) and cloned into the lentiviral vector pLenti CMV Puro DEST (Addgene #17452) using the same approach as pLenti-VP16 PPARD. pLenti wtGOT2 PCR product was generated using sense primer 5'-GGGGACAAGTTTGTACA AAAAAGCAGGCTTAATGGCCCTGCTGCACT-3' and antisense primer 5'-GGGGACCACTTTGTACAAGAAAGCTGGGTTTTAGTGATGGT GGTGATGATGGTGG-3'. Triple mutant GOT2 was constructed using Q5 Site-Directed Mutagenesis Kit (New England E0552S) in two subsequent steps. Two sets of primers were used to generate three site mutations; primer set 1 for K234A mutation (F:5'-AACAGTGGTG GCGAAAAGGAATCTC-3'; R:5'-GCTATTTCTTCCACTGTTC-3') and primer set 2 for K296A and R303 mutations (F:5'-GTCTGCGCAGATGCGGATGAAGCCAAAGCGGTAGA GTC-3'; R:5'-CATAGTGAAGG CTCCTACACGC-3'). pLenti tmGOT2 was then generated using the same approach and primers as pLenti wtGOT2.

### ***Cell Lines***

Human pancreatic cancer cell lines MIAPaCa-1, PA-TU-8988T, Panc1, HPAF-II, and Capan-2 were obtained from ATCC and grown in Dulbecco's modified Eagle's medium (DMEM) containing 10% fetal bovine serum. Non-transformed, TERT-immortalized human pancreatic ductal epithelial cells were kindly provided by Dr. Rosalie Sears (OHSU)[251]. FC1245 PDAC cells were generated from a primary tumor in *Kras<sup>LSL-G12D/+</sup>;Trp53<sup>LSL-R172H/+</sup>;Pdx1-Cre* mice and were kindly provided by Dr. David Tuveson (Cold Spring Harbor Laboratory)[249]. 688M PDAC cells were generated from a liver metastasis in *Kras<sup>LSL-G12D/+</sup>;Trp53<sup>LSL-R172H/+</sup>;Pdx1-Cre;Rosa26<sup>LSL-tdTomato/+</sup>* mice and were kindly provided by Dr. Monte Winslow (Stanford University School of Medicine)[250]. Cell lines were routinely tested for *Mycoplasma* at least monthly (MycAlert Detection Kit, Lonza).

The pSpCas9(BB)-2A-Puro(PX459) v2.0 plasmid (Addgene #62988) was used to clone guide sequences targeting *Got2* per supplier's protocol; sgRNA A: GACGCGGGTCCACGCCGGT, sgRNA B: ACGCGGGTCCACGCCGGTG. The 688M or FC1245 cell line was transfected with control plasmid or plasmid containing either of the sg*Got2* sequences and subject to selection with 2 µg/ml puromycin for 4 days. Single-cell clones were expanded and screened for GOT2 protein expression by Western blot.

Lentivirus preparation for stable cell line generation was done with pMD2.G envelope plasmid (Addgene #12259) and psPAX2 packaging plasmid (Addgene 12260) in 293T-LentiX cells. Briefly, 5µg pMD2.G, 5µg psPAX2 and 10µg of plasmid DNA (shGOT2 KD, VP16-PPARdelta, wtGOT2, tmGOT2, or scramble Ctrl) were combined with 600ul optimum and 20ul lipofectamine 2000 for 20 mins at room temp. 10cm dishes of 293T-LentiX were kept in 0% FBS DMEM and the mixture was added in a dropwise manner. 12hrs later media was changed to 10% FBS DMEM. At 24hrs after transduction and 48hrs after transduction, media was collected and filtered through a 0.25µm filter, aliquoted, and frozen at -80C. The shGOT2 plasmids were purchased from addgene. Human shGOT2 lot #04161910MN TRCN0000034824, TRCN0000034827, TRCN0000034826, TRCN0000034825. Mouse shGOT2 lot #04161910MN TRCN00000326018, TRCN00000325946, TRCN00000119800, TRCN00000119798, TRCN00000119801.

Lentiviral transduction of human and mouse cell lines: cells were plated to 6-well plates. 10µg/mL polybrene (EMD Millipore TR-1003-G) was added to 1mL 10% FBS DMEM and 300ul of filtered lentivirus media. 24hrs later media was changed to fresh 10% FBS DMEM. 48hrs after initial transduction, cells were treated with 2µg/mL puromycin (Thermo Fisher A1113803), or 4µg/mL puromycin depending on cell line. A control well of non-transduced cells was used as an indicator for proper selection.

### **RNA Extract and Real-Time qPCR**

The isolated total RNA (1 µg) was reverse-transcribed to produce cDNA using iScript Reverse Transcription Supermix kit (Bio-Rad). Real-time PCR was performed using SYBR Green supermix (Bio-Rad). The cDNA sequences for specific gene targets were obtained from the human genome assembly (<http://genome.ucsc.edu>) and gene specific primer pairs were designed using the Primer3 program ([http://frodo.wi.mit.edu/primer3/primer3\\_code.html](http://frodo.wi.mit.edu/primer3/primer3_code.html)). Relative gene expression was normalized using the 36B4 housekeeping gene. The following primer sequences were used: human and mouse 36B4 (*RPLP0*): F:5'-GTGCTGATGGCAAGAAC-3'; R:5'-AGGTCCTCCTTGGTGAAC-3'; human *PTGS2*: F: 5'-CTGGCGCTCAGCCATACAG-3'; R:5'-CGCACTTATACTGGTCAAATCCC-3'; human *PDK4*: F:5'-AGAAAAGCCCAGATGACCAGA-3'; R:5'TGGTTCATCAGCATCCGAGT-3'; human *CPT1A*: F:5'-CTGTGGCCTTTCAGTTCACG-3'; R:5'-CCACCACGATAAGCCAACTG-3'; human *TGFBI*: F:5'-GGCCTTCTGCTTCTCAT-3'; R:5'-CAGAAGTTGGCATGGTAGCC-3'; human *CXCL1*: F:5'-AGGGAATTCACCCCAAGAAC-3'; R:5'-ACTATGGGGGATGCAGGATT-3'; human *CXCL9*: F:5'-ATTGGAGTGCAAGGAACCCC-3'; R:5'-ATTTTCTCGCAGGAAGGGCT-3'; human *CXCL10*: F:5'-GTGGCATTCAAGGAGTACCTC-3'; R:5'-TGATGGCCTTCGATTCTGGATT-3'; mouse *Ptgs2*: F:5'-TGAGTGGGGTGATGAGCAAC-3'; R:5'-TTCAGAGGCAATGCGGTTCT-3'; mouse *Pdk4*: F:5'-TGAACACTCCTTCGGTGCAG-3'; R:5'-GTCCACTGTGCAGGTGTCTT-3'; mouse *Pparg1a*: F:5'-GCTTGACTGGCGTCATTCGG-3'; R:5'-TGTTTCGAGGCTCATTGTTG-3'; mouse *Tgfb1*: F:5'-CACTCCCGTGGCTTCTAGTG-3'; R:5'-GTTGTACAAAGCGAGCACCG-3'; mouse *Cxcl1*: F:5'-TGGCTGGGATTCACCTCAAG-3'; R:5'-CCGTTACTTGGGGACACCTT-3'; mouse *Cxcl9*: F:5'-AACGTTGTCCACCTCCCTC-3'; R:5'-CACAGGCTTTGGCTAGTCGT-3'; mouse

*Cxcl10*: F:5'-CAAGCCATGGTCCTGAGACA-3'; and R:5'-TGAGCTAGGGAGGACAAGGA-3'.

### ***Chromatin-precipitation Immunohistochemistry (ChIP) qPCR***

Chromatin immunoprecipitation was performed as described previously<sup>5</sup>. Briefly, PDAC cells were fixed in 1% formaldehyde, and nuclei were isolated and lysed in buffer containing 1% SDS, 10 mM EDTA, 50 mM Tris-HCl pH 8.0, and protease inhibitors, and sheared with a Diagenode Bioruptor to chromatin fragment sizes of 200–1000 base pairs. Chromatin was immunoprecipitated with antibodies to PPAR $\delta$  (Abcam ab178866), or acetylated histone H3K9 (Cell Signaling Technology 9649). PPAR $\delta$  binding or histone acetylation at known PPAR $\delta$  target gene promoter regions was assessed by ChIP-qPCR and enrichment values were normalized to a control intergenic region of the genome. The following primer sequences were used: *Pparg* F: tgatgttgcgcaaggatg, R: agggttctatgctgaaggcttct, *Tgfb1* F: ggtgctcgtttgtacaaca, R: gggtaatttctcccgggtga, *Cxcl10* F: gcatccctgagagaatcagc, R: gccaaatttagccagatcca, Intergenic A F: gacttctcaccacacatgc, R: acagaggaaacagaaatggct, *Ptgs2* F: gggactcctcaggctcag, R: aagtgggttgctgcttctca, *Angptl4* F: tcagcctaccaggagagaa, R: ggaggaaaggcgtacaaat, *Cpt1a* F: ccaaacaaccaacaaca, R: cggcagacctaggacaacat, *Il6* F: gttctctgggaaatcgtgga, R: tccaacctccactcaaac, *Hmgcs2* F: ggcagagaatgtttgagc, R: acctgcaacagcctctttgt, Intergenic B F: tggcttcttggatcaatca, R: aggacaaaacagcaaccaaca.

### ***Western Blots***

PDAC cells were treated as described in the text, and whole cell lysates were prepared in RIPA buffer containing protease inhibitor cocktail (Sigma-Aldrich 11836170001). Alternatively, sub-cellular fractions were prepared by several different fractionation methods.

Detergent Free Fractionation protocol: Cells are scraped and collected from 10cm dishes. Washed with PBS (450g x 5mins) and 1/5 of the volume is separated for whole cell lysis in RIPA (Amresco N653-100mL) + cOmplete EDTA-free Protease inhibitor cocktail (Sigma-Aldrich 11836170001). Remain 4/5 of cell mass is centrifuged (450g x 5mins), PBS is removed and cells are lysed on ice for 15 mins in Lysis buffer (5x of cell pellet volume). Lysis Buffer: 10mM HEPES pH 7.9, 1.5mM MgCl<sub>2</sub>, 10mM KCl with 1mM DTT and EDTA-Free cOmplete mini protease inhibitor cocktail. Centrifuge (450g x 5mins), decant super, add lysis buffer (2x cell volume) and grind on ice with a plastic homogenizer 10x in 1.5mL Eppendorf tubes. Centrifuge (10,000g x 20mins) collect supernatant as cytosolic fraction. Wash with 200ul lysis buffer (10,000g x 5mins) decant super and add extraction buffer (2/3x cell pellet volume). Extraction buffer: 20mM HEPES pH 7.9, 1.5mM MgCl<sub>2</sub>, 0.42M NaCl, 0.2uM EDTA, 25% glycerol (V/V), 1mM DTT and cOmplete mini EDTA-free protease inhibitor cocktail. Grind nuclei with plastic homogenizer in 1.5mL Eppendorf tubes 20x. Incubate at 4C with gentle shaking for 10 mins. Centrifuge (20,000g x 5mins) and transfer supernatant to cold Eppendorf tube, label as Nuclear portion.

Cell Signaling Tech Cell Fractionation Kit (CST 9038S) was performed following the manufacturer's recommendations. Briefly cells were collected with scraping and washed in PBS (350g x 5mins). Resuspend in 500ul PBS and remove 100ul for whole cell lyses in RIPA buffer + cOmplete mini EDTA-free protease inhibitor cocktail. Remaining cell pellet was centrifuged (500g x 5 mins), PBS was decanted and 500ul CIB + 5ul Protease Inhibitor and 2.5ul PMSF was added. Vortex and store on ice 5 mins. Centrifuge (500g x 5mins) supernatant is cytosolic fraction. Wash with CIB. Decant supernatant. Add 500ul MIB + 5ul Protease Inhibitor and 2.5ul PMSF to the cell pellet. Vortex 15 seconds, incubate on ice 5 mins, and centrifuge (8000gx 5 mins). Supernatant is the membrane & organelle fraction. Wash in MIB. Decant supernatant. Add 250ul CyNIB + 2.5ul Protease Inhibitor + 1.25ul PMSF to the cell pellet. Sonicate for 5 sec at

20% power 3x. For western blot add 60ul 3X LDS loading buffer with 10X reducing agent for every 100ul of supernatant per fraction. Boil for 5 mins at 95C and centrifuge for 3 mins at 15,000g. Load 15ul of each fraction along with 15ul of whole cell lysate.

Protein concentration was quantitated using the BCA protein assay kit (Pierce). Equal amounts of protein were loaded in each lane and separated on a 4-12% Bis-Tris NuPAGE® gel (Invitrogen), then transferred onto a PVDF membrane. Membranes were probed with primary antibodies and infrared secondary antibodies: anti-GOT2 (Thermo Fisher PA5-77990), anti-His-tag (R&D Systems MAB050-100), anti-PPAD (Abcam ab178866), anti-Lamin A/C (Cell Signaling Technology 4777S), anti-COX IV (Cell Signaling Technology 11967S), anti-rabbit Alexa Fluor Plus 680 (Thermo Fisher A32734) and anti-mouse Alexa Fluor Plus 800 (Invitrogen A32730). Protein bands were detected using the Odyssey CLx infrared imaging system (LICOR Biosciences).

### ***PPAR $\delta$ Transcription Factor Activity Assay***

Nuclear lysates were prepared using a detergent-free fractionation protocol. Cells were scraped and collected from 10 cm dishes, washed with PBS, pelleted (450 x g 5mins), resuspended in PBS and 1/5 of the volume was reserved for whole cell lysis in RIPA (Amresco N653-100mL) + cOmplete EDTA-free Protease inhibitor cocktail (Sigma-Aldrich 11836170001). The remaining 4/5 of cell suspension was centrifuged (450 x g 5mins), PBS removed and cells were lysed on ice for 15 mins in Lysis buffer (5x of cell pellet volume). Lysis Buffer: 10mM HEPES pH 7.9, 1.5mM MgCl<sub>2</sub>, 10mM KCl with 1mM DTT and EDTA-Free cOmplete mini protease inhibitor cocktail. Lysates were centrifuged (450 x g 5mins), supernatant decanted, lysis buffer added (2x cell volume) and suspensions ground on ice with a plastic homogenizer 10x in 1.5mL Eppendorf tubes. Lysates were centrifuged (10,000 x g 20mins) and supernatant collected as cytosolic fraction. Remaining pellet was washed with 200  $\mu$ l lysis buffer (10,000 x g 5mins), supernatant decanted and extraction buffer added (2/3x cell pellet volume). Extraction buffer: 20mM HEPES pH 7.9, 1.5mM MgCl<sub>2</sub>, 0.42M NaCl, 0.2uM EDTA, 25% glycerol (V/V), 1mM DTT and cOmplete mini EDTA-free protease inhibitor cocktail. Nuclei were ground with plastic homogenizer in 1.5mL Eppendorf tubes 20x, and incubated at 4°C with gentle shaking for 10 mins. Samples were centrifuged (20,000 x g 5mins) and supernatant transferred to cold Eppendorf tubes, as nuclear fraction. Lysates were measured with BCA and an equal protein amount was added per sample for each well. Manufacturer's instructions were followed for the PPAR delta transcription factor kit (Abcam ab133106). Briefly CTFB was prepared and added to blank and NSB wells, nuclear lysates were added to each sample well containing immobilized PPRE-containing DNA and the plate was incubated overnight at 4°C without agitation. The next day the wells were washed 5x in 1X wash buffer and incubated in PPARdelta primary antibody (1:100) for 1hr at room temperature in the dark, without agitation. Wells were washed 5x in 1X wash buffer and incubated in goat anti-rabbit HRP conjugate (1:100) for 1hr at room temperature in the dark without agitation. Wells were washed 5x in 1X wash buffer and 100  $\mu$ l developing solution was added to each well. Plate was incubated for 15-45 minutes on a room temperature shaker, in the dark, until color developed. 100  $\mu$ l stop solution was added to wells and the absorbance at 450nm was taken.

### ***Immunofluorescence***

Cells plated on coverslips were fixed in 10% neutral buffered formalin for 10 minutes at room temperature, washed three times with PBS, and permeabilized with .1% Triton X-100 for 10 min at room temperature. When MitoTracker staining was performed, cells plated on coverslips were stained with 100 nM MitoTracker (Thermo Fisher M22462) at 37°C for 15 minutes prior to fixation. Following permeabilization, coverslips were blocked for one hour at room temperature

in blocking solution (Aqua block buffer, Abcam ab166952) and then transferred to a carrier solution (Aqua block) containing diluted primary antibodies: GOT2 (Sigma-Aldrich HPA018139), GOT2 (Thermo Fisher PA5-77990), COX IV (Cell Signaling Technology 11967S), COX2 (Abcam ab15191), His (R&D Systems MAB050-100). Coverslips were incubated with the primary antibody at 4°C overnight and then washed five times for 5 minutes each in PBS following which, secondary Alexa-fluor conjugated antibodies diluted in the same carrier solution (1:400) were added to the coverslips for one hour at room temperature. After the secondary antibody incubation, coverslips were washed five times for five minutes each in PBS and mounted with Vectashield mounting media containing DAPI (Vector Laboratories H-1500). Images were captured on a Zeiss LSM 880 laser-scanning inverted confocal microscope in the OHSU Advanced Light Microscopy Shared Resource, and a 40x/ 1.1 NA water objective or 63x/1.4 NA oil objective was used to image the samples.

### ***Dual Luciferase Assay***

PPRE x3-TK-Luc (PPAR response element driving luciferase) plasmid #1015 was purchased from Addgene and the Renilla plasmid (pRL-SV40) was generously provided by Dr. Ellen Langer (OHSU). Cells were transfected with 2.5 µg PPRE x3-TK-Luc, 15 ng pRL-SV40, and 4 µl Lipofectamine 2000 in 6-well plates. Briefly, cells were plated at  $1 \times 10^6$  per well of a 6-well plate and allowed to adhere overnight. Plasmids were combined in 150 µl Opti-MEM while lipofectamine 2000 was combined in a separate tube with 150 µl Opti-MEM. After 5 mins the tubes were combined. 300 µl of the mixture was added, in a dropwise manner, to 700 µl of Opti-MEM on each well for transfection. The cells were incubated overnight at 37°C, collected, counted, and replated to white-walled 96-well plates in triplicates. 24 hours later a dual luciferase assay was completed, following the manufacturer's instructions: Dual-Luciferase Reporter Assay System (Promega E1910). Briefly, cells were lysed in white-walled 96-well plates with 20 µl 1X Passive Lysis Buffer and shaken on a room temp shaker. 100 µl LARII was added to each well and luminescence was measured over 5 seconds. 100 µl of Stop and Glo were then added and Renilla activity was measured with luminescence over 5 seconds. Activity was calculated by normalizing luciferase signal to renilla for each well.

### ***Orthotopic Implantation In Vivo Model***

The orthotopic transplant method used here was described previously<sup>6</sup>. In brief, 8- to 10-week-old wild-type male C57BL/6J (for FC1245) or B6129SF1/J (for 688M) mice were orthotopically transplanted as described previously with  $5 \times 10^3$  FC1245 cells or  $8 \times 10^4$  688M cells in 50% Matrigel (Corning 356231), 50% DMEM. For experiments with 688M cells harboring VP16-PPARD,  $6 \times 10^4$  688M cells were used. For T cell neutralization experiments, mice received intraperitoneal injection of 0.2 mg of αCD8 (2.43), αCD4 (GK1.5), or an IgG2b isotype control (LTF-2) diluted in 100 µl sterile PBS. Antibodies were purchased from BioXcell and were administered beginning 2 days pre-implantation with  $6 \times 10^4$  688M cells and every 4 days thereafter until euthanasia, as previously described<sup>7</sup>. Mice were euthanized when control animals were moribund, and tumors were excised, weighed, and immediately fixed in formalin.

### ***Immunohistochemistry of Tumor Tissue***

Mice were anesthetized and euthanized according to institutional guidelines. Pancreatic tumors were excised carefully and fixed overnight in 10% phosphate-buffered formalin. Tissue samples were paraffin embedded and sectioned by the OHSU Histopathology Shared Resource. Human PDAC tissue sections from formalin-fixed, paraffin-embedded blocks were obtained from the OPTR. In brief, tissue sections were de-paraffinized and rehydrated through an ethanol series and ultimately in PBS. Following antigen retrieval, tissue samples were blocked for 1 hour at room temperature in blocking solution (8% BSA solution) and then transferred to a carrier solution (8%

BSA solution) containing diluted antibodies: GOT2 (Sigma-Aldrich HPA018139), GOT2 (Thermo Fisher PA5-77990), COX IV (Cell Signaling Technology 11967S), COX2 (Abcam ab15191), CD3 (Abcam ab5690), CD4 D7D2Z (Cell Signaling Technology 25229S), CD8 (Abcam ab203035), Granzyme B (Abcam ab4059), F4/80 (Cell Signaling Technology 70076T), Arginase-1 (Sigma-Aldrich ABS535)). Sections were incubated overnight at 4°C and then washed five times for 5 minutes each in PBS. For fluorescence imaging, secondary Alexa-fluor conjugated antibodies diluted in the same carrier solution (1:400) were added to the sections for one hour at room temperature. Sections were then washed five times for five minutes each in PBS and were mounted with Vectashield mounting media containing DAPI. For DAB chromogen imaging, sections were stained with primary antibody as described above, then the samples were incubated in polymeric horseradish peroxidase (HRP) conjugated secondary antibody (Leica PV6121) for one hour followed by 5 five-minute 1xTBST washes. HRP was detected using DAB chromogen (3,3'-Diaminobenzidine) solution (BioCare Medical BDB2004) prepared per manufacturer instructions. Tissues were exposed to chromogen solution until a brown precipitate was detected produced from oxidized DAB where secondary poly-HRP antibody is located. As soon as DAB chromogen is detected the tissue-slides were washed in diH<sub>2</sub>O, counterstained in hematoxylin, dehydrated and cleared for mounting. Stained tissue sections were scanned on a Leica Biosystems Ariol digital fluorescence scanner or Leica Biosystems Aperio brightfield digital scanner. Quantification was performed for single stains using QuPath quantitative pathology and bioimage analysis software v0.2.3. For co-stains (CD8/GRZB and F4/80/ARG1), manual counting was performed on at least 10 high-powered fields per tumor sample.

### ***Flow Cytometry***

Mouse PDAC tumors were harvested from mice 24-28 days post tumor transplant and minced. Tumors were digested for 1 hr at 37°C in DMEM containing 1mg/ml collagenase IV, 0.1% soybean trypsin inhibitor, 50 U/ml DNase, 0.125 mg/ml Dispase. Tumors were manually dissociated and spun down at 300 g for 5 minutes, and further digested with 0.25% Trypsin-EDTA for 10 minutes at 37°C. Digested tumors were washed with DMEM containing 10% FBS and filtered through a 100 µm mesh strainer. The digest was pelleted and washed with 10% FBS DMEM. Digested were then lysed with ACK lysis buffer for 3 min at room temperature before being washed with FACS. Cells were resuspended at 10<sup>6</sup> and incubated with CD8-FITC (1:200)(BioLegend 155004), CD4-BV605 (1:100)(BioLegend 100451), CD3-APC-Cy7 (1:200)(BioLegend 100221), and CD45-PE-Cy7 (1:100)(BioLegend 103131) were added and samples incubated for 30 minutes on ice. Cells were washed with FACS and resuspended in FACS. Cells were run on Fortessa and analyzed using FLOWJO.

### ***Metascape Analysis***

PDA TCGA Firehose Legacy data base provides mRNA expression data for co-expression analysis accessible through cBioportal. The data set includes Spearman's correlation analysis and P-values for each gene comparison. The data set was used to identify genes negatively correlated with GOT2 expression in PDA patients. A list of genes with Spearman's correlation value of equal or less than -0.25 and a P-value of less than 0.01 was generated. The list of genes was submitted to online bioinformatics tool Metascape for identification of enriched gene ontology clusters in the data set. The output from Metascape analysis was graphed using GraphPad Prism.

### ***Statistical Analysis***

GraphPad Prism software was used for all statistical analysis. Welches unpaired T-tests were used to compare two treatment groups to each other. One-Way Anova was used to compare multiple treatment groups for one variable. A P value of < 0.05 was considered significant.

## **Results:**

We initially looked into the possible role of GOT2 in nuclear receptors by performing a metascope analyses of genes inversely correlated to GOT2 (Fig 3.1a). We found that many of the genes most inversely correlated to GOT2 were also involved in immune system regulation. These include lymphocyte activation, T cell activation, leukocyte differentiation, lymphocyte differentiation, leukocyte activation, and T cell differentiation. Based on this analysis, we decided to check if GOT2 could be regulating abundance and/or activity of intratumoral T cells, and if the decrease in tumor size seen in our GOT2-null system could be related to a difference in immune response.

We used IHC to quantify T cells in our GOT2 loss-of function models and found that CD3 positive T cells are increased in our KO and KD in vivo tumors along with both CD8 and CD4 populations (Fig 3.1b-d). Investigation into the macrophages of these mice showed that there was a restoration in M2-like macrophages (CD68+ and Arg1+) in sgGot2 KD tumors (Fig 3.1e). We saw an overall increase in macrophage abundance and decrease in frequency of Arg1+ macrophages out of total macrophages in the sgGot2 setting, consistent with macrophage polarization to a less immune-suppressive phenotype that's more permissive to T cell recruitment. We also saw an increase in the frequency of GRZB+ CD8+ out of all CD8+ cells in the sgGot2 setting (Fig 3.1f) suggesting that the limited T cells found within the control tumors are more likely to be immune-suppressive than cytotoxic and supporting the idea that the T cells of the sgGot2 tumors are cytotoxic and active.

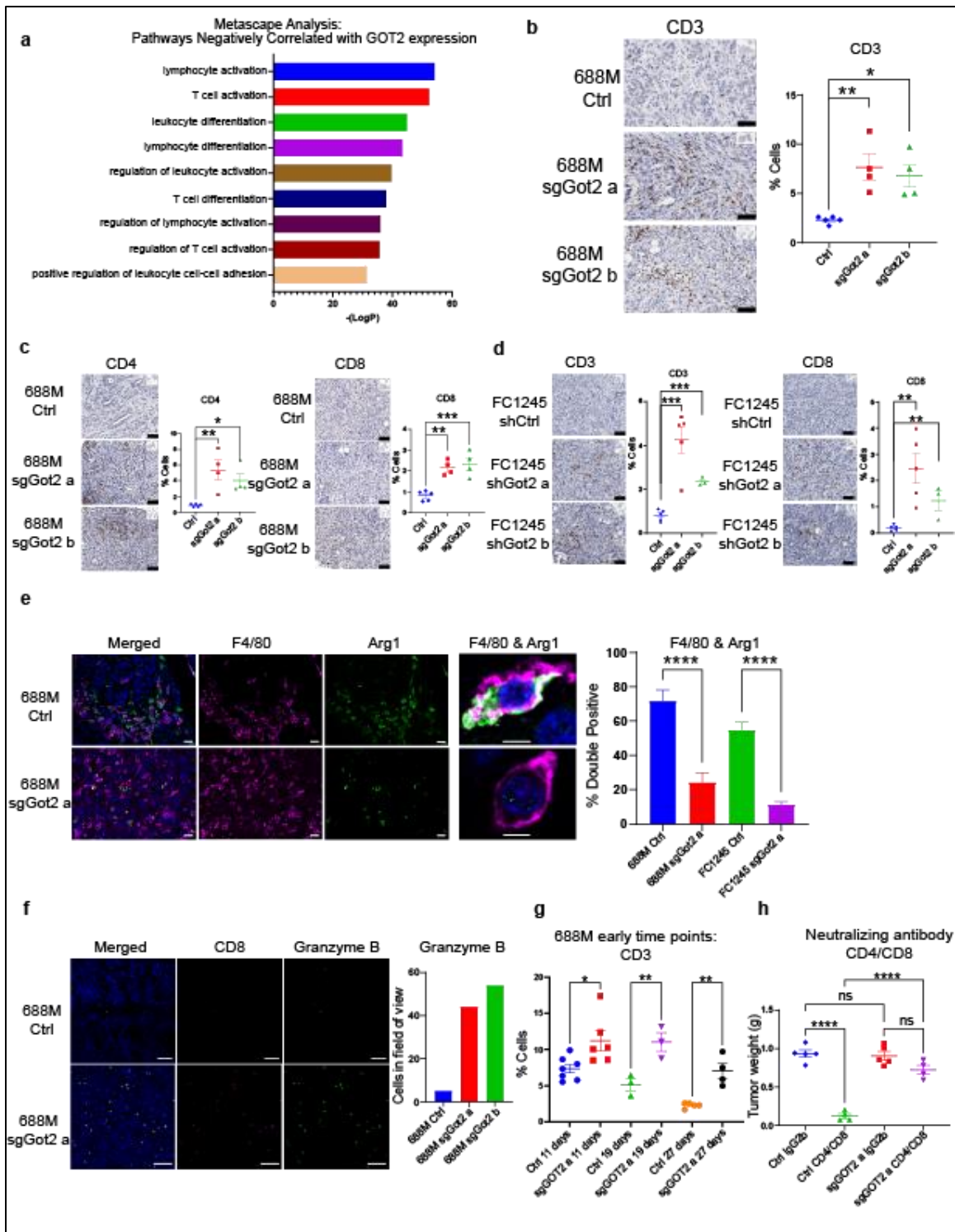


Figure 3.1 PDAC cell-intrinsic GOT2 suppresses T cell-dependent immunologic control of tumor growth.

**a**, Metascape pathway analysis depicting transcriptional programs inversely correlated with GOT2 expression in human PDAC. **b,c**, Immunohistochemical staining of control and sgGot2 688M tumors for T cell marker CD3 (**b**) and subtype markers CD4 and CD8 (**c**). Representative images are shown on the left (scale bar = 50  $\mu$ m), with quantification on the right (Ctrl: n = 5, sgGot2 a: n = 4, sgGot2 b: n = 4). **d**, Immunohistochemical staining of control and shGot2 FC1245 tumors for T cell markers CD3 and CD8. Representative images are shown on the left (scale bar = 50  $\mu$ m), with quantification on the right (Ctrl: n = 5, shGot2 a: n = 5, shGot2 b: n = 3). **e**, Immunohistochemical co-staining of control and sgGot2 or shGot2 PDAC for macrophage marker F4/80 and immunosuppressive factor arginase-1. Representative images are from 688M tumors (scale bar on 20X images = 10  $\mu$ m, scale bar on 63X images = 5  $\mu$ m). Quantification of double-positive cells out of total F4/80<sup>+</sup> cells in the 688M and FC1245 models is on the right; data are presented as mean  $\pm$  s.e.m. \*\*\*\*p < 0.0001 by unpaired t-test. **f**, Immunohistochemical co-staining of control and sgGot2 688M tumors for T cell marker CD8 and granzyme B (scale bar = 50  $\mu$ m), with granzyme B quantification on the right. **g**, Quantification of CD3 immunohistochemistry on 688M PDAC at the indicated time points post-transplantation (Ctrl d11: n = 7, sgGot2 d11: n = 6, Ctrl d19: n = 3, sgGot2 d19: n = 3, Ctrl d27: n = 5, sgGot2 d27: n = 4). \*p < 0.05, \*\*p < 0.01 by unpaired t-test. **h**, PDAC tumor weight at experimental endpoint, 27 days after orthotopic transplantation of 688M cells and treatment with isotype control or T cell neutralizing antibodies (details in Methods). Ctrl: n = 5 per cohort, sgGot2: n = 4 per cohort. For **b-h**, data are presented as mean  $\pm$  s.e.m. For **b-e & h**, \*p < 0.05, \*\*p < 0.01, \*\*\*p < 0.001, \*\*\*\*p < 0.0001 by one-way ANOVA.

Our initial thought to further investigate this aspect of the project was to repeat the orthotopic implantations in an immune-incompetent nude mouse model. In this model we saw that while the sgGot2 KD tumors were able to grow larger, they still remained significantly smaller than the ctrl tumors (Fig 3.2a). We also saw that the macrophages of the mice were affected by the decrease in

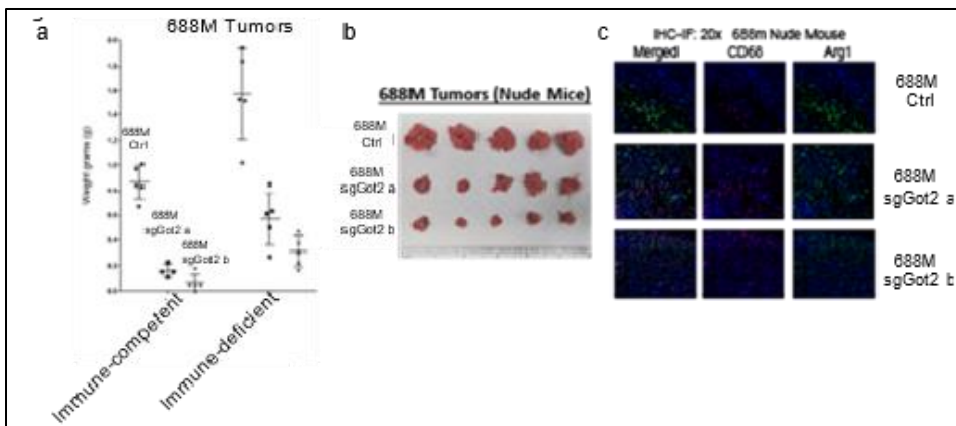


Figure 2.2 PDAC cell-intrinsic GOT2 suppresses tumor growth in a nude mouse model.

a-b. Comparison of tumor growth in immune-competent and immune-deficient mouse models. While tumor growth was enhanced in the nude mice, the proportion of decrease from control tumors remained similar. c. IHC co-staining of macrophage marker CD68 and immunosuppressive factor arginase-1.

GOT2. The control tumors showed the M2 (immune-suppressive) - like phenotype typical of

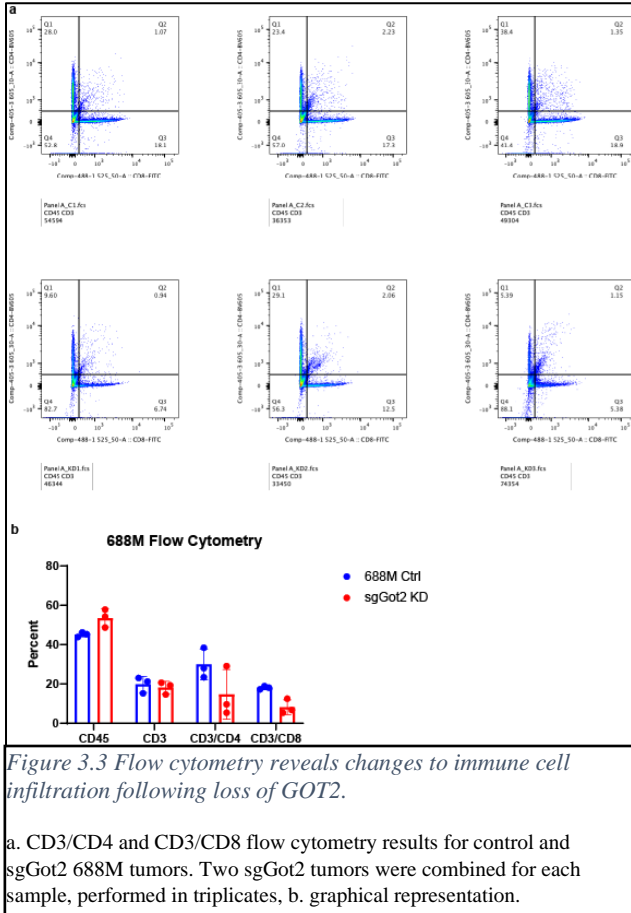
PDAC – with Arg1 co-staining with CD68 – while the sgGot2 KD tumors showed more of an M1-like phenotype with reduced co-staining of Arg1 and CD68 (Fig 3.2c). While nude mice are an important investigative tool, they are not skid mice and still have a functional immune system despite impaired T cell function due to lack of a thymus. This could be leading to complication in our analysis, as many different immune cells of the TME could be involved in this process.

However, it is interesting that even in a nude mouse model GOT2 KD was able to decrease tumor size and change immune response to PDAC. This suggests that there is a great deal left to be discovered about the cross-talk between PDAC and the TME, particularly with regards to immune cells, and where GOT2 fits into this interaction.

To test if T cell abundance was secondary to differences in tumor size, we performed a time course study in immune-competent mice and harvested tumors soon after transplantation to quantify intratumor T cells (Fig 3.1g). We found that while the amount of CD3 positive T cells decreased along with tumor progression, from day 11, day 19, to day 29, the amount of CD3 positive T cells remained significantly higher in the KO tumors throughout tumor development. It is important to note that at day 11 the tumors are not yet different in size, yet still showed increased CD3+ T cells in the sgGot2 setting. This suggests that the increase in CD3 positive T cells is an intrinsic factor of the GOT2 KO tumor and not something that develops over time.

To test if T cells were functional in suppressing tumor progression, we performed a CD4/CD8 neutralizing antibody experiment in immunocompetent mice (Fig 3.1h). Here we found that treatment with CD4/CD8 neutralizing antibody significantly restored sgGot2 KD tumor growth in this model compared to IgG2B treated controls. The treatment of CD4/CD8 neutralizing antibody had no impact on the growth of control tumors, in agreement with previous studies showing a lack of T cell-mediated antitumor immunity in mouse models of PDAC[275], but was able to restore growth of sgGot2 tumors agreeing with the idea that GOT2 promotes PDAC progression at least partially by suppressing T cell-dependent antitumor immunity. It is interesting to note that for the first 2 weeks of the study it appeared that the CD4/CD8 neutralizing antibody would have no significant impact on the tumor, and that the last few weeks of the study were key for tumor growth. This again supports the hypothesis that the adaptive immune response to the tumor is the main cause for the growth defect, as it can take around 2 weeks for the adaptive immune response

to be primed for response. Had we ended the experiment at only 2.5 weeks it is doubtful there would be any significant difference between the IgG2B treated sgGot2 KD implanted mice and the CD4/CD8 treated sgGot2 KD implanted mice. This could also help explain why there is still such a large tumor growth defect compared to ctrl in the nude mouse model. The control tumors



grow so rapidly in this model that the human endpoint was just below 3 weeks rather than the typical 3-4 of the immunocompetent mouse models. Our hypothesis suggests that adaptive immune response is driving a decrease in tumor growth, therefore it is unsurprising that length of experiment plays an important role. An interesting future direction could be following the orthotopically implanted mice out for survival curves for the FC1245 Got2 ctrl and Got2 KO tumors.

Along with IHC analysis, we also performed flow cytometry on 688M orthotopically implanted ctrl and sgGot2 KD tumors (Fig 3.3 a-b). Flow cytometry was complicated by the fact that our control tumors were nearly 10x the size of the KD tumors. Along with that increase in tumor size comes with an increase in possible lymph node contamination, and indeed we noticed several lymph structures in our large 688M tumors during IHC analysis. Despite this complication, we were able to see that CD45 positive cells are enriched in the sgGot2 KD tumors, but because of the extreme size difference in tumors IHC remains the best option for immune cell analysis.

Nuclear fatty acid trafficking is regulated by fatty acid binding proteins and have functional significance as ligands for the peroxisome proliferator-activated receptor (PPAR) members of the nuclear receptor superfamily of transcription factors, including PPAR $\alpha$ , PPAR $\gamma$ , and PPAR $\delta$ [262, 276]. PPAR $\alpha$  and PPAR $\gamma$  are expressed in a tissue-restricted manner, but PPAR $\delta$  is ubiquitously expressed in all PDAC cell lines we examined and was not affected by GOT2 status. In the literature, PPAR $\delta$  promotes tumorigenesis with tissue-specific metabolic and immune-modulatory mechanisms[193, 199, 277, 278] which appeared to match well with the phenotype observed in our control models, while PPAR $\delta$  deficiency appeared to match well with the observed phenotype of our sgGot2 KO model. This led us to test if a functional relationship could exist between GOT2 and PPAR $\delta$  which could underlie the phenotypes of GOT2-null PDAC.

We used a few different assays to test transcriptional activity of PPAR $\delta$  in our control and GOT2-null systems, including dual-luciferase and an ABCAM kit for PPAR $\delta$  response element. We saw a large reduction in the amount of PPAR $\delta$  activity measured by dual-luciferase, or with the PPRE ABCAM kit in GOT2 KD or KO cells vs control in three different cell lines tested (Fig 3.4 a,b). Our results from both assays suggest that GOT2 positively regulates PPAR $\delta$  activity in PDAC cells (Fig 3.4 a,b). We observed changes in ChIP-qPCR and mRNA expression of target PPAR $\delta$  consistent with a decrease in PPAR $\delta$  activity. PPAR $\delta$  is constitutively nuclear and bound to DNA but upon binding with nuclear fatty acids, it undergoes a conformational change enabling PPAR $\delta$  to interact with coactivator complexes and cause downstream induction of target gene expression[279]. Our results from chromatin immunoprecipitation (ChIP) and qPCR for PPAR $\delta$  and acetylated histone H3K9, further support a reduction of PPAR $\delta$  transcriptional activity in the absence of GOT2 (Fig 3.4 c, d).

We further examined the link between GOT2 status and PPAR $\delta$  activity by looking at mRNA expression of genes which have been known to be PPAR $\delta$  targets. We found that the majority of known PPAR $\delta$  target genes we tested were affected by GOT2 status and that treatment with a

synthetic PPAR $\delta$  agonist, GW501516, restored target gene expression (Fig 3.4 e). This suggested that the genes which are decreased by loss of GOT2 can have their expression restored through activation of PPAR $\delta$ , thus supporting the idea that loss of GOT2 may be leading to a decrease in PPAR $\delta$  activity, as PPAR $\delta$  activity was enough to push mRNA expression of genes decreased by GOT2 loss towards basal level of control cells. One of the more interesting genes we found to be affected by GOT2 loss was *PTGS2*, which encodes for the enzyme COX-2. Recent studies using gain- and loss-of-function experiments with COX-2 suggest that T cell exclusion in the PDAC microenvironment could be linked to COX-2 activity and that *PTGS2*, the gene encoding for COX-2, is correlated to poor patient survival[206]. These results matched our phenotype observation *in vivo* and our mRNA COX-2 expression, and ChIP-qPCR H3K9ac pulldown of *PTGS2*, so we decided to further investigate the downstream regulation of COX-2 by GOT2 (Fig 3.4 c,d). We found that along with transcriptional changes, COX-2 protein levels were decreased in GOT2-null PDAC cells both *in vitro* and *in vivo* (Fig 3.4 f-h). This decrease in COX-2 protein levels was rescuable with GW501516 treatment *in vitro* and *in vivo*. Altogether this links known literature supported roles of COX-2 and immune suppression with GOT2 status in PDAC and supports the idea that GOT2 promotes transcriptional activity of PPAR $\delta$  in PDAC cells both *in vitro* and *in vivo*.

We decided to take this data to the next logical step and specifically activate PPAR $\delta$  in PDAC cells by introducing a fusion of PPAR $\delta$  with VP16 transactivation domain from herpes simplex virus[274] to enable ligand-independent activation in both control and sgGot2 PDAC cells. *In vitro* growth was unchanged between PDAC control and sgGot2 cells (Fig 3.5 a,b), but *in vivo* growth showed a partial rescue of tumor growth in the sgGot2 tumors in two independent models (Fig 3.5 a,b). In the FC1245 model, humane endpoint was reached for the control group at 18 days post-implantation resulting in a very early take down. This may have been the cause for the

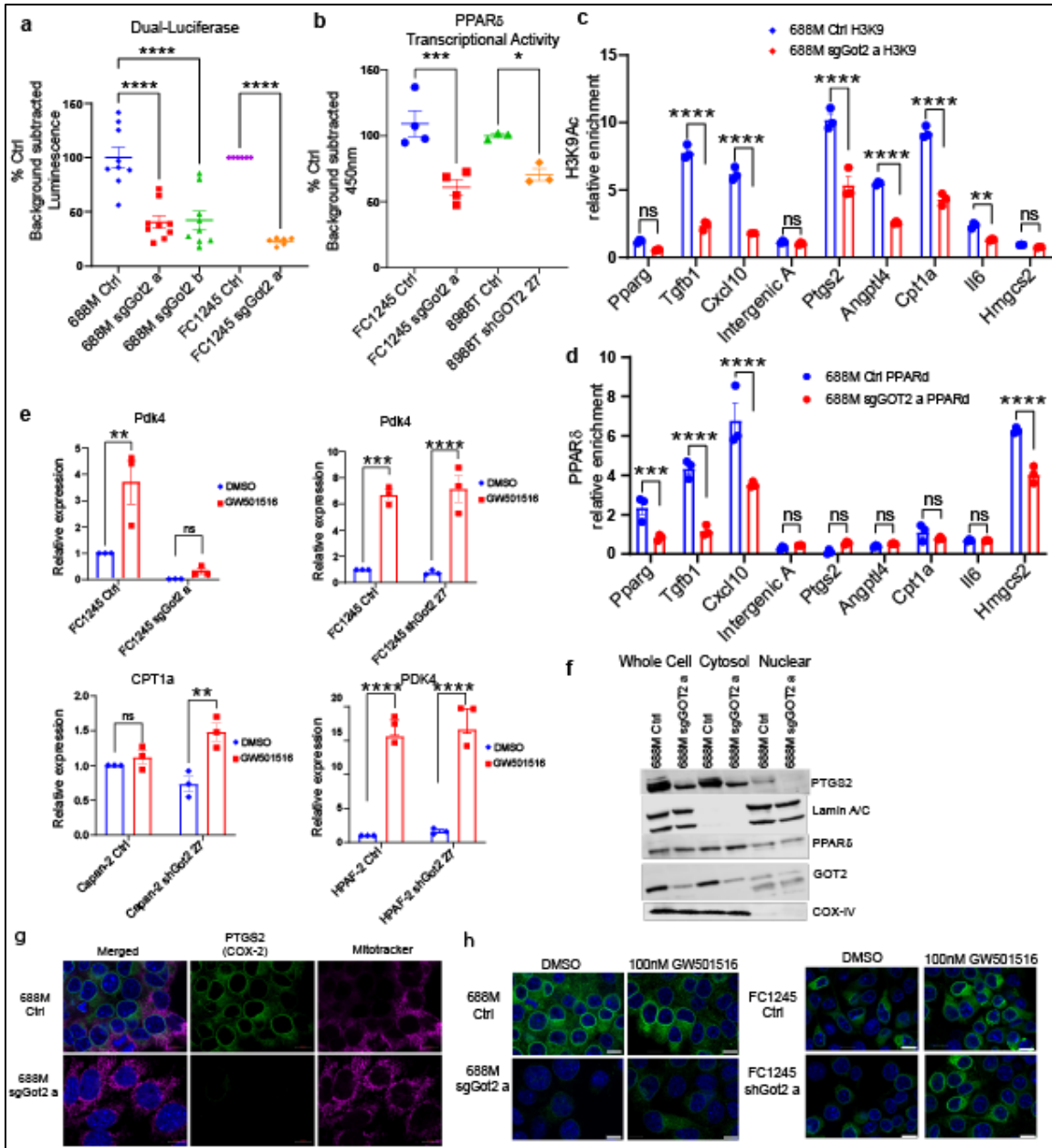


Figure 3.4 GOT2 positively regulates PPAR $\delta$  activity and target gene expression.

**a**, Luciferase assay for PPRE activity in the indicated cell lines, normalized to renilla, presented as mean  $\pm$  s.e.m. \*\*\*\* $p$  < 0.0001 by one-way ANOVA (688M) or unpaired t-test (FC1245). **b**, PPAR $\delta$  transcriptional activity assay, reading out binding to immobilized DNA containing PPREs, in the indicated cell lines. Data are presented as mean  $\pm$  s.e.m. from 4 (FC1245) or 3 (8988T) independent experiments. \* $p$  < 0.05, \*\*\* $p$  < 0.001 by unpaired t-test. **c,d**, Chromatin immunoprecipitation (ChIP) for (c) H3K9Ac and (d) PPAR $\delta$  in control or sgGot2 688M PDAC cells, followed by qPCR for proximal promoter regions of the indicated genes. Data were normalized to an intergenic region (intergenic B; intergenic A was an additional control region) and are presented as mean  $\pm$  s.e.m. from biological triplicates. \*\* $p$  < 0.01, \*\*\* $p$  < 0.001 \*\*\*\* $p$  < 0.0001 by unpaired t-test. **e**, qPCR for the indicated PPAR $\delta$ -regulated genes in control or GOT2-knockdown PDAC cells, treated with vehicle (DMSO) or PPAR $\delta$  synthetic agonist GW501516 (100 nM). Data are presented as mean  $\pm$  s.e.m. from biological triplicates. \*\* $p$  < 0.01, \*\*\* $p$  < 0.001, \*\*\*\* $p$  < 0.0001 by unpaired t-test. **f**, Western blots indicating levels of GOT2, PPAR $\delta$ , and PPAR $\delta$  target PTGS2/COX2 in the indicated PDAC lines. **g**, Immunofluorescent staining of ctrl and sgGot2 688M cells, as well as ctrl and shGot2 FC1245 cells, for PTGS2/COX2 with (h) or without (g) 100 nM GW501516 treatment. Scale bar = 10  $\mu$ m.

partial rescue rather than a full rescue. Daily palpation of the sgGot2-VP16-PPAR $\delta$  tumors

showed that in the last 5 days of the study they had reached log-phase and were rapidly increasing in size while the sgGot2 tumors remained small and slow growing. We believe that if this model were taken out to longer timepoints the sgGot2-VP16-PPAR $\delta$  construct would have completely

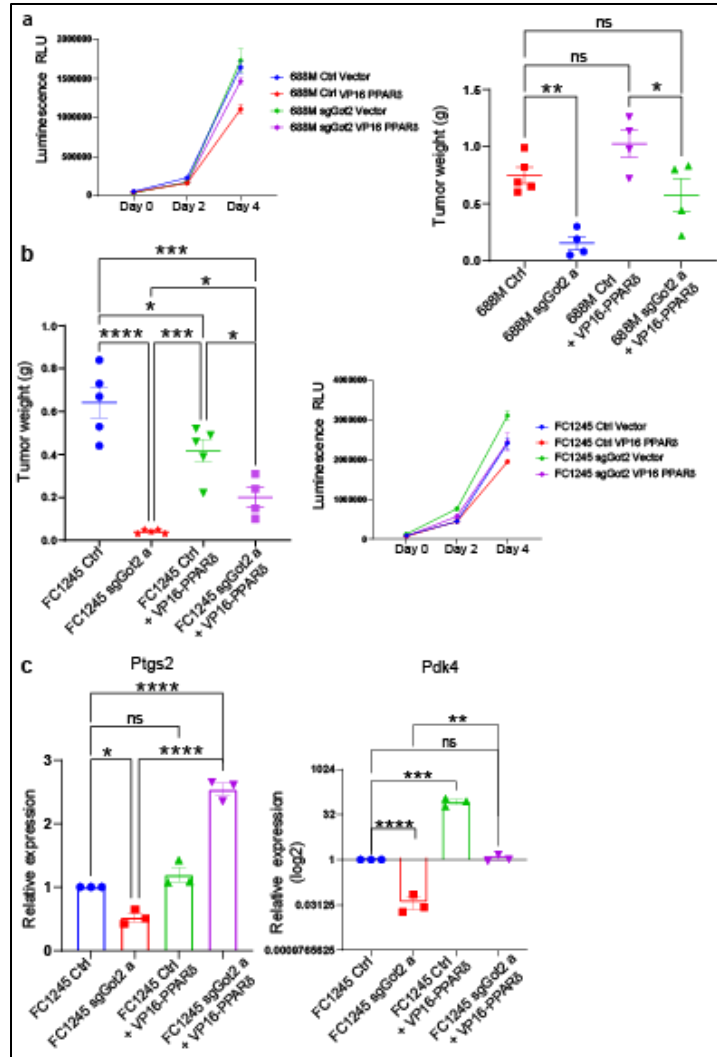


Figure 3.5 genetic activation of PPAR $\delta$  restores tumor growth in the absence of GOT2.

**a,b** Viable cell measurements in control or sgGot2 PDAC cells stably transduced with empty vector or VP16-PPAR $\delta$ . Data are presented as mean  $\pm$  s.e.m. PDAC tumor weight at experimental endpoint in the indicated (a) 688M and (b) FC1245 lines. 688M: Ctrl: n = 5, sgGot2: n = 4, Ctrl VP16-PPAR $\delta$ : n = 4, sgGot2 VP16-PPAR $\delta$ : n = 4, endpoint = day 27. FC1245: Ctrl: n = 5, sgGot2: n = 5, Ctrl VP16-PPAR $\delta$ : n = 5, sgGot2 VP16-PPAR $\delta$ : n = 4, endpoint = day 18. Ctrl and sgGot2 FC1245 arms here are also depicted in Figure 1e. \*p < 0.05, \*\*p < 0.01, \*\*\*p < 0.001, \*\*\*\*p < 0.0001 by one-way ANOVA. c, qPCR for PPAR $\delta$ -regulated genes in the indicated FC1245 stable cell lines, normalized to *36b4*. Data are presented as mean  $\pm$  s.e.m. from biological triplicates. \*p < 0.05, \*\*p < 0.01, \*\*\*p < 0.001, \*\*\*\*p < 0.0001 by one-way ANOVA.

rescued tumor growth. The same thing was noticed in the 688M model, with the sgGot2-VP16-PPAR $\delta$  tumors entering the log-phase at around 15 days post-implantation and rapidly growing for the last week of the experiment. The extra few days allowed by the 688M model showed a more significant rescue in tumor growth with the sgGot2-VP16-PPAR $\delta$  than the faster growing FC1245 model and the combination of the two supports the hypothesis that the rapid growth of the sgGot2-VP16-PPAR $\delta$  tumors relies on suppression of T cell mediated immunity, which occurs roughly around 2 weeks post-implantation as the tumor develops. mRNA

expression supports the idea that sgGot2-VP16-PPAR $\delta$  constitution was able to rescue the effect of GOT2 knockout in the FC1245 cells *in vitro* (Fig 3.5 c). We saw that Ptg2 and Pdk4

expression were increased in sgGot2-VP16-PPAR $\delta$  compared to sgGot2 cells, suggesting that the activity of VP16-PPAR $\delta$  was able to overcome the changes in transcription of these genes following GOT2 loss.

## **Discussion:**

Our results suggest that GOT2 plays a critical role in promoting a growth-permissive immune microenvironment in the pancreas, which is at least partially attributable to direct fatty acid binding and activation of the nuclear receptor PPAR $\delta$ . Future studies are needed to understand regulatory mechanisms of GOT2 subcellular localization, and the potential significance of GOT2 enzymatic activity in the nucleus.

We have shown that GOT2 transports fatty acids, including arachidonic acid, to the nucleus where they act as signaling ligands for PPAR $\delta$ . Once active, PPAR $\delta$  causes transcriptional changes which support secretion of factors that communicate with the TME, causing the immune-suppressive pathophysiology typical of PDAC. We show here that this novel GOT2-PPAR $\delta$  axis plays a role in both the protumorigenic M2, Treg immune-suppressive TME, and in the exclusion of T cells from the PDAC tumor. We also demonstrate that this GOT2-PPAR $\delta$  and immune-suppressive TME is intrinsic to the PDAC tumor, and early in development – before tumors are different sizes – GOT2-null tumors still show increased levels of intratumor CD3+ cells compared to control tumors. We also found that the dramatic decrease in tumor size with the removal of GOT2 is dependent on T cell activity in the immune-competent model and that antibody neutralizing of CD4/CD8 T cells restores growth of the GOT2-null tumor. In the nude mouse model, we expected to see similar results, however we were not able to see a completely rescue of GOT2-null tumor growth. While the GOT2-null tumors grew to the size of control tumors in the immune-competent model, the control tumors in the nude mice also grew much larger. Leading to a proportional decrease in size between control tumors and GOT2-null tumors. This suggests that immune cells other than T cells play a role in the decrease seen in GOT2-null tumors, but in the immune-competent model T cells are the primary cause for this decrease in growth.

Alongside our data showing PPAR $\delta$  activity decreases in GOT2-null cells and that known PPAR $\delta$  ligand arachidonic acid, is decreased in the nuclei of GOT2-null cells this gives strong support to our hypothesis that GOT2 binds to fatty acids, including arachidonic acid, and transports them to the nucleus where they activate nuclear transcription receptors, such as PPAR $\delta$ . Along with other potential activity of GOT2 now that it has been described in the nucleus of human pancreatic cancer. There are many mechanisms involved in the immune evasion of PDAC[20], but GOT2 may provide a potential treatment approach to foster improved immune response against this dangerous cancer. Recent publications suggest that PPAR $\gamma$  antagonists, in combination with Gemcitabine, may provide a protective benefit to PDAC patients[280, 281] and that FABP5 transports fatty acids to the nucleus for PPAR $\delta$  activation[264, 265], providing substantial support for our proposed mechanism of the GOT2-PPAR $\delta$ -axis and its potential as a therapeutic target in PDAC.

Inflammation of the TME has been shown to be a crucial factor for development of PDAC. With increased inflammation through obesity, diabetes, or injury linked to increased risk of developing PDAC and mouse models showing that chronic inflammation alone is enough to initiate starting stages of PDAC while *Kras* underlying mutations are not[170, 175, 269, 270, 282, 283]. In our work, we show that GOT2 status has an effect on COX-2, a key inflammatory mediator, expression both *in vitro* and *in vivo* and on PPAR $\delta$  activity, which has been described as important for inflammatory and immune response[199, 251, 284, 285]. We have also shown evidence that GOT2 status affects the infiltration of T cells and the polarization of macrophages, which both have been linked to inflammatory signaling, including fatty acid nuclear signaling, in PDAC and other cancers[12, 27, 167, 175, 218, 282, 286-289].

We have previously shown that the metabolic plasticity of PDAC allows for recovery from GOT2-loss such that GOT2-null cells both *in vitro* and *in vivo* do not show a proliferation defect, however there is a decrease in tumor growth *in vivo* with GOT2 loss. We have shown evidence

that the decrease in tumor growth *in vivo* in GOT2-null tumors is due to a T cell dependent immune response of the TME that occurs in the absence of GOT2. This strongly suggests that in normal PDAC tumors GOT2 acts as a coordinator for signaling between PDAC cells and supporting cells of the TME. The PPAR family of nuclear receptors, including PPAR $\delta$ , have been described as key mediators of TME-tumor communication[197]. Our results showing GOT2 status affects PPAR $\delta$  activity suggest that the transportation of fatty acid ligands to the nucleus by GOT2 for signaling of nuclear receptors is key for this novel GOT2-PPAR $\delta$  axis and subsequent changes to the TME and immune response.

These results raise interesting questions into possible future research. Since inflammation has been linked so strongly to the development of PDAC it would be interesting to see if GOT2 status affects the development of inflammation in the pancreas. Mouse models of inflammation have been used to show PDAC progression depends on inflammation[287], but does inflammation depend on GOT2 status and ligand signaling of nuclear receptors? Development of a mouse model with GOT2 removed only in the pancreas could be an interesting way of addressing this question. Full systemic removal of GOT2 is homozygous lethal as listed in the Jax MGI database, this means a mouse model would either need to have inducible GOT2 removal as an adult or have selective GOT2 removal at the pancreas only. In either case, our data suggests that the GOT2-PPAR $\delta$  axis could provide important insights into the communication between PDAC and the TME, especially in regards to the development of the inflammatory milieu and immune-suppressive phenotype which typifies PDAC.

**Acknowledgements:**

This study was supported by a postdoctoral fellowship from the OHSU Fellowship for Diversity in Research (to JA), a graduate student fellowship from the Knight Cancer Institute Cancer Center Support Grant P30 CA069533 (to HSC), NIH grants R00 CA188259 and RO1 CA229580 (to MHS) including CA229580-S1 (awarded to MHS in support of JA), American Cancer Society grant RSG-18-142-01-CSM (to MHS), and an OHSU Faculty Innovation Fund Award (to MHS). Members of the OHSU histopathology shared resource, medicinal chemistry core, and advanced light microscopy shared resources provided support for this study as well.

## Chapter 4: The fatty acid binding role of GOT2 presents an opportunity for a unique drug target in PDAC.

Portions of this chapter were included in a publication submitted to Nature and undergoing revisions as of Jan 25<sup>th</sup>, 2021.

“A cancer cell-intrinsic GOT2-PPAR $\delta$  axis suppresses antitumor immunity”

Hannah Sanford-Crane, Jaime Abrego, Chet Oon, Xu Xiao, Shanthi Nagarajan, Sohinee Bhattacharyya, Peter Tontonoz, Mara H. Sherman  
bioRxiv 2020.12.25.424393; doi: <https://doi.org/10.1101/2020.12.25.424393>

**Abstract:**

Loss of GOT2 results in a decrease in PPAR $\delta$  activity and increase in immune-response to the tumor, resulting in an active cytotoxic CD8<sup>+</sup> T cell response, M1-like phenotype of macrophages, and subsequent reduction in tumor growth. This novel tumor cell intrinsic GOT2-PPAR $\delta$  axis promotes the immune-suppressive phenotype of PDAC through activation of PPAR $\delta$  by fatty acid ligands transported to the nucleus by GOT2. PPAR $\delta$  activation results in wide-scale downstream transcriptional changes, including increased PTGS2 transcription and expression, which allows the tumor cells to communicate with the TME to create an immune-suppressive environment. Treatment of mice with a PPAR $\delta$  agonist rescues the growth defect of GOT2-null tumors and returns the TME to an immune-suppressive state. A tmGOT2, with changes to the predicted hydrophobic binding pocket of arachidonic acid, decreases tumor growth compared to wtGOT2 and PPAR $\delta$  activity, while leaving mitochondrial activity intact. The tmGOT2 also appears to have preferential localization to the mitochondria in PDAC cells and translocates to the nucleus in lower amounts than wtGOT2. This suggests that the binding of fatty acid to GOT2 may play a role in the nuclear trafficking of GOT2, possibly via interaction with a nuclear localizing chaperone protein, and that targeting this interaction may be an important future target for anti-cancer therapeutics. Which could return PDAC to a state where it is immunologically “hot” and responsive to immune-therapies.

## **Personal contribution:**

HSC's contribution to this chapter are as follows:

Figure 4.1 wtGOT2 and tmGOT2 plasmids were created by CO. HSC created wtGOT2 and tmGOT2 FC1245 and 688M stable cell lines. Cell titer glo was done by CO. *in vivo* implantations and collections were done by HSC and JA. IHC-DAB and analysis was done by JA.

Figure 4.2 GOT2 binding site *in silico* modeling was done by SN of the OHSU medicinal core. Transient transfection of UM-UC-3 was done by CO, imaging was done by HSC. ICC-IF of FC1245 and creation of wtGOT2 and tmGOT2 FC1245 and 688M cell lines was done by HSC, western blots were done by HSC, IP pulldown was done by HSC, PPAR $\delta$  transcriptional activity assay was done by HSC.

Figure 4.3 qPCR was done by HSC, AST assay was done by JA – reconstituted wtGOT2 and tmGOT2 8988-T cell lines were made by HSC, *in vivo* implantations and collections were done by HSC and JA.

## **Introduction:**

One of the key pathophysiological features of PDAC is an early infiltration of many immunosuppressive leukocytes into the tumor stroma, matched by low levels of intratumoral effector T cells[12]. Patient samples reveal similar results with the vast majority showing limited tumor-reactive T cell response and highly variable T cell infiltration in IHC imaging[13]. Tumors that showed increased CD8<sup>+</sup> T cells, also showed increased markers for M2 macrophages, suggesting an immunosuppressive phenotype, and that the majority of the CD8<sup>+</sup> T cells were unlikely to be active[13]. This potentially has some therapeutic benefit, as PDAC tumors would remain sensitive to T cell activity, if T cells were able to infiltrate into them. Taken together, this data suggests that the development of therapeutics which would reduce immunosuppressive mechanisms of PDAC and allow T cells into the tumor would be highly effective. Our results suggest the nuclear import of fatty acids by GOT2 and subsequent activation of PPAR $\delta$  may be playing an important role in the development of this immunosuppressive phenotype in PDAC. The binding of GOT2 to arachidonic acid also opens new avenues for research into the role of GOT2 in both cancer and other disorders. Arachidonic acid is known to be a ligand for several different ligand-activated transcription factors involved in development, metabolism, and reproduction; which, beyond the PPAR family, include the retinoid X receptor (RXR)[290] and the liver X receptor (LXR)[263]. LXR is also highly upregulated in macrophages, where they regulated lipid homeostasis and inflammation, with activation reducing macrophage response[261, 263]. Along with their role in macrophages, it is interesting to note that LXR-mediated changes in T cells was linked to reduced T cell proliferation and increased production of IL-2 and IL-4, reducing T cell function[261]. The effect of LXR activation on T cell activity is further shown by the fact that inhibition of LXRs in triple negative breast cancer, with pharmacologic inhibitor SR9243, lead to a significant increase in Th1 and cytotoxic CD8<sup>+</sup> T cells with a matched decrease in myeloid derived suppressor cells (MDSCs)[291].

The majority of researched arachidonic acid effects are believed to be through conversion by oxygenases to prostaglandins and leukotrienes[292] but recent research has shown the importance of fatty acids in a secondary role as ligands for nuclear receptors. Along with Free Fatty Acid Receptors (FFARs), Fatty Acid-Binding Proteins (FABPs), and PPARs, compounds derived from fatty acids have been known to be ligands for cannabinoid receptors with involvement in inflammation[258]. Fatty acids are being discovered to have roles as precursors of signaling molecules and as direct ligands themselves with involvement in many molecular mechanisms, regulatory functions through highly specific receptors[293].

We have previously shown that loss of GOT2 results in a decrease in PPAR $\delta$  activity and increase in immune-response to the tumor, resulting in an active cytotoxic CD8<sup>+</sup> T cell response, M1-like phenotype of macrophages, and subsequent reduction in tumor growth. We wanted to know if this cell intrinsic GOT2-PPAR $\delta$  axis promotion of the immune-suppressive phenotype of PDAC could be reversed by blocking either activation of PPAR $\delta$  with a PPAR $\delta$  agonist or by blocking the binding of fatty acids to GOT2. The feasibility of this idea is supported by work done in the literature on FABP5, which shows that the FABP5-PPAR $\delta$  axis could play a role in inflammation and tumorigenesis[264, 265]. This axis has been described to behave similarly with our novel GOT2-PPAR $\delta$  discovery, where FABP5 binds to fatty acids – including arachidonic acid – and transports them to the nucleus where they act as ligands for PPAR $\delta$  resulting in downstream pro-inflammatory and immune-suppressive transcriptional changes[264, 265]. It has also been shown that targeting PPAR $\gamma$  in cancer may be a viable treatment option, as combinational therapies of PPAR $\gamma$  inhibitors and Gemcitabine appeared to have synergistic effects and there have been publications suggesting that PPAR $\gamma$  may play a role in metastasis[254, 281].

Altogether this suggests that targeting the nuclear fatty acid transport role of GOT2 and the GOT2-PPAR $\delta$  axis could be an effective therapeutic for restore an immune-active TME in PDAC, increasing response to immune-therapies, and improving patient outcome.

## **Materials and methods:**

### ***Animals***

All experiments were reviewed and overseen by the institutional animal use and care committee at Oregon Health and Science University in accordance with NIH guidelines for the humane treatment of animals. C57BL/6J (000664, for models with FC1245[249]) or B6129SF1/J (101043, for models with 688M[250]) mice from Jackson Laboratory were used for orthotopic transplant experiments at 8-10 weeks of age. Tissues from 6- or 12-month-old  $Kras^{LSL-G12D/+};Pdx1-Cre$  (KC) mice were kindly provided by Dr. Ellen Langer (OHSU).

### ***Plasmids***

The pCMV3 plasmid containing C-terminal His-tagged human GOT2 cDNA was purchased from Sino Biological (HG14463-CH) and cloned into the lentiviral vector pLenti CMV Puro DEST (Addgene #17452) using the same approach as pLenti-VP16 PPARΔ. pLenti wtGOT2 PCR product was generated using sense primer 5'-GGGGACAAGTTTGTACAAAAAAGCAGGCTTAATGGCCCTGCTGCACT-3' and antisense primer 5'-GGGGACCACTTTGTACAAGAAAGCTGGGTTTTTAGTGATGGTGGTGATGATGGTGG-3'. Triple mutant GOT2 was constructed using Q5 Site-Directed Mutagenesis Kit (New England E0552S) in two subsequent steps. Two sets of primers were used to generate three site mutations; primer set 1 for K234A mutation (F:5'-AACAGTGGTG GCGAAAAGGAATCTC-3'; R:5'-GCTATTTCCCTTCCACTGTTC-3') and primer set 2 for K296A and R303 mutations (F:5'-GTCTGCGCAGATGCGGATGAAGCCAAAGCGGTAGA GTC-3'; R:5'-CATAGTGAAGG CTCCTACACGC-3'). pLenti tmGOT2 was then generated using the same approach and primers as pLenti wtGOT2.

### ***Cell Lines***

Human pancreatic cancer cell lines MIAPaCa-1, PA-TU-8988T, Panc1, HPAF-II, and Capan-2 were obtained from ATCC and grown in Dulbecco's modified Eagle's medium (DMEM) containing 10% fetal bovine serum. Non-transformed, TERT-immortalized human pancreatic ductal epithelial cells were kindly provided by Dr. Rosalie Sears (OHSU)[251]. FC1245 PDAC cells were generated from a primary tumor in  $Kras^{LSL-G12D/+};Trp53^{LSL-R172H/+};Pdx1-Cre$  mice and were kindly provided by Dr. David Tuveson (Cold Spring Harbor Laboratory)[249]. 688M PDAC cells were generated from a liver metastasis in  $Kras^{LSL-G12D/+};Trp53^{LSL-R172H/+};Pdx1-Cre;Rosa26^{LSL-tdTomato/+}$  mice and were kindly provided by Dr. Monte Winslow (Stanford University School of Medicine)[250]. Cell lines were routinely tested for Mycoplasma at least monthly (MycAlert Detection Kit, Lonza).

The pSpCas9(BB)-2A-Puro(PX459) v2.0 plasmid (Addgene #62988) was used to clone guide sequences targeting *Got2* per supplier's protocol; sgRNA A: GACGCGGGTCCACGCCGGT, sgRNA B: ACGCGGGTCCACGCCGGTG. The 688M or FC1245 cell line was transfected with control plasmid or plasmid containing either of the sg*Got2* sequences and subject to selection with 2 μg/ml puromycin for 4 days. Single-cell clones were expanded and screened for GOT2 protein expression by Western blot.

Lentivirus preparation for stable cell line generation was done with pMD2.G envelope plasmid (Addgene #12259) and psPAX2 packaging plasmid (Addgene 12260) in 293T-LentiX cells. Briefly, 5ug pMD2.G, 5ug psPAX2 and 10ug of plasmid DNA (shGOT2 KD, VP16-PPARΔ, wtGOT2, tmGOT2, or scramble Ctrl) were combined with 600ul optimum and 20ul lipofectamine 2000 for 20 mins at room temp. 10cm dishes of 293T-LentiX were kept in 0% FBS DMEM and the mixture was added in a dropwise manner. 12hrs later media was changed to 10% FBS DMEM. At 24hrs after transduction and 48hrs after transduction, media was collected and filtered

through a 0.25µm filter, aliquoted, and frozen at -80C. The shGOT2 plasmids were purchased from addgene. Human shGOT2 lot #04161910MN TRCN0000034824, TRCN0000034827, TRCN0000034826, TRCN0000034825. Mouse shGOT2 lot #04161910MN TRCN00000326018, TRCN00000325946, TRCN00000119800, TRCN00000119798, TRCN00000119801.

Lentiviral transduction of human and mouse cell lines: cells were plated to 6-well plates. 10ug/mL polybrene (EMD Millipore TR-1003-G) was added to 1mL 10% FBS DMEM and 300ul of filtered lentivirus media. 24hrs later media was changed to fresh 10% FBS DMEM. 48hrs after initial transduction, cells were treated with 2ug/mL puromycin (Thermo Fisher A1113803), or 4ug/mL puromycin depending on cell line. A control well of non-transduced cells was used as an indicator for proper selection.

### **RNA Extract and Real-Time qPCR**

The isolated total RNA (1 µg) was reverse-transcribed to produce cDNA using iScript Reverse Transcription Supermix kit (Bio-Rad). Real-time PCR was performed using SYBR Green supermix (Bio-Rad). The cDNA sequences for specific gene targets were obtained from the human genome assembly (<http://genome.ucsc.edu>) and gene specific primer pairs were designed using the Primer3 program ([http://frodo.wi.mit.edu/primer3/primer3\\_code.html](http://frodo.wi.mit.edu/primer3/primer3_code.html)). Relative gene expression was normalized using the 36B4 housekeeping gene. The following primer sequences were used: human and mouse 36B4 (*RPLP0*): F:5'-GTGCTGATGGGCAAGAAC-3'; R:5'-AGGTCCTCCTTGGTGAAC-3'; human *PTGS2*: F: 5'-CTGGCGCTCAGCCATACAG-3'; R:5'-CGCACTTATACTGGTCAAATCCC-3'; human *PK4*: F:5'-AGAAAAGCCCAGATGACCAGA-3'; R:5'-TGGTTCATCAGCATCCGAGT-3'; human *CPT1A*: F:5'-CTGTGGCCTTTCAGTTCACG-3'; R:5'-CCACCACGATAAGCCAACTG-3'; human *TGFBI*: F:5'-GGCCTTTCCTGCTTCTCAT-3'; R:5'-CAGAAGTTGGCATGGTAGCC-3'; human *CXCL1*: F:5'-AGGGAATTCACCCCAAGAAC-3'; R:5'-ACTATGGGGGATGCAGGATT-3'; human *CXCL9*: F:5'-ATTGGAGTGCAAGGAACCCC-3'; R:5'-ATTTTCTCGCAGGAAGGGCT-3'; human *CXCL10*: F:5'-GTGGCATTCAAGGAGTACCTC-3'; R:5'-TGATGGCCTTCGATTCTGGATT-3'; mouse *Ptgs2*: F:5'-TGAGTGGGGTGATGAGCAAC-3'; R:5'-TTCAGAGGCAATGCGGTTCT-3'; mouse *Pdk4*: F:5'-TGAACACTCCTTCGGTGCAG-3'; R:5'-GTCCACTGTGCAGGTGTCTT-3'; mouse *Pparg1a*: F:5'-GCTTGACTGGCGTCATTCGG-3'; R:5'-TGTTTCGAGGCTCATTGTTG-3'; mouse *Tgfb1*: F:5'-CACTCCCCTGGCTTCTAGTG-3'; R:5'-GTTGTACAAAGCGAGCACCG-3'; mouse *Cxcl1*: F:5'-TGGCTGGGATTCACCTCAAG-3'; R:5'-CCGTTACTTGGGGACACCTT-3'; mouse *Cxcl9*: F:5'-AACGTTGTCCACCTCCCTC-3'; R:5'-CACAGGCTTTGGCTAGTCGT-3'; mouse *Cxcl10*: F:5'-CAAGCCATGGTCCTGAGACA-3'; and R:5'-TGAGCTAGGGAGGACAAGGA-3'.

### **Western Blots**

PDAC cells were treated as described in the text, and whole cell lysates were prepared in RIPA buffer containing protease inhibitor cocktail (Sigma-Aldrich 11836170001). Alternatively, sub-cellular fractions were prepared by several different fractionation methods.

Detergent Free Fractionation protocol: Cells are scraped and collected from 10cm dishes. Washed with PBS (450g x 5mins) and 1/5 of the volume is separated for whole cell lysis in RIPA (Amresco N653-100mL) + cOmplete EDTA-free Protease inhibitor cocktail (Sigma-Aldrich 11836170001). Remain 4/5 of cell mass is centrifuged (450g x 5mins), PBS is removed and cells are lysed on ice for 15 mins in Lysis buffer (5x of cell pellet volume). Lysis Buffer: 10mM HEPES pH 7.9, 1.5mM MgCl<sub>2</sub>, 10mM KCl with 1mM DTT and EDTA-Free cOmplete mini protease inhibitor cocktail. Centrifuge (450g x 5mins), decant super, add lysis buffer (2x cell

volume) and grind on ice with a plastic homogenizer 10x in 1.5mL Eppendorf tubes. Centrifuge (10,000g x 20mins) collect supernatant as cytosolic fraction. Wash with 200ul lysis buffer (10,000g x 5mins) decant super and add extraction buffer (2/3x cell pellet volume). Extraction buffer: 20mM HEPES pH 7.9, 1.5mM MgCl<sub>2</sub>, 0.42M NaCl, 0.2uM EDTA, 25% glycerol (V/V), 1mM DTT and cOmplete mini EDTA-free protease inhibitor cocktail. Grind nuclei with plastic homogenizer in 1.5mL Eppendorf tubes 20x. Incubate at 4C with gentle shaking for 10 mins. Centrifuge (20,000g x 5mins) and transfer supernatant to cold Eppendorf tube, label as Nuclear portion.

Cell Signaling Tech Cell Fractionation Kit (CST 9038S) was performed following the manufacturer's recommendations. Briefly cells were collected with scraping and washed in PBS (350g x 5mins). Resuspend in 500ul PBS and remove 100ul for whole cell lyses in RIPA buffer + cOmplete mini EDTA-free protease inhibitor cocktail. Remaining cell pellet was centrifuged (500g x 5 mins), PBS was decanted and 500ul CIB + 5ul Protease Inhibitor and 2.5ul PMSF was added. Vortex and store on ice 5 mins. Centrifuge (500g x 5mins) supernatant is cytosolic fraction. Wash with CIB. Decant supernatant. Add 500ul MIB + 5ul Protease Inhibitor and 2.5ul PMSF to the cell pellet. Vortex 15 seconds, incubate on ice 5 mins, and centrifuge (8000gx 5 mins). Supernatant is the membrane & organelle fraction. Wash in MIB. Decant supernatant. Add 250ul CyNIB + 2.5ul Protease Inhibitor + 1.25ul PMSF to the cell pellet. Sonicate for 5 sec at 20% power 3x. For western blot add 60ul 3X LDS loading buffer with 10X reducing agent for every 100ul of supernatant per fraction. Boil for 5 mins at 95C and centrifuge for 3 mins at 15,000g. Load 15ul of each fraction along with 15ul of whole cell lysate.

Protein concentration was quantitated using the BCA protein assay kit (Pierce). Equal amounts of protein were loaded in each lane and separated on a 4-12% Bis-Tris NuPAGE® gel (Invitrogen), then transferred onto a PVDF membrane. Membranes were probed with primary antibodies and infrared secondary antibodies: anti-GOT2 (Thermo Fisher PA5-77990), anti-His-tag (R&D Systems MAB050-100), anti-PPAD (Abcam ab178866), anti- Lamin A/C (Cell Signaling Technology 4777S), anti-COX IV ( Cell Signaling Technology 11967S), anti-rabbit Alexa Fluor Plus 680 (Thermo Fisher A32734) and anti-mouse Alexa Flour Plus 800 (Invitrogen A32730). Protein bands were detected using the Odyssey CLx infrared imaging system (LICOR Biosciences).

### ***PPAR $\delta$ Transcription Factor Activity Assay***

Nuclear lysates were prepared using a detergent-free fractionation protocol. Cells were scraped and collected from 10 cm dishes, washed with PBS, pelleted (450 x g 5mins), resuspended in PBS and 1/5 of the volume was reserved for whole cell lysis in RIPA (Amresco N653-100mL) + cOmplete EDTA-free Protease inhibitor cocktail (Sigma-Aldrich 11836170001). The remaining 4/5 of cell suspension was centrifuged (450 x g 5mins), PBS removed and cells were lysed on ice for 15 mins in Lysis buffer (5x of cell pellet volume). Lysis Buffer: 10mM HEPES pH 7.9, 1.5mM MgCl<sub>2</sub>, 10mM KCl with 1mM DTT and EDTA-Free cOmplete mini protease inhibitor cocktail. Lysates were centrifuged (450 x g 5mins), supernatant decanted, lysis buffer added (2x cell volume) and suspensions ground on ice with a plastic homogenizer 10x in 1.5mL Eppendorf tubes. Lysates were centrifuged (10,000 x g 20mins) and supernatant collected as cytosolic fraction. Remaining pellet was washed with 200  $\mu$ l lysis buffer (10,000 x g 5mins), supernatant decanted and extraction buffer added (2/3x cell pellet volume). Extraction buffer: 20mM HEPES pH 7.9, 1.5mM MgCl<sub>2</sub>, 0.42M NaCl, 0.2uM EDTA, 25% glycerol (V/V), 1mM DTT and cOmplete mini EDTA-free protease inhibitor cocktail. Nuclei were ground with plastic homogenizer in 1.5mL Eppendorf tubes 20x, and incubated at 4°C with gentle shaking for 10 mins. Samples were centrifuged (20,000 x g 5mins) and supernatant transferred to cold Eppendorf tubes, as nuclear fraction. Lysates were measured with BCA and an equal protein

amount was added per sample for each well. Manufacturer's instructions were followed for the PPAR delta transcription factor kit (Abcam ab133106). Briefly CTFB was prepared and added to blank and NSB wells, nuclear lysates were added to each sample well containing immobilized PPRE-containing DNA and the plate was incubated overnight at 4°C without agitation. The next day the wells were washed 5x in 1X wash buffer and incubated in PPARdelta primary antibody (1:100) for 1hr at room temperature in the dark, without agitation. Wells were washed 5x in 1X wash buffer and incubated in goat anti-rabbit HRP conjugate (1:100) for 1hr at room temperature in the dark without agitation. Wells were washed 5x in 1X wash buffer and 100 µl developing solution was added to each well. Plate was incubated for 15-45 minutes on a room temperature shaker, in the dark, until color developed. 100 µl stop solution was added to wells and the absorbance at 450nm was taken.

### ***Nuclear Fatty Acid Uptake Assay***

MiaPaca2 ctrl and sh27 cells were plated at  $5 \times 10^5$  in a 6 well plate and allowed to adhere overnight. Media was changed to 0% FBS DMEM and the cells were incubated for 24hrs. The media was changed to 0.5% Fatty-Acid Free BSA DMEM with either chloroform (ctrl) or 2.5 µM NBD-arachidonic acid (Avanti Polar Lipids 810106C). Media was made before being added to cells, heated to 37°C and vortexed until fatty acid was completely in solution. Cells were incubated at 37°C for durations indicated in the manuscript and collected and fractionated using the Detergent Free Method described above (PPARδ transcription factor activity assay). Nuclear lysates were placed in a white-walled 96-well plate and fluorescence was measured at 480 nm excitation and 540 nm emission. Lysate concentration was measured using a BCA kit. FC1245 cells were plated  $5 \times 10^5$  per well and treated as described above, but treatment was reduced to 2 µM NBD-arachidonic acid for 15 minutes due to lipid toxicity in this cell line.

### ***Aspartate Aminotransferase Assay***

AST Activity Assay Kit (Sigma-Aldrich MAK055) was used to determine aspartate aminotransferase activity per manufacturer instructions. Briefly, this assay determines the transfer of an amino group from aspartate to alpha-ketoglutarate in the generation of glutamate which produces a colorimetric product (450 nm) that is proportional to aspartate aminotransferase activity in the sample. For this assay Pa-Tu-8988T cells with stable expression of doxycycline inducible GOT2 shRNA were transiently transfected with wtGOT2 and tmGOT2. After 48hrs these cells were exposed to doxycycline for 48hrs to knockdown endogenous GOT2 in cells with GOT2 shRNA. Cells were seeded at  $5 \times 10^6$  and collected via trypsin disassociation after cells were adhered. The cells were then resuspended in 1ml of ice-cold 1X PBS and 200 µl ( $1 \times 10^6$  cells) were collected for AST assay and 800 µl ( $4 \times 10^6$  cells) were collected for protein concentration estimation and Western blot protein expression analysis. Using AST assay kit buffers, cells were lysed to obtain a supernatant which was combined with the kit reagent master mix to detect glutamate in a colorimetric reaction. The samples were read every 5 minutes for 30 minutes. AST activity and concentration in the samples were determined using instructions from the manufacturer.

### ***Immunofluorescence***

Cells plated on coverslips were fixed in 10% neutral buffered formalin for 10 minutes at room temperature, washed three times with PBS, and permeabilized with .1% Triton X-100 for 10 min at room temperature. When MitoTracker staining was performed, cells plated on coverslips were stained with 100 nM MitoTracker (Thermo Fisher M22462) at 37°C for 15 minutes prior to fixation. Following permeabilization, coverslips were blocked for one hour at room temperature in blocking solution (Aqua block buffer, Abcam ab166952) and then transferred to a carrier solution (Aqua block) containing diluted primary antibodies: GOT2 (Sigma-Aldrich

HPA018139), GOT2 (Thermo Fisher PA5-77990), COX IV (Cell Signaling Technology 11967S), COX2 (Abcam ab15191), His (R&D Systems MAB050-100). Coverslips were incubated with the primary antibody at 4°C overnight and then washed five times for 5 minutes each in PBS following which, secondary Alexa-fluor conjugated antibodies diluted in the same carrier solution (1:400) were added to the coverslips for one hour at room temperature. After the secondary antibody incubation, coverslips were washed five times for five minutes each in PBS and mounted with Vectashield mounting media containing DAPI (Vector Laboratories H-1500). Images were captured on a Zeiss LSM 880 laser-scanning inverted confocal microscope in the OHSU Advanced Light Microscopy Shared Resource, and a 40×/ 1.1 NA water objective or 63×/1.4 NA oil objective was used to image the samples.

### ***Proliferation Assays***

PDAC cells were seeded into 96-well plates at  $2 \times 10^3$  cells per well in DMEM containing 10% FBS. Cells were treated as indicated in the manuscript text with 100nM GW501516 (Cayman Chemical 10004272) at the time of cell seed or 5mg/mL doxycycline (Sigma-Aldrich D9891) 48 hours prior to cell seeding. GW501516 and doxycycline treatments were both replenished every 48 hours for extended time points. After 72 hours, cells were lysed with CellTiter-Glo® Luminescent Cell Viability Assay reagent (Promega) and luminescence was read using a GloMax plate reader.

### ***Dual Luciferase Assay***

PPRE x3-TK-Luc (PPAR response element driving luciferase) plasmid #1015 was purchased from Addgene and the Renilla plasmid (pRL-SV40) was generously provided by Dr. Ellen Langer (OHSU). Cells were transfected with 2.5 µg PPRE x3-TK-Luc, 15 ng pRL-SV40, and 4 µl Lipofectamine 2000 in 6-well plates. Briefly, cells were plated at  $1 \times 10^6$  per well of a 6-well plate and allowed to adhere overnight. Plasmids were combined in 150 µl Opti-MEM while lipofectamine 2000 was combined in a separate tube with 150 µl Opti-MEM. After 5 mins the tubes were combined. 300 µl of the mixture was added, in a dropwise manner, to 700 µl of Opti-MEM on each well for transfection. The cells were incubated overnight at 37°C, collected, counted, and replated to white-walled 96-well plates in triplicates. 24 hours later a dual luciferase assay was completed, following the manufacturer's instructions: Dual-Luciferase Reporter Assay System (Promega E1910). Briefly, cells were lysed in white-walled 96-well plates with 20 µl 1X Passive Lysis Buffer and shaken on a room temp shaker. 100 µl LARII was added to each well and luminescence was measured over 5 seconds. 100 µl of Stop and Glo were then added and Renilla activity was measured with luminescence over 5 seconds. Activity was calculated by normalizing luciferase signal to renilla for each well.

### ***Orthotopic Implantation In Vivo Model***

The orthotopic transplant method used here was described previously<sup>6</sup>. In brief, 8- to 10-week-old wild-type male C57BL/6J (for FC1245) or B6129SF1/J (for 688M) mice were orthotopically transplanted as described previously with  $5 \times 10^3$  FC1245 cells or  $8 \times 10^4$  688M cells in 50% Matrigel (Corning 356231), 50% DMEM. For experiments with 688M cells harboring VP16-PPARD,  $6 \times 10^4$  688M cells were used. For pharmacologic activation of PPAR $\delta$ , mice were treated with vehicle (5% PEG-400, 5% Tween-80 in diH<sub>2</sub>O) or with 4 mg/kg GW501516 in vehicle by intraperitoneal injection once daily. Vehicle was created and autoclaved before use. GW501516 was created in 10 mM stock in DMSO and stored in 250 µl aliquots at -20°C (one for each day of treatment). On the day of treatment, a vial was thawed, diluted 1:10 in vehicle, and mice were dosed at 4 mg/kg. For T cell neutralization experiments, mice received intraperitoneal injection of 0.2 mg of  $\alpha$ CD8 (2.43),  $\alpha$ CD4 (GK1.5), or an IgG2b isotype control (LTF-2) diluted in 100 µl sterile PBS. Antibodies were purchased from BioXcell and were administered

beginning 2 days pre-implantation with  $6 \times 10^4$  688M cells and every 4 days thereafter until euthanasia, as previously described<sup>7</sup>. Mice were euthanized when control animals were moribund, and tumors were excised, weighed, and immediately fixed in formalin.

### ***Immunohistochemistry of Tumor Tissue***

Mice were anesthetized and euthanized according to institutional guidelines. Pancreatic tumors were excised carefully and fixed overnight in 10% phosphate-buffered formalin. Tissue samples were paraffin embedded and sectioned by the OHSU Histopathology Shared Resource. Human PDAC tissue sections from formalin-fixed, paraffin-embedded blocks were obtained from the OPTR. In brief, tissue sections were de-paraffinized and rehydrated through an ethanol series and ultimately in PBS. Following antigen retrieval, tissue samples were blocked for 1 hour at room temperature in blocking solution (8% BSA solution) and then transferred to a carrier solution (8% BSA solution) containing diluted antibodies: GOT2 (Sigma-Aldrich HPA018139), GOT2 (Thermo Fisher PA5-77990), COX IV (Cell Signaling Technology 11967S), COX2 (Abcam ab15191), CD3 (Abcam ab5690), CD4 D7D2Z (Cell Signaling Technology 25229S), CD8 (Abcam ab203035), Granzyme B (Abcam ab4059), F4/80 (Cell Signaling Technology 70076T), Arginase-1 (Sigma-Aldrich ABS535). Sections were incubated overnight at 4°C and then washed five times for 5 minutes each in PBS. For fluorescence imaging, secondary Alexa-flour conjugated antibodies diluted in the same carrier solution (1:400) were added to the sections for one hour at room temperature. Sections were then washed five times for five minutes each in PBS and were mounted with Vectashield mounting media containing DAPI. For DAB chromogen imaging, sections were stained with primary antibody as described above, then the samples were incubated in polymeric horseradish peroxidase (HRP) conjugated secondary antibody (Leica PV6121) for one hour followed by 5 five-minute 1xTBST washes. HRP was detected using DAB chromogen (3,3'-Diaminobenzidine) solution (BioCare Medical BDB2004) prepared per manufacturer instructions. Tissues were exposed to chromogen solution until a brown precipitate was detected produced from oxidized DAB where secondary poly-HRP antibody is located. As soon as DAB chromogen is detected the tissue-slides were washed in diH<sub>2</sub>O, counterstained in hematoxylin, dehydrated and cleared for mounting. Stained tissue sections were scanned on a Leica Biosystems Ariol digital fluorescence scanner or Leica Biosystems Aperio brightfield digital scanner. Quantification was performed for single stains using QuPath quantitative pathology and bioimage analysis software v0.2.3. For co-stains (CD8/GRZB and F4/80/ARG1), manual counting was performed on at least 10 high-powered fields per tumor sample.

### ***Long Chain Fatty Acid Binding Site Prediction***

The arachidonic acid binding site on the human GOT2 surface is predicted using the molecular modeling technique. The protein structure was prepared using the protein prep tool of Maestro-2014-3 (Schrödinger, LLC, New York, NY, 2013). Arachidonic acid is a 20 carbon long-chain fatty acid (LCFA) with greasy carbons and a carboxylate group. The available structural information suggests that the binding pocket must be hydrophobic with the positively charged residues to accommodate LCFA. Five sites were predicted on the GOT2 structure, and these sites had a site score of  $> 0.8$ , composed of hydrophobic, hydrogen bond acceptor, and donor volumes. The top-ranked site-1 is a catalytic site, and site-2 to 5 are allosteric. Arachidonic acid docked against all the predicted sites. The Induced-Fit docking protocol adopted here allows both the ligand and the surrounding residues of protein to be flexible. A total of five docking runs were performed on the predicted site. The docking grid boxes are defined based on the residues suggested by the SiteMap analysis (Site-1: N215, H210; Site-2: N270, F239; Site-3: A260, W226, H373, G385, Q390; Site-4: R337, G254; Site-5: N332, D93). The site-2  $\sim 25$  Å away from the catalytic site resulted in a binding pose with favorable energy and interaction complementarity between the protein and ligand. Compared to other sites, Site-2 has increased

hydrophobic volume, which may recognize LCFA like arachidonic acid. Triple mutants K234A/K296/R303 were proposed to validate the predicted binding pose. K234 interacts with the carboxylate group of LCFA. K296, which is in proximity to making ionic interaction (in dynamics) and perturbation of the positive charge to neutral alanine residues, prevents the charged interaction. From the docking pose, R303 is making the hydrophobic interaction with the lipid tail of arachidonic acid. R303A mutation reduces the hydrophobic interaction by the sidechain of arginine. The proposed triple mutations have the potential to abolish the arachidonic acid binding.

### ***Statistical Analysis***

GraphPad Prism software was used for all statistical analysis. Welches unpaired T-tests were used to compare two treatment groups to each other. One-Way Anova was used to compare multiple treatment groups for one variable. A P value of  $< 0.05$  was considered significant.

## Results:

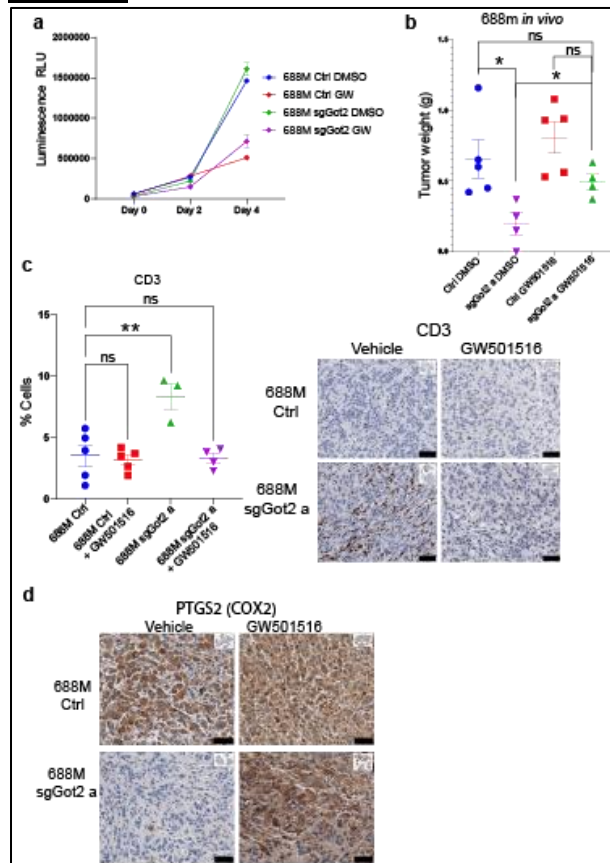


**Figure 4.1** Pharmacological activation of PPAR $\delta$  restores tumor growth and T cell exclusion in a GOT2-null setting.

**a**, Viable cell measurements in control or sgGot2 PDAC cells treated with vehicle or 100 nM GW501516. **b**, PDAC tumor weight at experimental endpoint, 30 days after orthotopic transplantation of the control or sgGot2 cells, with daily i.p. injection of vehicle or 4 mg/kg GW501516. Ctrl: n = 5 per cohort, sgGot2: n = 4 per cohort. Data are presented as mean  $\pm$  s.e.m. \* $p$  < 0.05 by one-way ANOVA. **c**, Immunohistochemical staining of control and sgGot2 688M tumors treated with vehicle or GW501516 as in **b** for T cell marker CD3. Representative images are shown above (scale bar = 50  $\mu$ m), with quantification below (Ctrl: n = 5, Ctrl + GW501516: n = 5, sgGot2: n = 3, sgGot2 + GW501516: n = 4). Data are presented as mean  $\pm$  s.e.m. \*\* $p$  < 0.01 by one-way ANOVA. **d**, Immunohistochemical staining for PTGS2/COX2 in control or sgGot2 PDAC treated with vehicle or GW501516 (representative of n = 3-5 per cohort). Scale bar = 50  $\mu$ m.

We previously showed the existence of a novel location for GOT2 at the nucleus of PDAC cells, and characterized a pancreatic cancer cell-intrinsic GOT2-PPAR $\delta$  axis.

We showed the importance of PPAR $\delta$  activation for the immune-suppressive TME of PDAC and that genetic activation of PPAR $\delta$  with VP16 was capable of overcoming the decreased tumor growth resulting from loss of GOT2. We wanted to see if pharmacological activation of PPAR $\delta$  could restore PDAC growth in a GOT2-null setting. To test this, we treated PDAC cells with GW501516, a PPAR $\delta$  agonist, and found that PPAR $\delta$  activity – as seen through PPAR $\delta$  target gene expression – was increased in sgGot2 cells *in vitro* but did not observe any difference in proliferation (Fig 4.1 a). We then implanted 688M control and sgGot2 cells

*in vivo* and performed daily treatments of 4mg/kg GW501516 IP. We found that this daily treatment resulted in restored growth of GOT2-null PDAC, but did not impact control tumor growth, (Fig 4.1 b) while also restoring intra-tumoral T cell suppression (Fig 4.1 c) and induction of COX-2 expression in the GOT2-null PDAC (Fig 4.1 d). GW501516 had additional systemic effects, resulting in cachexia in the GOT2-null PDAC mice and ascites in the control PDAC mice

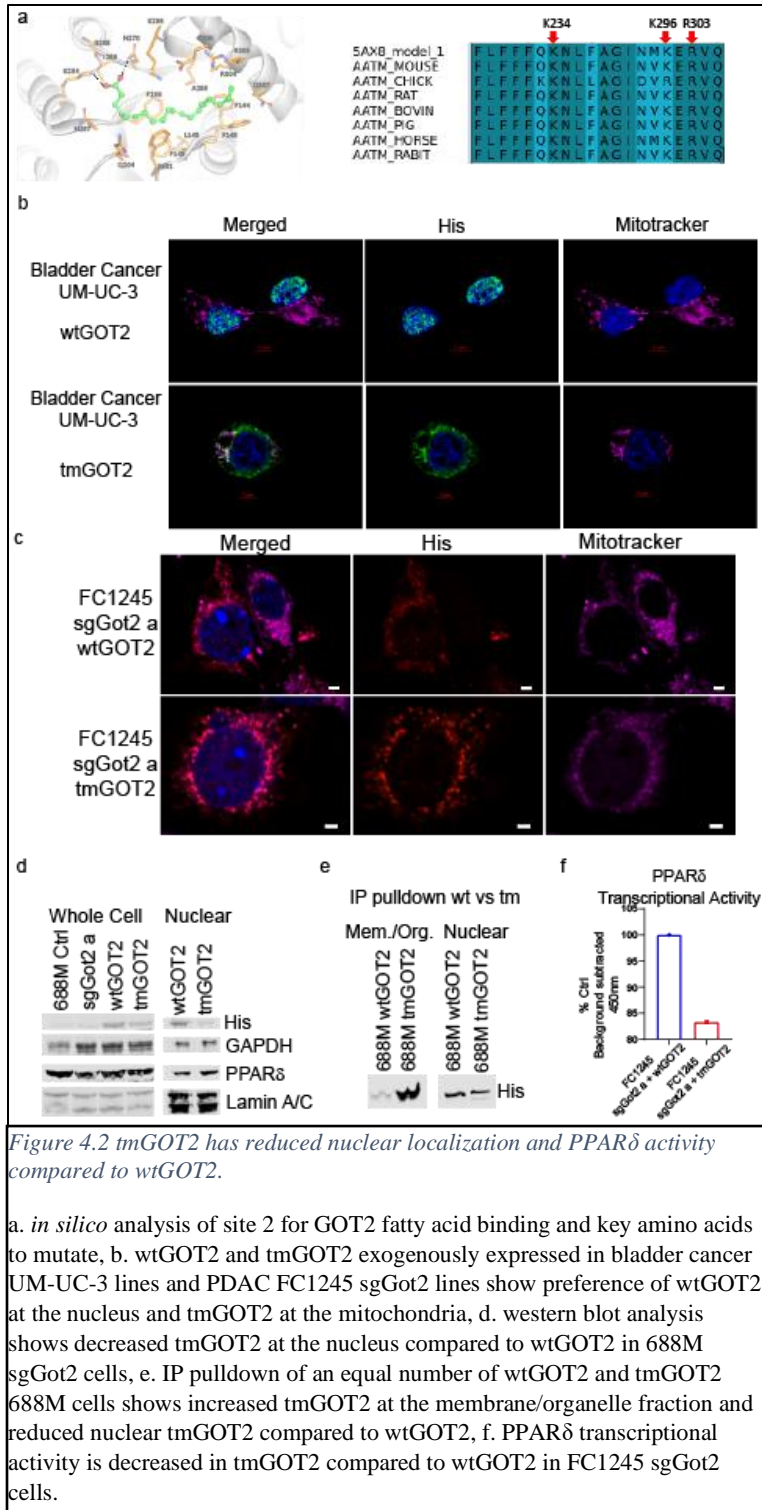


Figure 4.2 tmGOT2 has reduced nuclear localization and PPAR $\delta$  activity compared to wtGOT2.

a. *in silico* analysis of site 2 for GOT2 fatty acid binding and key amino acids to mutate, b. wtGOT2 and tmGOT2 exogenously expressed in bladder cancer UM-UC-3 lines and PDAC FC1245 sgGot2 lines show preference of wtGOT2 at the nucleus and tmGOT2 at the mitochondria, d. western blot analysis shows decreased tmGOT2 at the nucleus compared to wtGOT2 in 688M sgGot2 cells, e. IP pulldown of an equal number of wtGOT2 and tmGOT2 688M cells shows increased tmGOT2 at the membrane/organelle fraction and reduced nuclear tmGOT2 compared to wtGOT2, f. PPAR $\delta$  transcriptional activity is decreased in tmGOT2 compared to wtGOT2 in FC1245 sgGot2 cells.

necessitating an early take-down and end of the study. The difference in response of the mice to GOT2-null PDAC suggests the potential for future studies into the role of GOT2 in metastasis and cachexic response, mechanisms which have been linked to PPAR $\delta$  and LXR activity in some cancers[254, 263, 280].

Our previous work showed that GOT2 directly binds free fatty acids and GOT2 status affects the amount of arachidonic acid taken up by the nucleus of PDAC cells.

We also showed that GOT2 status has an effect on PPAR $\delta$  activity, with the hypothesis that GOT2 transported free fatty acids act as ligands for

PPAR $\delta$ . We have now shown that activation of PPAR $\delta$  both genetically and pharmacologically restores tumor growth in the GOT2-null setting, so we decided to take the hypothesis a step

further and test if blocking binding to our predicted fatty acid binding site on GOT2 could inhibit both PPAR $\delta$  activation and tumor growth. To do this, we created a triple-mutant GOT2 (tmGOT2) with 3 key amino acid residues mutated in a His-tagged GOT2 (Fig 4.2a). To create this mutant, we used site-directed mutagenesis to mutate K234, K296, and R303 to alanine. The *in silico* analysis of GOT2 structure suggested that these three residues could be key for the formation of hydrophobic site 2 (Fig 4.2 a) where GOT2 was predicted to bind to arachidonic acid. By mutating these residues to alanine, a non-bulky, chemically inert amino acid, we hoped to reduce the binding capability for fatty acids of the pocket and creation of these plasmids allowed us to compare tmGOT2 with wild-type GOT2 (wtGOT2) in functional assays both *in vitro* and *in vivo* by reconstituting either tmGOT2 or wtGOT2 into our sgGot2 null PDAC cells. We did not observe any difference in proliferation between the two reconstituted cell lines, but we did observe that long-term cell passage decreases the amount of wtGOT2 or tmGOT2 being expressed in the lines making *in vitro* work difficult.

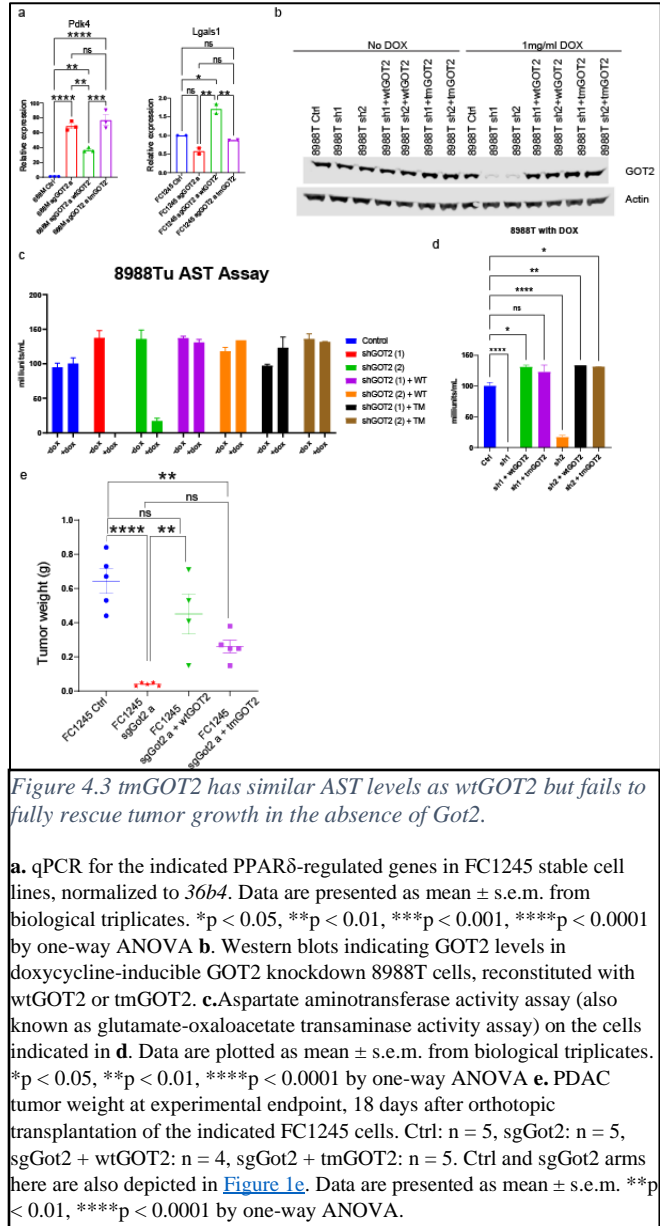
Interestingly, while we observed nuclear and mitochondrial localization of wtGOT2, the tmGOT2 re-constituted cells appeared to have a stronger localization to mitochondria and a reduced localization to the nucleus when imaged with IF (Fig 4.2 b-g). IP pulldown with His-tag in an equal cell-number of wtGOT2 and tmGOT2 reconstituted into 688M sgGot2 cells showed a higher amount of tmGOT2 pulldown in the membrane/organelle fraction and a reduced amount of tmGOT2 pulled down in the nuclear fraction (Fig 4.2 g). Along with a reduction of tmGOT2 compared to wtGOT2 in the nuclei of reconstituted 688M cells, we also saw a reduction in

PPAR $\delta$  transcriptional activity using the PPARE ABCAM kit (Fig 4.2 h). This decrease in PPAR $\delta$  activity was reflected in mRNA expression of PPAR $\delta$  target genes, Galectin and Pdk4 (Fig 4.3 a).

Following our observations on the different localizations of wtGOT2 and tmGOT2 we confirmed that tmGOT2 retains enzymatic activity (Fig 4.3 b-d). This AST assay measures both GOT1 and GOT2 activity. We saw that our shGOT2 stable KD cell lines showed no decrease in AST activity, agreeing with our proliferation data that alternative metabolic pathways are capable of overcoming a long-term loss of GOT2. However, in the DOX-inducible model

we were able to see a decrease in AST levels in the GOT2 KD lines treated with DOX. When we reconstituted these cell lines with either wtGOT2 or tmGOT2 the loss of AST activity no longer occurred, with no observed difference between wtGOT2 and tmGOT2 AST activity.

With *in vitro* results showing no change in mitochondrial activity or proliferative ability, we transplanted immune-competent mice with control, sgGot2, sgGot2 + wtGOT2, or sgGot2 + tmGOT2 PDAC cells to see if there was a change in *in vivo* tumor growth (Fig 4.3 e). Intriguingly we found that wtGOT2 reconstitution was able to completely restore tumor growth, but tmGOT2



reconstitution only partially rescued tumor growth (Fig 4.3 e). This data supports the hypothesis that GOT2 fatty acid transport has a significant role in GOT2-mediated PDAC progression and that the residues targeted by our tmGOT2 construct may be key for this role.

## **Discussion:**

Previously reported literature activity of LXR, another type of nuclear receptor activated by fatty acids, appears to parallel well with our observed PPAR $\delta$  activity through GOT2 activation, and suggests that GOT2 transport of fatty acids to the nucleus may have an even larger impact on immune control of the TME than shown through our work[263, 291]. Alternative pathways for fatty acids transported by GOT2 and their link to immune exclusion and suppression of the TME show even stronger support for why further characterization of this enzyme could have the potential to lead to a variety of improved treatments for cancers that are marked by an immune-exclusive phenotype. An FABP5-PPAR $\delta$  axis has been suggested as a target for a new class of fatty acid transport cancer therapeutics[265], and our results suggest that GOT2/FABP5 should be considered as a front-runner for consideration as well.

Though the combination of a reduction of tmGOT2 at the nuclei and a reduction of PPAR $\delta$  activity raises the question of whether tmGOT2 is binding fatty acids at a reduced rate or is simply translocating at a reduced rate, or is translocating at a reduced rate due to binding fatty acid at a reduced rate. There is substantial literature support for fatty acid binding proteins translocating to the nucleus following binding of fatty acid, including evidence that FABP5 undergoes nuclear localization following fatty acid binding where its transported ligands then activate PPAR $\delta$ [264, 265]. We suggest that binding site 2 is a key site for fatty acid binding in GOT2 and that blocking binding at this pocket either through genetic mutations or pharmacological inhibitors could result in a therapeutic that blocks this novel GOT2-PPAR $\delta$  axis in PDAC.

The nuclear localization of GOT2 was an unexpected discovery, as GOT2 lacks known nuclear localization sequences (NLS). The discovery and confirmation of specific binding sites for fatty acids on GOT2 and subsequent decreased nuclear location with mutations made to this site, suggests that the nuclear translocation of GOT2 may be contingent upon fatty acid binding. The binding of a fatty acid to GOT2 could be changing charge or conformation enough that a different

binding partner is capable of binding to GOT2 and chaperoning it to the nucleus. Interesting future studies could look at MS pulldown studies of wtGOT2 and tmGOT2 to see if binding partners and co-factors change depending on binding site activity and fatty acid availability. Identifying binding partners of GOT2 could provide a great deal of insight into the regulation of GOT2 location.

As this study has mostly been involved in showing that GOT2 status appears to change the way PDAC TME responds to tumors, our results showing different whole-body responses to the tumor based on GOT2 status presents a fascinating future direction to be considered. Metabolic reprogramming of tumors has been considered to be one of the main factors involved in the development of cachexia[98, 100, 105, 107, 133, 135, 294, 295], and our results - though preliminary and observatory only - suggest that GOT2 may be involved in the development of this complicated and devastating symptom of cancer. It has been shown that there is a link between fibroblasts and the TME, ligands from tumor cells, and the development of cachexia and so our described GOT2-PPAR $\delta$  axis fits well within the literature. Future research into this area could yield exciting and interesting results.

**Acknowledgements:**

Dr. Shanthi Nagarajan of the OHSU Medicinal Chemistry Core performed GOT2 binding *in silico* modeling and analysis for design of triple-mutant GOT2.

This study was supported by a postdoctoral fellowship from the OHSU Fellowship for Diversity in Research (to JA), a graduate student fellowship from the Knight Cancer Institute Cancer Center Support Grant P30 CA069533 (to HSC), NIH grants R00 CA188259 and RO1 CA229580 (to MHS) including CA229580-S1 (awarded to MHS in support of JA), American Cancer Society grant RSG-18-142-01-CSM (to MHS), and an OHSU Faculty Innovation Fund Award (to MHS). Members of the OHSU histopathology shared resource, medicinal chemistry core, and advanced light microscopy shared resources provided support for this study as well.

## Chapter 5: Conclusions, limitations, and future directions.

Our results showed that PPAR $\delta$  activity was linked to GOT2 status, and that loss of GOT2 decreased PPAR $\delta$  activity. We have also demonstrated that GOT2 binds to arachidonic acid and status of GOT2 affects the amount of arachidonic acid in the nucleus of PDAC cells. The PPAR family of nuclear receptors- PPAR $\alpha$ , PPAR $\delta$ , and PPAR $\gamma$ , are all believed to be activated by arachidonic acid[296]. While PPAR $\delta$  has not been extensively studied in PDAC, high levels of PPAR $\gamma$  in PDAC patients is correlated with poor prognosis and with inhibition of cytotoxic effects of gemcitabine and 5-fluorouracil in PDAC cells *in vitro*[280]. This effect of PPAR $\gamma$  on the typical treatment regimen of PDAC, was further supported when research showed that ligands against PPAR $\gamma$  (pioglitazone or rosiglitazone) is synergistic when combined with gemcitabine for PDAC treatment[281]. However, not all research of PPAR $\gamma$  supports the hypothesis that activation is always going to be protumorigenic. It has been reported that PPAR $\gamma$  coactivator 1- $\alpha$  agonists have synergistic effects with PD-1 blockade treatments[297]. This would suggest that a GOT2-PPAR $\gamma$  axis could potentially be anti-tumorigenic rather than pro-tumorigenic in certain situations. Further research into the impact of GOT2 fatty acid transport on nuclear receptor signaling is important before moving forward with drug designs. Our results describing GOT2 binding directly to arachidonic acid and affecting PPAR $\delta$  activation suggest that future studies could show a GOT2-PPAR $\gamma$  and GOT2-PPAR $\alpha$  axis as well in cells which express either PPAR family member. Just because our results have focused on the activation of PPAR $\delta$  as an indicator for GOT2 having an effect on nuclear arachidonic acid levels, and other potential nuclear receptor ligands, doesn't mean that no other nuclear receptors are affected by GOT2 status. Our main hypothesis is that GOT2 affects PPAR $\delta$  activity by transporting ligands required for PPAR $\delta$  activation to the nucleus, where these ligands are then released and act as signaling molecules. Nuclear fatty acids can have roles beyond activation of nuclear receptors, and based on our proposed model for the GOT2-PPAR $\delta$  axis, the transport of fatty acids to the nucleus by GOT2 could affect any nuclear mechanism dependent upon nuclear fatty acids.

As PPAR $\gamma$  has already been shown to be involved in PDAC development and that high expression is linked to poor prognosis, it would make sense to begin further investigation into a link between GOT2 fatty acid transport capabilities and nuclear PPAR $\gamma$  activity. As we have shown that GOT2 status affects PPAR $\delta$  signaling, most likely by decreasing nuclear ligand availability, it is entirely rational to suggest that GOT2 status would affect the activity of any nuclear receptor which relies upon the same pool of nuclear fatty acids as signaling molecules. Whether all of these nuclear changes affected by decreased fatty acids would be anti-tumorigenic is yet to be discerned, but research into disruption of PPAR $\delta$  in colon cancer has been shown to decrease tumorigenicity[284] which matches well with our results showing decreased PDAC tumor growth in GOT2-null systems. Together this data strongly supports that decreasing signaling of fatty acids by blocking this newly described GOT2-PPAR $\delta$  axis could be highly beneficial for patient outcomes.

We found in our model that the GOT2-PPAR $\delta$  axis resulted in increased COX-2 levels, both protein and mRNA, which were reduced upon GOT2 loss. The inflammatory response of tumors, partially through COX-2 expression, has been linked to T cell exclusion and the immune-suppressive TME of PDAC[12, 207, 218, 286, 288, 289]. Research into the EPHA2/TGF- $\beta$ /COX-2 axis has shown that deletion of *Epha2*, sensitized tumors to immunotherapy and reversed T cell exclusion and that *Ptgs2* deletion worked similarly[206]. The exclusion of anti-tumor specific T cells from the tumor is one of the key signs of adaptive immune escape and an indicator that checkpoint blockade therapy will be ineffective in the patient[207]. Research into T cell-inflamed phenotypes vs non-T cell-inflamed phenotypes and the underlying molecular mechanisms mediating the T cell-inflamed TME need to be understood before therapeutics can be used to regulate tumor cell-intrinsic immune exclusion and allow all patients to be responsive to immunotherapies. The main difficulty in immune-therapeutics is getting cytotoxic T cells into the tumor, with patients who have tumors showing poor infiltration having the worst outcomes.

Based on our results showing a similar relation to GOT2-PPAR $\delta$  signaling and COX-2 levels, along with our results showing increased T cell infiltration in GOT2-null tumors, these findings are highly suggestive that disruption of the GOT2-PPAR $\delta$  axis could sensitize PDAC tumors to immunotherapy agents and reverse T cell exclusion.

Beyond the role of immunotherapies, we found that the GOT2-PPAR $\delta$  axis could play a role in EMT switch, metastasis, and possibly in cachexic response. When we decreased GOT2 in our cell lines *in vitro* it transitioned them from a more mesenchymal-like phenotype to a more epithelial-like phenotype. These results are interesting because they link with published EMT activities of PPAR $\delta$  in melanoma[298]. However, while we would hypothesize that a reduction of GOT2-PPAR $\delta$  induced activity would result in reduced inflammation and reduced seeding, in melanoma PPAR $\delta$  antagonism is was linked to increased tumor cell extravasation and higher pulmonary metastasis rates[298]. Other research on PPAR $\gamma$  has suggested conflicting information, with some suggesting that activation of PPAR $\gamma$  is linked to EMT and other research suggesting antagonism of PPAR $\gamma$  may result in EMT and metastasis[254, 280, 299]. The conflicting literature on the role of PPAR signaling and EMT and metastasis matches with what we have observed with the effect of GOT2 loss *in vitro*. In our model cells were capable of switching from either a starting mesenchymal-like phenotype to one more epithelial following GOT2 loss, or of switching from a more epithelial-like phenotype to a more mesenchymal-like phenotype following GOT2 loss. The starting morphology of the cell line seemed to play more of a role in which direction switching occurred following GOT2 loss. Both our DOX-inducible cell lines and our shRNA or sgGot2 CRISPR cell lines showed morphological changes following GOT2 loss, with some cell lines showing more readily apparent changes than others. In our hands EMT switching appears to occur following GOT2 loss, but it can move in either direction and depends on starting cell morphology. If this observation holds in mouse and human models, it could help explain why the literature is inconclusive on the role of nuclear receptors, especially PPARs, and EMT. Studying

the role of the GOT2-PPAR $\delta$  axis in EMT and metastasis could lead to important pathway regulation and further the knowledge of this important field.

We performed a preliminary metastasis experiment using tail-vein injections of 688M control and 688M sgGot2 cells, which produce TdTomato, and examined lung and livers with flow cytometry to observe if a change in initial seeding was detected with loss of GOT2. While our numbers of successfully injected mice were too low for statistics, it did appear that GOT2 status may affect initial seeding by decreasing the number of TdTomato positive cells in the lungs and livers of mice injected with sgGot2 cells. We also observed that there appeared to be fewer lung and liver mets at the end point stages of our 688M sgGot2 tumor experiments than with control 688M tumors. Staining of metastatic human PDAC tumors for GOT2 showed increased GOT2 levels in the PanCK negative cells surrounding PanCK positive tumor cells. These tumor cells also showed GOT2 at the plasma membrane, mitochondria, and nucleus of PanCK positive cells. The staining images are suggestive that GOT2 may increase as cells become more mesenchymal, losing their PanCK expression in the process. Combined with our results showing an effect *in vitro* on EMT switching and our *in vivo* data suggesting GOT2 could play a role in metastasis, this data is extremely intriguing and suggests that future exploration into the role of GOT2, and other fatty acid transporters, in EMT and metastasis could be fruitful.

Along with the potential for a role in EMT and metastasis, our results with GW501516 provide some interesting aspects to consider for future study as well. The GW501516 treatment appeared to produce a different systemic effect depending on the GOT2 status of implanted tumors. Mice implanted with control 688M cells developed ascites, while the mice implanted with sgGot2 688M cells appeared to develop cachexia. This was a completely unexpected result, but in the scope of the project it becomes more understandable, as really this project has been on the communication between PDAC tumor cells and the TME through transport of fatty acids to the nucleus by GOT2. Cachexia research has suggested that the metabolic activity of a tumor may

play a role in the metabolic response of the host body[100, 300]. As we did show that metabolic plasticity of PDAC cells resulted in a rescue of metabolic activity following long term GOT2 loss, this leads to some initial complication in interpreting how GOT2 status could be affecting development of cachexia. However, on further examination our results support possible mechanisms of GOT2-PPAR $\delta$  in cachexic response might be discovered with further exploration. Our results suggest that while metabolic reprogramming is capable of overcoming the effect of long term GOT2 loss on AST mitochondrial activity, there is insufficient nuclear fatty acid transporter redundancy to entirely rescue the effect of long term GOT2 loss on nuclear fatty acid levels. This can be seen by the fact that nuclear levels of fatty acids were affected in GOT2-null systems along with signaling of the fatty acid ligand activated PPAR $\delta$  nuclear receptor. It should be noted the metabolism is a complicated topic and that while the malate-aspartate shuttle role of GOT2 may be compensated for with the use of alternative metabolic enzymes, there are also potential metabolic roles for GOT2 through the nuclear receptors activated by its transport of fatty acids to the nucleus. It has been shown that PPARs have lipid and mitochondrial metabolic effects on cells and that PPAR activation may be related to muscle wasting seen in experimental cancer cachexia[301]. With the identification of a novel GOT2-PPAR $\delta$  axis and our observations of differences in systemic responses to tumor development, depending on GOT2 status, it would be an interesting future project to tease out the differences in full body response to tumor cells depending on tumor GOT2-PPAR $\delta$  axis status.

The potential role of GOT2-PPAR $\alpha/\delta/\gamma$  signaling in cachexia and muscle-wasting could be an interesting research direction to tie together the literature described metabolic effects of GOT2 and its newly described nuclear fatty acid transport roles. The tmGOT2 created by our lab would add to the potential of this research direction, as it would allow for the separation of mitochondrial GOT2 functions from nuclear fatty acid transport derived metabolic activity. Changes in transcriptional metabolic activity, due to nuclear receptor signaling, have already been

linked as potential modulators of cachexic response[301], and so researching the impact of GOT2 on this whole systemic response seems an intriguing direction.

GOT2 is one of many fatty acid transporters and literature shows similar nuclear receptor activation by transport of fatty acids to the nucleus by other fatty acid transporters, lending support to our described GOT2-PPAR $\delta$  axis. Transport of long chain fatty acids by FABP5 from the cytosol to the nucleus has been shown to activate PPAR $\delta$ , leading to increased carcinogenesis in some cancer types[264]. It has also been shown that binding of saturated long chain fatty acids to FABP5 can outcompete binding of FABP5 to retinoic acid, and prevent transport of retinoic acid to the nucleus where it would be capable of activating retinoic acid-activate nuclear receptor RAR and PPAR $\delta$ . The blocking of retinoic acid nuclear activity then leads to suppressed tumorigenesis in some model systems and suggests that FABP5 inhibitors could be a new class of anticarcinogenic drugs[264]. With this in mind, we suggest that future GOT2/FABP5 inhibitors could be part of this new class of anticarcinogenic drugs and function through similar mechanisms.

We have shown that GOT2 binds directly to arachidonic acid and to oleic acid, though not as strongly as to arachidonic. It is possible that GOT2 binds to a variety of other fatty acids, as our results have suggested that a loss of GOT2 may have more of an impact on the import of C16 nuclear fatty acids than C12, and that the transport of fatty acids is highly regulated. As more data is added to the field showing the importance of various fatty acids as signaling ligands, it will be interesting to see which fatty acids can be transported by GOT2 and which nuclear receptors can be activated by them. Ligand activation of nuclear receptors can also be quite complicated with ligand activation sometimes resulting in suppression of certain transcriptional sites and activation of others. Indeed, when combined with the possibility that different fatty acids can out-compete each other for binding to fatty acid transporters, such as GOT2, it makes the importance of fatty acid availability, either from TME secretions or dietary, a key aspect of the plasticity of nuclear

ligand signaling. What fatty acids are currently being transported by GOT2 to the nucleus could depend on cell state and TME state, and changes to fatty acids being transported could then cause downstream changes to cell state and TME state again affecting which fatty acids are transported to the nucleus by GOT2.

The identification of a GOT2 fatty acid binding site, and creation of a tmGOT2 - with reduced PPAR $\delta$  activity and decreased tumor growth *in vivo* - suggests the viability of designing inhibitors that directly target the fatty acid binding capabilities of GOT2 and not the mitochondrial enzymatic roles. This would potentially reduce any non-specific side-effects from the important mitochondrial roles of GOT2 being lost upon inhibition. We acknowledge that while the mitochondrial enzymatic roles of GOT2 are plastic enough in PDAC to be compensated for in the long term, they may be essential in other cell types, and so avoiding off-target inhibition would be ideal when designing GOT2 inhibitors. Our results seem to support the hypothesis that the pro-tumorigenic TME role of GOT2 is mainly due to fatty acid transport by GOT2 to the nucleus where PPAR $\delta$  activation causes downstream systemic changes within the tumor, allowing for communication with the TME to create the immunosuppressive pathophysiology typical in PDAC.

While we have not studied whether inhibition of GOT2 is capable of reversing tumor growth and changing the immunosuppressive pathophysiology in a developed tumor, dynamic signaling changes and communication between PDAC and the TME suggest the possibility that inhibition of GOT2 in a fully developed tumor may be enough to change immune response. The limitation of our DOX-inducible cells was that they were human derived, and could not be implanted into an immune-competent mouse model. Future research into GOT2 inhibitors, especially those developed to target our identified tmGOT2 binding site, could help answer the question of whether the immunosuppressive pathophysiology of PDAC is reversible or if it is an inherent mainstay of PDAC. The importance of inflammation in the development of PDAC has been well described and our results showing the importance of the GOT2-PPAR $\delta$  axis on COX-2 levels

along with published results by others showing that disruption of the EPHA2/TGF- $\beta$ /COX-2 axis was able to restore T cell infiltration and activity in tumors[206] support the idea that inhibition of GOT2 may have an effect on patient survival. If GOT2-PPAR $\delta$  signaling is directly linked to COX-2 activity, in the same way that EPHA2/TGF- $\beta$  is, then disruption of COX-2 activity by either GOT2-PPAR $\delta$  inhibition or EPHA2/TGF- $\beta$  inhibition should lead to similar restoration of T cell infiltration and activity. With a potential for synergy between drugs that target both.

Immune evasion in PDAC is complicated with many underlying diverse mechanisms contributing, but targeting the nuclear fatty acid transport role of GOT2 may provide a treatment option for increasing immune response against this deadly cancer. Combined therapies with a drug which would decrease the ability of GOT2 to transport ligands to the nucleus of tumor cells, resulting in increased T cell infiltration and cytotoxicity, and with an immune-therapeutic is particularly exciting research direction to envision.

Our research has been entirely focused on the GOT2-PPAR $\delta$  axis, but long chain fatty acids are known to be signaling ligands for many different types of nuclear receptors. Suggesting a fruitful future in studying potential interactions between fatty acid transport to the nucleus and changes to signaling by various nuclear receptors. This also is one of the limitations of our study, as GOT2 transport of fatty acids to the nucleus could be important for other nuclear receptors which are key for different cell types. There is evidence in the literature that GOT2 is highly upregulated in immune cells, and may be important for the differentiation program of macrophages, DCs, and T cells[302, 303]. One of the more interesting research publications shows that CAR T-cells co-expressing GOT2 have enhanced T-cell metabolic function and activity against solid tumors[302]. Our work has been focused on the tumor cell-intrinsic GOT2-PPAR $\delta$  axis, but there is the potential for this axis to exist alongside mitochondrial GOT2 roles in cells of the TME, including immune cells. While we believe that LXR, CD36, PPAR $\delta$ , and PPAR $\gamma$  inhibitor research in cancer is promising and supportive of our hypothesis that reducing the nuclear import of fatty acids could be an anticancer therapeutic, we do not yet know how these inhibitors would

affect the activity of immune cells. It would be an unfortunate type of scientific irony if our treatment to improve tumor response to immune-therapeutics ended up causing immune cells to no longer be functional.

It is known that the malate-aspartate shuttle is required for CD4 T cell differentiation and activation and that increased GOT2 expression enhances T cell metabolic function and activity[302, 304]. We believe that these roles of GOT2 would not be affected by a therapeutic targeting the binding region of FFAs, as our results show that mitochondrial AST activity was unchanged in tmGOT2 cells compared to wtGOT2 cells. It is also shown that PPAR activation in T cells leads to increased FAO levels and number of tumor-reactive CD8+ T cells with matched improvement in anti-PD-1 therapy[297]. However, it has also been shown that PPAR $\delta$  is also important for FAO regulation and that KO of PPAR $\delta$  in CD8 T cells is dispensable for proliferation and survival, suggesting compensatory metabolic pathways are in place to replace the FAO roles of PPAR $\delta$  in T cells[285]. It is possible that this compensation is done by PPAR $\gamma$  or a different nuclear receptor and that inhibition of GOT2, resulting in a decrease of nuclear ligands, could lead to a reduction of any possible compensatory pathway. All of this shows the difficulty of designing anti-cancer therapeutics.

Our results describing the PDAC tumor cell intrinsic GOT2-PPAR $\delta$  axis combined with literature understanding of COX-2 and PPAR $\delta$  signaling suggests that we have strong evidence that blocking this axis could be a potential anti-cancer therapeutic. Based on our research, a drug which blocks the transport of fatty acids by GOT2 to the nucleus may have the potential to help ameliorate T cell exclusion and the immune-suppressive TME of PDAC, while also helping to restore tumor response to immune-based anti-cancer therapeutics. However, further exploration of the roles of GOT2 and nuclear receptors in other cell types, especially immune cells, is important before moving forward with full systemic GOT2 inhibitor treatments. Despite complication with how much is currently unknown about this newly described role of GOT2 in

transporting fatty acids to the nucleus, we believe that there is a great deal of potential for anti-cancer therapeutics in this field of research and look forward to seeing what future research reveals. Future research linking fatty acid transporters, like GOT2 and FABP5, with nuclear receptor signaling and fatty acid ligand activity can spread new insight into an area of signaling which is currently understudied. The studies described here set groundwork for large branches of future studies. With interesting aspects to potentially uncover in signaling of ligands for metabolic changes, TME communication, cachexic response, and immune response. It will be intriguing to see how the field develops over time.

## **References:**

1. Orth, M., et al., *Pancreatic ductal adenocarcinoma: biological hallmarks, current status, and future perspectives of combined modality treatment approaches*. Radiation Oncology, 2019. **14**(1): p. 141.
2. Sanford-Crane, H., J. Abrego, and M.H. Sherman, *Fibroblasts as Modulators of Local and Systemic Cancer Metabolism*. Cancers (Basel), 2019. **11**(5).
3. Sherman, M.H., et al., *Vitamin D Receptor-Mediated Stromal Reprogramming Suppresses Pancreatitis and Enhances Pancreatic Cancer Therapy*. Cell, 2014. **159**(1): p. 80-93.
4. Sherman, M.H., et al., *Stromal cues regulate the pancreatic cancer epigenome and metabolome*. Proc Natl Acad Sci U S A, 2017. **114**(5): p. 1129-34.
5. Sousa, C.M., et al., *Pancreatic stellate cells support tumour metabolism through autophagic alanine secretion*. Nature, 2016. **536**(7617): p. 479-83.
6. Pandol, S.J., *Normal Pancreatic Function*. 2015, American Pancreatic Association: Pancreapedia: Exocrine Pancrease Knowledge Base.
7. WHO. *Global Cancer Observatory*. 2020 [cited 2020 April 29]; Available from: <https://gco.iarc.fr/>.
8. Ying, H., et al., *Genetics and biology of pancreatic ductal adenocarcinoma*. Genes Dev, 2016. **30**(4): p. 355-85.
9. Ryan, D.P., T.S. Hong, and N. Bardeesy, *Pancreatic adenocarcinoma*. N Engl J Med, 2014. **371**(11): p. 1039-49.
10. Clark, C.E., et al., *Dynamics of the immune reaction to pancreatic cancer from inception to invasion*. Cancer Res, 2007. **67**(19): p. 9518-27.
11. Li, J., et al., *Tumor Cell-Intrinsic Factors Underlie Heterogeneity of Immune Cell Infiltration and Response to Immunotherapy*. Immunity, 2018. **49**(1): p. 178-193.e7.
12. Vonderheide, R.H. and L.J. Bayne, *Inflammatory networks and immune surveillance of pancreatic carcinoma*. Curr Opin Immunol, 2013. **25**(2): p. 200-5.
13. Stromnes, I.M., et al., *T-cell Localization, Activation, and Clonal Expansion in Human Pancreatic Ductal Adenocarcinoma*. Cancer Immunol Res, 2017. **5**(11): p. 978-991.
14. van Karnebeek, C.D.M., et al., *Bi-allelic GOT2 Mutations Cause a Treatable Malate-Aspartate Shuttle-Related Encephalopathy*. Am J Hum Genet, 2019. **105**(3): p. 534-548.
15. Yang, H., et al., *SIRT3-dependent GOT2 acetylation status affects the malate-aspartate NADH shuttle activity and pancreatic tumor growth*. Embo j, 2015. **34**(8): p. 1110-25.
16. Yang, S., et al., *Mitochondrial glutamine metabolism via GOT2 supports pancreatic cancer growth through senescence inhibition*. Cell Death Dis, 2018. **9**(2): p. 55.

17. Pandol, S.J., *The Exocrine Pancreas*. Vol. Anatomy. 2010, San Rafael (CA): Morgan & Claypool Life Sciences.
18. Bekkali, N.L.H. and K.W. Opping, *Pancreatic ductal adenocarcinoma epidemiology and risk assessment: Could we prevent? Possibility for an early diagnosis*. Endoscopic ultrasound, 2017. **6**(Suppl 3): p. S58-S61.
19. Hidalgo, M., et al., *Consensus guidelines for diagnosis, treatment and follow-up of patients with pancreatic cancer in Spain*. Clinical and Translational Oncology, 2017. **19**(6): p. 667-681.
20. Zhang, Y., H.C. Crawford, and M.P.d. Magliano, *Epithelial-Stromal Interactions in Pancreatic Cancer*. Annual Review of Physiology, 2019. **81**(1): p. 211-233.
21. Neuzillet, C., et al., *Pancreatic cancer: French clinical practice guidelines for diagnosis, treatment and follow-up (SNFGE, FFCD, GERCOR, UNICANCER, SFCD, SFED, SFRO, ACHBT, AFC)*. Digestive and Liver Disease, 2018. **50**(12): p. 1257-1271.
22. Yu, J., et al., *Time to progression of pancreatic ductal adenocarcinoma from low-to-high tumour stages*. Gut, 2015. **64**(11): p. 1783-1789.
23. Ducreux, M., et al., *Cancer of the pancreas: ESMO Clinical Practice Guidelines for diagnosis, treatment and follow-up*. Annals of Oncology, 2015. **26**: p. v56-v68.
24. Søreide, K., et al., *Molecular biology in pancreatic ductal adenocarcinoma: implications for future diagnostics and therapy*. European Surgery, 2019. **51**(3): p. 126-134.
25. Brosens, L.A.A., et al., *Pancreatic adenocarcinoma pathology: changing "landscape"*. Journal of Gastrointestinal Oncology, 2015. **6**(4): p. 358-374.
26. An, Y., et al., *Crosstalk between cancer-associated fibroblasts and immune cells in cancer*. J Cell Mol Med, 2020. **24**(1): p. 13-24.
27. Awaji, M. and R.K. Singh, *Cancer-Associated Fibroblasts' Functional Heterogeneity in Pancreatic Ductal Adenocarcinoma*. Cancers (Basel), 2019. **11**(3).
28. Chan, T.S., Y. Shaked, and K.K. Tsai, *Targeting the Interplay Between Cancer Fibroblasts, Mesenchymal Stem Cells, and Cancer Stem Cells in Desmoplastic Cancers*. Front Oncol, 2019. **9**.
29. Elyada, E., et al., *Cross-species single-cell analysis of pancreatic ductal adenocarcinoma reveals antigen-presenting cancer-associated fibroblasts*. Cancer Discov, 2019. **9**(8): p. 1102-23.
30. Fiori, M.E., et al., *Cancer-associated fibroblasts as abettors of tumor progression at the crossroads of EMT and therapy resistance*. Mol Cancer, 2019. **18**.
31. Kawase, T., et al., *Fibroblast activation protein- $\alpha$ -expressing fibroblasts promote the progression of pancreatic ductal adenocarcinoma*. BMC Gastroenterol, 2015. **15**.

32. Nielsen, M.F.B., M.B. Mortensen, and S. Detlefsen, *Key players in pancreatic cancer-stroma interaction: Cancer-associated fibroblasts, endothelial and inflammatory cells*. World J Gastroenterol, 2016. **22**(9): p. 2678-700.
33. Chang, Y.T., et al., *Pancreatic cancer-derived small extracellular vesical Ezrin regulates macrophage polarization and promotes metastasis*. Am J Cancer Res, 2020. **10**(1): p. 12-37.
34. Metzger, P., et al., *Immunostimulatory RNA leads to functional reprogramming of myeloid-derived suppressor cells in pancreatic cancer*. J Immunother Cancer, 2019. **7**.
35. Hu, S., et al., *Natural killer cell-based adoptive transfer immunotherapy for pancreatic ductal adenocarcinoma in a Kras<sup>LSL-G12D</sup>p53<sup>LSL-R172HPdx1-Cre</sup> mouse model*. Am J Cancer Res, 2019. **9**(8): p. 1757-65.
36. Yao, W., et al., *Profilin-1 suppresses tumorigenicity in pancreatic cancer through regulation of the SIRT3-HIF1 $\alpha$  axis*. Mol Cancer, 2014. **13**.
37. Aktekin, A., et al., *The effects of systemic inflammatory response on prognosis of pancreatic ductal adenocarcinoma*. Ann Hepatobiliary Pancreat Surg, 2019. **23**(2): p. 155-62.
38. Konings, I., et al., *Surveillance for pancreatic cancer in high-risk individuals*. BJS Open, 2019. **3**(5): p. 656-65.
39. Roberts, N.J., et al., *Whole Genome Sequencing Defines the Genetic Heterogeneity of Familial Pancreatic Cancer*. Cancer Discovery, 2016. **6**(2): p. 166.
40. Xiao, Q., et al., *Cancer associated fibroblasts in pancreatic cancer are reprogrammed by tumor-induced alterations in genomic DNA methylation*. Cancer Res, 2016. **76**(18): p. 5395-404.
41. Yoshida, G.J., *Metabolic reprogramming: the emerging concept and associated therapeutic strategies*. Experimental and clinical cancer research, 2015. **34**(111).
42. Angelica Avagliano, G.G., Maria Rosaria Ruocco, Veronica Romano, Immacolata Belviso, Antonia Carfora, Stefania Montagnani, Alessandro Arucci, *Metabolic reprogramming of cancer associated fibroblasts: the slavery of stromal fibroblasts*. Biomed Res Int., 2018: p. 6075403.
43. G. Gentric, V.M., F. Mechta-Grigoriou, *Heterogeneity in cancer metabolism: new concepts in an old field*. Antioxidants and redox signaling, 2017. **26**(9): p. 462-485.
44. V. Catalano, A.T., S. Di Franco, F. Dieli, M. Todaro, G. Stassi, *Tumor and its microenvironment: a synergistic interplay*. Seminars in Cancer Biology, 2013. **23**(6): p. 522-532.
45. A. Arcucci, M.R.R., G. Granato, A. M. Sacco, S. Montagnani, *Cancer: an oxidative crosstalk between solid tumor cells and cancer associated fibroblasts*. Biomed Res Int., 2016. **2016**(article ID 4502846): p. 7.

46. Y. Fu, S.L., S. Yin, *The reverse Warburg effect is likely to be an Achilles' heel of cancer that can be exploited for cancer therapy*. *Oncotarget*, 2017. **8**(34): p. 57813-57825.
47. Y. Kitano, Y.B., S. Nakagawa, *Nrf2 promotes oesophageal cancer cell proliferation via metabolic reprogramming and detoxification of reactive oxygen species*. *Journal of pathology*, 2018. **244**(3): p. 346-357.
48. Z. Liao, Z.W.T., P. Zhu, N. S. Tan, *Cancer-associated fibroblasts in tumor microenvironment- accomplices in tumor malignancy*. *Cellular immunology*, 2017.
49. A. Santi, F.G.K., S. Zanivan, *Cancer associated fibroblasts: an essential role in the tumor microenvironment*. *Proteomics*, 2018. **18**(5-6): p. 1700167.
50. M. L. Taddei, L.C., G. Comito, et al, *Senescent stroma promotes prostate cancer progression: the role of miR-210*. *Mol. Oncology*, 2014. **8**(8): p. 1729-1746.
51. C. Guido, D.W.-M., C. Capparelli, et al, *Metabolic reprogramming of cancer-associated fibroblasts by TGF- $\beta$  drives tumor growth: connecting TGF- $\beta$  signaling with 'Warburg-like' cancer metabolism and L-lactate production*. *Cell Cycle*, 2012. **11**(16): p. 3019-3035.
52. X. Hou, J.Z., Y. Wang, W. Xiong, J. Mi, *TGFBR-IDH1-Cav1 axis promotes TGF- $\beta$  signaling in cancer-associated fibroblasts*. *Oncotarget*, 2017. **8**(48): p. 83962-83974.
53. U. E. Martinez-Outschoorn, M.P.L., F. Sotgia, *Catabolic cancer-associate fibroblasts transfer energy and biomass to anabolic cancer cells, fueling tumor growth*. *Seminars in Cancer Biology*, 2014. **25**(47-60).
54. C. Capparelli, D.W.-M., C. Guido, et al, *CTGF drives autophagy, glycolysis and senescence in cancer-associated fibroblasts via HIF1 activation, metabolically promoting tumor growth*. *Cell Cycle*, 2012. **11**(12): p. 2272-2284.
55. M. T. Wang, K.V.H., D. Nie, *Cyclooxygenases, prostanoids, and tumor progression*. *Cancer and metastasis reviews*, 2007. **26**(3-4): p. 525-534.
56. Erez, N., et al., *Cancer-Associated Fibroblasts Are Activated in Incipient Neoplasia to Orchestrate Tumor-Promoting Inflammation in an NF-kappaB-Dependent Manner*. *Cancer Cell*, 2010. **17**(2): p. 135-47.
57. J. S. K. Chan, M.J.T., M. K. Sng, et al, *Cancer-associated fibroblasts enact field cancerization by promoting extratumoral oxidative stress*. *Cell Death Dis.*, 2017. **8**(1): p. e2562.
58. D. Zhang, Y.W., Z. Shi, et al, *Metabolic reprogramming of cancer-associated fibroblasts by IDH3 $\alpha$  downregulation*. *cell reports*, 2015. **10**(8): p. 1335-1348.
59. H. Shim, C.D., B. C. Lewis, et al, *c-Myc transactivation of LDH-A: implications for tumor metabolism and growth*. *proceedings of the national acadamy of sciences of the united states of america*, 1997. **94**(13): p. 6658-6663.

60. Liu, H.M., Q; Xu, Q; Lei, J; Li, X; Wang, Z; Wu, E, *Therapeutic potential of perineural invasion, hypoxia and desmoplasia in pancreatic cancer*. Current Pharmaceutical Design, 2012. **18**(17): p. 2395-2403.
61. S. Peppicelli, F.B., L. Calorini, *Extracellular acidity, a "reappreciated" trait of tumor environment driving malignancy: perspectives in diagnosis and therapy*. Cancer and metastasis reviews, 2014. **33**(2-3): p. 823-832.
62. F. Baltazar, C.P., F. Morais-Santos, et al, *Monocarboxylate transporters as targets and mediators in cancer therapy response*. Histology and Histopathology, 2014. **29**(12): p. 1511-1524.
63. E. Berra, E.B., A. Ginouves, V. Volmat, D. Roux, J. Pouyssegur, *HIF prolyl-hydroxylase 2 is the key oxygen sensor setting low steady-state levels of HIF-1 $\alpha$  in normoxia*. EMBO Journal, 2003. **22**(16): p. 4082-4090.
64. Q. Ke, M.C., *Hypoxia-inducible factor-1 (HIF-1)*. Molecular pharmacology, 2006. **70**(5): p. 1469-1480.
65. T. Fiaschi, A.M., E. Giannoni, et al, *Reciprocal metabolic reprogramming through lactate shuttle coordinately influences tumor-stroma interplay*. Cancer Res, 2012. **72**(19): p. 5130-5140.
66. Chiarugi, P. and P. Cirri, *Metabolic exchanges within tumor microenvironment*. Cancer Lett, 2016. **380**(1): p. 272-80.
67. A. Santi, A.C., F. Ranaldi, et al, *Cancer associated fibroblasts transfer lipids and proteins to cancer cells through cargo vesicles supporting tumor growth*. Biochimica et Biophysica Acta - Molecular Cell Research, 2015. **1853**(12): p. 3211-3223.
68. William J. Sullivan, P.J.M., Ernst W. Schmid, Aimee Flores, Milica Momcilovic, Mark S. Sharpley, David Jelinek, Andrew E. Whiteley, Matthew B. Maxwell, Blake R. Wilde, Utpal Banerjee, Hilary A. Collier, David B. Shackelford, Daniel Braas, Donald E. Ayer, Thomas Q. de Aguiar Vallim, William E. Lowry, Heather R. Cristofk., *Extracellular matrix remodeling regulates glucose metabolism through TXNIP destabilization*. Cell, 2018. **175**: p. 117-132.
69. Thomas Bertero, W.M.O., Eloise M. Grasset, Isabelle Bourget, Etienne Boulter, Sabrina Pisano, Paul Hofman, Floriant Bellvert, Guerrino Meneguzzi, Dmitry V. Bulavin, Soline Estrach, Chloe C. Feral, Stephen Y. Chan, Alexandre Bozec, Cedric Gaggioli, *Tumor-Stroma Mechanics Coordinate Amino Acid Availability to Sustain Tumor Growth and Malignancy*. Cell Metab, 2019. **29**: p. 124-140.
70. Mara H. Sherman, R.T.Y., Tiffany W. Tseng, Cristovao M. Sousa, Sihao Liu, Morgan L. Truitt, Nanhai He, Ning Ding, Christopher Liddle, Annette R. Atkins, Mathias Leblanc, Eric A. Collisson, John M. Asara, Alec C. Kimmelman, Michael Downes, Ronald M. Evans., *Stromal cues regulate the pancreatic cancer epigenome and metabolome*. PNAS, 2017. **114**(5): p. 1129-1134.
71. HF, D., *Tumors: wounds that do not heal. Similarities between stumor stroma generation and wound healing*. N. Engl. J. Med., 1986. **315**(26): p. 1650-1659.

72. Ziani, L., S. Chouaib, and J. Thiery, *Alteration of the Antitumor Immune Response by Cancer-Associated Fibroblasts*. *Frontiers in Immunology*, 2018. **9**(414).
73. Alberts, B.J., A; Lewis, J, *Molecular Biology of the Cell (5th ed.)*. 2008: Garland Science, Taylor & Francis Group. 1164–1165, 1178–1195.
74. Foda, H.D.Z., Stanley, *Matrix metalloproteinases in cancer invasion, metastasis and angiogenesis*. *Drug Discovery Today*, 2001. **6**(9): p. 478-482.
75. Taniguchi, Y., *The bromodomain and extra-terminal domain (BET) family: functional anatomy of BET paralogous proteins*. *Int J. Mol Sci*, 2016. **17**(11): p. 1849.
76. Bissel MJ, H.W., *Why don't we get more cancer? A proposed role of the microenvironment in restraining cancer cell progression*. *Nat Med*, 2011. **17**(3): p. 320-329.
77. Hanahan, D. and L.M. Coussens, *Accessories to the crime: functions of cells recruited to the tumor microenvironment*. *Cancer Cell*, 2012. **21**(3): p. 309-22.
78. Riss J, e.a., *Cancers as wounds that do not heal: Differences and similarities between renal regeneration/repair and renal cell carcinoma*. *Cancer Res*, 2006. **66**(14): p. 7216-7224.
79. Quail DF, J.J., *Microenvironmental regulation of tumor progression and metastasis*. *Nat Med*, 2013. **19**(11): p. 1423-1437.
80. Guerra C, e.a., *Chronic pancreatitis is essential for induction of pancreatic ductal adenocarcinoma by K-ras oncogenes in adult mice*. *Cancer Cell*, 2007. **11**(3): p. 291-302.
81. Provenzano PP, e.a., *Enzymatic targeting of the stroma ablates physical barriers to treatment of pancreatic ductal adenocarcinoma*. *Cancer Cell*, 2012. **21**(3): p. 418-429.
82. Jacobetz MA, e.a., *Hyaluronan impairs vascular function and drug delivery in a mouse model of pancreatic cancer*. *Gut*, 2013. **62**(1): p. 112-120.
83. Feig, C., et al., *Targeting CXCL12 from FAP-expressing carcinoma-associated fibroblasts synergizes with anti-PD-L1 immunotherapy in pancreatic cancer*. *Proc Natl Acad Sci U S A*, 2013. **110**(50): p. 20212-7.
84. Beatty GL, e.a., *Exclusion of T cells from pancreatic carcinomas in mice is regulated by Ly6C F4/80 extra-tumor macrophages*. *Gastroenterology*, 2015. **149**(1): p. 201-210.
85. Sherman, M.H., et al., *Vitamin D receptor-mediated stromal reprogramming suppresses pancreatitis and enhances pancreatic cancer therapy*. *Cell*, 2014. **159**(1): p. 80-93.
86. Riopel MM, L.J., Liu S, Leask A, Wang R, *β1 integrin-extracellular matrix interactions are essential for maintaining exocrine pancreas architecture and function*. *Lab Invest*, 2013. **93**(1): p. 31-40.
87. Wilson JS, P.R., Apte MV, *Stars and stripes in pancreatic cancer: role of stellate cells and stroma in cancer progression*. *Front Physiol*, 2014. **5**(52).

88. Wagray M, e.a., *GM-CSF mediates mesenchymal-epithelial cross-talk in pancreatic cancer*. *Cancer Discov*, 2016. **6**(8): p. 886-899.
89. Sousa CM, e.a., *Pancreatic stellate cells support tumour metabolism through autophagic alanine secretion*. *Nature*, 2016. **536**(7617): p. 479-483.
90. Rhim, A.D., et al., *Stromal elements act to restrain, rather than support, pancreatic ductal adenocarcinoma*. *Cancer Cell*, 2014. **25**(6): p. 735-47.
91. Ozdemir, B.C., et al., *Depletion of carcinoma-associated fibroblasts and fibrosis induces immunosuppression and accelerates pancreas cancer with reduced survival*. *Cancer Cell*, 2014. **25**(6): p. 719-34.
92. Lee, J.J., et al., *Stromal response to Hedgehog signaling restrains pancreatic cancer progression*. *Proc Natl Acad Sci U S A*, 2014. **111**(30): p. E3091-100.
93. Norihiro Sato, S.K., Keiji Hirata, Michael Goggins, *Role of hyaluronan in pancreatic cancer biology and therapy: once again in the spotlight*. *Cancer Science*, 2016. **107**: p. 569-575.
94. Weimin Wang, I.K., Lubomir Dostal, Heng Lin, Lijun Tan, Lili Zhao, et al, *Effector T cells abrogate stroma-mediated chemoresistance in ovarian cancer*. *Cell*, 2016. **165**: p. 1092-1105.
95. Amanpreet Kaur, M.R.W., Katie Marchbank, Reeti Behera, Abibatou Ndoye, Curtis H. Kugel III, Vanessa M. Dang, Jessica Appleton, Michael P. O'Connell, Phil Cheng, Alexander A. Valiga, Rachel Morissette, Nazli B. McDonnell, Luigi Ferrucci, Andrew V. Kossenkov, Katrina Meeth, Hsin-Yao Tang, Xiangfan Yin, William H. Wood III, Elin Lehrmann, Kevin G. Becker, Keith T. Flaherty, Dennie T. Frederick, Jennifer A. Wargo, et al, *sFRP2 in the aged microenvironment drives melanoma metastasis and therapy resistance*. *Nature*, 2016. **532**(7598): p. 250-254.
96. Marion Curtis, H.A.K., Bradley Ashcroft, Abir Mukherjee, Alyssa Johnson, Yilin Zhang, Ynes Helou, Raquel Batlle, Xiaojing Liu, Nuria Gutierrez, Xia Gao, S. Diane Yamada, Ricardo Lastra, Anthony Montag, Nagib Ahsan, Jason W. Locasale, Arthur R. Salomon, Angel R. Nebreda, Ernst Lengyel., *Fibroblasts mobilize tumor cell glycogen to promote proliferation and metastasis*. *Cell Metab*, 2018. **29**: p. 141-155.
97. Haidong Tang, Y.-X.F., *Immune Evasion in Tumor's Own Sweet Way*. *Cell Metab*, 2018. **27**: p. 945-946.
98. Petruzzelli, M. and E.F. Wagner, *Mechanisms of metabolic dysfunction in cancer-associated cachexia*. *Genes Dev*, 2016. **30**(5): p. 489-501.
99. Fearon, K., et al., *Definition and classification of cancer cachexia: an international consensus*. *Lancet Oncol*, 2011. **12**(5): p. 489-95.
100. Fearon, K.C., D.J. Glass, and D.C. Guttridge, *Cancer cachexia: mediators, signaling, and metabolic pathways*. *Cell Metab*, 2012. **16**(2): p. 153-66.

101. Mayers, J.R., et al., *Elevation of circulating branched-chain amino acids is an early event in human pancreatic adenocarcinoma development*. Nat Med, 2014. **20**(10): p. 1193-1198.
102. Kitagawa, M., S. Haji, and T. Amagai, *High Serum Essential Amino Acids as a Predictor of Skeletal Muscle Depletion in Patients With Cachexia and Advanced Gastrointestinal Cancers*. Nutr Clin Pract, 2017. **32**(5): p. 645-651.
103. Garin-Chesa, P., L.J. Old, and W.J. Rettig, *Cell surface glycoprotein of reactive stromal fibroblasts as a potential antibody target in human epithelial cancers*. Proc Natl Acad Sci U S A, 1990. **87**(18): p. 7235-9.
104. Brokopp, C.E., et al., *Fibroblast activation protein is induced by inflammation and degrades type I collagen in thin-cap fibroatheromata*. Eur Heart J, 2011. **32**(21): p. 2713-22.
105. Roberts, E.W., et al., *Depletion of stromal cells expressing fibroblast activation protein-alpha from skeletal muscle and bone marrow results in cachexia and anemia*. J Exp Med, 2013. **210**(6): p. 1137-51.
106. Flint, T.R., et al., *Tumor-Induced IL-6 Reprograms Host Metabolism to Suppress Anti-tumor Immunity*. Cell Metab, 2016. **24**(5): p. 672-684.
107. Argiles, J.M., S. Busquets, and F.J. Lopez-Soriano, *Cytokines in the pathogenesis of cancer cachexia*. Curr Opin Clin Nutr Metab Care, 2003. **6**(4): p. 401-6.
108. Ohe, Y., et al., *Interleukin-6 cDNA transfected Lewis lung carcinoma cells show unaltered net tumour growth rate but cause weight loss and shortened survival in syngeneic mice*. Br J Cancer, 1993. **67**(5): p. 939-44.
109. Tsujinaka, T., et al., *Muscle undergoes atrophy in association with increase of lysosomal cathepsin activity in interleukin-6 transgenic mouse*. Biochem Biophys Res Commun, 1995. **207**(1): p. 168-74.
110. Black, K., I.R. Garrett, and G.R. Mundy, *Chinese hamster ovarian cells transfected with the murine interleukin-6 gene cause hypercalcemia as well as cachexia, leukocytosis and thrombocytosis in tumor-bearing nude mice*. Endocrinology, 1991. **128**(5): p. 2657-9.
111. Strassmann, G., et al., *Evidence for the involvement of interleukin 6 in experimental cancer cachexia*. J Clin Invest, 1992. **89**(5): p. 1681-4.
112. Strassmann, G., et al., *Suramin interferes with interleukin-6 receptor binding in vitro and inhibits colon-26-mediated experimental cancer cachexia in vivo*. J Clin Invest, 1993. **92**(5): p. 2152-9.
113. Tamura, S., et al., *Involvement of human interleukin 6 in experimental cachexia induced by a human uterine cervical carcinoma xenograft*. Clin Cancer Res, 1995. **1**(11): p. 1353-8.

114. Staal-van den Brekel, A.J., et al., *Increased resting energy expenditure and weight loss are related to a systemic inflammatory response in lung cancer patients*. J Clin Oncol, 1995. **13**(10): p. 2600-5.
115. Fearon, K.C., et al., *Elevated circulating interleukin-6 is associated with an acute-phase response but reduced fixed hepatic protein synthesis in patients with cancer*. Ann Surg, 1991. **213**(1): p. 26-31.
116. Okada, S., et al., *Elevated serum interleukin-6 levels in patients with pancreatic cancer*. Jpn J Clin Oncol, 1998. **28**(1): p. 12-5.
117. Bonetto, A., et al., *STAT3 activation in skeletal muscle links muscle wasting and the acute phase response in cancer cachexia*. PLoS One, 2011. **6**(7): p. e22538.
118. Ohlund, D., et al., *Distinct populations of inflammatory fibroblasts and myofibroblasts in pancreatic cancer*. J Exp Med, 2017. **214**(3): p. 579-596.
119. Qiao, Y., et al., *IL6 derived from cancer-associated fibroblasts promotes chemoresistance via CXCR7 in esophageal squamous cell carcinoma*. Oncogene, 2018. **37**(7): p. 873-883.
120. Wu, X., et al., *IL-6 secreted by cancer-associated fibroblasts promotes epithelial-mesenchymal transition and metastasis of gastric cancer via JAK2/STAT3 signaling pathway*. Oncotarget, 2017. **8**(13): p. 20741-20750.
121. Duluc, C., et al., *Pharmacological targeting of the protein synthesis mTOR/4E-BP1 pathway in cancer-associated fibroblasts abrogates pancreatic tumour chemoresistance*. EMBO Mol Med, 2015. **7**(6): p. 735-53.
122. Zhang, Y., et al., *Interleukin-6 is required for pancreatic cancer progression by promoting MAPK signaling activation and oxidative stress resistance*. Cancer Res, 2013. **73**(20): p. 6359-74.
123. Wang, J. and A.J. Dunn, *Mouse interleukin-6 stimulates the HPA axis and increases brain tryptophan and serotonin metabolism*. Neurochem Int, 1998. **33**(2): p. 143-54.
124. Murata, T., et al., *HB-EGF and PDGF mediate reciprocal interactions of carcinoma cells with cancer-associated fibroblasts to support progression of uterine cervical cancers*. Cancer Res, 2011. **71**(21): p. 6633-42.
125. Neufert, C., et al., *Tumor fibroblast-derived epiregulin promotes growth of colitis-associated neoplasms through ERK*. J Clin Invest, 2013. **123**(4): p. 1428-43.
126. Cros, M., et al., *Constitutive production of parathyroid hormone-related protein (PTHrP) by fibroblasts derived from normal and pathological human breast tissue*. Oncol Res, 2002. **13**(3): p. 137-46.
127. Blomme, E.A., et al., *Parathyroid hormone-related protein is a positive regulator of keratinocyte growth factor expression by normal dermal fibroblasts*. Mol Cell Endocrinol, 1999. **152**(1-2): p. 189-97.

128. Foley, J., et al., *At the crossroads: EGFR and PTHrP signaling in cancer-mediated diseases of bone*. *Odontology*, 2012. **100**(2): p. 109-29.
129. Kir, S., et al., *Tumour-derived PTH-related protein triggers adipose tissue browning and cancer cachexia*. *Nature*, 2014. **513**(7516): p. 100-4.
130. Bing, C., et al., *Increased gene expression of brown fat uncoupling protein (UCP)1 and skeletal muscle UCP2 and UCP3 in MAC16-induced cancer cachexia*. *Cancer Res*, 2000. **60**(9): p. 2405-10.
131. Brooks, S.L., et al., *Sympathetic activation of brown-adipose-tissue thermogenesis in cachexia*. *Biosci Rep*, 1981. **1**(6): p. 509-17.
132. Shellock, F.G., M.S. Riedinger, and M.C. Fishbein, *Brown adipose tissue in cancer patients: possible cause of cancer-induced cachexia*. *J Cancer Res Clin Oncol*, 1986. **111**(1): p. 82-5.
133. Tsoli, M., et al., *Activation of thermogenesis in brown adipose tissue and dysregulated lipid metabolism associated with cancer cachexia in mice*. *Cancer Res*, 2012. **72**(17): p. 4372-82.
134. Kir, S. and B.M. Spiegelman, *Cachexia & Brown Fat: A Burning Issue in Cancer*. *Trends Cancer*, 2016. **2**(9): p. 461-463.
135. Song, W., et al., *Tumor-Derived Ligands Trigger Tumor Growth and Host Wasting via Differential MEK Activation*. *Dev Cell*, 2019.
136. Yasmeen, R., et al., *Epregeulin induces leptin secretion and energy expenditure in high-fat diet-fed mice*. *J Endocrinol*, 2018. **239**(3): p. 377-388.
137. Hicks, M.J., et al., *Anti-Epidermal Growth Factor Receptor Gene Therapy for Glioblastoma*. *PLoS One*, 2016. **11**(10): p. e0162978.
138. Hensley, C.T., et al., *Metabolic Heterogeneity in Human Lung Tumors*. *Cell*, 2016. **164**(4): p. 681-94.
139. Zhang, Y., et al., *Addressing metabolic heterogeneity in clear cell renal cell carcinoma with quantitative Dixon MRI*. *JCI Insight*, 2017. **2**(15).
140. Muir, A., L.V. Danai, and M.G. Vander Heiden, *Microenvironmental regulation of cancer cell metabolism: implications for experimental design and translational studies*. *Dis Model Mech*, 2018. **11**(8).
141. Mayers, J.R., et al., *Tissue of origin dictates branched-chain amino acid metabolism in mutant Kras-driven cancers*. *Science*, 2016. **353**(6304): p. 1161-5.
142. Gui, D.Y., et al., *Environment Dictates Dependence on Mitochondrial Complex I for NAD<sup>+</sup> and Aspartate Production and Determines Cancer Cell Sensitivity to Metformin*. *Cell Metab*, 2016. **24**(5): p. 716-727.

143. Miller, A., et al., *Exploring Metabolic Configurations of Single Cells within Complex Tissue Microenvironments*. Cell Metab, 2017. **26**(5): p. 788-800 e6.
144. Hulea, L., et al., *Translational and HIF-1alpha-Dependent Metabolic Reprogramming Underpin Metabolic Plasticity and Responses to Kinase Inhibitors and Biguanides*. Cell Metab, 2018. **28**(6): p. 817-832 e8.
145. Campbell, S.L. and K.E. Wellen, *Metabolic Signaling to the Nucleus in Cancer*. Mol Cell, 2018. **71**(3): p. 398-408.
146. Buck, M.D., et al., *Metabolic Instruction of Immunity*. Cell, 2017. **169**(4): p. 570-586.
147. Yao, W., A. Maitra, and H. Ying, *Recent insights into the biology of pancreatic cancer*. EBioMedicine, 2020. **53**.
148. Perkhofer, L., et al., *DNA damage repair as a target in pancreatic cancer: state-of-the-art and future perspectives*. Gut, 2020: p. gutjnl-2019-319984.
149. Jones, S., et al., *Core Signaling Pathways in Human Pancreatic Cancers Revealed by Global Genomic Analyses*. Science, 2008. **321**(5897): p. 1801.
150. Waddell, N., et al., *Whole genomes redefine the mutational landscape of pancreatic cancer*. Nature, 2015. **518**(7540): p. 495-501.
151. Saldia, A., et al., *Outcome of Pancreatic Cancer Surveillance Among High-Risk Individuals Tested for Germline Mutations in BRCA1 and BRCA2*. Cancer Prev Res (Phila), 2019. **12**(9): p. 599-608.
152. Gupta, M., R. Iyer, and C. Fountzilias, *Poly(ADP-Ribose) Polymerase Inhibitors in Pancreatic Cancer: A New Treatment Paradigms and Future Implications*. Cancers (Basel), 2019. **11**(12).
153. O'Reilly, E.M., et al., *Randomized, Multicenter, Phase II Trial of Gemcitabine and Cisplatin With or Without Veliparib in Patients With Pancreas Adenocarcinoma and a Germline BRCA/PALB2 Mutation*. Journal of Clinical Oncology, 2020. **38**(13): p. 1378-1388.
154. Stolz, A., N. Ertych, and H. Bastians, *Tumor Suppressor &CHK2&: Regulator of DNA Damage Response and Mediator of Chromosomal Stability*. Clinical Cancer Research, 2011. **17**(3): p. 401.
155. Brand, R., et al., *Prospective study of germline genetic testing in incident cases of pancreatic adenocarcinoma*. Cancer, 2018. **124**(17): p. 3520-3527.
156. Orth, M., et al., *Pancreatic ductal adenocarcinoma: biological hallmarks, current status, and future perspectives of combined modality treatment approaches*. Radiat Oncol, 2019. **14**.
157. Sarantis, P., et al., *Pancreatic ductal adenocarcinoma: Treatment hurdles, tumor microenvironment and immunotherapy*. World J Gastrointest Oncol, 2020. **12**(2): p. 173-81.

158. Sinha, S. and S.D. Leach, *New insights in the development of pancreatic cancer*. *Curr Opin Gastroenterol*, 2016. **32**(5): p. 394-400.
159. Raphael, B.J., et al., *Integrated Genomic Characterization of Pancreatic Ductal Adenocarcinoma*. *Cancer Cell*, 2017. **32**(2): p. 185-203.e13.
160. Korc, M., *Driver mutations: a roadmap for getting close and personal in pancreatic cancer*. *Cancer biology & therapy*, 2010. **10**(6): p. 588-591.
161. Zhou, J., et al., *Identification of novel genes associated with a poor prognosis in pancreatic ductal adenocarcinoma via a bioinformatics analysis*. *Biosci Rep*, 2019. **39**(8).
162. Hingorani, S.R., et al., *Preinvasive and invasive ductal pancreatic cancer and its early detection in the mouse*. *Cancer Cell*, 2003. **4**(6): p. 437-50.
163. Lee, A.Y.L., et al., *Cell of origin affects tumour development and phenotype in pancreatic ductal adenocarcinoma*. *Gut*, 2019. **68**(3): p. 487.
164. Bailey, J.M., et al., *p53 mutations cooperate with oncogenic Kras to promote adenocarcinoma from pancreatic ductal cells*. *Oncogene*, 2016. **35**(32): p. 4282-4288.
165. Stanger, B.Z., et al., *Pten constrains centroacinar cell expansion and malignant transformation in the pancreas*. *Cancer Cell*, 2005. **8**(3): p. 185-95.
166. Makohon-Moore, A.P., et al., *Precancerous neoplastic cells can move through the pancreatic ductal system*. *Nature*, 2018. **561**(7722): p. 201-205.
167. Farrow, B. and B.M. Evers, *Inflammation and the development of pancreatic cancer*. *Surg Oncol*, 2002. **10**(4): p. 153-69.
168. Niederau, C., L.D. Ferrell, and J.H. Grendell, *Caerulein-induced acute necrotizing pancreatitis in mice: protective effects of proglumide, benzotript, and secretin*. *Gastroenterology*, 1985. **88**(5 Pt 1): p. 1192-204.
169. Carrière, C., et al., *Acute pancreatitis markedly accelerates pancreatic cancer progression in mice expressing oncogenic Kras*. *Biochemical and biophysical research communications*, 2009. **382**(3): p. 561-565.
170. Guerra, C., et al., *Pancreatitis-induced inflammation contributes to pancreatic cancer by inhibiting oncogene-induced senescence*. *Cancer Cell*, 2011. **19**(6): p. 728-39.
171. Collins, M.A., et al., *MAPK signaling is required for dedifferentiation of acinar cells and development of pancreatic intraepithelial neoplasia in mice*. *Gastroenterology*, 2014. **146**(3): p. 822-834.e7.
172. Collisson, E.A., et al., *Molecular subtypes of pancreatic cancer*. *Nature Reviews Gastroenterology & Hepatology*, 2019. **16**(4): p. 207-220.
173. Feigin, M.E., et al., *Recurrent noncoding regulatory mutations in pancreatic ductal adenocarcinoma*. *Nature Genetics*, 2017. **49**(6): p. 825-833.

174. Ligorio, M., et al., *Stromal Microenvironment Shapes the Intratumoral Architecture of Pancreatic Cancer*. Cell, 2019. **178**(1): p. 160-175.e27.
175. Khalafalla, F.G. and M.W. Khan, *Inflammation and Epithelial-Mesenchymal Transition in Pancreatic Ductal Adenocarcinoma: Fighting Against Multiple Opponents*. Cancer Growth Metastasis, 2017. **10**.
176. Hanahan, D. and R.A. Weinberg, *Hallmarks of cancer: the next generation*. Cell, 2011. **144**(5): p. 646-74.
177. Nickle, T. and I. Barrette-Ng, *Hallmarks of Cancer*. 2020.
178. Warburg, O., *On the Origin of Cancer Cells*. Science, 1956. **123**(3191): p. 309.
179. Swierczynski, J., A. Hebanowska, and T. Sledzinski, *Role of abnormal lipid metabolism in development, progression, diagnosis and therapy of pancreatic cancer*. World journal of gastroenterology, 2014. **20**(9): p. 2279-2303.
180. Vander Heiden, M.G., L.C. Cantley, and C.B. Thompson, *Understanding the Warburg Effect: The Metabolic Requirements of Cell Proliferation*. Science, 2009. **324**(5930): p. 1029.
181. Boren, J., et al., *Gleevec (STI571) influences metabolic enzyme activities and glucose carbon flow toward nucleic acid and fatty acid synthesis in myeloid tumor cells*. J Biol Chem, 2001. **276**(41): p. 37747-53.
182. Tennant, D.A., et al., *Metabolic transformation in cancer*. Carcinogenesis, 2009. **30**(8): p. 1269-80.
183. Hanahan, D. and R.A. Weinberg, *The hallmarks of cancer*. Cell, 2000. **100**(1): p. 57-70.
184. Lu, C.W., et al., *Induction of pyruvate dehydrogenase kinase-3 by hypoxia-inducible factor-1 promotes metabolic switch and drug resistance*. J Biol Chem, 2008. **283**(42): p. 28106-14.
185. Hitosugi, T., et al., *Tyrosine phosphorylation of mitochondrial pyruvate dehydrogenase kinase 1 is important for cancer metabolism*. Mol Cell, 2011. **44**(6): p. 864-77.
186. Shlomi, T., et al., *Genome-scale metabolic modeling elucidates the role of proliferative adaptation in causing the Warburg effect*. PLoS Comput Biol, 2011. **7**(3): p. e1002018.
187. DeBerardinis, R.J., et al., *The Biology of Cancer: Metabolic Reprogramming Fuels Cell Growth and Proliferation*. Cell Metabolism, 2008. **7**(1): p. 11-20.
188. Ying, H., et al., *Oncogenic Kras maintains pancreatic tumors through regulation of anabolic glucose metabolism*. Cell, 2012. **149**(3): p. 656-70.
189. Sonoda, J., L. Pei, and R.M. Evans, *Nuclear receptors: decoding metabolic disease*. FEBS letters, 2008. **582**(1): p. 2-9.

190. Nagy, L. and J.W. Schwabe, *Mechanism of the nuclear receptor molecular switch*. Trends Biochem Sci, 2004. **29**(6): p. 317-24.
191. Pratt, W.B. and D.O. Toft, *Steroid receptor interactions with heat shock protein and immunophilin chaperones*. Endocr Rev, 1997. **18**(3): p. 306-60.
192. Rosenfeld, M.G., V.V. Lunyak, and C.K. Glass, *Sensors and signals: a coactivator/corepressor/epigenetic code for integrating signal-dependent programs of transcriptional response*. Genes Dev, 2006. **20**(11): p. 1405-28.
193. Semple, R.K., V.K. Chatterjee, and S. O'Rahilly, *PPAR gamma and human metabolic disease*. J Clin Invest, 2006. **116**(3): p. 581-9.
194. Lefebvre, P., et al., *Sorting out the roles of PPAR alpha in energy metabolism and vascular homeostasis*. J Clin Invest, 2006. **116**(3): p. 571-80.
195. Dawson, M.I. and Z. Xia, *The retinoid X receptors and their ligands*. Biochimica et biophysica acta, 2012. **1821**(1): p. 21-56.
196. Li, A.C. and W. Palinski, *Peroxisome proliferator-activated receptors: how their effects on macrophages can lead to the development of a new drug therapy against atherosclerosis*. Annu Rev Pharmacol Toxicol, 2006. **46**: p. 1-39.
197. Sherman, M.H., M. Downes, and R.M. Evans, *Minireview: Nuclear Receptors as Modulators of the Tumor Microenvironment*. Cancer Prev Res (Phila), 2012. **5**(1): p. 3-10.
198. Szatmari, I., et al., *Activation of PPARgamma specifies a dendritic cell subtype capable of enhanced induction of iNKT cell expansion*. Immunity, 2004. **21**(1): p. 95-106.
199. Barish, G.D., V.A. Narkar, and R.M. Evans, *PPAR delta: a dagger in the heart of the metabolic syndrome*. J Clin Invest, 2006. **116**(3): p. 590-7.
200. Liu, Y., et al., *The Role of PPAR- $\delta$  in Metabolism, Inflammation, and Cancer: Many Characters of a Critical Transcription Factor*. Int J Mol Sci, 2018. **19**(11).
201. Orimo, A., et al., *Stromal fibroblasts present in invasive human breast carcinomas promote tumor growth and angiogenesis through elevated SDF-1/CXCL12 secretion*. Cell, 2005. **121**(3): p. 335-48.
202. Knopfova, L. and J. Smarda, *The use of Cox-2 and PPAR $\gamma$  signaling in anti-cancer therapies*. Experimental and therapeutic medicine, 2010. **1**(2): p. 257-264.
203. Seibert, K. and J.L. Masferrer, *Role of inducible cyclooxygenase (COX-2) in inflammation*. Receptor, 1994. **4**(1): p. 17-23.
204. Urban, M.K., *COX-2 specific inhibitors offer improved advantages over traditional NSAIDs*. Orthopedics, 2000. **23**(7 Suppl): p. S761-4.

205. Conejo-Garcia, J.R., *Breaking barriers for T cells by targeting the EPHA2/TGF- $\beta$ /COX-2 axis in pancreatic cancer*. The Journal of Clinical Investigation, 2019. **129**(9): p. 3521-3523.
206. Markosyan, N., et al., *Tumor cell-intrinsic EPHA2 suppresses anti-tumor immunity by regulating PTGS2 (COX-2)*. J Clin Invest, 2019. **129**(9): p. 3594-3609.
207. Spranger, S., *Mechanisms of tumor escape in the context of the T-cell-inflamed and the non-T-cell-inflamed tumor microenvironment*. Int Immunol, 2016. **28**(8): p. 383-91.
208. Liu, B., L. Qu, and S. Yan, *Cyclooxygenase-2 promotes tumor growth and suppresses tumor immunity*. Cancer Cell International, 2015. **15**(1): p. 106.
209. Li, Q., et al., *Interleukin-17 Indirectly Promotes M2 Macrophage Differentiation through Stimulation of COX-2/PGE2 Pathway in the Cancer Cells*. Cancer research and treatment : official journal of Korean Cancer Association, 2014. **46**(3): p. 297-306.
210. Dubey, P., et al., *Cyclooxygenase-2 inhibition attenuates hypoxic cancer cells induced m2-polarization of macrophages*. Cell Mol Biol (Noisy-le-grand), 2014. **60**(3): p. 10-5.
211. Holt, D., et al., *Prostaglandin E(2) (PGE (2)) suppresses natural killer cell function primarily through the PGE(2) receptor EP4*. Cancer immunology, immunotherapy : CII, 2011. **60**(11): p. 1577-1586.
212. Martinet, L., et al., *PGE2 inhibits natural killer and  $\gamma\delta$  T cell cytotoxicity triggered by NKR and TCR through a cAMP-mediated PKA type I-dependent signaling*. Biochemical Pharmacology, 2010. **80**(6): p. 838-845.
213. Mahic, M., et al., *FOXP3+CD4+CD25+ adaptive regulatory T cells express cyclooxygenase-2 and suppress effector T cells by a prostaglandin E2-dependent mechanism*. J Immunol, 2006. **177**(1): p. 246-54.
214. Hori, S., T. Nomura, and S. Sakaguchi, *Control of regulatory T cell development by the transcription factor Foxp3*. Science, 2003. **299**(5609): p. 1057-61.
215. Yuan, X.L., et al., *Elevated expression of Foxp3 in tumor-infiltrating Treg cells suppresses T-cell proliferation and contributes to gastric cancer progression in a COX-2-dependent manner*. Clin Immunol, 2010. **134**(3): p. 277-88.
216. Harizi, H., C. Grosset, and N. Gualde, *Prostaglandin E2 modulates dendritic cell function via EP2 and EP4 receptor subtypes*. Journal of Leukocyte Biology, 2003. **73**(6): p. 756-763.
217. Chen, E.P., et al., *Myeloid Cell COX-2 deletion reduces mammary tumor growth through enhanced cytotoxic T-lymphocyte function*. Carcinogenesis, 2014. **35**(8): p. 1788-1797.
218. Na, Y.-R., et al., *Cyclooxygenase-2 inhibition blocks M2 macrophage differentiation and suppresses metastasis in murine breast cancer model*. PloS one, 2013. **8**(5): p. e63451-e63451.

219. Danai, L.V., et al., *Altered exocrine function can drive adipose wasting in early pancreatic cancer*. *Nature*, 2018. **558**(7711): p. 600-4.
220. Fu, Y., et al., *The critical roles of activated stellate cells-mediated paracrine signaling, metabolism and onco-immunology in pancreatic ductal adenocarcinoma*. *Mol Cancer*, 2018. **17**.
221. Hessmann, E., et al., *Fibroblast drug scavenging increases intratumoural gemcitabine accumulation in murine pancreas cancer*. *Gut*, 2018. **67**(3): p. 497-507.
222. Ying, H., et al., *Genetics and biology of pancreatic ductal adenocarcinoma*. *Genes & development*, 2016. **30**(4): p. 355-385.
223. Yan, L., et al., *Glucose Metabolism in Pancreatic Cancer*. *Cancers (Basel)*, 2019. **11**(10).
224. Son, J., et al., *Glutamine supports pancreatic cancer growth through a Kras-regulated metabolic pathway*. *Nature*, 2013. **496**(7443): p. 101-5.
225. Abrego, J., et al., *GOT1-Mediated Anaplerotic Glutamine Metabolism Regulates Chronic Acidosis Stress In Pancreatic Cancer Cells*. *Cancer Lett*, 2017. **400**: p. 37-46.
226. Li, D., et al., *Inhibition of glutamine metabolism counteracts pancreatic cancer stem cell features and sensitizes cells to radiotherapy*. *Oncotarget*, 2015. **6**(31): p. 31151-63.
227. Daemen, A., et al., *Metabolite profiling stratifies pancreatic ductal adenocarcinomas into subtypes with distinct sensitivities to metabolic inhibitors*. *Proceedings of the National Academy of Sciences*, 2015. **112**(32): p. E4410-E4417.
228. Rajeshkumar, N., et al., *Treatment of Pancreatic Cancer Patient-Derived Xenograft Panel with Metabolic Inhibitors Reveals Efficacy of Phenformin*. *Clin Cancer Res*, 2017. **23**(18): p. 5639-47.
229. Sousa, C.M., et al., *Pancreatic stellate cells support tumour metabolism through autophagic alanine secretion*. *Nature*, 2016. **536**(7617): p. 479-483.
230. Auciello, F.R., et al., *A stromal lysolipid-autotaxin signaling axis promotes pancreatic tumor progression*. *Cancer Discov*, 2019. **9**(5): p. 617-27.
231. Ding, N., et al., *A Vitamin D Receptor/SMAD Genomic Circuit Gates Hepatic Fibrotic Response*. *Cell*, 2013. **153**(3): p. 601-13.
232. Wei, Z., et al., *Vitamin D switches BAF complexes to protect  $\beta$  cells*. *Cell*, 2018. **173**(5): p. 1135-1149.e15.
233. Hollinshead, K.E.R., et al., *Respiratory Supercomplexes Promote Mitochondrial Efficiency and Growth in Severely Hypoxic Pancreatic Cancer*. *Cell Reports*, 2020. **33**(1).
234. Sorrentino, D., et al., *Oleate uptake by cardiac myocytes is carrier mediated and involves a 40-kD plasma membrane fatty acid binding protein similar to that in liver, adipose tissue, and gut*. *J Clin Invest*, 1988. **82**(3): p. 928-35.

235. Stremmel, W., G. Strohmeyer, and P.D. Berk, *Hepatocellular uptake of oleate is energy dependent, sodium linked, and inhibited by an antibody to a hepatocyte plasma membrane fatty acid binding protein*. Proceedings of the National Academy of Sciences, 1986. **83**(11): p. 3584-3588.
236. Chakrabarti, G., et al., *Targeting glutamine metabolism sensitizes pancreatic cancer to PARP-driven metabolic catastrophe induced by  $\beta$ -lapachone*. Cancer & Metabolism, 2015. **3**(1): p. 12.
237. Pascual, G., et al., *Targeting metastasis-initiating cells through the fatty acid receptor CD36*. Nature, 2017. **541**(7635): p. 41-45.
238. Pupo, E., et al., *KRAS-Driven Metabolic Rewiring Reveals Novel Actionable Targets in Cancer*. Front Oncol, 2019. **9**.
239. Toda, K., et al., *Metabolic Alterations Caused by KRAS Mutations in Colorectal Cancer Contribute to Cell Adaptation to Glutamine Depletion by Upregulation of Asparagine Synthetase12*. Neoplasia, 2016. **18**(11): p. 654-65.
240. Jing, X.Y., et al., *Roles of the lipid metabolism in hepatic stellate cells activation  $\Delta$* . Chin Med Sci J, 2013. **28**(4): p. 233-6.
241. Lu, M., et al., *Role of the malate-aspartate shuttle on the metabolic response to myocardial ischemia*. Journal of theoretical biology, 2008. **254**(2): p. 466-475.
242. Dawson, A.G., *Oxidation of cytosolic NADH formed during aerobic metabolism in mammalian cells*. Trends in Biochemical Sciences, 1979. **4**(8): p. 171-176.
243. Yoshida, T., et al., *A covalent small molecule inhibitor of glutamate-oxaloacetate transaminase 1 impairs pancreatic cancer growth*. Biochemical and Biophysical Research Communications, 2020. **522**(3): p. 633-638.
244. Zhou, X., et al., *Inhibition of glutamate oxaloacetate transaminase 1 in cancer cell lines results in altered metabolism with increased dependency of glucose*. BMC Cancer, 2018. **18**(1): p. 559.
245. Simon, T.C., K.A. Roth, and J.I. Gordon, *Use of transgenic mice to map cis-acting elements in the liver fatty acid-binding protein gene (Fabpl) that regulate its cell lineage-specific, differentiation-dependent, and spatial patterns of expression in the gut epithelium and in the liver acinus*. J Biol Chem, 1993. **268**(24): p. 18345-58.
246. Clarke, D.C., et al., *Overexpression of membrane-associated fatty acid binding protein (FABPpm) in vivo increases fatty acid sarcolemmal transport and metabolism*. Physiol Genomics, 2004. **17**(1): p. 31-7.
247. Lehner, R. and A.D. Quiroga, *Chapter 5 - Fatty Acid Handling in Mammalian Cells*, in *Biochemistry of Lipids, Lipoproteins and Membranes (Sixth Edition)*, N.D. Ridgway and R.S. McLeod, Editors. 2016, Elsevier: Boston. p. 149-184.

248. Chabowski, A., et al., *Evidence for concerted action of FAT/CD36 and FABPpm to increase fatty acid transport across the plasma membrane*. Prostaglandins, Leukotrienes and Essential Fatty Acids, 2007. **77**(5): p. 345-353.
249. Engle, D.D., et al., *The glycan CA19-9 promotes pancreatitis and pancreatic cancer in mice*. Science, 2019. **364**(6446): p. 1156-1162.
250. Gruner, B.M., et al., *An in vivo multiplexed small-molecule screening platform*. Nat Methods, 2016. **13**(10): p. 883-889.
251. Farrell, A.S., et al., *MYC regulates ductal-neuroendocrine lineage plasticity in pancreatic ductal adenocarcinoma associated with poor outcome and chemoresistance*. Nat Commun, 2017. **8**(1): p. 1728.
252. Feist, M., et al., *Cooperative STAT/NF- $\kappa$ B signaling regulates lymphoma metabolic reprogramming and aberrant GOT2 expression*. Nature Communications, 2018. **9**(1): p. 1514.
253. Yang, S., et al., *Mitochondrial glutamine metabolism via GOT2 supports pancreatic cancer growth through senescence inhibition*. Cell Death Dis, 2018. **9**(2).
254. Reka, A.K., et al., *Peroxisome proliferator-activated receptor-gamma activation inhibits tumor metastasis by antagonizing Smad3-mediated epithelial-mesenchymal transition*. Mol Cancer Ther, 2010. **9**(12): p. 3221-32.
255. Jiang, X., et al., *Recombinant expression, purification and crystallographic studies of the mature form of human mitochondrial aspartate aminotransferase*. BioScience Trends, 2016. **10**(1): p. 79-84.
256. Bradbury, M.W., et al., *Molecular Modeling and Functional Confirmation of a Predicted Fatty Acid Binding Site of Mitochondrial Aspartate Aminotransferase*. Journal of Molecular Biology, 2011. **412**(3): p. 412-422.
257. Amiri, M., et al., *Diverse roles of fatty acid binding proteins (FABPs) in development and pathogenesis of cancers*. Gene, 2018. **676**: p. 171-183.
258. Falomir-Lockhart, L.J., et al., *Fatty Acid Signaling Mechanisms in Neural Cells: Fatty Acid Receptors*. Frontiers in Cellular Neuroscience, 2019. **13**(162).
259. Chiou, S.-H., et al., *BLIMP1 Induces Transient Metastatic Heterogeneity in Pancreatic Cancer*. Cancer Discovery, 2017. **7**(10): p. 1184-1199.
260. Wang, T., et al., *Acetyl-CoA from inflammation-induced fatty acids oxidation promotes hepatic malate-aspartate shuttle activity and glycolysis*. Am J Physiol Endocrinol Metab, 2018. **315**(4): p. E496-e510.
261. Waddington, K.E., et al., *Activation of the liver X receptors alters CD4<sup>+</sup> T cell membrane lipids and signalling through direct regulation of glycosphingolipid synthesis*. bioRxiv, 2019: p. 721050.

262. Esteves, A., et al., *Fatty acid binding proteins have the potential to channel dietary fatty acids into enterocyte nuclei*. J Lipid Res, 2016. **57**(2): p. 219-32.
263. Ishibashi, M., et al., *Liver x receptor regulates arachidonic acid distribution and eicosanoid release in human macrophages: a key role for lysophosphatidylcholine acyltransferase 3*. Arterioscler Thromb Vasc Biol, 2013. **33**(6): p. 1171-9.
264. Levi, L., et al., *Saturated fatty acids regulate retinoic acid signalling and suppress tumorigenesis by targeting fatty acid-binding protein 5*. Nat Commun, 2015. **6**: p. 8794.
265. Armstrong, E.H., et al., *Structural basis for ligand regulation of the fatty acid-binding protein 5, peroxisome proliferator-activated receptor  $\beta/\delta$  (FABP5-PPAR $\beta/\delta$ ) signaling pathway*. J Biol Chem, 2014. **289**(21): p. 14941-54.
266. Olivares, O., et al., *Collagen-derived proline promotes pancreatic ductal adenocarcinoma cell survival under nutrient limited conditions*. Nat Commun, 2017. **8**.
267. Valle, S., et al., *The Ever-Evolving Concept of the Cancer Stem Cell in Pancreatic Cancer*. Cancers (Basel), 2018. **10**(2).
268. Li, J.T., et al., *Metabolism remodeling in pancreatic ductal adenocarcinoma*. Cell Stress. **3**(12): p. 361-8.
269. Chang, H.H. and G. Eibl, *Obesity-Induced Adipose Tissue Inflammation as a Strong Promotional Factor for Pancreatic Ductal Adenocarcinoma*. Cells, 2019. **8**(7).
270. Cascetta, P., et al., *Pancreatic Cancer and Obesity: Molecular Mechanisms of Cell Transformation and Chemoresistance*. Int J Mol Sci, 2018. **19**(11).
271. Li, N., et al., *Hypoxia Inducible Factor 1 (HIF-1) Recruits Macrophage to Activate Pancreatic Stellate Cells in Pancreatic Ductal Adenocarcinoma*. Int J Mol Sci, 2016. **17**(6).
272. Bechard, M.E., et al., *Pentose conversions support the tumorigenesis of pancreatic cancer distant metastases*. Oncogene, 2018. **37**(38): p. 5248-56.
273. Clark, C.E., G.L. Beatty, and R.H. Vonderheide, *Immunosurveillance of pancreatic adenocarcinoma: insights from genetically engineered mouse models of cancer*. Cancer Lett, 2009. **279**(1): p. 1-7.
274. Narkar, V.A., et al., *AMPK and PPARdelta agonists are exercise mimetics*. Cell, 2008. **134**(3): p. 405-15.
275. Evans, R.A., et al., *Lack of immunoediting in murine pancreatic cancer reversed with neoantigen*. JCI Insight, 2016. **1**(14).
276. Lawrence, J.W., D.J. Kroll, and P.I. Eacho, *Ligand-dependent interaction of hepatic fatty acid-binding protein with the nucleus*. J Lipid Res, 2000. **41**(9): p. 1390-401.

277. Wang, D., et al., *Peroxisome proliferator-activated receptor  $\delta$  promotes colonic inflammation and tumor growth*. Proceedings of the National Academy of Sciences, 2014. **111**(19): p. 7084.
278. Pollock, C.B., et al., *Induction of metastatic gastric cancer by peroxisome proliferator-activated receptor $\delta$  activation*. PPAR research, 2010. **2010**: p. 571783.
279. Adhikary, T., et al., *Genomewide analyses define different modes of transcriptional regulation by peroxisome proliferator-activated receptor- $\beta/\delta$  (PPAR $\beta/\delta$ )*. PloS one, 2011. **6**(1): p. e16344-e16344.
280. Zhang, Y., et al., *Prognostic significance and therapeutic implications of peroxisome proliferator-activated receptor  $\gamma$  overexpression in human pancreatic carcinoma*. Int J Oncol, 2015. **46**(1): p. 175-84.
281. Koga, H., et al., *PPAR $\gamma$  potentiates anticancer effects of gemcitabine on human pancreatic cancer cells*. Int J Oncol, 2012. **40**(3): p. 679-85.
282. Rahn, S., et al., *Inflammation Associated Pancreatic Tumorigenesis: Upregulation of Succinate Dehydrogenase (Subunit B) Reduces Cell Growth of Pancreatic Ductal Epithelial Cells*. Cancers (Basel), 2020. **12**(1).
283. Eibl, G. and E. Rozengurt, *KRAS, YAP, and obesity in pancreatic cancer: a signaling network with multiple loops*. Semin Cancer Biol, 2019. **54**: p. 50-62.
284. Park, B.H., B. Vogelstein, and K.W. Kinzler, *Genetic disruption of PPARdelta decreases the tumorigenicity of human colon cancer cells*. Proc Natl Acad Sci U S A, 2001. **98**(5): p. 2598-603.
285. Brown, R.A., et al., *The Role of PPARd in Alloreactive CD8 T cell Metabolism*. The Journal of Immunology, 2020. **204**(1 Supplement): p. 87.5.
286. Gajewski, T.F., et al., *Cancer Immunotherapy Targets Based on Understanding the T Cell-Inflamed Versus Non-T Cell-Inflamed Tumor Microenvironment*. Adv Exp Med Biol, 2017. **1036**: p. 19-31.
287. Spear, S., et al., *Discrepancies in the Tumor Microenvironment of Spontaneous and Orthotopic Murine Models of Pancreatic Cancer Uncover a New Immunostimulatory Phenotype for B Cells*. Front Immunol, 2019. **10**.
288. Lee, B. and P. Gibbs, *Inflammation, Biomarkers and Immuno-Oncology Pathways in Pancreatic Cancer*. J Pers Med, 2019. **9**(2).
289. Liou, G.Y., *Inflammatory Cytokine Signaling during Development of Pancreatic and Prostate Cancers*. J Immunol Res, 2017. **2017**.
290. Lengqvist, J., et al., *Polyunsaturated Fatty Acids Including Docosahexaenoic and Arachidonic Acid Bind to the Retinoid X Receptor Ligand-binding Domain*. Molecular & cellular proteomics : MCP, 2004. **3**: p. 692-703.

291. Carpenter, K.J., et al., *Pharmacologic inhibition of liver X receptors enhances T cell anti-tumor function in triple negative breast cancer*. The Journal of Immunology, 2019. **202**(1 Supplement): p. 137.7.
292. Brash, A.R., *Arachidonic acid as a bioactive molecule*. The Journal of Clinical Investigation, 2001. **107**(11): p. 1339-1345.
293. Sum, C.S., et al., *Identification of residues important for agonist recognition and activation in GPR40*. J Biol Chem, 2007. **282**(40): p. 29248-55.
294. Petrusel, L., et al., *Relationship between cachexia and perineural invasion in pancreatic adenocarcinoma*. World J Gastrointest Oncol, 2019. **11**(12): p. 1126-40.
295. Zhong, X., et al., *The systemic activin response to pancreatic cancer: implications for effective cancer cachexia therapy*. J Cachexia Sarcopenia Muscle, 2019. **10**(5): p. 1083-101.
296. Fang, X., et al., *20-carboxy-arachidonic acid is a dual activator of peroxisome proliferator-activated receptors alpha and gamma*. Prostaglandins Other Lipid Mediat, 2007. **82**(1-4): p. 175-84.
297. Chowdhury, P.S., et al., *PPAR-Induced Fatty Acid Oxidation in T Cells Increases the Number of Tumor-Reactive CD8(+) T Cells and Facilitates Anti-PD-1 Therapy*. Cancer Immunol Res, 2018. **6**(11): p. 1375-1387.
298. Lim, J.C.W., et al., *The Role of PPAR $\beta/\delta$  in Melanoma Metastasis*. International journal of molecular sciences, 2018. **19**(10): p. 2860.
299. Kesanakurti, D., et al., *A novel interaction of PAK4 with PPAR $\gamma$  to regulate Nox1 and radiation-induced epithelial-to-mesenchymal transition in glioma*. Oncogene, 2017. **36**(37): p. 5309-5320.
300. Rohm, M., et al., *Energy metabolism in cachexia*. EMBO reports, 2019. **20**(4): p. e47258.
301. Fuster, G., et al., *Are Peroxisome Proliferator-Activated Receptors Involved in Skeletal Muscle Wasting during Experimental Cancer Cachexia? Role of  $\beta$ -Adrenergic Agonists*. Cancer Research, 2007. **67**(13): p. 6512.
302. Choi, E., et al., *Abstract 2184: BOXR1030: A first-in-class CAR T-cell therapy co-expressing GOT2 enhances T-cell metabolic function for the treatment of GPC3-positive solid tumors*. Cancer Research, 2020. **80**(16 Supplement): p. 2184.
303. Le Bourgeois, T., et al., *Targeting T Cell Metabolism for Improvement of Cancer Immunotherapy*. Frontiers in Oncology, 2018. **8**(237).
304. Shyer, J.A., R.A. Flavell, and W. Bailis, *Metabolic signaling in T cells*. Cell Research, 2020. **30**(8): p. 649-659.



## **Appendices:**

**Hannah Sanford-Crane, Jaime Abrego, Mara Sherman.** *Fibroblasts as modulators of local and systemic cancer metabolism.* *Cancers* 11(5), 619, 2019.

### **Abstract:**

Fibroblast activation is an accompanying feature of solid tumor progression, resembling a conserved host response to tissue damage. Cancer-associated fibroblasts (CAFs) comprise a heterogeneous and plastic population with increasingly appreciated roles in tumor growth, metastatic capacity, and response to therapy. Classical features of fibroblasts in a wound-healing response, including profound extracellular matrix production and cytokine release, are recapitulated in cancer. Emerging evidence suggests that fibroblastic cells in the microenvironments of solid tumors also critically modulate cellular metabolism in the neoplastic compartment through mechanisms including paracrine transfer of metabolites or non-cell-autonomous regulation of metabolic signaling pathways. These metabolic functions may represent common mechanisms by which fibroblasts stimulate growth of the regenerating epithelium during a wound-healing reaction, or may reflect unique co-evolution of cancer cells and surrounding stroma within the tumor microenvironment. Here we review the recent literature supporting an important role for CAFs in regulation of cancer cell metabolism, and relevant pathways that may serve as targets for therapeutic intervention.

**Keywords:** cancer metabolism; cancer-associated fibroblast; tumor-stroma crosstalk.

### **Personal contribution:**

HSC wrote the “wound-healing mediators as metabolic regulators” section and created figure 1.

### **Introduction:**

The increasingly appreciated role of activated fibroblasts in cancer progression and response to therapy [1] has prompted investigation of growth-permissive fibroblast functions in cancer. Cancer-associated fibroblasts (CAFs) derived from activated resident fibroblast pools or from mesenchymal progenitors recruited to the tumor microenvironment [2,3,4] have displayed diverse pro-tumorigenic functions that cooperate with cell-autonomous mechanisms to promote the hallmarks of cancer [5]. While CAF functional diversity is increasingly appreciated across tissue sites [6,7,8] and precise functions may vary in a tissue-specific manner, CAFs have conserved and well-documented roles in establishing key components of a wound-healing reaction in solid tumor tissues. While fibroblastic cells evolved to play roles in tissue homeostasis and wound healing, CAFs reflect both the classical role of fibroblasts in tissue biology and unique roles resulting from co-evolution with neoplastic growths. CAFs are typically abundant in solid tumors [9], and are the principal producers of extracellular matrix (ECM) components and remodeling enzymes [10]. In addition, CAFs secrete numerous signaling proteins including mitogenic growth factors that can stimulate proliferation in the epithelial compartment [1], as well as pro-inflammatory mediators that can modulate intratumoral immune infiltration [7,11,12,13]. These established CAF functions resemble those of activated fibroblasts to support regeneration and repair. More recently, however, evidence has emerged to support a critical role for CAFs as regulators of critical metabolic processes in cancer [14]. These metabolic roles may be specific to fibroblastic cells in tumor microenvironments, as adaptive mechanisms to support the metabolic demands of rapidly proliferating cancer cells. Supporting this connection, recent analysis of

metabolic networks in human breast cancer in situ showed significant correlation of intracellular metabolic states of cancer cells and adjacent CAFs [15], and mechanistic studies are beginning to uncover the importance of this bioenergetic coupling of tumor and stroma. Below, we discuss the emerging roles of CAFs in regulation of cellular and organismal metabolism in cancer.

### **Wound-Healing Mediators as Metabolic Regulators**

As critical regulators of the wound-healing reaction, activated fibroblasts are key producers of soluble secreted factors such as cytokines, growth factors, and ECM components that orchestrate wounding-associated inflammation, regeneration, and tissue repair. CAFs similarly produce classical wound-healing mediators, and emerging evidence suggests that beyond their long-appreciated roles in repair processes, these factors also regulate metabolic functions of neighboring cancer cells. Among solid tumors, pancreatic ductal adenocarcinoma (PDAC) has a particularly prominent stromal compartment, characterized in part by a prominent CAF population and a dense, collagen-rich ECM [16]. This ECM has been shown to restrict vascular perfusion in the PDAC tumor microenvironment (TME) [17,18], and perhaps due to low serum availability, the PDAC milieu is nutrient-poor [19]. Under conditions of low nutrients, mutant KRAS, a main oncogene of PDAC, is able to drive macropinocytosis as a source of amino acids from extracellular proteins for the cancer cells [20]. Recent work has shown that the abundant, CAF-derived collagen in the PDAC ECM can serve as an extracellular protein source, and one particularly rich in prolines (25% of the amino acids in collagen) [21]. PDAC cells can take up collagen fragments, through macropinocytosis-dependent and -independent mechanisms, and subsequently metabolize proline via proline oxidase (POX/PRODH1) to fuel the TCA cycle and promote proliferation and survival under nutrient-restricted conditions in vitro or during tumor growth in vivo. Consistent with this study, soluble CAF-derived proteins together with 3D type I collagen induce transcriptional and metabolic alterations in PDAC cells supporting anabolic programs, which overlaps significantly with networks regulated by oncogenic KRAS and suggests points of convergence between cell-intrinsic and microenvironmental mechanisms that regulate cancer cell metabolism [22]. CAF-derived cytokines including CCL5, IL6, and CXCL10 can also regulate cancer cell metabolism by promoting phosphorylation of phosphoglucomutase 1 and increasing glycogen mobilization in cancer cells, promoting NADPH synthesis and the TCA cycle and thus enabling cancer cell proliferation and metastatic spread of ovarian cancer cells [23] (Figure 1).

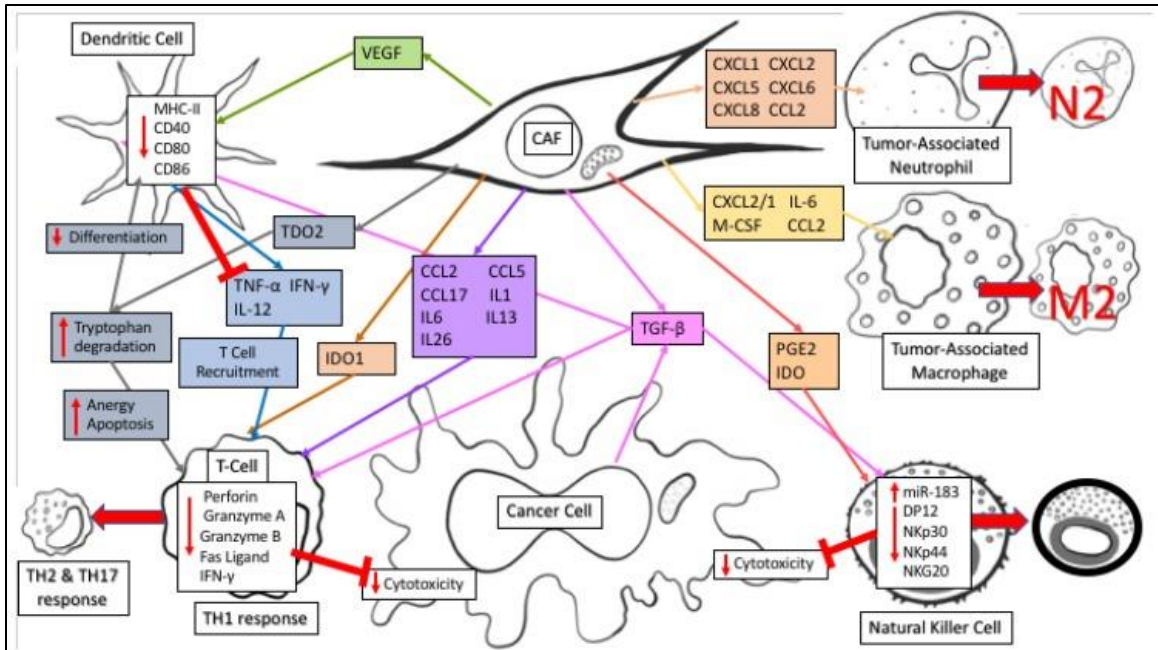


**Figure 1**

CAF secretions of immunomodulatory factors regulate anti-tumor immune response. CAF secretion of CXCL12/SDF1, M-CSF/CSF-1, IL-6, and CCL2/MCP-1 recruits tumor-associated macrophages to the TME and helps differentiate them to an M2 Immunosuppressive phenotype. CXCL1, CXCL2, CXCL5, CXCL6, CXCL8, and CCL2 recruits tumor-associated neutrophils and polarizes them to an N2 pro-tumoral phenotype. CAF and cancer cell secretion of TGF- $\beta$  induces miR-183 to inhibit DAP12 transcription and reduce natural killer (NK) activating receptors (NKp30, NKp44, NKG2D), while PGE2 and IDO secretion decreases NK cell cytotoxicity against cancer cells. TGF- $\beta$  also promotes cell death of CD8+ T cells by inhibiting expression of Bcl-2 and causes dendritic cells (DC) to downregulate expression of MHC class II, CD40, CD80, and CD86 leading to decreased antigen presentation efficiency along with decreased production of TNF- $\alpha$ , IFN- $\gamma$ , and IL-12. TDO2 and IDO1 secretion promotes tryptophan metabolism to kynurenines (Kyn), inhibiting DC differentiation and damages T cell response by catabolizing tryptophan degradation into Kyn, causing T cell anergy and apoptosis through depletion of tryptophan and accumulation of immunosuppressive tryptophan catabolites. VEGF secretion inhibits DC generation and maturation by reducing MHC class II expression and antigen presenting abilities. Secretion of CCL2, CCL5, and CCL17 along with polarizing cytokines IL-1, IL-6, IL-13, and IL-26 switch CD4+ helper T lymphocytes from an anti-tumor TH1 response to a pro-tumor TH2 and TH17 response.

Beyond uptake, ECM components produced by CAFs also regulate cancer cell metabolism via activation of diverse signaling mechanisms. In addition to collagens, CAFs also produce and secrete high levels of hyaluronan (HA), as well as enzymes that break down and remodel the ECM. A recent study demonstrated that HA fragments can signal through receptor tyrosine kinases to induce ZFP36, causing degradation of TXNIP transcripts and subsequently blocking TXNIP-mediated internalization of glucose transporter GLUT1 [24]. This leads to an increase of GLUT1 transporter on the plasma membrane, increasing the amount of glucose transport, and inducing glycolysis within the cancer cell. ECM signals act on TXNIP for acute and protracted

regulation of glucose uptake, showing that external cues can regulate cellular metabolism and migration. Increased ECM stiffness during tumor progression and downstream mechanosensing induces CAFs to release aspartate, supporting cancer cell proliferation, while cancer cells in turn secrete glutamate and balance the redox state of CAFs to further promote ECM remodeling [25]. A stiff ECM mechanoactivates the YAP/TAZ pathway which plays a central role in cell proliferation, survival, and polarity, especially in tumor cells. Mechanostimuli of the ECM is thus linked to tumor cell metabolism, while tumor cell metabolism is linked to responses by the CAFs to increase ECM stiffness, resulting in a positive feedback between CAFs and cancer cells. While ECM stiffness and poor perfusion can reduce drug delivery and promote chemoresistance, CAFs can also promote chemoresistance through the release of glutathione and cysteine [26]. Glutathione and cysteine are released by CAFs leading to increased GSH levels in cancer cells, and to a reduction of platinum accumulation in cells treated with platinum-based therapies. Interestingly, CD8 T cells reverse this chemoresistance mechanism through release of interferon-gamma, which causes upregulation of gamma-glutamyltransferase activity in CAFs and to transcriptional repression of system xc<sup>-</sup> cystine and glutamate antiporter via JAK/STAT signaling.

CAFs regulate the anti-tumor immune response through secretion of numerous immunomodulatory factors (reviewed in reference [27]). Fibroblasts secrete similar factors as part of the wound-healing response to recruit immune factors to an injury, however during cancer progression CAF secreted factors generally have an immune-suppressive function. The immune cells regulated by CAFs can in turn impact cancer cell metabolism, highlighting the complexity of metabolic regulation within an intact TME. CAF secretion of CXCL12/SDF1, M-CSF/CSF-1, IL-6, and CCL2/MCP-1 recruits tumor-associated macrophages (TAM) to the TME and actively differentiates TAMs into an M2 immunosuppressive phenotype. In addition, CAF secretion of CXCL1, CXCL2, CXCL5, CXCL6, CXCL8, and CCL2 recruits tumor-associated neutrophils (TANs) to the TME and polarizes them to an N2 pro-tumoral phenotype. TGF- $\beta$ , secreted by CAFs, induces miR-183 to inhibit DAP12 transcription and results in reduced natural killer (NK) activating receptors (NKp30, NKp44, NKG2D) on the NK cell surface. Along with its impact on NK cells, TGF- $\beta$  also causes dendritic cells (DC) to downregulate MHC class II expression, along with CD40, CD80, and CD86 leading to decreased antigen presentation efficiency and decreased production of TNF- $\alpha$ , IFN- $\gamma$ , and IL-12, ultimately causing a reduction in T cell recruitment and survival in the TME. PGE2 and IDO secretion by CAFs affects NK cells by decreasing their cytotoxicity against cancer cells [28]. In lung cancer, TDO2 secretion by CAFs promotes tryptophan metabolism to kynurenes (Kyn), inhibiting DC differentiation while VEGF secretion inhibits DC generation and maturation by reducing MHC class II expression and antigen presenting abilities [29]. TGF- $\beta$  promotes cell death of CD8<sup>+</sup> T cells by inhibiting expression of the pro-survival factor Bcl-2. IDO1 secretion further damages T cell response by catabolizing tryptophan degradation into Kyn, creating an immunosuppressive TME and causing T cell energy and apoptosis through depletion of tryptophan combined with an accumulation of immunosuppressive tryptophan catabolites. CD4<sup>+</sup> helper T lymphocytes react to CAF secretion of CCL2, CCL5, and CCL17 along with polarizing cytokines IL-1, IL-6, IL-13, and IL-26 by switching from an anti-tumor T<sub>H</sub>1 response to a pro-tumor T<sub>H</sub>2 and T<sub>H</sub>17 response. CAFs secrete immunomodulatory factors that regulate the immune response within the tumor niche by creating an immunosuppressive environment which decreases the antigen presenting capabilities of NKs and DCs while simultaneously decreasing cytotoxicity and survival of T cells. Together, these immunomodulatory functions of CAFs can profoundly impact cancer metabolism, and regulate cancer progression through both immune effector and metabolic mechanisms.

Aging adds another variable to the impact of the TME on cancer development. The effect of age on the TME is so significant that genetically identical cells can have varying metastasis levels and therapy response based on whether they are in an aged TME or young TME, suggesting that the aged TME is capable of profoundly influencing cancer cell behavior [30]. Indeed, aged fibroblasts secrete sFRP2, a Wnt antagonist, which causes a downstream cascade of signals and subsequent loss of  $\beta$ -catenin and MITF, as well as redox effector APE1. This loss of APE1 makes melanoma cells less responsive to ROS-induced DNA damage and causes an increase in targeted therapy resistance. sFRP2-induced  $\beta$ -catenin loss promotes invasion and causes increases in ROS, which has been linked to BRAF inhibitor resistance, suggesting that aged patients could benefit from anti-oxidant therapy more than younger patients. The TME is a complicated, unique aspect of cancer which warrants consideration for personalized oncology wherein age, genetics, and tumor mutational load are combined to generate the ideal cancer treatment plan. While much previous research into cancer has focused on genetic modifications and oncogenes, such as KRAS, it has become increasingly clear that a dynamic ECM and TME co-evolving with tumor cells may have a profound effect on proliferation, immune evasion, and metastasis together with the underlying genetic mutations which support tumor initiation. Though tissue-specific aspects of CAF-cancer cell interaction have been reported, other tumor-stroma effects are seen across cancer types and relate to conserved features of a wound-healing response, suggesting a potential avenue for stroma-directed and broadly applicable anticancer therapies.

### **A Role for Fibroblast-Derived Metabolites in Tumor-Stroma Interaction**

Upon activation, quiescent fibroblasts undergo transcriptomic and metabolic programming that mimics the “Warburg Effect” metabolic phenotype, which is further exaggerated in the hypoxic TME [1,31,32] (Figure 2). The hypoxia response is a universally conserved response to insufficient oxygen availability wherein the hypoxia-inducible factor (HIF) complex is stabilized and transported to hypoxia response element (HRE) promoter sequences to engage in transcription of over 100 genes, many of which are directly involved in increasing anaerobic glycolysis rate [33]. Competition for glucose between CAFs and cancer cells seems counterproductive for tumorigenesis. Instead there are several lines of evidence suggesting metabolic reprogramming to coordinate glucose and lactate metabolism in the TME. Metabolic tracing experiments have shown that well-oxygenated cancer cells support high glycolysis rate of cells in hypoxia by increasing lactate uptake [34,35]. This is further validated by differential expression of monocarboxylate transporters (MCT) with cells experiencing hypoxia increasing MCT4 levels, lactate efflux, and cells in normoxia increasing MCT1 for lactate import [34,35]. In the context of tumor metabolism, this phenomenon has been dubbed as the “Reverse Warburg Effect,” from the perspective of cancer cells reacting to metabolic reprogramming in CAFs [36]. This observation was first made in genetic analyses of breast cancer CAFs that exhibited low caveolin-1 (CAV1) expression [37]. Upon knockout of CAV1, fibroblasts gained myofibroblastic markers and increased rate of aerobic glycolysis [37]. Further analysis demonstrated that the metabolic program of CAFs in breast cancer is supported by cancer cells’ increased lactate uptake to support their own bioenergetic needs [37,38]. The same metabolic reprogramming has been shown in prostate cancer CAFs upon direct contact with cancer cells in co-culture studies [39]. The “Warburg Effect” in CAFs is also exhibited through classic fibroblast activators, TGF- $\beta$  and PDGF, which have been shown to downregulate isocitrate dehydrogenase (IDH) expression resulting in decreased of cellular levels of  $\alpha$ -ketoglutarate ( $\alpha$ -KG), due to impaired isocitrate to  $\alpha$ -KG conversion [40].  $\alpha$ -KG and oxygen are critical co-factors for PHD enzymes, which negatively regulate stability of glycolysis master regulator HIF1 $\alpha$  by promoting its ubiquitin-mediated

proteasome degradation in normoxia [40,41]. Moreover, TGF- $\beta$  signaling in CAFs has been shown to trigger increased oxidative stress, autophagy/mitophagy, and aerobic glycolysis—all known factors enhancing HIF1 $\alpha$  stability [42,43]. The “Reverse Warburg Effect” does not reflect all metabolic crosstalk across fibrotic tumors as evidenced by studies in breast and pancreatic cancer showing CAFs increasing lactate uptake and re-purposing it for bioenergetics [44,45]. In turn, clearance of lactate by CAFs enhances higher glycolysis rate in cancer cells. It is not clear why well-oxygenated cancer cells will switch to lactate in preference of glucose, but these observations showing the “Reverse Warburg Effect” seem to conform with the concept of metabolic symbiosis required for tumor progression wherein CAFs’ ability to support cancer cell metabolism through glycolysis byproducts is necessary for tumor formation.

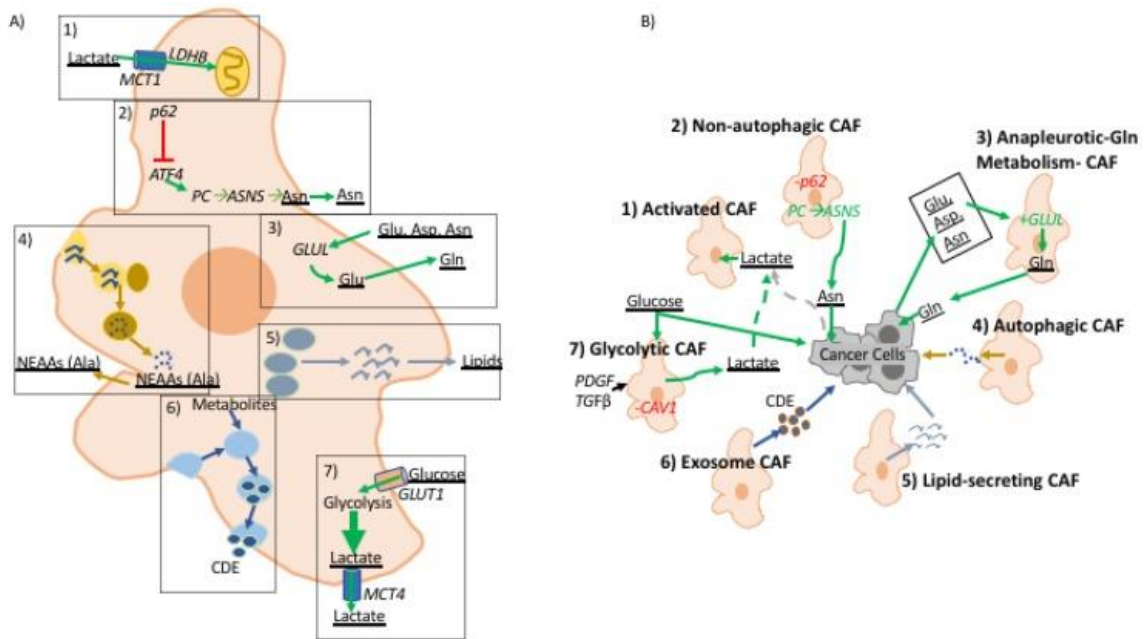


**Figure 2**

*A role for fibroblast-derived metabolites in tumor-stroma interactions. (A) illustrates metabolic reprogramming in CAFs and (B) illustrates the effect of metabolites derived from CAFs to cancer cells in the TME. (1) Activated CAFs uptake excess TME lactate produced by glycolytic cells in the TME. (2) p62 deficient CAFs are autophagy defective and have upregulation of ATF4 which activates metabolic flux through pyruvate carboxylase (PC) → asparagine synthase (ASNS) pathway producing asparagine that is consumed by cancer cells. (3) CAFs characterized by upregulation of anapleurotic glutamine metabolism where cancer cell-derived aspartate, asparagine, and glutamate are used to generate glutamate that is fed to cancer cells; glutamine amino ligase (GLUL) is overexpressed in these CAFs. (4) Cancer cells induce autophagy in CAFs increasing turnover of non-essential amino acids, alanine has been shown to be up-taken by cancer cells to support growth. (5) Upon activation pancreatic and hepatic CAFs shift from lipid storing to lipid-secreting wherein CAF-derived lipids support proliferation and migratory potential of cancer cells. (6) Exosome releasing CAFs pack metabolic molecules used by cancer cells. (7) CAV1 deficient CAFs are known to upregulate glycolytic metabolism, as well as, fibroblast activation by PDGF and TGF $\beta$ . (A) describes metabolic alterations in CAFs in dashed*

*boxes. In both figures metabolic pathways are denoted with green arrows, cellular processes are assigned specific colors, and metabolic molecules are underlined.*

Upon malignant transformation, cancer cells become increasingly dependent on an exogenous supply of amino acids, especially glutamine, the most abundant amino acid in plasma [46]. In ovarian cancer, CAFs have been shown to harness carbon and nitrogen from aspartate, asparagine, and lactate to generate glutamine [47]. Thus, through upregulation of anapleurotic glutamine metabolism CAFs are able to support glutamine-addicted cancer cells in the glutamine-starved TME. This relationship was shown by blocking expression of glutamate ammonia ligase, thereby impairing CAF ability to provide glutamine to cancer cells, which hindered tumor growth [47]. A similar effect was achieved by blocking glutamine catabolism through genetic ablation of glutamate synthase. Combining the effects of inhibiting glutamine synthesis in CAFs and glutamine catabolism in cancer cells prevented formation and metastasis of ovarian cancer. In the nutrient-poor PDAC TME, alanine derived from autophagic CAFs is utilized by pancreatic cancer cells as a carbon source to fuel bioenergetic and biosynthetic processes, compensating for low levels of glucose/glutamine in the TME [44]. Moreover, through the provision of alanine, CAFs further enhance carcinogenesis by allowing cancer cells to fuel TCA cycle, support lipid and NEAA synthesis, as well as diverting glucose metabolism to serine and glycine synthesis both of which are essential for cancer cell survival [44,48]. In contrast to autophagy activation in pancreatic cancer, genetic analyses of prostate and liver tumor stroma shows a decrease of autophagy substrate signaling adaptor protein, p62, resulting in defective autophagy [49,50]. p62 depletion increases expression of ATF4, targeted for ubiquitin-mediated proteasomal degradation in normal fibroblasts with normal expression of p62 [51]. ATF4-positive CAFs support neoplastic cell growth in low glutamine conditions through activation of the pyruvate carboxylase-asparagine synthase pathway [51]. In this instance, CAF-derived asparagine supports cancer cells bioenergetics and nitrogen needs in the glutamine-poor TME. These studies reveal the significance of CAFs as regulators of TME metabolism by providing glutamine and amino acids that serve as intermediates to glutamine metabolic pathways, supporting tumor establishment and metastasis.

One of the challenges in understanding the role of CAFs in carcinogenesis is the fact that fibroblasts are found in most tissues, yet they remain poorly characterized. Interestingly, a well-known feature of particular pancreatic fibroblasts and hepatic fibroblasts, known as pancreatic and hepatic stellate cells, is their ability to store lipids in their quiescent phenotype [52]. Upon activation and during carcinogenesis, stellate cells lose their ability to store lipids, but the relevance of stromal lipid metabolism in cancer remains poorly understood. Interestingly, metabolomic studies of KRAS mutant cells experiencing hypoxia demonstrate inability to undergo de novo lipogenesis and instead show more reliance on lipid scavenging, suggesting a potential metabolic function of lipids secreted by activated fibroblasts [53]. Recently, work from our lab demonstrated that activated stellate cells secrete abundant lysophosphatidylcholines (LPC), the preferred fatty acid scavenging substrate for RAS-transformed cells, which can support PDAC cells growth both via uptake and biomass production and via hydrolysis by the secreted enzyme autotaxin to yield mitogenic lysophosphatidic acid (LPA) [54]. Reprogramming of lipid metabolism has also been demonstrated in prostate CAFs compared to normal prostate fibroblasts [55]. Prostate CAFs have elevated neutral lipid storage, and these lipid stores cooperate with pigment epithelium-derived growth factor to amplify microtubule-organizing centers. Further roles of CAF lipid secretion remain to be elucidated as several lines of evidence suggest that exogenous lipids support auxotrophic cancer cell growth [56,57].

Another little-explored aspect of CAFs is exosome-mediated metabolic crosstalk. Recent studies have shown that exosomes carry proteins, nucleic acids, miRNAs, and metabolic molecules [58]. CAF-derived exosomes, CDEs, of prostate and pancreatic cancer have been shown to reprogram metabolism of cancer cells by significantly up-regulating glycolysis while down-regulating oxidative metabolism by promoting glutamine decarboxylation and at the same time generating metabolites for de novo lipogenesis [59]. Metabolomic analysis of CDE contents reveal that they carry lactate, acetate, and amino acids—shown to be taken by cancer cells through carbon tracing analyses. Interestingly, CDE metabolic reprogramming was shown to be independent of oncogenic KRAS in pancreatic cancer, thereby demonstrating CAFs' ability to reprogram and support cancer cell metabolism independent of oncogene activation. CDEs have been shown to enhance gemcitabine resistance in pancreatic cancer cells by enhancing proliferation and glycolysis [60]. The extent to which CDEs modulate the metabolism of cells in the TME remains to be further explored.

The TME is highly dynamic and the accessibility to oxygen and nutrients is never constant forcing cancer cells to reprogram their metabolism accordingly. The studies summarized in this section highlight the role CAFs play in sustaining tumor cell metabolism. Further studies are required to understand the way in which CAFs provide metabolic support to cancer cells in order to identify novel therapeutic avenues.

### **Fibroblasts as Determinants of Systemic Metabolism in Cancer**

Beyond metabolic dysregulation in its local tissue context, cancer is associated with metabolic alterations in the host [61]. Abnormal whole-body metabolic responses to cancer include cancer cachexia, a potentially lethal wasting syndrome driven by negative energy balance and associated with loss of adipose and muscle tissue [62]. Cachexia has been mechanistically linked to the inflammatory response to cancer, and particularly to elevated levels of systemic pro-inflammatory cytokines [63]. Cachexia is a common and early event in the pathogenesis of some cancer types, and evidence of tissue breakdown associated with cachexia may even be a biomarker of early tumorigenesis [64,65]. Though mechanisms driving cancer cachexia are complex and remain to be elucidated, early evidence has emerged that CAFs may play a role in tissue wasting, in part by mediating an inflammatory response and in part through direct interactions with relevant host tissues. Fibroblast activation protein- $\alpha$  (FAP $\alpha$ ) marks activated fibroblastic cells in tumors [66] and other pathologic inflammatory conditions, including atherosclerosis [67]. FAP $\alpha$ -positive cells in the primary tumor microenvironment have been associated with immune suppression, promoting T cell exclusion via secretion of CXCL12 [68]. However, recent work using a FAP $\alpha$  reporter in mice showed that these FAP $\alpha$ -expressing fibroblastic cells can be found in numerous tissues in the adult mouse, including skeletal muscle [69]. FAP $\alpha$ -positive cells across tissue contexts have similar transcriptomes, suggesting a common lineage. Depletion of FAP $\alpha$ -positive cells in healthy mice caused a cachexia-like syndrome, characterized by rapid weight loss and reduced muscle mass despite adequate food intake. FAP $\alpha$ -positive fibroblasts in skeletal muscle were shown to be the predominant source of Lama2 and Follistatin (Fst288 and Fst315), key regulators of myofiber thickness and muscle growth. Thus, loss of FAP $\alpha$ -positive fibroblasts from skeletal muscle was proposed to play a causal role in the muscle-wasting aspect of cachexia. Strikingly, the authors observed significant loss of FAP $\alpha$ -positive cells from skeletal muscle in cachectic tumor models. These findings implicate fibroblastic cells in maintenance of muscle mass, and raise the possibility that fibroblast loss from skeletal muscle promotes the muscle wasting observed in cancer cachexia, with major implications for systemic metabolism.

The host metabolic perturbations associated with cancer progression have been partly attributed to increased systemic levels of pro-inflammatory cytokines [63]. IL6 in particular has been functionally linked to cachexia [70,71,72,73,74,75,76,77], and is elevated in patients with cachexia-associated cancers [78,79,80]. Further, activation of STAT3 downstream of IL6 has been linked to muscle wasting in cancer [81]. In multiple cancer types, CAFs are reported as a significant source of IL6 in the tumor microenvironment [7,82,83,84,85], highlighting CAF-derived IL6 as a potential link to cancer cachexia. Shining light on the role of IL6 in cancer cachexia, recent work demonstrated that the elevated IL6 in cachexia-associated tumor models suppresses hepatic ketogenesis, by downregulating expression of master ketogenic regulator PPAR $\alpha$  in the liver [70]. IL6 promoted metabolic stress in response to caloric restriction, including elevated corticosterone levels, and recombinant IL6 lowered fasting ketone and glucose levels. Interestingly, the increase in systemic glucocorticoids in response to IL6-mediated suppression of hepatic ketogenesis was associated with a suppression of anti-tumor immunity. Reduced food intake was a driver of the increase in glucocorticoids and immune suppression, and caloric deficiency is commonly seen among patients with cachexia-associated cancers. Notably, IL6 can also directly regulate the hypothalamic-pituitary-adrenal axis [86], and may further contribute to cachexia through its activity in the brain. While CAFs can function to locally suppress anti-tumor immunity, these findings raise the possibility that CAFs participate in a complex metabolic and inflammatory host response, leading to systemic elevation of glucocorticoids and immune suppression. The role of IL6 specifically derived from CAFs has yet to be tested in this axis.

While studies of the metabolic, immune-modulatory, or paracrine signaling functions of CAFs in various solid tumors suggest tumor-supportive roles for these cells, three papers published in 2014 demonstrated a protective role for CAFs in pancreatic cancer with respect to survival outcome [87,88,89]. To probe the roles of the abundant CAF population in these tumors, the authors used genetic or pharmacologic approaches to ablate CAFs during pancreatic tumorigenesis, either ablating Shh-dependent CAFs [87,89] or  $\alpha$ SMA-positive CAFs [88]. Though these different systems yielded somewhat different results, these studies together provide compelling evidence that CAF ablation causes mice to succumb significantly earlier to the disease compared to CAF-replete controls. Interestingly, in the study by Rhim et al. employing both genetic and pharmacologic inhibition of Shh to ablate CAFs, the authors report that mice succumb with very small tumors, but with severe cachexia, including wasting of adipose tissue and muscle exceeding that seen in controls. Data are shown from systemic Shh inhibition, but the authors report that the same phenotype was observed in their genetic model which specifically targets Shh in the pancreas, and therefore specifically inhibits Shh-dependent CAFs within the local tumor microenvironment. This raises the intriguing possibility that pancreatic CAFs promote improved survival outcomes in part by inhibiting pro-cachectic mechanisms within the primary tumor. A mechanistic connection between Shh-dependent CAF function and critical mediators of cancer cachexia has not been established. However, further investigation into this axis may be warranted, as therapies targeting pancreatic CAFs would ideally leave any such cachexia-suppressive mechanisms intact.

Likely related to their evolutionary role in the wound-healing response, CAFs are important sources of growth factors in the tumor microenvironment, as discussed above. In multiple solid tumor types, CAFs have been described as significant sources of growth factor ligands for the epidermal growth factor receptor (EGFR), including high-affinity ligands betacellulin (BTC) [90] and heparin-binding EGF-like growth factor (HB-EGF) [91] as well as lower-affinity ligand

epiregulin (EREG) [92]. CAFs and normal fibroblasts are also prominent producers of parathyroid hormone-related protein (PTHrP) [93,94], a developmental regulatory molecule activated by EGFR signaling [95]. A recent study aimed to identify novel regulators of cancer cachexia, and found a novel connection between factors that promote adipose tissue browning and the onset of features of cachexia including weight loss and muscle atrophy [96]. Cachexia is characterized in part by increased resting energy expenditure, which has been linked to increased thermogenesis by brown adipose tissue [97,98,99,100] and to browning of white adipose tissue [101]. Kir et al. found that Lewis lung carcinoma (LLC) cells induce adipose tissue browning and cachexia. By comparing gene expression in more thermogenic versus less thermogenic clones, they identified candidate paracrine thermogenic regulators. By testing candidate recombinant proteins, the authors found that the 3 EGFR ligands discussed above—BTC, HB-EGF, and EREG—as well as PTHrP all stimulate thermogenic gene expression in primary adipocytes. Though the study focused on cancer cell-derived PTHrP as a key regulator of adipose tissue browning in the LLC system, a link between EGFR ligand production and cancer cachexia is intriguing and warrants further study. Activation of EGFR/MEK signaling in the primary tumor has been recently linked to MEK activation and wasting in host tissues [102], and while CAFs as a source for these ligands or for PTHrP have not been specifically addressed, EGFR signaling has been functionally linked to cachexia and/or energy expenditure in additional systems [103,104]. Providing ligands which act either via tumor cells or directly on adipocytes to promote thermogenesis might suggest a deleterious role for CAFs as promoters of cancer cachexia, and such a role may indeed be tissue- and context-dependent.

### **Conclusions and Future Directions**

Non-malignant cells of the tumor microenvironment, including but not limited to CAFs, exert an important influence on key metabolic pathways in cancer cells and on intratumoral metabolite levels. The significance of these paracrine interactions warrants further study in vivo, as cancer cells exhibit specific and complex metabolic requirements within host tissues [105,106,107,108,109] that are difficult to model using in vitro systems. CAFs present a limitation in this regard, as specific Cre lines to achieve genetic manipulation in these cells are presently lacking. Further, while studies of metabolite exchange in vitro have established important modes of cell-cell contact within the tumor microenvironment, validation and further investigation of these interactions will be bolstered by emerging means to study intercellular metabolic relationships within tissues [15]. In considering CAF-cancer cell interactions as potential therapeutic targets, it will be important to understand the critical and non-redundant metabolic functions of CAFs that enable cancer cells to maintain their proliferative capacity within a nutrient-poor tumor microenvironment. As cancer cells exhibit metabolic plasticity [110,111], therapies targeting metabolism-modulating pathways will likely need to target parallel mechanisms fulfilling bioenergetic needs, or to combine metabolic inhibitors with therapeutic interventions that suppress cancer cell plasticity and thus the capacity for metabolic adaptation. Further, as suppression of anti-tumor immunity is increasingly linked to intratumoral metabolite levels and to activity of key metabolic pathways in immune cells [112], the consequence of the CAF secretome on the metabolism and function of immune cells in the tumor microenvironment warrants investigation.

### ***Acknowledgments:***

We thank Erin Helms and Kathrina Onate for their constructive input.

## ***Funding***

J.A. is supported by an OHSU Fellowship for Diversity in Research. M.H.S. is supported by NIH grants R00 CA188259 and R01 CA229580, American Cancer Society Research Scholar Grant 132898-RSG-18-142-01-CSM, V Foundation V Scholar Award, DOD Peer Reviewed Cancer Research Program Career Development Award W81XWH-18-1-0437, Hirshberg Foundation Seed Grant, Medical Research Foundation New Investigator Grant, OHSU Brenden-Colson Center Pilot Award, start-up funds from the OHSU Knight Cancer Institute, and an OHSU Cancer Early Detection Advanced Research Pilot Award.

## ***References:***

1. Kalluri R. The biology and function of fibroblasts in cancer. *Nat. Rev. Cancer.* 2016;16:582–598. doi: 10.1038/nrc.2016.73. [[PubMed](#)] [[CrossRef](#)] [[Google Scholar](#)]
2. Pietras K., Ostman A. Hallmarks of cancer: Interactions with the tumor stroma. *Exp. Cell Res.* 2010;316:1324–1331. doi: 10.1016/j.yexcr.2010.02.045. [[PubMed](#)] [[CrossRef](#)] [[Google Scholar](#)]
3. Hanahan D., Coussens L.M. Accessories to the crime: Functions of cells recruited to the tumor microenvironment. *Cancer Cell.* 2012;21:309–322. doi: 10.1016/j.ccr.2012.02.022. [[PubMed](#)] [[CrossRef](#)] [[Google Scholar](#)]
4. Paunescu V., Bojin F.M., Tatu C.A., Gavriluc O.I., Rosca A., Gruia A.T., Tanasie G., Bunu C., Crisnic D., Gherghiceanu M., et al. Tumour-associated fibroblasts and mesenchymal stem cells: More similarities than differences. *J. Cell. Mol. Med.* 2011;15:635–646. doi: 10.1111/j.1582-4934.2010.01044.x. [[PMC free article](#)] [[PubMed](#)] [[CrossRef](#)] [[Google Scholar](#)]
5. Hanahan D., Weinberg R.A. Hallmarks of cancer: The next generation. *Cell.* 2011;144:646–674. doi: 10.1016/j.cell.2011.02.013. [[PubMed](#)] [[CrossRef](#)] [[Google Scholar](#)]
6. Raz Y., Cohen N., Shani O., Bell R.E., Novitskiy S.V., Abramovitz L., Levy C., Milyavsky M., Leider-Trejo L., Moses H.L., et al. Bone marrow-derived fibroblasts are a functionally distinct stromal cell population in breast cancer. *J. Exp. Med.* 2018;215:3075–3093. doi: 10.1084/jem.20180818. [[PMC free article](#)] [[PubMed](#)] [[CrossRef](#)] [[Google Scholar](#)]
7. Ohlund D., Handly-Santana A., Biffi G., Elyada E., Almeida A.S., Ponz-Sarvisé M., Corbo V., Oni T.E., Hearn S.A., Lee E.J., et al. Distinct populations of inflammatory fibroblasts and myofibroblasts in pancreatic cancer. *J. Exp. Med.* 2017;214:579–596. doi: 10.1084/jem.20162024. [[PMC free article](#)] [[PubMed](#)] [[CrossRef](#)] [[Google Scholar](#)]
8. Biffi G., Oni T.E., Spielman B., Hao Y., Elyada E., Park Y., Preall J., Tuveson D.A. IL-1-induced JAK/STAT signaling is antagonized by TGF-beta to shape CAF heterogeneity in pancreatic ductal adenocarcinoma. *Cancer Discov.* 2018 doi: 10.1158/2159-8290.CD-18-0710. [[PMC free article](#)] [[PubMed](#)] [[CrossRef](#)] [[Google Scholar](#)]
9. Cirri P., Chiarugi P. Cancer associated fibroblasts: The dark side of the coin. *Am. J. Cancer Res.* 2011;1:482–497. [[PMC free article](#)] [[PubMed](#)] [[Google Scholar](#)]
10. Kalluri R., Zeisberg M. Fibroblasts in cancer. *Nat. Rev. Cancer.* 2006;6:392–401. doi: 10.1038/nrc1877. [[PubMed](#)] [[CrossRef](#)] [[Google Scholar](#)]

11. Celis J.E., Moreira J.M., Gromova I., Cabezon T., Ralfkiaer U., Guldborg P., Straten P.T., Mouridsen H., Friis E., Holm D., et al. Towards discovery-driven translational research in breast cancer. *FEBS J.* 2005;272:2–15. doi: 10.1111/j.1432-1033.2004.04418.x. [[PubMed](#)] [[CrossRef](#)] [[Google Scholar](#)]
12. Dirat B., Bochet L., Dabek M., Daviaud D., Dauvillier S., Majed B., Wang Y.Y., Meulle A., Salles B., Le Gonidec S., et al. Cancer-associated adipocytes exhibit an activated phenotype and contribute to breast cancer invasion. *Cancer Res.* 2011;71:2455–2465. doi: 10.1158/0008-5472.CAN-10-3323. [[PubMed](#)] [[CrossRef](#)] [[Google Scholar](#)]
13. Erez N., Truitt M., Olson P., Arron S.T., Hanahan D. Cancer-Associated Fibroblasts Are Activated in Incipient Neoplasia to Orchestrate Tumor-Promoting Inflammation in an NF-kappaB-Dependent Manner. *Cancer Cell.* 2010;17:135–147. doi: 10.1016/j.ccr.2009.12.041. [[PubMed](#)] [[CrossRef](#)] [[Google Scholar](#)]
14. Chiarugi P., Cirri P. Metabolic exchanges within tumor microenvironment. *Cancer Lett.* 2016;380:272–280. doi: 10.1016/j.canlet.2015.10.027. [[PubMed](#)] [[CrossRef](#)] [[Google Scholar](#)]
15. Miller A., Nagy C., Knapp B., Laengle J., Ponweiser E., Groeger M., Starkl P., Bergmann M., Wagner O., Haschemi A. Exploring Metabolic Configurations of Single Cells within Complex Tissue Microenvironments. *Cell Metab.* 2017;26:788–800.e6. doi: 10.1016/j.cmet.2017.08.014. [[PubMed](#)] [[CrossRef](#)] [[Google Scholar](#)]
16. Neesse A., Algul H., Tuveson D.A., Gress T.M. Stromal biology and therapy in pancreatic cancer: A changing paradigm. *Gut.* 2015;64:1476–1484. doi: 10.1136/gutjnl-2015-309304. [[PubMed](#)] [[CrossRef](#)] [[Google Scholar](#)]
17. Provenzano P.P., Cuevas C., Chang A.E., Goel V.K., Von Hoff D.D., Hingorani S.R. Enzymatic targeting of the stroma ablates physical barriers to treatment of pancreatic ductal adenocarcinoma. *Cancer Cell.* 2012;21:418–429. doi: 10.1016/j.ccr.2012.01.007. [[PMC free article](#)] [[PubMed](#)] [[CrossRef](#)] [[Google Scholar](#)]
18. Jacobetz M.A., Chan D.S., Neesse A., Bapiro T.E., Cook N., Frese K.K., Feig C., Nakagawa T., Caldwell M.E., Zecchini H.I., et al. Hyaluronan impairs vascular function and drug delivery in a mouse model of pancreatic cancer. *Gut.* 2013;62:112–120. doi: 10.1136/gutjnl-2012-302529. [[PMC free article](#)] [[PubMed](#)] [[CrossRef](#)] [[Google Scholar](#)]
19. Kamphorst J.J., Nofal M., Commisso C., Hackett S.R., Lu W., Grabocka E., Vander Heiden M.G., Miller G., Drebin J.A., Bar-Sagi D., et al. Human pancreatic cancer tumors are nutrient poor and tumor cells actively scavenge extracellular protein. *Cancer Res.* 2015;75:544–553. doi: 10.1158/0008-5472.CAN-14-2211. [[PMC free article](#)] [[PubMed](#)] [[CrossRef](#)] [[Google Scholar](#)]
20. Commisso C., Davidson S.M., Soydaner-Azeloglu R.G., Parker S.J., Kamphorst J.J., Hackett S., Grabocka E., Nofal M., Drebin J.A., Thompson C.B., et al. Macropinocytosis of protein is an amino acid supply route in Ras-transformed cells. *Nature.* 2013;497:633–637. doi: 10.1038/nature12138. [[PMC free article](#)] [[PubMed](#)] [[CrossRef](#)] [[Google Scholar](#)]
21. Olivares O., Mayers J.R., Gouirand V., Torrence M.E., Gicquel T., Borge L., Lac S., Roques J., Lavaut M.N., Berthezene P., et al. Collagen-derived proline promotes pancreatic ductal adenocarcinoma cell survival under nutrient limited conditions. *Nat. Commun.* 2017;8:16031. doi: 10.1038/ncomms16031. [[PMC free article](#)] [[PubMed](#)] [[CrossRef](#)] [[Google Scholar](#)]

22. Sherman M.H., Yu R.T., Tseng T.W., Sousa C.M., Liu S., Truitt M.L., He N., Ding N., Liddle C., Atkins A.R., et al. Stromal cues regulate the pancreatic cancer epigenome and metabolome. *Proc. Natl. Acad. Sci. USA*. 2017;114:1129–1134. doi: 10.1073/pnas.1620164114. [[PMC free article](#)] [[PubMed](#)] [[CrossRef](#)] [[Google Scholar](#)]
23. Curtis M., Kenny H.A., Ashcroft B., Mukherjee A., Johnson A., Zhang Y., Helou Y., Batlle R., Liu X., Gutierrez N., et al. Fibroblasts Mobilize Tumor Cell Glycogen to Promote Proliferation and Metastasis. *Cell Metab*. 2019;29:141–155.e9. doi: 10.1016/j.cmet.2018.08.007. [[PMC free article](#)] [[PubMed](#)] [[CrossRef](#)] [[Google Scholar](#)]
24. Sullivan W.J., Mullen P.J., Schmid E.W., Flores A., Momcilovic M., Sharpley M.S., Jelinek D., Whiteley A.E., Maxwell M.B., Wilde B.R., et al. Extracellular Matrix Remodeling Regulates Glucose Metabolism through TXNIP Destabilization. *Cell*. 2018;175:117–132.e121. doi: 10.1016/j.cell.2018.08.017. [[PMC free article](#)] [[PubMed](#)] [[CrossRef](#)] [[Google Scholar](#)]
25. Bertero T., Oldham W.M., Grasset E.M., Bourget I., Boulter E., Pisano S., Hofman P., Bellvert F., Meneguzzi G., Bulavin D.V., et al. Tumor-Stroma Mechanics Coordinate Amino Acid Availability to Sustain Tumor Growth and Malignancy. *Cell Metab*. 2019;29:124–140.e10. doi: 10.1016/j.cmet.2018.09.012. [[PMC free article](#)] [[PubMed](#)] [[CrossRef](#)] [[Google Scholar](#)]
26. Wang W., Kryczek I., Dostal L., Lin H., Tan L., Zhao L., Lu F., Wei S., Maj T., Peng D., et al. Effector T Cells Abrogate Stroma-Mediated Chemoresistance in Ovarian Cancer. *Cell*. 2016;165:1092–1105. doi: 10.1016/j.cell.2016.04.009. [[PMC free article](#)] [[PubMed](#)] [[CrossRef](#)] [[Google Scholar](#)]
27. Ziani L., Chouaib S., Thierry J. Alteration of the Antitumor Immune Response by Cancer-Associated Fibroblasts. *Front. Immunol*. 2018;9:414. doi: 10.3389/fimmu.2018.00414. [[PMC free article](#)] [[PubMed](#)] [[CrossRef](#)] [[Google Scholar](#)]
28. Li T., Yang Y., Hua X., Wang G., Liu W., Jia C., Tai Y., Zhang Q., Chen G. Hepatocellular carcinoma-associated fibroblasts trigger NK cell dysfunction via PGE2 and IDO. *Cancer Lett*. 2012;318:154–161. doi: 10.1016/j.canlet.2011.12.020. [[PubMed](#)] [[CrossRef](#)] [[Google Scholar](#)]
29. Hsu Y.L., Hung J.Y., Chiang S.Y., Jian S.F., Wu C.Y., Lin Y.S., Tsai Y.M., Chou S.H., Tsai M.J., Kuo P.L. Lung cancer-derived galectin-1 contributes to cancer associated fibroblast-mediated cancer progression and immune suppression through TDO2/kynurenine axis. *Oncotarget*. 2016;7:27584–27598. doi: 10.18632/oncotarget.8488. [[PMC free article](#)] [[PubMed](#)] [[CrossRef](#)] [[Google Scholar](#)]
30. Kaur A., Webster M.R., Marchbank K., Behera R., Ndoye A., Kugel C.H., 3rd, Dang V.M., Appleton J., O’Connell M.P., Cheng P., et al. sFRP2 in the aged microenvironment drives melanoma metastasis and therapy resistance. *Nature*. 2016;532:250–254. doi: 10.1038/nature17392. [[PMC free article](#)] [[PubMed](#)] [[CrossRef](#)] [[Google Scholar](#)]
31. Eales K.L., Hollinshead K.E., Tennant D.A. Hypoxia and metabolic adaptation of cancer cells. *Oncogenesis*. 2016;5:e190. doi: 10.1038/oncsis.2015.50. [[PMC free article](#)] [[PubMed](#)] [[CrossRef](#)] [[Google Scholar](#)]
32. Vander Heiden M.G., Cantley L.C., Thompson C.B. Understanding the Warburg effect: The metabolic requirements of cell proliferation. *Science*. 2009;324:1029–1033. doi: 10.1126/science.1160809. [[PMC free article](#)] [[PubMed](#)] [[CrossRef](#)] [[Google Scholar](#)]

33. Majmundar A.J., Wong W.J., Simon M.C. Hypoxia-inducible factors and the response to hypoxic stress. *Mol. Cell.* 2010;40:294–309. doi: 10.1016/j.molcel.2010.09.022. [[PMC free article](#)] [[PubMed](#)] [[CrossRef](#)] [[Google Scholar](#)]
34. Sonveaux P., Vegran F., Schroeder T., Wergin M.C., Verrax J., Rabbani Z.N., De Saedeleer C.J., Kennedy K.M., Diepart C., Jordan B.F., et al. Targeting lactate-fueled respiration selectively kills hypoxic tumor cells in mice. *J. Clin. Invest.* 2008;118:3930–3942. doi: 10.1172/JCI36843. [[PMC free article](#)] [[PubMed](#)] [[CrossRef](#)] [[Google Scholar](#)]
35. Guillaumond F., Leca J., Olivares O., Lavaut M.N., Vidal N., Berthezene P., Dusetti N.J., Loncle C., Calvo E., Turrini O., et al. Strengthened glycolysis under hypoxia supports tumor symbiosis and hexosamine biosynthesis in pancreatic adenocarcinoma. *Proc. Natl. Acad. Sci. USA.* 2013;110:3919–3924. doi: 10.1073/pnas.1219555110. [[PMC free article](#)] [[PubMed](#)] [[CrossRef](#)] [[Google Scholar](#)]
36. Fu Y., Liu S., Yin S., Niu W., Xiong W., Tan M., Li G., Zhou M. The reverse Warburg effect is likely to be an Achilles' heel of cancer that can be exploited for cancer therapy. *Oncotarget.* 2017;8:57813–57825. doi: 10.18632/oncotarget.18175. [[PMC free article](#)] [[PubMed](#)] [[CrossRef](#)] [[Google Scholar](#)]
37. Pavlides S., Whitaker-Menezes D., Castello-Cros R., Flomenberg N., Witkiewicz A.K., Frank P.G., Casimiro M.C., Wang C., Fortina P., Addya S., et al. The reverse Warburg effect: Aerobic glycolysis in cancer associated fibroblasts and the tumor stroma. *Cell Cycle.* 2009;8:3984–4001. doi: 10.4161/cc.8.23.10238. [[PubMed](#)] [[CrossRef](#)] [[Google Scholar](#)]
38. Sotgia F., Martinez-Outschoorn U.E., Pavlides S., Howell A., Pestell R.G., Lisanti M.P. Understanding the Warburg effect and the prognostic value of stromal caveolin-1 as a marker of a lethal tumor microenvironment. *Breast Cancer Res.* 2011;13:213. doi: 10.1186/bcr2892. [[PMC free article](#)] [[PubMed](#)] [[CrossRef](#)] [[Google Scholar](#)]
39. Fiaschi T., Marini A., Giannoni E., Taddei M.L., Gandellini P., De Donatis A., Lanciotti M., Serni S., Cirri P., Chiarugi P. Reciprocal metabolic reprogramming through lactate shuttle coordinately influences tumor-stroma interplay. *Cancer Res.* 2012;72:5130–5140. doi: 10.1158/0008-5472.CAN-12-1949. [[PubMed](#)] [[CrossRef](#)] [[Google Scholar](#)]
40. Zhang D., Wang Y., Shi Z., Liu J., Sun P., Hou X., Zhang J., Zhao S., Zhou B.P., Mi J. Metabolic reprogramming of cancer-associated fibroblasts by IDH3alpha downregulation. *Cell Rep.* 2015;10:1335–1348. doi: 10.1016/j.celrep.2015.02.006. [[PubMed](#)] [[CrossRef](#)] [[Google Scholar](#)]
41. Iommarini L., Porcelli A.M., Gasparre G., Kurelac I. Non-Canonical Mechanisms Regulating Hypoxia-Inducible Factor 1 Alpha in Cancer. *Front. Oncol.* 2017;7:286. doi: 10.3389/fonc.2017.00286. [[PMC free article](#)] [[PubMed](#)] [[CrossRef](#)] [[Google Scholar](#)]
42. Fuyuhiko Y., Yashiro M., Noda S., Kashiwagi S., Matsuoka J., Doi Y., Kato Y., Hasegawa T., Sawada T., Hirakawa K. Upregulation of cancer-associated myofibroblasts by TGF-beta from scirrhous gastric carcinoma cells. *Br. J. Cancer.* 2011;105:996–1001. doi: 10.1038/bjc.2011.330. [[PMC free article](#)] [[PubMed](#)] [[CrossRef](#)] [[Google Scholar](#)]
43. Guido C., Whitaker-Menezes D., Capparelli C., Balliet R., Lin Z., Pestell R.G., Howell A., Aquila S., Ando S., Martinez-Outschoorn U., et al. Metabolic reprogramming of cancer-

- associated fibroblasts by TGF-beta drives tumor growth: Connecting TGF-beta signaling with “Warburg-like” cancer metabolism and L-lactate production. *Cell Cycle*. 2012;11:3019–3035. doi: 10.4161/cc.21384. [[PMC free article](#)] [[PubMed](#)] [[CrossRef](#)] [[Google Scholar](#)]
44. Sousa C.M., Biancur D.E., Wang X., Halbrook C.J., Sherman M.H., Zhang L., Kremer D., Hwang R.F., Witkiewicz A.K., Ying H., et al. Pancreatic stellate cells support tumour metabolism through autophagic alanine secretion. *Nature*. 2016;536:479–483. doi: 10.1038/nature19084. [[PMC free article](#)] [[PubMed](#)] [[CrossRef](#)] [[Google Scholar](#)]
45. Rattigan Y.I., Patel B.B., Ackerstaff E., Sukenick G., Koutcher J.A., Glod J.W., Banerjee D. Lactate is a mediator of metabolic cooperation between stromal carcinoma associated fibroblasts and glycolytic tumor cells in the tumor microenvironment. *Exp. Cell Res.* 2012;318:326–335. doi: 10.1016/j.yexcr.2011.11.014. [[PMC free article](#)] [[PubMed](#)] [[CrossRef](#)] [[Google Scholar](#)]
46. Wise D.R., Thompson C.B. Glutamine addiction: A new therapeutic target in cancer. *Trends Biochem. Sci.* 2010;35:427–433. doi: 10.1016/j.tibs.2010.05.003. [[PMC free article](#)] [[PubMed](#)] [[CrossRef](#)] [[Google Scholar](#)]
47. Yang L., Achreja A., Yeung T.L., Mangala L.S., Jiang D., Han C., Baddour J., Marini J.C., Ni J., Nakahara R., et al. Targeting Stromal Glutamine Synthetase in Tumors Disrupts Tumor Microenvironment-Regulated Cancer Cell Growth. *Cell Metab.* 2016;24:685–700. doi: 10.1016/j.cmet.2016.10.011. [[PMC free article](#)] [[PubMed](#)] [[CrossRef](#)] [[Google Scholar](#)]
48. Amelio I., Cutruzzola F., Antonov A., Agostini M., Melino G. Serine and glycine metabolism in cancer. *Trends Biochem. Sci.* 2014;39:191–198. doi: 10.1016/j.tibs.2014.02.004. [[PMC free article](#)] [[PubMed](#)] [[CrossRef](#)] [[Google Scholar](#)]
49. Valencia T., Kim J.Y., Abu-Baker S., Moscat-Pardos J., Ahn C.S., Reina-Campos M., Duran A., Castilla E.A., Metallo C.M., Diaz-Meco M.T., et al. Metabolic reprogramming of stromal fibroblasts through p62-mTORC1 signaling promotes inflammation and tumorigenesis. *Cancer Cell*. 2014;26:121–135. doi: 10.1016/j.ccr.2014.05.004. [[PMC free article](#)] [[PubMed](#)] [[CrossRef](#)] [[Google Scholar](#)]
50. Duran A., Hernandez E.D., Reina-Campos M., Castilla E.A., Subramaniam S., Raghunandan S., Roberts L.R., Kisseleva T., Karin M., Diaz-Meco M.T., et al. p62/SQSTM1 by Binding to Vitamin D Receptor Inhibits Hepatic Stellate Cell Activity, Fibrosis, and Liver Cancer. *Cancer Cell*. 2016;30:595–609. doi: 10.1016/j.ccell.2016.09.004. [[PMC free article](#)] [[PubMed](#)] [[CrossRef](#)] [[Google Scholar](#)]
51. Linares J.F., Cordes T., Duran A., Reina-Campos M., Valencia T., Ahn C.S., Castilla E.A., Moscat J., Metallo C.M., Diaz-Meco M.T. ATF4-Induced Metabolic Reprogramming Is a Synthetic Vulnerability of the p62-Deficient Tumor Stroma. *Cell Metab.* 2017;26:817–829.e6. doi: 10.1016/j.cmet.2017.09.001. [[PMC free article](#)] [[PubMed](#)] [[CrossRef](#)] [[Google Scholar](#)]
52. Sherman M.H. Stellate Cells in Tissue Repair, Inflammation, and Cancer. *Annu. Rev. Cell Dev. Biol.* 2018;34:333–355. doi: 10.1146/annurev-cellbio-100617-062855. [[PubMed](#)] [[CrossRef](#)] [[Google Scholar](#)]
53. Kamphorst J.J., Cross J.R., Fan J., de Stanchina E., Mathew R., White E.P., Thompson C.B., Rabinowitz J.D. Hypoxic and Ras-transformed cells support growth by scavenging unsaturated

- fatty acids from lysophospholipids. *Proc. Natl. Acad. Sci. USA.* 2013;110:8882–8887. doi: 10.1073/pnas.1307237110. [[PMC free article](#)] [[PubMed](#)] [[CrossRef](#)] [[Google Scholar](#)]
54. Auciello F.R., Bulusu V., Oon C., Tait-Mulder J., Berry M., Bhattacharyya S., Tumanov S., Allen-Petersen B.L., Link J., Kendersky N.D., et al. A stromal lysolipid-autotaxin signaling axis promotes pancreatic tumor progression. *Cancer Discov.* 2019 doi: 10.1158/2159-8290.CD-18-1212. [[PMC free article](#)] [[PubMed](#)] [[CrossRef](#)] [[Google Scholar](#)]
55. Nardi F., Fitchev P., Franco O.E., Ivanisevic J., Scheibler A., Hayward S.W., Brendler C.B., Welte M.A., Crawford S.E. PEDF regulates plasticity of a novel lipid-MTOC axis in prostate cancer-associated fibroblasts. *J. Cell Sci.* 2018;131 doi: 10.1242/jcs.213579. [[PMC free article](#)] [[PubMed](#)] [[CrossRef](#)] [[Google Scholar](#)]
56. Vasseur S., Guillaumond F. LDL Receptor: An open route to feed pancreatic tumor cells. *Mol. Cell Oncol.* 2016;3:e1033586. doi: 10.1080/23723556.2015.1033586. [[PMC free article](#)] [[PubMed](#)] [[CrossRef](#)] [[Google Scholar](#)]
57. Garcia-Bermudez J., Baudrier L., Bayraktar E.C., Shen Y., La K., Guarecuco R., Yucel B., Fiore D., Tavora B., Freinkman E., et al. Squalene accumulation in cholesterol auxotrophic lymphomas prevents oxidative cell death. *Nature.* 2019;567:118–122. doi: 10.1038/s41586-019-0945-5. [[PMC free article](#)] [[PubMed](#)] [[CrossRef](#)] [[Google Scholar](#)]
58. Gangoda L., Boukouris S., Liem M., Kalra H., Mathivanan S. Extracellular vesicles including exosomes are mediators of signal transduction: Are they protective or pathogenic? *Proteomics.* 2015;15:260–271. doi: 10.1002/pmic.201400234. [[PMC free article](#)] [[PubMed](#)] [[CrossRef](#)] [[Google Scholar](#)]
59. Zhao H., Yang L., Baddour J., Achreja A., Bernard V., Moss T., Marini J.C., Tudawe T., Seviour E.G., San Lucas F.A., et al. Tumor microenvironment derived exosomes pleiotropically modulate cancer cell metabolism. *Elife.* 2016;5:e10250. doi: 10.7554/eLife.10250. [[PMC free article](#)] [[PubMed](#)] [[CrossRef](#)] [[Google Scholar](#)]
60. Richards K.E., Zeleniak A.E., Fishel M.L., Wu J., Littlepage L.E., Hill R. Cancer-associated fibroblast exosomes regulate survival and proliferation of pancreatic cancer cells. *Oncogene.* 2017;36:1770–1778. doi: 10.1038/onc.2016.353. [[PMC free article](#)] [[PubMed](#)] [[CrossRef](#)] [[Google Scholar](#)]
61. Petruzzelli M., Wagner E.F. Mechanisms of metabolic dysfunction in cancer-associated cachexia. *Genes Dev.* 2016;30:489–501. doi: 10.1101/gad.276733.115. [[PMC free article](#)] [[PubMed](#)] [[CrossRef](#)] [[Google Scholar](#)]
62. Fearon K., Strasser F., Anker S.D., Bosaeus I., Bruera E., Fainsinger R.L., Jatoi A., Loprinzi C., MacDonald N., Mantovani G., et al. Definition and classification of cancer cachexia: An international consensus. *Lancet Oncol.* 2011;12:489–495. doi: 10.1016/S1470-2045(10)70218-7. [[PubMed](#)] [[CrossRef](#)] [[Google Scholar](#)]
63. Fearon K.C., Glass D.J., Guttridge D.C. Cancer cachexia: Mediators, signaling, and metabolic pathways. *Cell Metab.* 2012;16:153–166. doi: 10.1016/j.cmet.2012.06.011. [[PubMed](#)] [[CrossRef](#)] [[Google Scholar](#)]

64. Mayers J.R., Wu C., Clish C.B., Kraft P., Torrence M.E., Fiske B.P., Yuan C., Bao Y., Townsend M.K., Tworoger S.S., et al. Elevation of circulating branched-chain amino acids is an early event in human pancreatic adenocarcinoma development. *Nat. Med.* 2014;20:1193–1198. doi: 10.1038/nm.3686. [[PMC free article](#)] [[PubMed](#)] [[CrossRef](#)] [[Google Scholar](#)]
65. Kitagawa M., Haji S., Amagai T. High Serum Essential Amino Acids as a Predictor of Skeletal Muscle Depletion in Patients With Cachexia and Advanced Gastrointestinal Cancers. *Nutr. Clin. Pract.* 2017;32:645–651. doi: 10.1177/0884533617724742. [[PubMed](#)] [[CrossRef](#)] [[Google Scholar](#)]
66. Garin-Chesa P., Old L.J., Rettig W.J. Cell surface glycoprotein of reactive stromal fibroblasts as a potential antibody target in human epithelial cancers. *Proc. Natl. Acad. Sci. USA.* 1990;87:7235–7239. doi: 10.1073/pnas.87.18.7235. [[PMC free article](#)] [[PubMed](#)] [[CrossRef](#)] [[Google Scholar](#)]
67. Brokopp C.E., Schoenauer R., Richards P., Bauer S., Lohmann C., Emmert M.Y., Weber B., Winnik S., Aikawa E., Graves K., et al. Fibroblast activation protein is induced by inflammation and degrades type I collagen in thin-cap fibroatheromata. *Eur. Heart J.* 2011;32:2713–2722. doi: 10.1093/eurheartj/ehq519. [[PMC free article](#)] [[PubMed](#)] [[CrossRef](#)] [[Google Scholar](#)]
68. Feig C., Jones J.O., Kraman M., Wells R.J., Deonarine A., Chan D.S., Connell C.M., Roberts E.W., Zhao Q., Caballero O.L., et al. Targeting CXCL12 from FAP-expressing carcinoma-associated fibroblasts synergizes with anti-PD-L1 immunotherapy in pancreatic cancer. *Proc. Natl. Acad. Sci. USA.* 2013;110:20212–20217. doi: 10.1073/pnas.1320318110. [[PMC free article](#)] [[PubMed](#)] [[CrossRef](#)] [[Google Scholar](#)]
69. Roberts E.W., Deonarine A., Jones J.O., Denton A.E., Feig C., Lyons S.K., Espeli M., Kraman M., McKenna B., Wells R.J., et al. Depletion of stromal cells expressing fibroblast activation protein- $\alpha$  from skeletal muscle and bone marrow results in cachexia and anemia. *J. Exp. Med.* 2013;210:1137–1151. doi: 10.1084/jem.20122344. [[PMC free article](#)] [[PubMed](#)] [[CrossRef](#)] [[Google Scholar](#)]
70. Flint T.R., Janowitz T., Connell C.M., Roberts E.W., Denton A.E., Coll A.P., Jodrell D.I., Fearon D.T. Tumor-Induced IL-6 Reprograms Host Metabolism to Suppress Anti-tumor Immunity. *Cell Metab.* 2016;24:672–684. doi: 10.1016/j.cmet.2016.10.010. [[PMC free article](#)] [[PubMed](#)] [[CrossRef](#)] [[Google Scholar](#)]
71. Argiles J.M., Busquets S., Lopez-Soriano F.J. Cytokines in the pathogenesis of cancer cachexia. *Curr Opin Clin. Nutr. Metab. Care.* 2003;6:401–406. doi: 10.1097/01.mco.0000078983.18774.cc. [[PubMed](#)] [[CrossRef](#)] [[Google Scholar](#)]
72. Ohe Y., Podack E.R., Olsen K.J., Miyahara Y., Miura K., Saito H., Koishihara Y., Ohsugi Y., Ohira T., Nishio K., et al. Interleukin-6 cDNA transfected Lewis lung carcinoma cells show unaltered net tumour growth rate but cause weight loss and shortened survival in syngeneic mice. *Br. J. Cancer.* 1993;67:939–944. doi: 10.1038/bjc.1993.174. [[PMC free article](#)] [[PubMed](#)] [[CrossRef](#)] [[Google Scholar](#)]
73. Tsujinaka T., Ebisui C., Fujita J., Kishibuchi M., Morimoto T., Ogawa A., Katsume A., Ohsugi Y., Kominami E., Monden M. Muscle undergoes atrophy in association with increase of lysosomal cathepsin activity in interleukin-6 transgenic mouse. *Biochem. Biophys Res. Commun.* 1995;207:168–174. doi: 10.1006/bbrc.1995.1168. [[PubMed](#)] [[CrossRef](#)] [[Google Scholar](#)]

74. Black K., Garrett I.R., Mundy G.R. Chinese hamster ovarian cells transfected with the murine interleukin-6 gene cause hypercalcemia as well as cachexia, leukocytosis and thrombocytosis in tumor-bearing nude mice. *Endocrinology*. 1991;128:2657–2659. doi: 10.1210/endo-128-5-2657. [[PubMed](#)] [[CrossRef](#)] [[Google Scholar](#)]
75. Strassmann G., Fong M., Kenney J.S., Jacob C.O. Evidence for the involvement of interleukin 6 in experimental cancer cachexia. *J. Clin. Invest.* 1992;89:1681–1684. doi: 10.1172/JCI115767. [[PMC free article](#)] [[PubMed](#)] [[CrossRef](#)] [[Google Scholar](#)]
76. Strassmann G., Fong M., Freter C.E., Windsor S., D’Alessandro F., Nordan R.P. Suramin interferes with interleukin-6 receptor binding in vitro and inhibits colon-26-mediated experimental cancer cachexia in vivo. *J. Clin. Invest.* 1993;92:2152–2159. doi: 10.1172/JCI116816. [[PMC free article](#)] [[PubMed](#)] [[CrossRef](#)] [[Google Scholar](#)]
77. Tamura S., Ouchi K.F., Mori K., Endo M., Matsumoto T., Eda H., Tanaka Y., Ishitsuka H., Tokita H., Yamaguchi K. Involvement of human interleukin 6 in experimental cachexia induced by a human uterine cervical carcinoma xenograft. *Clin. Cancer Res.* 1995;1:1353–1358. [[PubMed](#)] [[Google Scholar](#)]
78. Staal-van den Brekel A.J., Dentener M.A., Schols A.M., Buurman W.A., Wouters E.F. Increased resting energy expenditure and weight loss are related to a systemic inflammatory response in lung cancer patients. *J. Clin. Oncol.* 1995;13:2600–2605. doi: 10.1200/JCO.1995.13.10.2600. [[PubMed](#)] [[CrossRef](#)] [[Google Scholar](#)]
79. Fearon K.C., McMillan D.C., Preston T., Winstanley F.P., Cruickshank A.M., Shenkin A. Elevated circulating interleukin-6 is associated with an acute-phase response but reduced fixed hepatic protein synthesis in patients with cancer. *Ann. Surg.* 1991;213:26–31. doi: 10.1097/00000658-199101000-00005. [[PMC free article](#)] [[PubMed](#)] [[CrossRef](#)] [[Google Scholar](#)]
80. Okada S., Okusaka T., Ishii H., Kyogoku A., Yoshimori M., Kajimura N., Yamaguchi K., Kakizoe T. Elevated serum interleukin-6 levels in patients with pancreatic cancer. *Jpn. J. Clin. Oncol.* 1998;28:12–15. doi: 10.1093/jjco/28.1.12. [[PubMed](#)] [[CrossRef](#)] [[Google Scholar](#)]
81. Bonetto A., Aydogdu T., Kunzevitzky N., Guttridge D.C., Khuri S., Koniaris L.G., Zimmers T.A. STAT3 activation in skeletal muscle links muscle wasting and the acute phase response in cancer cachexia. *PLoS One*. 2011;6:e22538. doi: 10.1371/journal.pone.0022538. [[PMC free article](#)] [[PubMed](#)] [[CrossRef](#)] [[Google Scholar](#)]
82. Qiao Y., Zhang C., Li A., Wang D., Luo Z., Ping Y., Zhou B., Liu S., Li H., Yue D., et al. IL6 derived from cancer-associated fibroblasts promotes chemoresistance via CXCR7 in esophageal squamous cell carcinoma. *Oncogene*. 2018;37:873–883. doi: 10.1038/onc.2017.387. [[PubMed](#)] [[CrossRef](#)] [[Google Scholar](#)]
83. Wu X., Tao P., Zhou Q., Li J., Yu Z., Wang X., Li J., Li C., Yan M., Zhu Z., et al. IL-6 secreted by cancer-associated fibroblasts promotes epithelial-mesenchymal transition and metastasis of gastric cancer via JAK2/STAT3 signaling pathway. *Oncotarget*. 2017;8:20741–20750. doi: 10.18632/oncotarget.15119. [[PMC free article](#)] [[PubMed](#)] [[CrossRef](#)] [[Google Scholar](#)]
84. Duluc C., Moatassim-Billah S., Chalabi-Dchar M., Perraud A., Samain R., Breibach F., Gayral M., Cordelier P., Delisle M.B., Bousquet-Dubouch M.P., et al. Pharmacological targeting

- of the protein synthesis mTOR/4E-BP1 pathway in cancer-associated fibroblasts abrogates pancreatic tumour chemoresistance. *EMBO Mol. Med.* 2015;7:735–753. doi: 10.15252/emmm.201404346. [[PMC free article](#)] [[PubMed](#)] [[CrossRef](#)] [[Google Scholar](#)]
85. Zhang Y., Yan W., Collins M.A., Bednar F., Rakshit S., Zetter B.R., Stanger B.Z., Chung I., Rhim A.D., di Magliano M.P. Interleukin-6 is required for pancreatic cancer progression by promoting MAPK signaling activation and oxidative stress resistance. *Cancer Res.* 2013;73:6359–6374. doi: 10.1158/0008-5472.CAN-13-1558-T. [[PMC free article](#)] [[PubMed](#)] [[CrossRef](#)] [[Google Scholar](#)]
86. Wang J., Dunn A.J. Mouse interleukin-6 stimulates the HPA axis and increases brain tryptophan and serotonin metabolism. *Neurochem. Int.* 1998;33:143–154. doi: 10.1016/S0197-0186(98)00016-3. [[PubMed](#)] [[CrossRef](#)] [[Google Scholar](#)]
87. Lee J.J., Perera R.M., Wang H., Wu D.C., Liu X.S., Han S., Fitamant J., Jones P.D., Ghanta K.S., Kawano S., et al. Stromal response to Hedgehog signaling restrains pancreatic cancer progression. *Proc. Natl. Acad. Sci. USA.* 2014;111:E3091–E3100. doi: 10.1073/pnas.1411679111. [[PMC free article](#)] [[PubMed](#)] [[CrossRef](#)] [[Google Scholar](#)]
88. Ozdemir B.C., Pentcheva-Hoang T., Carstens J.L., Zheng X., Wu C.C., Simpson T.R., Laklai H., Sugimoto H., Kahlert C., Novitskiy S.V., et al. Depletion of carcinoma-associated fibroblasts and fibrosis induces immunosuppression and accelerates pancreas cancer with reduced survival. *Cancer Cell.* 2014;25:719–734. doi: 10.1016/j.ccr.2014.04.005. [[PMC free article](#)] [[PubMed](#)] [[CrossRef](#)] [[Google Scholar](#)]
89. Rhim A.D., Oberstein P.E., Thomas D.H., Mirek E.T., Palermo C.F., Sastra S.A., Dekleva E.N., Saunders T., Becerra C.P., Tattersall I.W., et al. Stromal elements act to restrain, rather than support, pancreatic ductal adenocarcinoma. *Cancer Cell.* 2014;25:735–747. doi: 10.1016/j.ccr.2014.04.021. [[PMC free article](#)] [[PubMed](#)] [[CrossRef](#)] [[Google Scholar](#)]
90. Sherman M.H., Yu R.T., Engle D.D., Ding N., Atkins A.R., Tiriach H., Collisson E.A., Connor F., Van Dyke T., Kozlov S., et al. Vitamin D receptor-mediated stromal reprogramming suppresses pancreatitis and enhances pancreatic cancer therapy. *Cell.* 2014;159:80–93. doi: 10.1016/j.cell.2014.08.007. [[PMC free article](#)] [[PubMed](#)] [[CrossRef](#)] [[Google Scholar](#)]
91. Murata T., Mizushima H., Chinen I., Moribe H., Yagi S., Hoffman R.M., Kimura T., Yoshino K., Ueda Y., Enomoto T., et al. HB-EGF and PDGF mediate reciprocal interactions of carcinoma cells with cancer-associated fibroblasts to support progression of uterine cervical cancers. *Cancer Res.* 2011;71:6633–6642. doi: 10.1158/0008-5472.CAN-11-0034. [[PubMed](#)] [[CrossRef](#)] [[Google Scholar](#)]
92. Neufert C., Becker C., Tureci O., Waldner M.J., Backert I., Floh K., Atreya I., Leppkes M., Jefremow A., Vieth M., et al. Tumor fibroblast-derived epiregulin promotes growth of colitis-associated neoplasms through ERK. *J. Clin. Invest.* 2013;123:1428–1443. doi: 10.1172/JCI63748. [[PMC free article](#)] [[PubMed](#)] [[CrossRef](#)] [[Google Scholar](#)]
93. Cros M., Cataisson C., Cho Y.M., Berthois Y., Bernard-Poenaru O., Denne M., Graulet A.M., De Vernejoul M.C., Foley J., Bouizaj Z. Constitutive production of parathyroid hormone-related protein (PTHrP) by fibroblasts derived from normal and pathological human breast tissue. *Oncol. Res.* 2002;13:137–146. [[PubMed](#)] [[Google Scholar](#)]

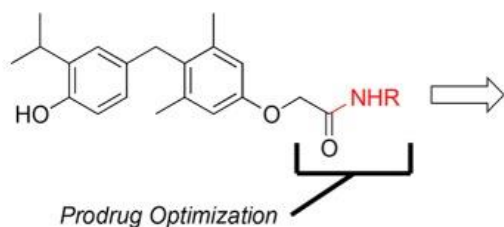
94. Blomme E.A., Sugimoto Y., Lin Y.C., Capen C.C., Rosol T.J. Parathyroid hormone-related protein is a positive regulator of keratinocyte growth factor expression by normal dermal fibroblasts. *Mol. Cell Endocrinol.* 1999;152:189–197. doi: 10.1016/S0303-7207(98)00252-4. [[PubMed](#)] [[CrossRef](#)] [[Google Scholar](#)]
95. Foley J., Nickerson N., Riese D.J., 2nd, Hollenhorst P.C., Lorch G., Foley A.M. At the crossroads: EGFR and PTHrP signaling in cancer-mediated diseases of bone. *Odontology.* 2012;100:109–129. doi: 10.1007/s10266-012-0070-5. [[PMC free article](#)] [[PubMed](#)] [[CrossRef](#)] [[Google Scholar](#)]
96. Kir S., White J.P., Kleiner S., Kazak L., Cohen P., Baracos V.E., Spiegelman B.M. Tumour-derived PTH-related protein triggers adipose tissue browning and cancer cachexia. *Nature.* 2014;513:100–104. doi: 10.1038/nature13528. [[PMC free article](#)] [[PubMed](#)] [[CrossRef](#)] [[Google Scholar](#)]
97. Bing C., Brown M., King P., Collins P., Tisdale M.J., Williams G. Increased gene expression of brown fat uncoupling protein (UCP)1 and skeletal muscle UCP2 and UCP3 in MAC16-induced cancer cachexia. *Cancer Res.* 2000;60:2405–2410. [[PubMed](#)] [[Google Scholar](#)]
98. Brooks S.L., Neville A.M., Rothwell N.J., Stock M.J., Wilson S. Sympathetic activation of brown-adipose-tissue thermogenesis in cachexia. *Biosci. Rep.* 1981;1:509–517. doi: 10.1007/BF01121584. [[PubMed](#)] [[CrossRef](#)] [[Google Scholar](#)]
99. Shellock F.G., Riedinger M.S., Fishbein M.C. Brown adipose tissue in cancer patients: Possible cause of cancer-induced cachexia. *J. Cancer Res. Clin. Oncol.* 1986;111:82–85. doi: 10.1007/BF00402783. [[PubMed](#)] [[CrossRef](#)] [[Google Scholar](#)]
100. Tsoli M., Moore M., Burg D., Painter A., Taylor R., Lockie S.H., Turner N., Warren A., Cooney G., Oldfield B., et al. Activation of thermogenesis in brown adipose tissue and dysregulated lipid metabolism associated with cancer cachexia in mice. *Cancer Res.* 2012;72:4372–4382. doi: 10.1158/0008-5472.CAN-11-3536. [[PubMed](#)] [[CrossRef](#)] [[Google Scholar](#)]
101. Kir S., Spiegelman B.M. Cachexia & Brown Fat: A Burning Issue in Cancer. *Trends Cancer.* 2016;2:461–463. doi: 10.1016/j.trecan.2016.07.005. [[PMC free article](#)] [[PubMed](#)] [[CrossRef](#)] [[Google Scholar](#)]
102. Song W., Kir S., Hong S., Hu Y., Wang X., Binari R., Tang H.W., Chung V., Banks A.S., Spiegelman B., et al. Tumor-Derived Ligands Trigger Tumor Growth and Host Wasting via Differential MEK Activation. *Dev. Cell.* 2019 doi: 10.1016/j.devcel.2018.12.003. [[PMC free article](#)] [[PubMed](#)] [[CrossRef](#)] [[Google Scholar](#)]
103. Yasmeen R., Shen Q., Lee A., Leung J.H., Kowdley D., DiSilvestro D.J., Xu L., Yang K., Maiseyeu A., Bal N.C., et al. Epiregulin induces leptin secretion and energy expenditure in high-fat diet-fed mice. *J. Endocrinol.* 2018;239:377–388. doi: 10.1530/JOE-18-0289. [[PMC free article](#)] [[PubMed](#)] [[CrossRef](#)] [[Google Scholar](#)]
104. Hicks M.J., Chiuchiolo M.J., Ballon D., Dyke J.P., Aronowitz E., Funato K., Tabar V., Havlicek D., Fan F., Sondhi D., et al. Anti-Epidermal Growth Factor Receptor Gene Therapy for Glioblastoma. *PLoS ONE.* 2016;11:e0162978. doi: 10.1371/journal.pone.0162978. [[PMC free article](#)] [[PubMed](#)] [[CrossRef](#)] [[Google Scholar](#)]

105. Hensley C.T., Faubert B., Yuan Q., Lev-Cohain N., Jin E., Kim J., Jiang L., Ko B., Skelton R., Loudat L., et al. Metabolic Heterogeneity in Human Lung Tumors. *Cell*. 2016;164:681–694. doi: 10.1016/j.cell.2015.12.034. [[PMC free article](#)] [[PubMed](#)] [[CrossRef](#)] [[Google Scholar](#)]
106. Zhang Y., Udayakumar D., Cai L., Hu Z., Kapur P., Kho E.Y., Pavia-Jimenez A., Fulkerson M., de Leon A.D., Yuan Q., et al. Addressing metabolic heterogeneity in clear cell renal cell carcinoma with quantitative Dixon MRI. *JCI Insight*. 2017;2 doi: 10.1172/jci.insight.94278. [[PMC free article](#)] [[PubMed](#)] [[CrossRef](#)] [[Google Scholar](#)]
107. Muir A., Danai L.V., Vander Heiden M.G. Microenvironmental regulation of cancer cell metabolism: Implications for experimental design and translational studies. *Dis. Model. Mech*. 2018;11 doi: 10.1242/dmm.035758. [[PMC free article](#)] [[PubMed](#)] [[CrossRef](#)] [[Google Scholar](#)]
108. Mayers J.R., Torrence M.E., Danai L.V., Papagiannakopoulos T., Davidson S.M., Bauer M.R., Lau A.N., Ji B.W., Dixit P.D., Hosios A.M., et al. Tissue of origin dictates branched-chain amino acid metabolism in mutant Kras-driven cancers. *Science*. 2016;353:1161–1165. doi: 10.1126/science.aaf5171. [[PMC free article](#)] [[PubMed](#)] [[CrossRef](#)] [[Google Scholar](#)]
109. Gui D.Y., Sullivan L.B., Luengo A., Hosios A.M., Bush L.N., Gitego N., Davidson S.M., Freinkman E., Thomas C.J., Vander Heiden M.G. Environment Dictates Dependence on Mitochondrial Complex I for NAD<sup>+</sup> and Aspartate Production and Determines Cancer Cell Sensitivity to Metformin. *Cell Metab*. 2016;24:716–727. doi: 10.1016/j.cmet.2016.09.006. [[PMC free article](#)] [[PubMed](#)] [[CrossRef](#)] [[Google Scholar](#)]
110. Hulea L., Gravel S.P., Morita M., Cargnello M., Uchenunu O., Im Y.K., Lehuede C., Ma E.H., Leibovitch M., McLaughlan S., et al. Translational and HIF-1alpha-Dependent Metabolic Reprogramming Underpin Metabolic Plasticity and Responses to Kinase Inhibitors and Biguanides. *Cell Metab*. 2018;28:817–832.e818. doi: 10.1016/j.cmet.2018.09.001. [[PMC free article](#)] [[PubMed](#)] [[CrossRef](#)] [[Google Scholar](#)]
111. Campbell S.L., Wellen K.E. Metabolic Signaling to the Nucleus in Cancer. *Mol. Cell*. 2018;71:398–408. doi: 10.1016/j.molcel.2018.07.015. [[PubMed](#)] [[CrossRef](#)] [[Google Scholar](#)]
112. Buck M.D., Sowell R.T., Kaech S.M., Pearce E.L. Metabolic Instruction of Immunity. *Cell*. 2017;169:570–586. doi: 10.1016/j.cell.2017.04.004. [[PMC free article](#)] [[PubMed](#)] [[CrossRef](#)] [[Google Scholar](#)]

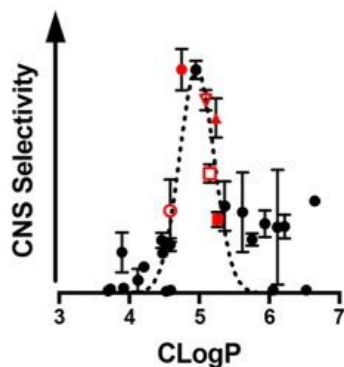
J. Matthew Meinig, Skylar J. Ferrara, Tapasree Banerji, Tania Banerji, **Hannah S. Sanford-Crane**, Dennis Bourdette, Thomas S. Scanlan. *Structure-Activity Relationships of Central Nervous System Penetration by Fatty Acid Amide Hydrolase (FAAH)-Targeted Thyromimetic Prodrugs*. ACS Med. Chem. Lett., 10(1) 111-116, 2019.

**Abstract:**

**CNS-Selective Thyromimetics**



**Structure-Activity Relationships**



Thyroid hormone (TH) action is of clinical interest in treating demyelinating diseases of the central nervous system (CNS). Two amide prodrugs of sobetirome, a potent thyroid hormone agonist, were previously shown to significantly improve CNS selective distribution of the parent drug through hydrolysis in the CNS by fatty acid amide hydrolase (FAAH). This concept is elaborated upon here with a series of 29 amide prodrugs targeting FAAH. We identify that conservative aliphatic modifications such as the *N*-methyl (**4**), *N*-ethyl (**5**), *N*-fluoroethyl (**15**), and *N*-cyclopropyl (**18**) substantially favor selective CNS distribution of the parent drug in mice. Additionally, lead compounds exhibit moderate to good rates of hydrolysis at FAAH *in vitro* suggesting both enzymatic and physicochemical properties are important parameters for optimization. Both **4** and **15** were orally bioavailable while retaining appreciable CNS parent drug delivery following an oral dose. The pharmacokinetic parameters of **4** over 24 h postdose (*i.v.* and *p.o.*) were determined.

**Keywords:** Prodrug, sobetirome, thyroid hormone, remyelination, CNS, FAAH

**Personal Contribution:**

HSC (also initialized as HSS) performed and optimized *in vivo* experiments.

**Introduction:**

The blood–brain barrier (BBB) represents a unique challenge for CNS drug development as it can significantly restrict therapeutic exposure from systemic circulation. Demyelinating diseases represent one class of therapeutically underserved CNS disorders with multiple sclerosis (MS), an autoinflammatory demyelinating disease, representing the most common demyelinating disorder. Current approved therapies for MS are mechanistically anti-inflammatory and do not promote

repair to damaged myelin.<sup>1</sup> Thyroid hormone (T3, **1**) action has garnered significant attention for remyelination therapy as T3 is important in both developmental myelination as well as myelin repair.<sup>2,3</sup> Unlike T3, the clinical stage thyroid hormone agonist (thyromimetic) sobetirome has a suitable therapeutic index for clinical use due to receptor- and tissue-specific action.<sup>4</sup> While sobetirome is unique in that it<sup>5,6</sup> and close analogues<sup>7</sup> are the only known thyromimetics to distribute to the CNS, efforts to develop sobetirome analogues with better CNS distribution have led to a new class of amide prodrugs termed sobetiramides.<sup>8</sup> Both the primary amide Sob-AM1 (**3**, [Figure Figure11](#)) and *N*-methylamide Sob-AM2 (**4**, [Figure Figure11](#)) were shown to deliver significantly more sobetirome to the CNS compared to a systemic dose of sobetirome. This improvement in CNS exposure was coupled with a concomitant decrease in peripheral exposure of sobetirome. This reversal from peripheral to central drug action makes the sobetiramides promising remyelination drug candidates with selective tissue action.

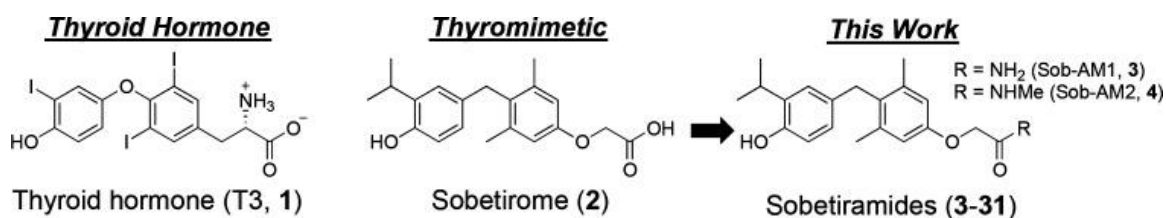


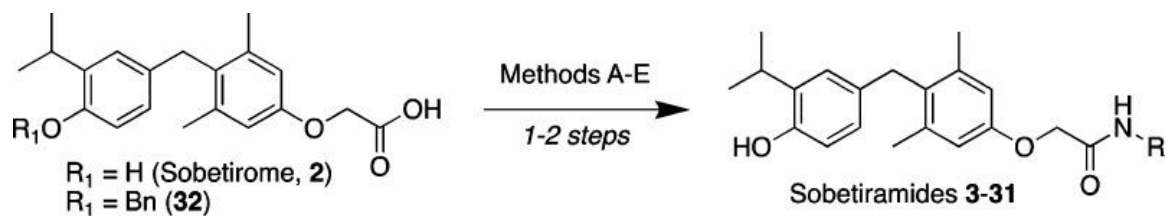
[Figure 1](#)

Structure of thyroid hormone, the clinical stage thyromimetic sobetirome, and sobetiramides.

From mechanistic studies of the unique CNS distribution of sobetiramides, we established that Sob-AM1 and Sob-AM2 are selectively hydrolyzed by fatty acid amide hydrolase (FAAH) and that FAAH activity is required for the selective CNS delivery of sobetirome from Sob-AM2.<sup>8</sup> FAAH catalyzes the hydrolysis of a diverse array of fatty acid amide signaling molecules including the endocannabinoid anandamide (AEA),<sup>9</sup> the hypnotic oleamide (OEA),<sup>10</sup> the anti-inflammatory *N*-palmitoylethanolamine (PEA),<sup>11</sup> and *N*-arachidonoyltaurine.<sup>12</sup> Structure–activity relationship (SAR) studies have shown that FAAH is also capable of hydrolyzing a diverse set of synthetic arachidonoyl amides including substituted derivatives of ethylamine and aniline as well as synthetic luciferin derivatives.<sup>13,14</sup> The pharmacology of FAAH inhibition has been of significant clinical interest for antinociception and has been extensively reviewed.<sup>15–17</sup> However, as a pharmacological substrate for FAAH, the scope of how existing SAR studies apply to the sobetiramide scaffold remains to be explored.

### Results:

Here we report a small library of sobetiramides ([Figure Figure11](#), [Table 1](#)) designed to probe the structural requirements of FAAH-mediated CNS delivery. The compound library consists of simple aliphatic amides (**5–8**, **20**), substituted ethylamines (**9–17**), a variety of anilines and aryl amines (**21–26**), and several polar derivatives (**27–31**). The compounds were synthesized from sobetirome in a direct manner from readily available starting materials in one or two steps. In certain cases (**5–6**, **14**), prodrug synthesis was accomplished in a protecting group-free manner from sobetirome identical to the report for **3** and **4** ([Scheme 1](#), Method A). The remaining sobetiramides were prepared from *O*-benzyl sobetirome (**32**, [Scheme 1](#), Methods B–E) using common amide bond coupling reactions followed by deprotection via transfer hydrogenation or treatment with boron trichloride.



### [Scheme 1](#)

**Synthesis of the Sobetiramide Library:** Reagents and conditions: Method A:  $R_1 = H$ , (i) MeOH,  $H_2SO_4$ , (ii) MeOH, amine. Method B:  $R_1 = Bn$ , (i) CDI, THF, (ii)  $BCl_3$ , DCM. Method C:  $R_1 = Bn$ , (i) oxalyl chloride, DCM, (ii) amine, (iii) Pd/C, TES. Method D:  $R_1 = Bn$ , (i) EDC, HOBT, DIEA, (ii) Pd/C, TES. Method E:  $R_1 = Bn$ , (i) DCC, NHS, (ii) amine. Note: compound 20 is a secondary amide ( $-NR_2$ )

Table 1

**Structure, Tissue Distribution, FAAH Hydrolysis Rates, and Physicochemical Parameters of the Library of Sobetiramide Prodrugs**

Compound	R group <sup>a</sup>	Method of synthesis <sup>b</sup>	[Sobetirome] <sub>brain</sub> (ng/g) <sup>c</sup>	[Sobetirome] <sub>serum</sub> (ng/g) <sup>c</sup>	K <sub>p</sub> <sup>th</sup>	Hydrolysis rate <sup>d</sup> (nmol mg <sup>-1</sup> min <sup>-1</sup> )	CLogP <sup>e</sup>	PSA <sup>f</sup>
Sobetirome		-	3.6 ± 0.2	318.6 ± 112.1	0.03 ± 0.001	-	-	-
Sob-AM1 (3)		A <sup>f</sup>	93.9 ± 37.1	79.5 ± 26	1.17 ± 0.45	4.7 ± 0.1	4.6	78.8
Sob-AM2 (4)		A <sup>f</sup>	53.1 ± 7.3	17.2 ± 3.4	3.17 ± 0.3	3.2 ± 0.2	4.7	58.6
5		A	58.2 ± 13.6	21.5 ± 5.5	2.74 ± 0.14	3.4 ± 0.1	5.1	58.6
6		A	20.2 ± 9	16.9 ± 4.3	1.15 ± 0.56	2.6 ± 0.1	5.6	58.6
7		B	33.4 ± 13.8	25.4 ± 3.4	1.23 ± 0.35	3.6 ± 0.6	5.4	58.6
8		B	59.5 ± 14.3	59.4 ± 4.6	0.99 ± 0.19	3.2 ± 0.1	5.9	58.6
9		C	25.5 ± 6.3	66.8 ± 4.6	0.37 ± 0.06	4.8 ± 0.2	4.2	78.8
10		C	22.3 ± 1.7	33.7 ± 5.5	0.69 ± 0.09	4.5 ± 0.2	4.6	78.8
11		C	38.7 ± 5	55.7 ± 10.9	0.72 ± 0.08	3.6 ± 0.1	4.5	72.6
12		E	2.6 ± 1	98 ± 41.2	0.03 ± 0.01	3.7 ± 0.2	3.7	99.0
13		C	0.8 ± 0.8	6.9 ± 1.9	0.07 ± 0.07	5.6 ± 0.8	3.9	84.6
14		A	7.1 ± 6.3	45.7 ± 3.6	0.18 ± 0.16	8.9 ± 0.3	4.1	121.3
15		B	107.1 ± 9.5	64.2 ± 8.5	1.7 ± 0.13	3.5 ± 0.1	5.1	58.6
16		B	125.4 ± 26.8	128.8 ± 43.1	1.04 ± 0.11	3.4 ± 0.2	5.3	58.6
17		B	59.4 ± 6.7	80.2 ± 14.2	0.76 ± 0.09	4.8 ± 2.2	5.8	58.6
18		B	58 ± 7.2	23.8 ± 3.3	2.49 ± 0.28	3.2 ± 0.2	5.2	58.6
19		B	79.2 ± 2.9	110.6 ± 17.2	0.75 ± 0.11	3.7 ± 0.2	4.5	67.8
20		B	32.2 ± 18.9	10.4 ± 6.4	3.17 ± 0.13	4.3 ± 0.3	5.0	49.8
21		D	7.4 ± 5.1	174.7 ± 112.7	0.04 ± 0.01	1.4 ± 0.3	6.1	78.8
22		D	12.8 ± 1.7	325.7 ± 66	0.04 ± 0.005	10.1 ± 0.8	6.1	78.8
23		B	15.7 ± 7.4	15.2 ± 7.4	0.95 ± 0.17	1.7 ± 0.1	6.2	101.7
24		B	11.3 ± 0.5	8.6 ± 0.3	1.31 ± 0.05	1.0 ± 0.1	6.7	58.6
25		B	7.4 ± 6.7	4.9 ± 2.1	0.94 ± 0.82	0.8 ± 0.1	6.1	99.0

Compound	R group <sup>a</sup>	Method of synthesis <sup>b</sup>	[Sobetirome] <sub>brain</sub> (ng/g) <sup>c</sup>	[Sobetirome] <sub>serum</sub> (ng/g) <sup>c</sup>	K <sub>p</sub> <sup>1h</sup>	Hydrolysis rate <sup>d</sup> (nmol mg <sup>-1</sup> min <sup>-1</sup> )	CLogP <sup>e</sup>	PSA <sup>f</sup>
26		B	15.4 ± 0.8	383.8 ± 44.4	0.04 ± 0.01	2.1 ± 0.2	6.5	58.6
27		B	2.8 ± 0.4	127.7 ± 50.4	0.03 ± 0.01	4.9 ± 0.2	4.5	78.8
28		B	68.2 ± 40.5	199.5 ± 87.4	0.58 ± 0.28	3.8 ± 0.2	3.9	84.6
29		B	8.4 ± 0.3	209.7 ± 31	0.04 ± 0.004	4.1 ± 0.1	4.6	67.8
30		B	59.9 ± 1.5	107.7 ± 12.9	0.57 ± 0.05	5 ± 0.1	4.5	82.4
31		D	1.6 ± 0.6	26.2 ± 8.2	0.06 ± 0.01	2.4 ± 0.1	3.7	113.1

<sup>a</sup>R group based on the sobetiramide structure in [Figure Figure 11](#). <sup>b</sup>Synthetic methods as described in [Scheme 1](#). <sup>c</sup>Concentrations expressed as ng sobetirome per gram tissue; data points represent mean ± SEM and n = 3. <sup>d</sup>Kinetics of prodrug hydrolysis in COS-7 cell homogenate overexpressing human FAAH, substrate concentration was 100 μM, data points represent mean ± SEM, and n = 3. <sup>e</sup>Calculated using Canvas (Schrödinger). <sup>f</sup>Previously published in ref ([8](#))

The sobetiramide library was initially screened using a 1 h tissue distribution experiment in male mice. The 1 h time point was selected because it approximates the  $T_{max}$  of sobetirome brain concentration observed previously with related sobetirome prodrugs.<sup>8,18,19</sup> Mice were dosed systemically (i.p.) with equimolar doses of test compounds, and brain and blood were collected at 1 h postdose. Using LC-MS/MS, the concentration of the parent drug sobetirome hydrolyzed from the prodrug was quantified in both the brain and serum ([Table 1](#)). Brain-to-serum concentration ratios ( $K_p^{1h}$ ) were calculated from these 1 h time points as a measure of central vs peripheral selectivity of distribution. A majority of tested sobetiramides show substantially elevated levels of sobetirome in the brain compared to an equimolar dose of sobetirome. Importantly, several derivatives including ethylamine **5**, propargylamine **8**, fluoroethylamine **15**, and difluoroethylamine **16** show comparable levels of sobetirome in the brain to those delivered by Sob-AM1 (**3**) and Sob-AM2 (**4**). With  $K_p^{1h}$  near or above unity, these prodrugs deliver sobetirome preferentially to the CNS at the 1 h time point. Combined with our previous results with Sob-AM1 and Sob-AM2, these data suggest that small, nonpolar modifications lead to favorable CNS distribution of sobetirome from sobetiramides.

As the sobetiramides were designed to include the amine components of known FAAH substrates, it is possible that the increased CNS distribution results from higher rates of FAAH-catalyzed hydrolysis. To test this hypothesis, compounds were screened in an in vitro hydrolysis assay using a cell homogenate containing expressed FAAH as previous described for Sob-AM1 and Sob-AM2.<sup>8</sup> Interestingly, the two prodrugs with the highest rates of cleavage in the in vitro enzymatic assay were the taurine derivative **14** ( $8.9 \pm 0.3$  nmol mg<sup>-1</sup> min<sup>-1</sup>) and 3-hydroxyaniline **22** ( $10.1 \pm 0.8$  nmol mg<sup>-1</sup> min<sup>-1</sup>). The remaining aromatic derivatives including the 2-hydroxyaniline demonstrated low rates of hydrolysis (**21**, **24–26**) while most of the other aliphatic and polar derivatives showed intermediate kinetics in this range similar to **4** ( $3.2 \pm 0.2$  nmol mg<sup>-1</sup> min<sup>-1</sup>). One possibility is that the charged nature of **14** precludes successful penetration of the BBB. Compound **22** demonstrated similar levels of serum sobetirome compared to an equimolar dose of sobetirome itself suggesting that this sobetiramide is cleaved by other hydrolases in addition to FAAH in vivo.

Comparing FAAH hydrolysis rates with  $K_p^{1h}$  (Figure 22A) reveals that the prodrugs with the highest CNS selectivity all have similar rates of in vitro hydrolysis ( $\sim 3\text{--}5\text{ nmol mg}^{-1}\text{ min}^{-1}$ ). This suggests that adequate enzyme kinetics is necessary but not sufficient to account for sobetirome tissue distribution in vivo.

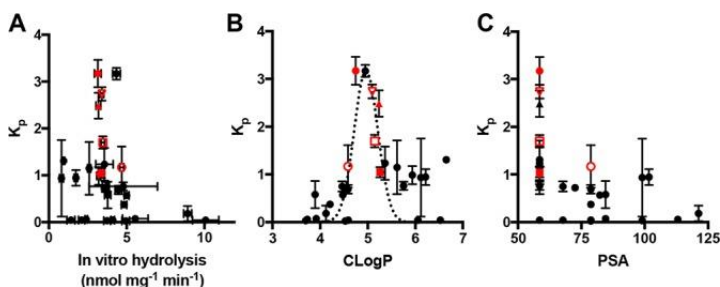


Figure 2

Comparative plots  $K_p^{1h}$  verse (A) in vitro hydrolysis in cell homogenate overexpressing

FAAH, (B) prodrug CLogP, and (C) PSA. For panel B, a Gaussian curve was fit to better illustrate the local maximum. A set of lead prodrugs from the in vivo screen are denoted by red  $\circ$  (Sob-AM1, 3), red  $\bullet$  (Sob-AM2, 4), red  $\square$  (15), red  $\blacksquare$  (16), red  $\blacktriangle$  (18), and red  $\nabla$  (5).

Compound physicochemical properties can play an outsized role in determining CNS drug penetration due to the unique nature of the BBB.<sup>20</sup> It has previously been shown by a number of QSAR studies that properties such as charged state, CLogP, polar surface area (PSA), and rotatable bonds can help predict whether a drug will be able to passively diffuse through the BBB. In the case of the sobetiramides, the complete SAR likely contains components favoring both enzymatic hydrolysis and passive diffusion through the BBB. To examine this relationship, physicochemical parameters were calculated for the sobetiramides (Table 1). When the relationship between  $K_p^{1h}$  and CLogP is plotted (Figure 22B), a bell-shaped response with an apparent maximum is found around  $\text{CLogP} \approx 5$ . While higher than average for approved CNS drugs, this value is consistent with the recommended range for CNS penetrating compounds.<sup>21-23</sup> PSA is another important parameter that correlates with known drug penetration of the brain. A plot of prodrug PSA values vs  $K_p^{1h}$  (Figure 22C) shows that the better brain penetrating prodrugs have smaller PSA values. This preference for low PSA is supported by QSAR analysis of approved CNS compounds.<sup>22</sup> It has recently been determined that drug molecules featuring PSA values  $\leq 90\text{ \AA}^2$  are optimal for BBB penetration, a claim that applies to the sobetiramides in this study.<sup>24</sup> While CLogP and PSA are two of the relevant properties affecting brain penetration, these factors could explain why lead compounds similar to 4 and 15 were selected from the in vivo screen, and more polar prodrugs with similar or better hydrolysis rates at FAAH did not perform well in vivo. This suggests that FAAH-targeted prodrugs must be optimized for enzymatic activity while also retaining CNS drug-like physicochemical properties.

As oral dosing is generally the preferred route of administration in clinical development, it is important to understand the CNS distribution of sobetirome from oral dosing of sobetiramide prodrugs. To this end, the tissue distribution of sobetirome from a subset of prodrugs was determined 1 h following oral gavage. Compared with an equimolar dose of sobetirome, both Sob-AM2 (4) and 15 show statistically significant improvement in total sobetirome in the brain and  $K_p^{1h}$  (Figure 33A).<sup>18</sup> Interestingly, the remainder of the prodrugs tested shows attenuated or nonsignificant improvements over sobetirome itself. These differences could be attributable to a more pronounced effect in first-pass metabolism for these prodrugs. With Sob-AM2 showing favorable properties in the 1 h time point, we aimed to fully characterize Sob-AM2

in a 24 h distribution experiment. Pharmacokinetic parameters for sobetirome and Sob-AM2 are summarized in [Tables 1, 2](#), and [S1](#). Sob-AM2 has an elimination half-life ( $t_{1/2}$ ) of 8.8 h, similar to that of sobetirome ( $t_{1/2} = 7.2$  h).<sup>18</sup> Exposure of sobetirome over a 24 h period following a systemic dose of Sob-AM2 shows a  $T_{max}$  of ~30 min ([Figure Figure33C](#)). The  $K_p$  of sobetirome from Sob-AM2 over the 24 h exposure ( $K_p^{0-24h} = 0.44$ ) is well within the range of typical CNS-active compounds.<sup>25</sup> When mice are dosed orally, total exposure in the brain is lower, and the  $K_p^{0-24h}$  is approximately half that compared to i.v. administration suggesting that more sobetirome is liberated in the periphery from orally administered Sob-AM2 compared to intravenous administration. It is known that FAAH is expressed in both the intestinal tract as well as the liver making it likely that FAAH-mediated cleavage of orally delivered Sob-AM2 occurs before Sob-AM2 crosses these first-pass barriers into systemic circulation, which could account for the additional peripheral prodrug cleavage observed from oral administration.<sup>26</sup>

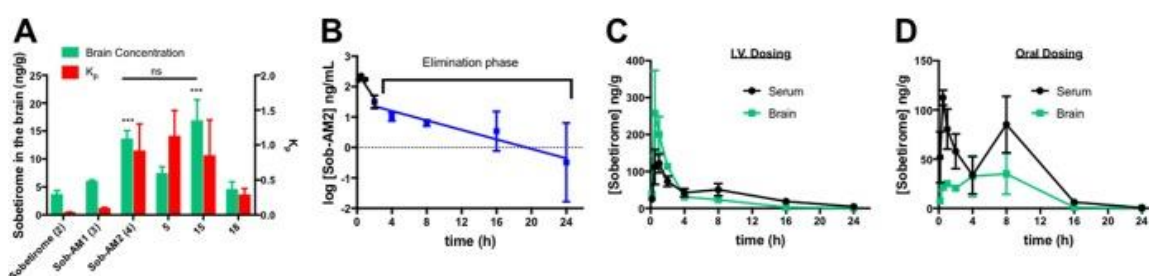


**Figure 3**

*Tissue distribution of lead prodrugs from oral dosing and 24 h pharmacokinetic analysis of Sob-AM2. (A) Distribution from dose (p.o., 9.15  $\mu\text{mol/kg}$ ) of sobetirome or lead prodrugs followed by tissue collection 1 h postdose. (B) Serum concentration of Sob-AM2 following single dose (9.15  $\mu\text{mol/kg}$ , i.v.) over 24 h. The elimination phase for Sob-AM2 is highlighted as blue. (C) Brain and serum distribution of sobetirome from a single dose of Sob-AM2 (9.15  $\mu\text{mol/kg}$ , i.v.) over 24 h postdose. (D) Same as that in panel C but dosed by oral gavage (p.o., 9.15  $\mu\text{mol/kg}$ ). Data points represent mean  $\pm$  SEM and  $n = 3$ .*

Table 2

**Summary of Pharmacokinetic and Pharmacodynamic Properties of Sobetirome and Sob-AM2**

properties <sup>a</sup>	sobetirome <sup>b</sup>	Sob-AM2
oral bioavailability, F (%)	92	19.5 <sup>c</sup>
terminal half-life (h)	7.2	8.8 <sup>c</sup>
clearance, Cl (mL/min/kg)	8	91.7 <sup>c</sup>
brain AUC <sub>0→24h</sub> (i.v., ng·h·g <sup>-1</sup> )		694 <sup>d</sup>
$K_p^{0-24h}$ (i.v., ng·h·g <sup>-1</sup> )		0.82 <sup>d</sup>



likely that FAAH-targeted prodrugs could be developed for additional drug scaffolds beyond sobetirome, this work may define at least some of the structural requirements needed for BBB penetration and FAAH activity. Recently, Sob-AM2 has been shown to be effective in delivering sobetirome to the brain to treat a mouse model of MCT8-deficiency (Allan–Herndon–Dudley syndrome), a condition of congenital CNS hypothyroidism characterized by profound cognitive impairment.<sup>30</sup> As such, this FAAH-targeted prodrug CNS delivery strategy is providing useful tools for studying thyroid hormone action in the CNS and potentially new therapeutic agents for CNS diseases that would benefit from CNS thyroid hormone action.

***Acknowledgements:***

We thank Lisa Bleyle (OHSU Bioanalytical Shared Resource/Pharmacokinetics Core) for technical assistance with LC–MS/MS, Prof. Martin Kaczocha (Stony Brook) for the pcDNA4-FAAH plasmid, and Prof. Michael Cohen (OHSU) for the COS-7 line.

This work was supported by the OHSU Laura Fund for Innovation in Multiple Sclerosis, the National Institutes of Health (DK 052798 to T.S.S.; F32GM125127 to J.M.M.; T32DK007680 to S.J.F.), and the National Multiple Sclerosis Society (RG 5199A4/1 to D.B.).

The authors declare the following competing financial interest(s): T.S.S., J.M.M., S.J.F., Tp.B., and Tn.B. are inventors on a licensed patent application claiming central nervous system-penetrating prodrugs of sobetirome and their uses. T.S.S. and D.B. are founders of Llama Therapeutics. The remaining authors have nothing to disclose.

***Abbreviations:***

- TH thyroid hormone
- SAR structure–activity relationship
- FAAH fatty-acid amide hydrolase
- CNS central nervous system
- BBB blood–brain barrier
- MS multiple sclerosis
- AEA anandamide
- OEA oleamide
- PEA *N*-palmitoylethanolamine
- i.p. intraperitoneal
- i.v. intravenous
- p.o. per os
- $K_p^{1h}$  brain-to-serum concentration ratio 1 h post dose

$K_p^{0-24h}$  brain-to-serum exposure ratio over 24 h postdose

### **Supporting Information Available**

The Supporting Information is available free of charge on the [ACS Publications website](https://doi.org/10.1021/acsmchemlett.8b00501) at DOI: [10.1021/acsmchemlett.8b00501](https://doi.org/10.1021/acsmchemlett.8b00501).

General methods, synthetic procedures and compound characterization, in vivo pharmacology, and in vitro assays ([PDF](#))

### **Author Contributions**

§ These authors contributed equally. J.M.M., S.J.F., and T.S.S. wrote the manuscript. J.M.M., S.J.F., T.S.S., and D.B. developed the concept. J.M.M., S.J.F., and Tp.B. synthesized the compounds. J.M.M., S.J.F., Tp.B, Tn.B, and H.S.S performed and optimized in vivo experiments. All authors analyzed results. All authors have given approval to the final version of the manuscript.

### **References:**

1. Compston A.; Coles A. Multiple sclerosis. *Lancet* 2008, 372 (9648), 1502.10.1016/S0140-6736(08)61620-7. [[PubMed](#)] [[CrossRef](#)] [[Google Scholar](#)]
2. Baxi E. G.; Schott J. T.; Fairchild A. N.; Kirby L. A.; Karani R.; Uapinyoying P.; Pardo-Villamizar C.; Rothstein J. R.; Bergles D. E.; Calabresi P. A. A selective thyroid hormone beta receptor agonist enhances human and rodent oligodendrocyte differentiation. *Glia* 2014, 62 (9), 1513.10.1002/glia.22697. [[PMC free article](#)] [[PubMed](#)] [[CrossRef](#)] [[Google Scholar](#)]
3. Zhang M.; Ma Z.; Qin H.; Yao Z. Thyroid Hormone Potentially Benefits Multiple Sclerosis via Facilitating Remyelination. *Mol. Neurobiol.* 2016, 53 (7), 4406.10.1007/s12035-015-9375-z. [[PubMed](#)] [[CrossRef](#)] [[Google Scholar](#)]
4. Baxter J. D.; Webb P. Thyroid hormone mimetics: potential applications in atherosclerosis, obesity and type 2 diabetes. *Nat. Rev. Drug Discovery* 2009, 8 (4), 308.10.1038/nrd2830. [[PubMed](#)] [[CrossRef](#)] [[Google Scholar](#)]
5. Trost S. U.; Swanson E.; Gloss B.; Wang-Iverson D. B.; Zhang H.; Volodarsky T.; Grover G. J.; Baxter J. D.; Chiellini G.; et al. The thyroid hormone receptor- $\beta$ -selective agonist GC-1 differentially affects plasma lipids and cardiac activity. *Endocrinology* 2000, 141 (9), 3057.10.1210/endo.141.9.7681. [[PubMed](#)] [[CrossRef](#)] [[Google Scholar](#)]
6. Takahashi N.; Asano Y.; Maeda K.; Watanabe N. In vivo evaluation of 1-benzyl-4-aminoindole-based thyroid hormone receptor  $\beta$  agonists: importance of liver selectivity in drug discovery. *Biol. Pharm. Bull.* 2014, 37 (7), 1103.10.1248/bpb.b13-00915. [[PubMed](#)] [[CrossRef](#)] [[Google Scholar](#)]
7. Devereaux J.; Ferrara S. J.; Banerji T.; Placzek A. T.; Scanlan T. S. Increasing Thyromimetic Potency through Halogen Substitution. *ChemMedChem* 2016, 11 (21), 2459.10.1002/cmhc.201600408. [[PMC free article](#)] [[PubMed](#)] [[CrossRef](#)] [[Google Scholar](#)]
8. Meinig J. M.; Ferrara S. J.; Banerji T.; Banerji T.; Sanford-Crane H. S.; Bourdette D.; Scanlan T. S. Targeting Fatty-Acid Amide Hydrolase with Prodrugs for CNS-Selective Therapy. *ACS Chem. Neurosci.* 2017, 8 (11), 2468.10.1021/acchemneuro.7b00239. [[PMC free article](#)] [[PubMed](#)] [[CrossRef](#)] [[Google Scholar](#)]
9. Cravatt B. F.; Giang D. K.; Mayfield S. P.; Boger D. L.; Lerner R. A.; Gilula N. B. Molecular characterization of an enzyme that degrades neuromodulatory fatty-acid

- amides. *Nature* 1996, 384 (6604), 83.10.1038/384083a0. [[PubMed](#)] [[CrossRef](#)] [[Google Scholar](#)]
10. Cravatt B. F.; Prospero-Garcia O.; Siuzdak G.; Gilula N. B.; Henriksen S. J.; Boger D. L.; Lerner R. A. Chemical characterization of a family of brain lipids that induce sleep. *Science* 1995, 268 (5216), 1506.10.1126/science.7770779. [[PubMed](#)] [[CrossRef](#)] [[Google Scholar](#)]
  11. Lambert D. M.; Vandevorde S.; Jonsson K. O.; Fowler C. J. The palmitoylethanolamide family: a new class of anti-inflammatory agents?. *Curr. Med. Chem.* 2002, 9 (6), 663.10.2174/0929867023370707. [[PubMed](#)] [[CrossRef](#)] [[Google Scholar](#)]
  12. Saghatelian A.; Trauger S. A.; Want E. J.; Hawkins E. G.; Siuzdak G.; Cravatt B. F. Assignment of Endogenous Substrates to Enzymes by Global Metabolite Profiling. *Biochemistry* 2004, 43 (45), 14332.10.1021/bi0480335. [[PubMed](#)] [[CrossRef](#)] [[Google Scholar](#)]
  13. Lang W.; Qin C.; Lin S.; Khanolkar A. D.; Goutopoulos A.; Fan P.; Abouzid K.; Meng Z.; Biegel D.; Makriyannis A. Substrate Specificity and Stereoselectivity of Rat Brain Microsomal Anandamide Amidohydrolase. *J. Med. Chem.* 1999, 42 (5), 896.10.1021/jm980461j. [[PubMed](#)] [[CrossRef](#)] [[Google Scholar](#)]
  14. Mofford D. M.; Adams S. T.; Reddy G. S. K. K.; Reddy G. R.; Miller S. C. Luciferin amides enable in vivo bioluminescence detection of endogenous fatty acid amide hydrolase activity. *J. Am. Chem. Soc.* 2015, 137 (27), 8684.10.1021/jacs.5b04357. [[PMC free article](#)] [[PubMed](#)] [[CrossRef](#)] [[Google Scholar](#)]
  15. Deng H. Recent advances in the discovery and evaluation of fatty acid amide hydrolase inhibitors. *Expert Opin. Drug Discovery* 2010, 5 (10), 961.10.1517/17460441.2010.513378. [[PubMed](#)] [[CrossRef](#)] [[Google Scholar](#)]
  16. Roques B. P.; Fournie-Zaluski M. C.; Wurm M. Inhibiting the breakdown of endogenous opioids and cannabinoids to alleviate pain. *Nat. Rev. Drug Discovery* 2012, 11 (4), 292.10.1038/nrd3673. [[PubMed](#)] [[CrossRef](#)] [[Google Scholar](#)]
  17. Di Marzo V. New approaches and challenges to targeting the endocannabinoid system. *Nat. Rev. Drug Discovery* 2018, 17 (9), 623.10.1038/nrd.2018.115. [[PubMed](#)] [[CrossRef](#)] [[Google Scholar](#)]
  18. Ferrara S. J.; Meinig J. M.; Placzek A. T.; Banerji T.; McTigue P.; Hartley M. D.; Sanford-Crane H. S.; Banerji T.; Bourdette D.; Scanlan T. S. Ester-to-amide rearrangement of ethanolamine-derived prodrugs of sobetirome with increased blood-brain barrier penetration. *Bioorg. Med. Chem.* 2017, 25 (10), 2743.10.1016/j.bmc.2017.03.047. [[PMC free article](#)] [[PubMed](#)] [[CrossRef](#)] [[Google Scholar](#)]
  19. Placzek A. T.; Ferrara S. J.; Hartley M. D.; Sanford-Crane H. S.; Meinig J. M.; Scanlan T. S. Sobetirome prodrug esters with enhanced blood-brain barrier permeability. *Bioorg. Med. Chem.* 2016, 24 (22), 5842.10.1016/j.bmc.2016.09.038. [[PMC free article](#)] [[PubMed](#)] [[CrossRef](#)] [[Google Scholar](#)]
  20. Rankovic Z. CNS drug design: balancing physicochemical properties for optimal brain exposure. *J. Med. Chem.* 2015, 58 (6), 2584.10.1021/jm501535r. [[PubMed](#)] [[CrossRef](#)] [[Google Scholar](#)]
  21. Hitchcock S. A.; Pennington L. D. Structure-brain exposure relationships. *J. Med. Chem.* 2006, 49 (26), 7559.10.1021/jm060642i. [[PubMed](#)] [[CrossRef](#)] [[Google Scholar](#)]
  22. Pajouhesh H.; Lenz G. R. Medicinal chemical properties of successful central nervous system drugs. *NeuroRx* 2005, 2 (4), 541.10.1602/neurorx.2.4.541. [[PMC free article](#)] [[PubMed](#)] [[CrossRef](#)] [[Google Scholar](#)]
  23. Wager T. T.; Hou X.; Verhoest P. R.; Villalobos A. Moving beyond Rules: The Development of a Central Nervous System Multiparameter Optimization (CNS MPO)

- Approach To Enable Alignment of Druglike Properties. ACS Chem. Neurosci. 2010, 1 (6), 435.10.1021/cn100008c. [[PMC free article](#)] [[PubMed](#)] [[CrossRef](#)] [[Google Scholar](#)]
24. Hitchcock S. A.; Pennington L. D. Structure-brain exposure relationships. J. Med. Chem. 2006, 49 (26), 7559.10.1021/jm060642i. [[PubMed](#)] [[CrossRef](#)] [[Google Scholar](#)]
  25. Doran A.; Obach R. S.; Smith B. J.; Hosea N. A.; Becker S.; Callegari E.; Chen C.; Chen X.; Choo E.; et al. The impact of P-glycoprotein on the disposition of drugs targeted for indications of the central nervous system: Evaluation using the MDR1A/1B knockout mouse model. Drug Metab. Dispos. 2005, 33 (1), 165.10.1124/dmd.104.001230. [[PubMed](#)] [[CrossRef](#)] [[Google Scholar](#)]
  26. Wei B. Q.; Mikkelsen T. S.; McKinney M. K.; Lander E. S.; Cravatt B. F. A Second Fatty Acid Amide Hydrolase with Variable Distribution among Placental Mammals. J. Biol. Chem. 2006, 281 (48), 36569.10.1074/jbc.M606646200. [[PubMed](#)] [[CrossRef](#)] [[Google Scholar](#)]
  27. Rutgers M.; Heusdens F. A.; Bonthuis F.; de Herder W. W.; Hazenberg M. P.; Visser T. J. Enterohepatic circulation of triiodothyronine (T3) in rats: importance of the microflora for the liberation and reabsorption of T3 from biliary T3 conjugates. Endocrinology 1989, 125 (6), 2822.10.1210/endo-125-6-2822. [[PubMed](#)] [[CrossRef](#)] [[Google Scholar](#)]
  28. Jorgensen E. C. Structure activity relationships of thyroxine analogs. Pharmacol. Ther., Part B 1976, 2 (4), 661.10.1016/0306-039X(76)90073-8. [[PubMed](#)] [[CrossRef](#)] [[Google Scholar](#)]
  29. Ahn K.; Johnson D. S.; Mileni M.; Beidler D.; Long J. Z.; McKinney M. K.; Weerapana E.; Sadagopan N.; Liimatta M.; et al. Discovery and Characterization of a Highly Selective FAAH Inhibitor that Reduces Inflammatory Pain. Chem. Biol. 2009, 16 (4), 411.10.1016/j.chembiol.2009.02.013. [[PMC free article](#)] [[PubMed](#)] [[CrossRef](#)] [[Google Scholar](#)]
  30. Barez-Lopez S.; Hartley M. D.; Grijota-Martinez C.; Scanlan T. S.; Guadano-Ferraz A. Sobetirome and its Amide Prodrug Sob-AM2 Exert Thyromimetic Actions in Mct8-Deficient Brain. Thyroid 2018, 28 (9), 1211.10.1089/thy.2018.0008. [[PMC free article](#)] [[PubMed](#)] [[CrossRef](#)] [[Google Scholar](#)]

**Hannah S. Sanford-Crane, Tanja Pejovic, Xiangshu Xiao.** *Drugging Homologous Recombination: Back to the Future.* Future Medicinal Chemistry, 10(11), 2018.

**Personal Contribution:**

HSC wrote the initial draft of the publication and assisted with downstream editing.

**Introduction**

If a person is lucky to live long enough, he/she will also have a significantly increased likelihood of developing a cancer. Cancer is caused by accumulation of gene mutations over time. Genomic instability is one of the two key enabling characteristics of cancer cells [1], first enabling initial tumorigenesis and later drug resistance. Genomic stability is critical to maintain cellular homeostasis and cellular identity. However, cellular DNA is constantly under the attack from both endogenous and exogenous threats, creating lesions. These lesions, particularly the DNA double-strand breaks (DSBs) are lethal to the cells. They must be repaired for the cells to survive and proliferate. There are two major pathways to repair the DSBs in mammalian cells. One is error-free homologous recombination repair (HR) and the other one is error-prone nonhomologous end-joining repair [2]. During HR, a homologous sister chromatin is used as a template to repair the breaks. In nonhomologous end-joining, on the other hand, the broken DNA ends are simply ligated together without a need for a homologous template, often leading to some deletions of the original DNA sequences. It is the HR process that maintains the integrity of our cellular genome.

**Reversing resistance**

While genomic instability is a hallmark of cancer cells, the genome cannot be too unstable. After passing a certain intolerable threshold, the cancer cells will die from excessive DSBs or genomic changes. This creates a unique opportunity to develop novel cancer therapies by targeting the HR pathway. The viability of targeting HR repair for anti-cancer therapeutics is supported by the recent US FDA approval of three different PARP inhibitors (olaparib, rucaparib and niraparib) for high-grade serous ovarian cancer (HGSOC). These PARP inhibitors are mostly effective in patients with preexisting somatic or germline BRCA mutations through a process called synthetic lethality [3]. BRCA1 and BRCA2 are two distinct breast and ovarian cancer-associated tumor suppressor genes. They are essential for instigating the HR repair pathway in collaboration with the nuclease MRN (Mre11-Rad50-NBS1) complex [2]. Mutations in BRCA genes result in deficient HR repair activity, a process which cancer cells are particularly reliant on due to high level of replication stress [4]. In the case of HGSOC, carriers of BRCA, which account for only approximately 30% of the patients are more sensitive to existing drugs including platinum salts and PARP inhibitors present significantly better prognosis than noncarriers. Even these BRCA carriers eventually develop resistance to the PARP inhibitors or platinum drugs. Although the mechanisms underlying the resistance are incompletely understood, restoration of HR function is a major cause [5,6]. Therefore, pharmacological strategies to drug the HR pathway can potentially expand the utility of existing PARP inhibitors and platinum drugs by priming the non-BRCA carriers and reversing the resistance mechanisms seen in the clinic with PARP inhibitors and platinum drugs. Practically, because HGSOC patients are routinely screened to assess BRCA mutations, this type of therapy can be easily incorporated into precision oncology therapy arena. If BRCA mutations (germline or somatic) are identified, the patients can be treated with existing

PARP inhibitors or platinum salts. Once these patients develop drug resistance through restoration of HR pathway, an HR inhibitor can be added to the patient's treatment regimen. If BRCA mutations are not found, the patients can be treated with an HR inhibitor alone or in combination with existing PARP inhibitors or platinum salts.

### **Targeting the homologous recombination repair pathway**

The HR pathway involves a hierarchical series of action of protein complexes at the DSB sites [7]. These proteins are primarily involved in protein–DNA and/or protein–protein interactions. Unfortunately, these interaction interfaces are challenging targets for small molecule inhibitors, which has significantly hindered development of potent and direct inhibitors of the HR pathway. In addition to small molecules that target the MRN complex (e.g., mirin [8], PFM01 and PFM39 [9]), chemical inhibitors of Rad51, the DNA recombinase involved in the final step of HR have also been identified [10]. However, most of these inhibitors suffer from low potency and/or selectivity, reflecting the challenges in directly drugging these protein complexes. Therefore, extensive efforts are ongoing to identify regulatory proteins of the HR pathway with the goal of indirectly drugging the HR pathway.

### **Transcriptional regulation**

Bromodomain-containing proteins can recognize acetylated lysine residues in histone and nonhistone proteins to regulate transcription and protein–protein interactions [11]. These proteins are found to be highly amenable for small molecules and numerous chemical inhibitors have been developed to target a number of bromodomains. Among these, inhibitors of BRD4 were recently shown to potently inhibit HR efficiency in many different types of cancer cells, including breast cancer, ovarian cancer and pancreatic cancer [12,13]. Different mechanisms have been proposed for how the BRD4 inhibitors inhibit HR. One mechanism involves the transcription repression of BRCA1 and Rad51 [12] by BRD4 inhibitors, while another is through transcription inhibition of CtIP [13], whose gene product enhances the MRN complex's nuclease activity to process the DSB sites to initiate HR. It is possible that different chromatin states in different cell types may favor one mechanism over the other.

### **Ubiquitination**

Another class of enzymes that have recently emerged as druggable targets to modulate the HR pathway is deubiquitinating enzymes (DUBs). Dynamic ubiquitination and deubiquitination of FANCD2, a protein component in the Fanconi anemia (FA) complex is required for proper function of the FA complex to promote HR [14]. USP1 is responsible for deubiquitinating FANCD2 and potent small molecule inhibitors (e.g., ML323) of USP1 have been developed [15]. These inhibitors have been shown to be able to suppress HR activity and resensitize cisplatin-resistant cancer cells to cisplatin [15]. UCHL3 is another DUB found to deubiquitinate Rad51 to promote its interaction with BRCA2 for loading to the processed DSB sites [16]. It will be interesting to see if potent and specific inhibitors of UCHL3 can be developed to sensitize the HR-proficient cells to PARP inhibitors or other DNA-damaging agents.

### **Future perspective**

While the roles of USP1 and UCHL3 mentioned above are not necessarily related to their substrates degradation, other DUBs may be identified as important regulators of HR protein turnover. It is anticipated that inhibitors of these DUBs will likely impact HR by modulating the

protein abundance. Along this same line of protein homeostasis, recently developed fragment-based screening strategies can be used to identify small molecule fragments that bind directly to HR proteins. Once these fragments are identified, they can be conjugated with a ubiquitin E3 ligase ligand (e.g., thalidomide) to create a proteolysis targeted chimera (PROTAC) for targeted protein degradation [17]. In conclusion, a better fundamental understanding of the regulation of the HR pathway and recent technology developments in designing inhibitors should facilitate rapid development of novel HR inhibitors as potential novel cancer therapies [18].

### Financial & competing interests disclosure

The authors are grateful for the financial support provided by the NIH (R01CA211866, R01GM122820 and R21CA220061) and the Elsa U Pardee Foundation. The authors have no other relevant affiliations or financial involvement with any organization or entity with a financial interest in or financial conflict with the subject matter or materials discussed in the manuscript apart from those disclosed.

### References:

1. Hanahan D, Weinberg RA. Hallmarks of cancer: the next generation. *Cell* 144(5), 646–674 (2011).[Crossref](#), [Medline](#), [CAS](#), [Google Scholar](#)
2. Chapman JR, Taylor MR, Boulton SJ. Playing the end game: DNA double-strand break repair pathway choice. *Mol. Cell* 47(4), 497–510 (2012).[Crossref](#), [Medline](#), [CAS](#), [Google Scholar](#)
3. Farmer H, McCabe N, Lord CJ et al. Targeting the DNA repair defect in BRCA mutant cells as a therapeutic strategy. *Nature* 434(7035), 917–921 (2005).[Crossref](#), [Medline](#), [CAS](#), [Google Scholar](#)
4. Halazonetis TD, Gorgoulis VG, Bartek J. An oncogene-induced DNA damage model for cancer development. *Science* 319(5868), 1352–1355 (2008).[Crossref](#), [Medline](#), [CAS](#), [Google Scholar](#)
5. Sakai W, Swisher EM, Karlan BY et al. Secondary mutations as a mechanism of cisplatin resistance in BRCA2-mutated cancers. *Nature* 451(7182), 1116–1120 (2008).[Crossref](#), [Medline](#), [CAS](#), [Google Scholar](#)
6. Norquist B, Wurz KA, Pennil CC et al. Secondary somatic mutations restoring BRCA1/2 predict chemotherapy resistance in hereditary ovarian carcinomas. *J. Clin. Oncol.* 29(22), 3008–3015 (2011).[Crossref](#), [Medline](#), [CAS](#), [Google Scholar](#)
7. Prakash R, Zhang Y, Feng W, Jasin M. Homologous recombination and human health: the roles of BRCA1, BRCA2, and associated proteins. *Cold Spring Harb. Perspect. Biol.* 7(4), a016600 (2015).[Crossref](#), [Medline](#), [Google Scholar](#)
8. Dupre A, Boyer-Chatenet L, Sattler RM et al. A forward chemical genetic screen reveals an inhibitor of the Mre11-Rad50-Nbs1 complex. *Nat. Chem. Biol.* 4(2), 119–125 (2008).[Crossref](#), [Medline](#), [CAS](#), [Google Scholar](#)
9. Shibata A, Moiani D, Arvai AS et al. DNA double-strand break repair pathway choice is directed by distinct MRE11 nuclease activities. *Mol. Cell* 53(1), 7–18 (2014).[Crossref](#), [Medline](#), [CAS](#), [Google Scholar](#)
10. Budke B, Lv W, Kozikowski AP, Connell PP. Recent developments using small molecules to target RAD51: how to best modulate RAD51 for anticancer therapy? *ChemMedChem* 11(22), 2468–2473 (2016).[Crossref](#), [Medline](#), [CAS](#), [Google Scholar](#)

11. Fujisawa T, Filippakopoulos P. Functions of bromodomain-containing proteins and their roles in homeostasis and cancer. **Nat. Rev. Mol. Cell Biol.** 18(4), 246–262 (2017).[Crossref](#), [Medline](#), [CAS](#), [Google Scholar](#)
12. Yang L, Zhang Y, Shan W et al. Repression of BET activity sensitizes homologous recombination-proficient cancers to PARP inhibition. **Sci. Transl. Med.** 9(400), ea11645 (2017).[Crossref](#), [Medline](#), [Google Scholar](#)
13. Sun C, Yin J, Fang Y et al. BRD4 inhibition is synthetic lethal with PARP inhibitors through the induction of homologous recombination deficiency. **Cancer Cell** 33(3), 401–416. (2018).[Crossref](#), [Medline](#), [CAS](#), [Google Scholar](#)
14. Kee Y, D'Andrea AD. Expanded roles of the Fanconi anemia pathway in preserving genomic stability. **Genes Dev.** 24(16), 1680–1694 (2010).[Crossref](#), [Medline](#), [CAS](#), [Google Scholar](#)
15. Liang Q, Dexheimer TS, Zhang P et al. A selective USP1-UAF1 inhibitor links deubiquitination to DNA damage responses. **Nat. Chem. Biol.** 10(4), 298–304 (2014).[Crossref](#), [Medline](#), [CAS](#), [Google Scholar](#)
16. Luo K, Li L, Li Y et al. A phosphorylation–deubiquitination cascade regulates the BRCA2-RAD51 axis in homologous recombination. **Genes Dev.** 30(23), 2581–2595 (2016).[Crossref](#), [Medline](#), [CAS](#), [Google Scholar](#)
17. Cromm PM, Crews CM. Targeted protein degradation: from chemical biology to drug discovery. **Cell Chem. Biol.** 24(9), 1181–1190 (2017).[Crossref](#), [Medline](#), [CAS](#), [Google Scholar](#)
18. Li BX, Chen J, Chao B. Anticancer pyrroloquinazoline LBL1 targets nuclear lamins. **ACS Chem. Biol.** 13(5), 1380–1387 (2018).[Crossref](#), [Medline](#), [CAS](#), [Google Scholar](#)

J. Matthew Meinig, Skylar J. Ferrara, Tania Banerji, Tapasree Banerji, **Hannah S. Sanford-Crane**, Dennis Bourdette, and Thomas S. Scanlan. *Targeting Fatty-Acid Amide Hydrolase with Prodrugs for CNS-Selective Therapy*. ACS Chemical Neuroscience, 8(11), 2468-2476, 2017.

**Abstract:**

The blood-brain barrier (BBB) can be a substantial impediment to achieving therapeutic levels of drugs in the CNS. Certain chemical functionality such as the carboxylic acid is a general liability for BBB permeability preventing significant CNS distribution of a drug from a systemic dose. Here, we report a strategy for CNS-selective distribution of the carboxylic acid containing thyromimetic sobetirome using prodrugs targeted to fatty-acid amide hydrolase (FAAH), which is expressed in the brain. Two amide prodrugs of sobetirome were shown to be efficient substrates of FAAH with  $V_{max}/K_M$  values comparable to the natural endocannabinoid FAAH substrate anandamide. In mice, a systemic dose of sobetirome prodrug, leads to a substantial ~60-fold increase in brain distribution ( $K_p$ ) of sobetirome compared to an equimolar systemic dose of the parent drug. The increased delivery of sobetirome to the brain from the prodrug was diminished by both pharmacological inhibition and genetic deletion of FAAH *in vivo*. The increased brain exposure of sobetirome arising from the prodrug corresponds to ~30-fold increased potency in brain target engagement compared to the parent drug. These results suggest that FAAH-targeted prodrugs can considerably increase drug exposure to the CNS with a concomitant decrease in systemic drug levels generating a desirable distribution profile for CNS acting drugs.

Keywords: blood-brain barrier, FAAH, thyromimetic, prodrug, sobetirome, thyroid hormone

**Personal contribution:**

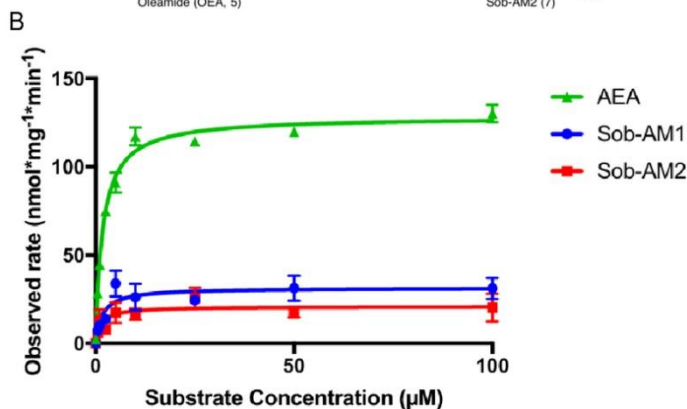
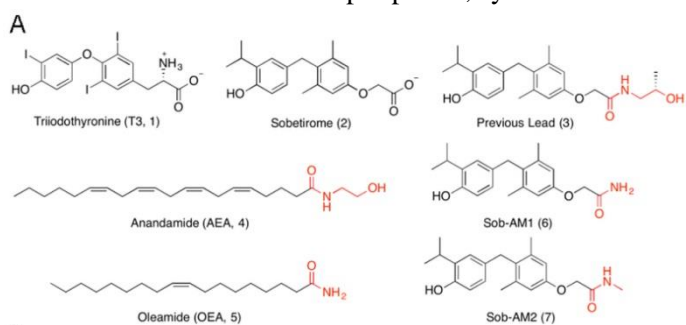
HSC (also initialized as HSS) performed and optimized *in vivo* experiments.

**Introduction:**

Central nervous system (CNS) drug development suffers from regulatory approval rates below those of peripheral drugs while also having longer average development times.<sup>1</sup> CNS drugs must achieve therapeutic exposure levels in the CNS, and this usually involves efficient penetration of the blood-brain barrier (BBB) from a peripherally administered systemic dose. The requirement for efficient distribution to the CNS is often an impediment in drug discovery, especially in cases involving lead generation from target screening where the physicochemical requirements for BBB permeability are not taken into account. The BBB primarily consists of the endothelial cell layer surrounding the capillary network in the CNS supported by astrocytes.<sup>2</sup> Through the use of tight-junctions and active transport, the BBB is responsible for controlling solute permeability into and out of the CNS.<sup>3</sup> Problems with BBB permeability have been implicated in clinical shortcomings of drugs for therapeutic areas as diverse as cancer, HIV, and lysosomal storage disorders (LSDs), among others.<sup>3-6</sup> New and general strategies for improving BBB penetration and increasing CNS-specific drug exposure are needed to improve the chances for success in CNS drug development.

Our interest in CNS acting drugs is connected to the potential use of thyroid hormone agonists for treating CNS disorders that may respond favorably to thyroid hormone action. Examples include the genetic diseases MCT-8-deficiency<sup>7</sup> and X-linked adrenoleukodystrophy (X-ALD),<sup>8,9</sup> as well

as multiple sclerosis (MS), a neurological disorder involving damage to the protective myelin sheaths that envelop nerve fibers.<sup>10</sup> Thyroid hormone stimulates both myelin development and repair, and therapeutic agents that promote remyelination are currently lacking in the collection of drugs used for treating MS and other demyelinating diseases.<sup>11</sup> However, thyroid hormone (**1**, [Figure 1A](#)) is not a suitable agent for chronic treatment of demyelinating disorders due to the lack of a therapeutic index (TI) between the beneficial and the thyrotoxic effects on tissues such as heart, bone, and skeletal muscle.<sup>12</sup> The thyromimetic sobetirome (**2**, [Figure 1A](#)) is an attractive alternative as it displays tissue selectivity resulting in an improved TI and has progressed into clinical trials for hyperlipidemia.<sup>13</sup> For the goal of treating CNS disorders, sobetirome is unique among thyromimetics as it<sup>14, 15</sup> and close analogues<sup>16</sup> are the only thyromimetics known to distribute to the brain from a peripheral, systemic dose.



were monitored by quantifying product formation by LC-MS/MS. A summary of  $V_{max}$  and  $K_m$  values can be found in [Table 1](#). For each substrate concentration, reaction time and protein levels were adjusted to maintain <10% substrate conversion. Data represent mean  $\pm$  SEM

While sobetirome does distribute to the CNS, the fraction of the administered dose that reaches the CNS is at the lower end of the range of approved CNS drugs.<sup>17</sup> We have been examining strategies to increase CNS distribution of sobetirome while concomitantly decreasing peripheral exposure in an effort to create new agents with improved CNS distribution profiles. These efforts have involved the creation of ester and amide prodrugs of sobetirome that mask sobetirome in circulation and peripheral tissues, but liberate sobetirome upon hydrolysis in the CNS.<sup>18, 19</sup> The discovery that the best-in-class sobetirome ethanolamine ester spontaneously rearranged to the corresponding ethanolamide (**3**, [Figure 1A](#)) under physiological conditions revealed the structural similarity between this sobetirome amide derivative and anandamide (AEA, **4**, [Figure 1A](#)), one of the endogenous cannabinoid substrates for fatty acid amide hydrolase (FAAH).<sup>19</sup> This led to the hypothesis that FAAH was responsible for cleavage of this amide prodrug to sobetirome,

[Figure 1.](#)

**Sobetiromides are substrates of FAAH.**

(A) Chemical structures of thyroid hormone (T3), sobetirome, two endogenous substrates of FAAH (AEA and OEA), and novel FAAH-targeted sobetirome amide (sobetiromide) prodrugs. (B) Using cell homogenate overexpressing human FAAH, Michaelis-Menten curves were produced for both Sob-AM1 and Sob-AM2 compared with the endogenous FAAH substrate AEA. Hydrolysis reactions (n=3)

suggesting that sobetirome amides (“sobetiramides”) tailored as substrates for FAAH would be a highly effective strategy for liberating sobetirome in the CNS while minimizing peripheral exposure. Here we report that FAAH-tailored sobetiramides are indeed efficient substrates for FAAH that deliver exceptionally high concentrations of sobetirome to the CNS with minimal peripheral exposure from a peripheral systemic dose.

## Results:

### Sobetiramides as FAAH substrates

From our previous studies, the best sobetirome prodrug for generating sobetirome in the brains of mice dosed peripherally with the prodrug was an ethanolamine amide (**3**) with a structural resemblance for the endogenous FAAH substrate AEA (**4**). FAAH is a membrane bound serine hydrolase found in the brain and select peripheral tissues and intercellular signaling by AEA, oleamide (OEA, **5**, [Figure 1A](#)), and other endogenous fatty-acid amides is terminated by FAAH-catalyzed hydrolysis to fatty acids.<sup>20, 21</sup> In addition to endogenous cannabinoids, FAAH accepts a number of structurally diverse natural and synthetic fatty-acid amides as substrates.<sup>22–24</sup> This known substrate promiscuity together with a recent report that synthetic luciferin amides were viable FAAH substrates,<sup>25</sup> led us to synthesize FAAH-targeted amide prodrugs of sobetirome.

Two such sobetiramides, Sob-AM1 (**6**) and Sob-AM2 (**7**, [Figure 1A](#)), were tested as FAAH substrates using COS7 cell homogenate with overexpressed human FAAH similar to previous reports.<sup>26, 27</sup> Both Sob-AM1 and Sob-AM2 demonstrated saturation kinetics of hydrolysis ([Figure 1B](#)) with observed  $V_{max}$  values ( $31.4 \pm 2.9$  and  $20.9 \pm 2.5$  nmol mg<sup>-1</sup> min<sup>-1</sup>, respectively) 4–6 fold lower than the endogenous substrate AEA ( $128.4 \pm 2.3$  nmol mg<sup>-1</sup> min<sup>-1</sup>). Interestingly, both prodrugs exhibited similar  $K_M$  values ( $1.7 \pm 0.7$  and  $1.3 \pm 0.8$  μM, respectively) to that observed for AEA ( $1.8 \pm 0.2$  μM) in our experiment, which leads to  $V_{max}/K_M$  ratios that are also 4–6 fold lower than AEA ([Table 1](#)). These findings demonstrate that FAAH is capable of efficiently hydrolyzing sobetiramides *in vitro* making these compounds a novel class of synthetic FAAH substrates.

Table 1.

A summary of Michaelis-Menten observed parameters for AEA, Sob-AM1, and Sob-AM2.

Substrate	$V_{max}$ (nmol * mg <sup>-1</sup> * min <sup>-1</sup> )	$K_M$ (μM)	$V_{max}/K_M$
AEA	$128.4 \pm 2.3$	$1.8 \pm 0.2$	$71.1 \pm 6.3$
Sob-AM1	$31.4 \pm 2.9$	$1.7 \pm 0.7$	$18.9 \pm 8.7$
Sob-AM2	$20.9 \pm 2.5$	$1.3 \pm 0.8$	$15.5 \pm 9.7$

### In vivo pharmacology of sobetiramides

We next evaluated whether a peripheral dose of Sob-AM1 or Sob-AM2 would deliver more sobetirome to the brain than a peripheral dose of sobetirome. Equimolar doses of the three compounds (i.p., 3.05 μmol/kg) were administered to different cohorts of mice and total brain and serum concentrations of sobetirome were quantified 1 hour post-injection. Compared to

sobetirome administration, Sob-AM1 and Sob-AM2 showed average total sobetirome levels in the brain approximately 17- to 20-fold higher (Figure 2A). This increase in sobetirome in the brain from the sobetiramides was accompanied by a substantial decrease in circulating levels of sobetirome (Figure 2B).

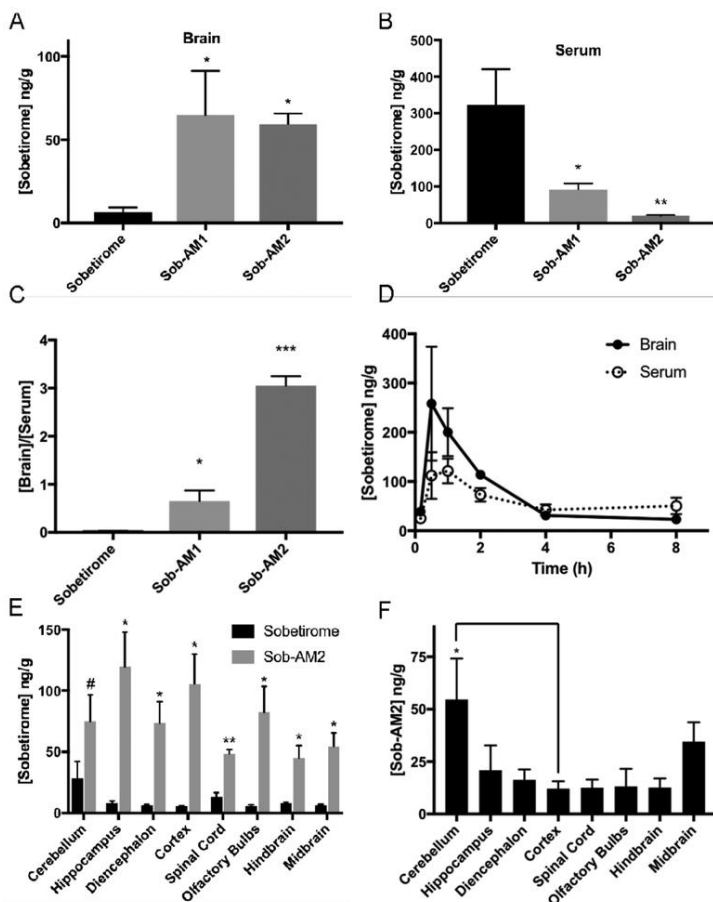


(Figure 2B).

Consistent with previous reports in mice,<sup>19</sup> sobetirome was found to have a [brain]/[serum] ratio ( $K_p$ ) of 0.03 from this single time-point experiment, whereas the sobetiramides had  $K_p$  values that were considerably larger (Figure 2C). The primary amide Sob-AM1 shows a ~20-fold increase in  $K_p$ , and the *N*-methyl amide Sob-AM2 demonstrates a remarkable 100-fold increase in  $K_p$  compared to sobetirome.

Figure 2.

**Sobetiramides substantially increase brain exposure while decreasing peripheral concentrations of sobetirome *in vivo*.**

Mouse cohorts ( $n=6$ ) were treated (*i.p.*,  $3.05 \mu\text{mol/kg}$ ) with sobetirome, Sob-AM1, or Sob-

AM2. After 1 h, tissues were collected and analyzed by LC-MS/MS for sobetirome levels in the (A) brain and (B) serum. (C) Brain-to-serum concentration ratios at this 1 h time point suggests significant increases in brain selective distribution of the prodrugs. Statistical analyses for A-C were done using one-way ANOVA (Fisher LSD) comparing prodrug values to sobetirome (A-C). To quantify sobetirome exposure from peripherally dosed Sob-AM over time, sobetirome levels the brain and serum (D) was measured from mouse cohorts treated at  $t=0$  (*i.v.*,  $9.15 \mu\text{mol/kg}$ ) and measured over 8 h post-dose. Each data point represents  $n=3$ . Calculated AUC values are summarized in Table 2. (E) Mice cohorts ( $n=3$ ) were treated with sobetirome or Sob-AM2 identical to A-C except brain regions were dissected and analyzed separately. Sobetirome concentrations were significantly increased in Sob-AM2 treated mice across almost all CNS regions including the cortex (18-fold) and spinal cord (3.5-fold). Statistical analyses for E were done using multiple two-tailed *t*-test comparing sobetirome/Sob-AM2 treatments. (F) Sob-AM2 levels were quantified in the same dissected CNS regions as (E) using LC-MS/MS monitoring the Sob-AM2 ion. Intact (non-hydrolyzed) prodrug can be observed across CNS regions at levels similar to the cortex with only the cerebellum displaying significantly elevated Sob-AM2. Statistical analysis for F was done using one-way ANOVA (Fisher LSD) comparing regions to the cortex. All data in A-F represent mean  $\pm$  SEM and are expressed as a function of tissue weight. (\*  $P < 0.05$ , \*\*  $P < 0.01$ , \*\*\*  $P < 0.001$ )

Due to its favorable CNS distribution in this 1 h assay, Sob-AM2 was further evaluated in an 8-hour time course experiment. In this experiment, mice were dosed peripherally with Sob-AM2 (i.v., 9.15  $\mu\text{mol/kg}$ ) and sobetirome levels in brain and serum were quantified at specific time points over the next 8 h (Figure 2D). Calculated area under the curve (AUC) values for Sob-AM2 compared with previously reported values for sobetirome and compound **3** are summarized in Table 2.<sup>19</sup> When comparing 8-hour exposure levels, Sob-AM2 maintains brain selectivity with  $K_p$  of  $1.20 \pm 0.27$ . This represents a 60-fold improvement over the parent drug sobetirome ( $0.02 \pm 0.006$ ) and a 9-fold improvement to the previous best-in-class prodrug compound **3** ( $0.13 \pm 0.03$ ).<sup>19</sup> Interestingly, Sob-AM2 exhibits a ~4-fold increased hydrolysis rate at FAAH *in vitro* compared to **3** (Table S1) suggesting the improvement in  $K_p$  could at least partially be attributed to higher cleavage rates.

Table 2.

Comparative brain and serum exposures for sobetirome, **3**, and Sob-AM2 showing systemic improvements in  $\text{AUC}_{\text{brain}}/\text{AUC}_{\text{serum}}$  ( $K_p$ ).

Compound	Brain-AUC <sub>0-8h</sub> (ng * h * g <sup>-1</sup> )	Serum-AUC <sub>0-8h</sub> (ng * h * g <sup>-1</sup> )	$K_p^a$
Sobetirome ( <b>2</b> ) <sup>b</sup>	$9.9 \pm 1.0$	$472.6 \pm 132.4$	$0.02 \pm 0.006$
<b>3</b> <sup>b</sup>	$17.2 \pm 2.3$	$136.5 \pm 21.0$	$0.13 \pm 0.03$
Sob-AM2 ( <b>7</b> ) <sup>c</sup>	$573.9 \pm 82.6$	$479.8 \pm 84.5$	$1.20 \pm 0.27$

<sup>a</sup> $K_p = \text{AUC}_{\text{brain}}/\text{AUC}_{\text{serum}}$

<sup>b</sup>Data reproduced from Ferrara, 2017 (i.p., 1.5  $\mu\text{mol/kg}$ )

<sup>c</sup>This work (i.v., 9.15  $\mu\text{mol/kg}$ )

We next sought to understand which regions of the brain and CNS received sobetirome exposure from a peripheral dose of Sob-AM2. Mice receiving equimolar doses (i.p., 3.05  $\mu\text{mol/kg}$ ) of sobetirome or Sob-AM2 were sacrificed after 1 h and brains were dissected into general anatomical regions. Concentrations of sobetirome (Figure 2E) and Sob-AM2 (Figure 2F) were quantified in the dissected regions revealing that Sob-AM2 treatment led to a general increase in sobetirome concentrations across all brain regions examined compared to the brains from animals treated with sobetirome. The largest observed changes sobetirome levels with Sob-AM2 treatment were seen in the cortex (18.9-fold), hippocampus (14.7-fold), and olfactory bulbs (14.7-fold). Increased sobetirome concentrations were also observed in the spinal cord indicating that the increased CNS penetration afforded by Sob-AM2 is not limited to the brain. In prodrug treated samples, each region contained lower levels of non-hydrolyzed Sob-AM2 compared to unmasked sobetirome and the amount of non-hydrolyzed Sob-AM2 was comparable across most regions (Figure 2F). These results demonstrate CNS-wide increases in sobetirome concentrations following peripheral doses of Sob-AM2, suggesting that prodrug cleavage is not confined to a specific region, which is consistent with the known ubiquitous expression pattern of FAAH in the CNS.<sup>20</sup>

In vivo validation of FAAH as prodrug target

We next endeavored to obtain evidence showing that FAAH was the hydrolase responsible for sobetiromide cleavage *in vivo*. PF-3845 is a FAAH inhibitor that readily distributes to the CNS from a peripheral dose,<sup>28</sup> and URB-937 is a peripherally restricted FAAH inhibitor that does not cross the BBB.<sup>29</sup> Mouse cohorts were injected with either vehicle or an inhibitor (i.p., 1 mg/kg) followed by a second injection of Sob-AM2 (3.05  $\mu\text{mol/kg}$ ). One hour later mice were sacrificed and sobetiromide concentration was measured in serum, brain, and peripheral tissues. Mice that received no FAAH inhibitor (vehicle, [Figure 3A–B](#)) showed high concentration of sobetiromide in the brain with substantially lower levels in the serum and peripheral tissues. Treatment with PF-3845 reduced sobetiromide concentration in brain by >8-fold compared to vehicle treatment ([Figure 3A](#)). Serum and peripheral tissue levels of sobetiromide were also reduced in PF-3845 treated mice. The peripherally restricted FAAH inhibitor URB-937 showed a similar pattern of decreased sobetiromide in the periphery; however, brain concentrations were unaffected compared to the vehicle control ([Figure 3B](#)).

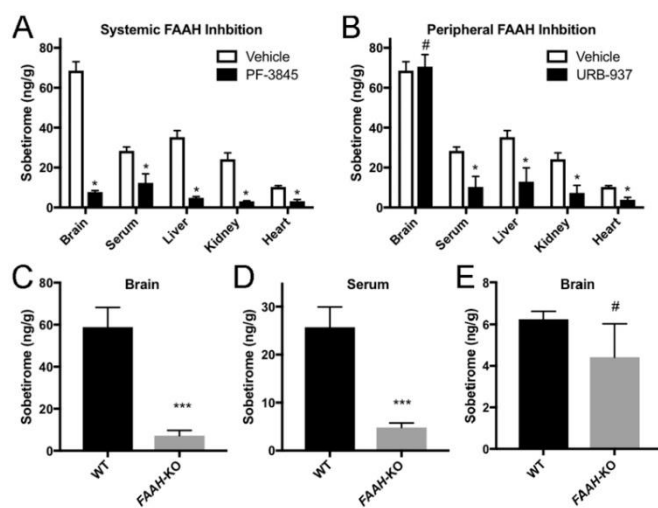


[Figure 3.](#)

**FAAH is the primary hydrolase responsible for sobetiromide hydrolysis *in vivo*.**

(A & B) FAAH inhibitors significantly decrease Sob-AM2 hydrolysis in target tissues. Mouse cohorts ( $n=3$ ) were treated with vehicle, PF-3845, or URB-937 (i.p., 1 mg/kg). 30 min post initial injection, mice were treated with Sob-

AM2 (i.p., 3.05  $\mu\text{mol/kg}$ ). Tissues were collected 1 h after the second injection. (A) Consistent with its known pharmacological distribution, PF-3845 significantly reduced sobetiromide levels in all tested tissues compared with vehicle. (B) Compared to the vehicle control, URB-937 reduced sobetiromide levels in all tested tissues except for the brain, consistent with its inability to cross the BBB. Data for vehicle treated animals is common to (A) and (B) and is replicated for clarity. Data represent mean  $\pm$  SEM and statistical analyses were performed using multiple *t*-test comparing inhibitor treatment to vehicle. (C–E). Wild type and FAAH-KO mice were treated with Sob-AM2 (i.p., 3.05  $\mu\text{mol/kg}$ ) and tissues were collected 1 h post-dose. Sobetiromide levels analyzed by LC-MS/MS. FAAH-KO mice exhibited significant lowering of sobetiromide in both the brain (C) and serum (D) compared to wild type animals that receiving an identical systemic dose. (E) Following a peripheral dose of the parent drug sobetiromide (i.p., 3.05  $\mu\text{mol/kg}$ ), FAAH-KO mice showed no significant difference in brain sobetiromide levels compared with wild type. Data represent mean  $\pm$  SEM. (C)  $n=6$ ; (D) and (E)  $n=3$ . Statistical analyses were performed using two-tailed Student *t*-tests (\*\* $P < 0.001$ , #  $P > 0.05$ )

To further validate the role of FAAH in activation of sobetiromide prodrugs, FAAH-KO mice were employed and *in vivo* concentrations of sobetiromide were measured following a peripheral dose (i.p., 3.05  $\mu\text{mol/kg}$ ) of Sob-AM2.<sup>30</sup> The FAAH-KO mice contained significantly lower sobetiromide levels in both the brain ([Figure 3C](#)) and serum ([Figure 3D](#)) compared with wild-type

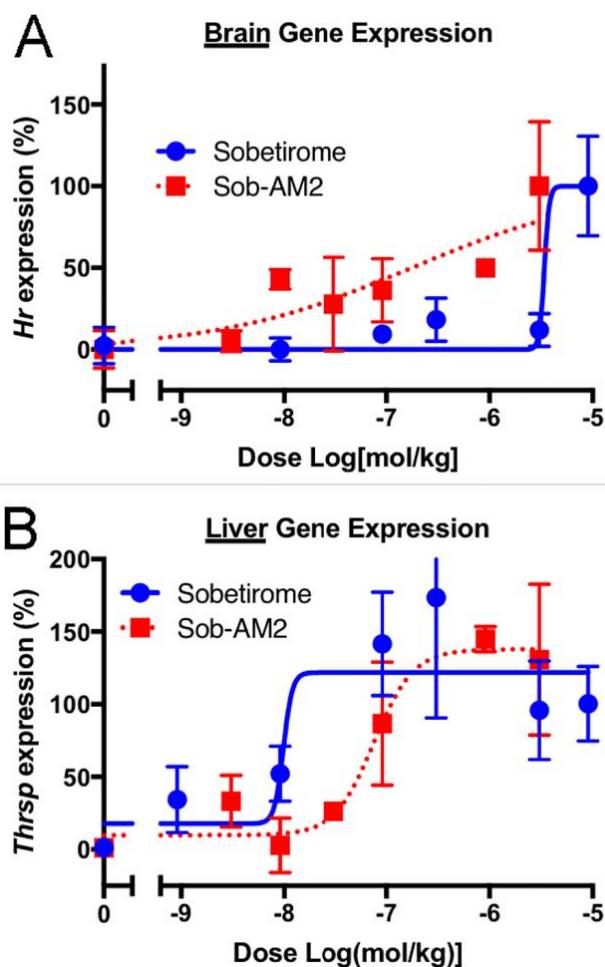
mice. Additionally, the deletion of FAAH had no significant impact on the brain accumulation of sobetirome from an equimolar peripheral dose of the parent drug (Figure 3E). The combined data from FAAH-specific inhibitors and *FAAH*-KO mice demonstrate unequivocally that FAAH is the major hydrolase responsible for generating sobetirome from sobetiramide prodrugs *in vivo*.

We next asked whether the increased brain and decreased peripheral concentrations of sobetirome delivered by Sob-AM2 translated into increased brain activity with decreased peripheral activity of the parent drug. Wild-type mice were dosed peripherally (i.p.) with Sob-AM2, and expression of *Hairless* (*Hr*) and *Thrsp*, T3-responsive genes in brain and liver, respectively, was quantified.<sup>31, 32</sup> Both sobetirome and Sob-AM2 showed the expected dose-dependent increase in brain *Hr* and liver *Thrsp* expression 6 hours post-dose. Prodrug Sob-AM2 was approximately 30-fold more potent in inducing brain *Hr* than sobetirome (Figure 4A). Likewise, Sob-AM2 was approximately 10-fold less potent than sobetirome at liver *Thrsp* induction (Figure 4B). Taken

together, these T3 target gene activation results are consistent with the regional distribution findings demonstrating that peripheral dosing of sobetiramide prodrugs leads to increased CNS and decreased peripheral levels of sobetirome via a CNS-selective prodrug cleavage mechanism involving FAAH.

Figure 4.

**Sob-AM2 is more potent in the brain and less potent in the liver at TR-activation than sobetirome.**



Following peripheral dosing (i.p.) of sobetirome or Sob-AM2 in wild type mice across a dose range, transcript levels of the known thyroid-responsive genes *Hr* and *Thrsp* were quantified in the brain (A) and liver (B), respectively. In the brain, Sob-AM2 ( $EC_{50} \sim 0.17 \mu\text{mol/kg}$ ) was more potent than sobetirome ( $EC_{50} \sim 3.4 \mu\text{mol/kg}$ ). This trend is reversed in the liver with *Thrsp* response (Sob-AM2  $EC_{50} \sim 76 \text{ nmol/kg}$ ; sobetirome  $EC_{50} \sim 10 \text{ nmol/kg}$ ). Data points represent mean  $\pm$  SEM and  $n=3$ .

### Discussion:

There are a few devastating CNS disorders that currently have no effective therapies and may benefit from a therapeutic strategy based on thyroid hormone action in the CNS. Allan-Herndon-Dudley Syndrome, or MCT-8-deficiency, is an X-linked inborn error that affects thyroid hormone transport from blood into certain tissues including the CNS.<sup>7</sup> As such, MCT-8-deficient patients

are born with a hypothyroid brain and suffer the expected cognitive deficits. These patients do not benefit from thyroid hormone replacement because transport of endogenous thyroid hormone across the BBB is impaired.<sup>7, 33</sup> X-Linked adrenoleukodystrophy (X-ALD) is an inborn error of metabolism that leads to the accumulation of very long chain fatty acids (VLCFA) resulting from loss-of-function mutations to a peroxisomal transporter called ABCD1 necessary for VLCFA degradation.<sup>34, 35</sup> The elevated VLCFA levels in the CNS lead to extensive demyelination producing debilitating neurological deficits. A related peroxisomal transporter called ABCD2 that is thyroid hormone regulated can complement defective ABCD1, and both T3 and sobetirome treatment lowers elevated VLCFA levels in the periphery and CNS of *Abcd1*-deficient mice.<sup>9</sup> Multiple sclerosis (MS) is a more prevalent inflammatory demyelinating disease in which some clinical progress has been made developing agents that are beneficial for the inflammatory component, but there are no available therapeutics that repair the damaged myelin.<sup>10</sup> Because thyroid hormone plays an important role in myelin production during development and myelin repair, thyromimetics capable of penetrating the BBB such as sobetirome have been proposed for the treatment of MS.<sup>11</sup>

The significance of these unmet clinical needs has motivated us to investigate new strategies for increasing the CNS distribution profile of thyromimetics such as sobetirome. We have undertaken a sobetirome prodrug approach, which has led us to discover a series of amide derivatives of sobetirome, sobetiramides, containing amine functionality consistent with endogenous FAAH substrates such as AEA and OEA. Here we show that these FAAH-targeted prodrugs are indeed excellent substrates for FAAH *in vitro* and *in vivo*. Peripheral dosing of these sobetiramide prodrugs generates large concentrations of sobetirome selectively in the brain compared to peripheral organs, with a considerable 60-fold increase to the [brain]/[serum] ratio ( $K_p$ ) compared to a peripheral dose of the parent drug sobetirome from an 8-hour AUC experiment. The observed  $K_p$  value of 1.2 for sobetirome delivered by Sob-AM2 represents a better CNS distribution profile than most approved CNS drugs and is an efficient example of a CNS prodrug delivery system.<sup>17, 36, 37</sup> This dramatic change in sobetirome distribution afforded by the FAAH-activated prodrug would be expected to confer therapeutic benefits for use as a CNS drug including the potential for using lower doses and an increased therapeutic index separating desired therapeutic effects in the CNS from peripheral effects.

The ability of FAAH to catalyze efficient hydrolysis of these non-natural substrates suggests that FAAH has wider substrate recognition with respect to the carboxylate side of the cleaved amide bond and is not limited to only fatty acids. Aromatic and biaryl ether containing carboxylic acid amides can also be FAAH substrates that are processed with high efficiency. The first reported glimpse of this property was the finding that luciferin amides were effective FAAH substrates that liberated luciferin in the CNS as an imaging tool.<sup>25</sup> This development led to the proposal that FAAH may be a suitable hydrolase to target for a CNS-selective prodrug,<sup>38</sup> an idea that is reduced to practice by the findings reported here. It will be helpful to understand the limits and generality of this approach for targeting molecules to the CNS for both research tools and therapeutic applications.

The BBB represents a formidable impediment for small molecule access to the CNS and the sobetiramide prodrugs presented here are able to penetrate this barrier with little apparent difficulty. That the carboxylic acid containing parent drug sobetirome is also BBB permeable, albeit to a considerably lesser degree, is remarkable as carboxylates are considered a significant liability for BBB permeability, and there are accordingly very few carboxylate-containing CNS

drugs.<sup>39</sup> Should the FAAH-targeting strategy prove to be a reasonably general one in terms of FAAH substrate selectivity, perhaps more carboxylate-containing drug candidates could be considered in CNS drug discovery. If, as is the case with sobetiramides, the amide-masked carboxylate is essential for therapeutic target engagement, then this strategy will block target engagement in tissues that do not express FAAH while facilitating target engagement in FAAH-expressing tissues like the brain. This confers a desirable and potentially therapeutically beneficial distribution profile for drugs acting in the CNS.

### ***Materials and methods:***

Chemistry. General Chemistry

<sup>1</sup>H and <sup>13</sup>C NMR were taken on a Bruker 400 MHz. All spectra were calibrated to the NMR solvent reference peak (chloroform-*d* or *d*<sub>3</sub>-MeCN). <sup>1</sup>H coupling constants (J<sub>HH</sub>, Hz) are reported as follows: chemical shift, multiplicity (br = broad, s = singlet, d = doublet, sept = septet, m = multiplet, dd = doublet of doublets), coupling constant, and integration. High-resolution mass spectrometry (HRMS) with electrospray ionization was performed by the Bioanalytical MS Facility at Portland State University. Sobetirome and *d*<sub>6</sub>-sobetirome were synthesized as previously described.<sup>40, 41</sup> All other reagents were purchased from Fisher, Sigma, or TCI and used as received. Analytical HPLC analysis was performed on a Varian ProStar HPLC with a Grace Altima C18, 5 μm column (4.6 × 250 mm) with a gradient (Solvent A: Water + 0.1% TFA; Solvent B: MeCN + 0.1% TFA) for B: 20–100% 0–20 minutes, 100% B 20–25min, 100%–20% B 25–26min, hold 20% B 26–30 min. Flowrate was 1 mL/min. Purity analysis of final compounds was determined to be >95% by HPLC (A<sub>235nm</sub>). HPLC traces can be found in the [Supplemental Information](#).

Synthesis of Compounds and Characterization

Sob-AM1 (6), 2-(4-(4-hydroxy-3-isopropylbenzyl)-3,5-dimethylphenoxy)acetamide

Sobetirome (250 mg, 0.76 mmol, 1 eq) is treated with MeOH (3 mL) in a sealed tube. Sulfuric acid (1 drop) is added and the reaction is sealed and then heated to 65 °C for 1 hour while stirring. The reaction is allowed to come to room temperature. TLC analysis (1:30 MeOH:DCM) shows complete conversion to the intermediate methyl ester. To the intermediate reaction mixture,

ammonia (7N in MeOH, 0.76 mL, 7 eq) is added. The reaction is resealed and, again, heated to 65 °C for 1 hour. The reaction flask is allowed to return to room temperature and is added to 0.5 N NaOH (20 mL) in a separatory funnel and subsequently extracted with DCM (3 × 100 mL). The organic layers are combined, dried with Na<sub>2</sub>SO<sub>4</sub>, and concentrated. Purification by flash chromatography (0–6% MeOH in DCM) gave the product as a white solid (157 mg, 0.48 mmol, 63%). Purity: 95% (HPLC). <sup>1</sup>H NMR (400 MHz, Chloroform-*d*) δ 6.93 (b, 1H), 6.65–6.56 (m, 5H), 5.85 (b, 1H), 5.19 (s, 1H), 4.51 (s, 2H), 3.92 (s, 2H), 3.19 (sept, *J* = 6.9, 1H), 2.24 (s, 6H), 1.23 (d, *J* = 6.9 Hz, 6H). <sup>13</sup>C NMR (101 MHz, CDCl<sub>3</sub>) δ 171.6, 155.1, 151.0, 138.9, 134.3, 131.7, 131.4, 126.1, 125.3, 115.2, 114.1, 67.0, 33.7, 27.1, 22.6, 20.5. HRMS (ESI) *m/z* [M+Na<sup>+</sup>] C<sub>20</sub>H<sub>25</sub>NNaO<sub>3</sub><sup>+</sup> requires 350.1727, found 350.1737

Sob-AM2 (7), 2-(4-(4-hydroxy-3-isopropylbenzyl)-3,5-dimethylphenoxy)-*N*-methylacetamide  
The synthesis was carried out identical to **6** with sobetirome (155 mg, 0.47 mmol), but using a solution of 40% methyl amine in water (610 μL, 7.05 mmol, 15 eq) instead of ammonia. The product was isolated as a white solid (144 mg, 90%). Purity: 97% (HPLC). <sup>1</sup>H NMR (400 MHz, CD<sub>3</sub>CN): 6.98 (br, 1 H), 6.89 (s, 1 H), 6.68 (s, 2 H), 6.62 (d, 1 H, *J* = 8.6 Hz), 6.54 (dd, *J* = 8.4, 2.4 Hz, 1 H), 4.37 (s, 2 H), 3.87 (s, 2 H), 3.16 (septet, *J* = 6.9 Hz, 1 H), 2.75 (d, *J* = 4.9 Hz, 3 H), 2.20 (s, 6 H), 1.12 (d, *J* = 6.9 Hz, 6 H). <sup>13</sup>C NMR (101 MHz, CDCl<sub>3</sub>) δ 169.4, 155.1, 151.0, 138.9, 134.3, 131.7, 131.2, 126.1, 125.2, 115.1, 114.0, 67.2, 33.7, 27.1, 25.8, 22.6, 20.5. HRMS (ESI) *m/z* [M+Na<sup>+</sup>] C<sub>21</sub>H<sub>27</sub>NO<sub>3</sub>Na<sup>+</sup> requires 364.1883, found *m/z* 364.1890.

*d*<sub>6</sub>-Sob-AM2 (8), 2-(4-(4-hydroxy-3-(propan-2-yl-1,1,1,3,3,3-*d*<sub>6</sub>)benzyl)-3,5-dimethylphenoxy)-*N*-methylacetamide  
The synthesis was carried out identical to **7** but using *d*<sub>6</sub>-sobetirome (scaled to 28 mg, 0.08 mmol) as a starting material. The product was isolated as a white solid (24.5 mg, 84%). Purity: 97% (HPLC). <sup>1</sup>H NMR (400 MHz, Chloroform-*d*): 6.94 (d, *J* = 1.8 Hz, 1 H), 6.68 (br, 1 H), 6.59 (m, 4 H), 5.30 (s, 1 H), 4.51 (s, 2 H), 3.92 (s, 2 H), 3.16 (s, 1 H), 2.94 (d, *J* = 5.0, 3 H), 2.23 (s, 6 H). <sup>13</sup>C NMR (101 MHz, CDCl<sub>3</sub>) δ 169.5, 155.1, 151.2, 138.9, 134.4, 131.5, 131.1, 126.1, 125.2,

115.1, 114.0, 67.2, 33.7, 26.6, 25.8, 20.5. HRMS (ESI)  $m/z$   $[M+H]^+$   $C_{21}H_{22}D_6NO_3^+$ :  $m/z$  348.2240, found  $m/z$  348.2444.

#### General Materials

Sobetirome and  $d_6$ -sobetirome were synthesized as previously described.<sup>40,41</sup> Anandamide (AEA, #90050), PF-3845 (#13279), and URB-937 (#10674) were purchased from Cayman. Arachidonic acid was purchased from Sigma (#23401).  $d_{11}$ -Arachidonic acid was purchased from Avanti (#861810E). Fatty-acid free BSA was from Alfa Aesar (#64682). Solvents were HPLC grade from Fisher.

#### Plasmids

Human FAAH cDNA in a pcDNA4 backbone was kindly provided by Prof. Martin Kaczocha (Stony Brook). A C-terminal FLAG sequence was inserted by PCR using the following primers: 5'-CGCAAATGGGCGGTAGGCGTG (f\_CMV) and 5'-AGACTCGAGTCACTTGTCGTCATCGTCTTTGTAGTCGGATGACTGCTTTTCAGGGGTCAT. The Kpn1/Xho1 digestion fragment was reinserted back into digested pcDNA4. The resulting pcDNA4-FAAH-FLAG construct was confirmed by sequencing (OHSU DNA Services Core).

#### LC-MS/MS analysis

Compound quantification was performed by LC-MS/MS as previously described<sup>19</sup> with modifications. Chromatography separation was performed on a Hamilton PRP-C18 column (5  $\mu$ m, 2.1  $\times$  50 mm, 100  $\text{\AA}$ ) fit with a Betabasic precolumn (Thermo). The gradient mobile phase was delivered at a flow rate of 0.5 mL/min, and consisted of two solvents, A: 10 mM ammonium formate in water and B: 10 mM ammonium formate in 90% acetonitrile, 10% water. The gradient was as follows: 0–0.5 min, hold 10% B; 0.5–5.1 min, 10–98% B; 5.1–7 min, hold 98% B; 7–7.1 min, 98–10% B; 7.1–8 min, hold 10%. Sample injections were 20  $\mu$ L. Either a 5500 QTRAP or 4000 QTRAP hybrid/triple quadrupole linear ion trap mass spectrometer (Applied Biosystems)

were used to detect analytes with multiple-reaction-monitoring (MRM) using parent ion  $m/z$  and a second transition. Instrument parameters were optimized for MRM transitions by direct infusion of pure compound. Sobetirome ( $m/z$  327.3  $\rightarrow$  269.3 and  $m/z$  327.3  $\rightarrow$  135.0; retention time 2.88 min),  $d_6$ -sobetirome ( $m/z$  333.0  $\rightarrow$  275.2 and 333.0  $\rightarrow$  141.1; retention time 2.86 min), arachidonic acid ( $m/z$  303.45  $\rightarrow$  259.1; retention time 5.75 min), and  $d_{11}$ -arachidonic acid ( $m/z$  314.45  $\rightarrow$  270.1; retention time 5.75 min) were detected with negative mode. Sob-AM2 ( $m/z$  342.2  $\rightarrow$  194 and 342.2  $\rightarrow$  135, retention time 4.35 min) and  $d_6$ -Sob-AM2 ( $m/z$  348.2  $\rightarrow$  194.1 and 348.2  $\rightarrow$  141.1) were detected in positive mode using a mode switch from negative to positive.

#### FAAH activity in cell homogenate

The COS-7 cell line was a kind gift of Prof. Michael Cohen (OHSU). COS-7 cells (from ATCC CRL-1651) were cultured in Dulbecco's Modified Eagle's Medium supplemented with FBS (10%), penicillin (100 units/L), and streptomycin (100  $\mu$ g/L). Cells (800,000/well) were seeded into 6-well plates (Falcon 353046) and left to adhere overnight. Cells were transfected with pcDNA4-FAAH-FLAG with Lipofectamine (Invitrogen) according to the manufacturer's protocol. Mock transfection controls were done with transfection reagent and no DNA. Cells were washed 4-days post transfection with cold PBS and scraped into cold TE buffer (125 mM Tris, 1 mM EDTA, pH 9) and sonicated (10 sec, 60Sonic Dismembrator, Fisher). Cell homogenates were stored at  $-80$  °C until use. Protein concentrations were determined by a BCA assay (Pierce). Cell homogenates were diluted into reaction buffer (TE buffer + 0.1% fatty-acid free BSA). Substrates were added as 50 $\times$  stocks in DMSO into 50  $\mu$ L aliquots of homogenate to final concentrations between 0.5  $\mu$ M and 100  $\mu$ M. Homogenate protein levels (0.25 – 10  $\mu$ g/mL) and time (5 – 15 min) were adjusted to maintain < 10% product conversion. Reactions were quenched with 100  $\mu$ L acetonitrile and vortexed for 20 s. Samples were clarified by centrifugation (10,000 rpm, 15 min, 4 °C). The supernatant was diluted 2–50 fold depending on

signal intensity into 2:1 MeCN:H<sub>2</sub>O containing 149 or 299 nM d<sub>11</sub>-arachidonic acid and 14.9 or 29.9 nM d<sub>6</sub>-sobetirome. Samples were centrifuged again (13,200 rpm, 15 min, 4 °C). Products were quantified by LC-MS/MS with standard curves generated from mock samples. Product concentrations were corrected for differences in method extraction efficiencies between sobetirome (0.48) and arachidonic acid (0.62). Extraction efficiencies were determined by the area ratio of known quantity of labeled product spiked into a mock sample before extraction to a known quantity of unlabeled product spiked into the final solution ([Figure S1](#)). Observed rates are expressed as nmol product per mg protein homogenate per min. Hydrolysis rates from nontransfected (mock) controls were determined to be minimal and did not effect calculated values ([Table S1](#)). Kinetic parameters were determined in GraphPad Prism 7 (Michaelis-Menton fitting) and are expressed as value ± SE.

#### Animal studies

Experimental protocols were in compliance with the National Institutes of Health Guide for the Care and Use of Laboratory Animals and approved by the Oregon Health & Science University Institutional Animal Care & Use Committee. *FAAH-KO* mice on a C57/BL6 background were a kind gift of Prof. Benjamin Cravatt (Scripps Research Institute).<sup>30</sup> Wild type C57BL/6 mice, aged 8–10 weeks, were purchased from Jackson Laboratory. All mice were housed in climate-controlled rooms with a 12h/12h light-dark cycle with ad libitum access to food and water. All injections were delivered intraperitoneally (i.p.) using 1:1 saline:DMSO as a vehicle except for AUC experiments, which were delivered intravenous (i.v., tail vein). Injection volumes were standardized to 150 µL/26 g mouse. When comparing sobetirome and sobetiramides, equimolar doses were given (i.e. 3.05 µmol/kg corresponds to 1 mg/kg for sobetirome). *FAAH* inhibitors PF-3845 and URB-937 were injected at 1 mg/kg. Time-points for the AUC experiment were: 0.167, 0.5, 1, 2, 4, and 8 h and match previous experiments.<sup>19</sup> Euthanasia was carried out with CO<sub>2</sub> followed by cervical dislocation.

### Tissue processing

Tissues were processed for LC-MS/MS analysis as previously described with slight modifications.<sup>19</sup> Standard curves were prepared in vehicle treated samples for each tissue to control for ion suppression in the analysis.

### Serum.

Whole blood was incubated for 15 min on ice and then clarified (7,800 rpm, 15 min, 4 °C). 100 µL of serum is transferred to a new tube and stored at -80 °C until further processed. Serum samples were thawed on ice prior to treatment with 10 µL internal standards (2.99 µM *d*<sub>6</sub>-sobetirome in water and/or 2.99 µM *d*<sub>6</sub>-Sob-AM2 in MeCN) followed by a crash with 400 µL MeCN. Following vigorous vortexing (~20 sec), samples were centrifuged (10,000 rpm, 15 min, 4 °C). The supernatant is dried under high vacuum. Samples were treated with 400 µL 1:1 MeCN:H<sub>2</sub>O with vigorous vortexing. When Sob-AM2 was analyzed, the resuspension step was carried out with 4:1 MeCN:H<sub>2</sub>O. Samples are centrifuged (10,000 rpm, 15 min, 4 °C), the supernatant is transferred, and centrifuged again (13,200 rpm, 15 min, 4 °C) prior to analysis by LC-MS/MS.

### Brain.

Tissue weights were determined prior to homogenization. Whole brains were treated with water (1 mL) containing 29.9 nM internal standard (*d*<sub>6</sub>-sobetirome and/or *d*<sub>6</sub>-Sob-AM2). Tissues were homogenized in 2 mL tubes containing 3 GoldSpec 1/8 chrome steel balls (Applied Industrial Technologies) using either a Bead Bug homogenizer or a Bead Ruptor 24. The homogenate was crashed and extracted with 4 mL MeCN and centrifuged (10,000 rpm, 15 min, 4 °C). The supernatant was transferred to glass culture tubes and dried under high vacuum. The sample residue was then treated with 400 µL 1:1 MeCN:H<sub>2</sub>O and vigorously vortexed (20 sec). When Sob-AM2 was analyzed, the resuspension step was carried out with 4:1 MeCN:H<sub>2</sub>O. The sample is centrifuged (10,000 rpm, 15 min, 4 °C) and the resulting supernatant is transferred to an

eppendorf tube. The supernatant is centrifuged again (13,200 rpm, 15 min, 4 °C) and submitted for LC-MS/MS analysis.

#### Liver/Kidney/Heart.

Peripheral tissues were processed identical to the brain with the following modifications. From the 1 mL liver homogenate, 0.1 g (~100 µL) of sample was further processed. The 100 µL of liver sample was extracted with 400 µL MeCN. Kidney and heart samples were homogenized in 400 µL water containing 75 nM internal standard (*d*<sub>6</sub>-sobetirome). Homogenization was carried out for 120 s. Sample extraction was done with 1.2 mL MeCN.

Dissected brain regions were processed as above but with slightly different volume/weight ratios. Each dissected sample was homogenized at 2.5 µL water per 1 µg tissue. The MeCN crash and extraction was performed with 10 µL MeCN per 1 µg tissue. Following drying under vacuum, samples were reconstituted in 2.5 µL 4:1 MeCN:Water per 1 µg original tissue weight. For each treatment, each region was carried out with n=5. Due to sample loss in processing, final replicates were reduced in number for some regions: sobetirome treated hippocampus (n=4); sobetirome treated olfactory bulbs (n=4); Sob-AM2 treated olfactory bulbs (n=2). All others points were done at n=5. Data represents mean ± SEM.

#### Quantitative PCR

Transcripts were quantified as previously described with slight modifications and are briefly described here.<sup>19</sup> Mice were injected (n=3 per point) once (i.p.) with sobetirome or Sob-AM2 over a dose range. Vehicle only treated mice were used as the control. Brain and liver were collected 6 h post-injection and preserved in RNAlater (Fisher). RNA was extracted from tissue and purified using Trizol (Invitrogen) and a Pure-Link RNA Mini Kit (Invitrogen) according to the manufacturer protocol. RNA was DNase treated on the column using an RNase-Free DNase kit (Qiagen). Extracted RNA was used to synthesize cDNA using a QuantiTect Reverse Transcription kit (Qiagen). Transcripts levels were measured by qPCR using the QuantiTect

SYBR green PCR kit (Qiagen). *Hairless (Hr)* expression (f-*Hr*: CCAAGTCTGGGCCAAGTTTG; r-*Hr*: TGTCCTTGGTCCGATTGGAA) was measured relative to *gapdh* in the brain (5' f-*Gapdh*: CCGCATCTTCTTGTGCAGTG 3'; r-*Gapdh* 5' GAGAAGGCAGCCCTGGTAAC 3'). *Thrsp* expression (f-*Thrsp*: 5' TGAGAACGACGCTGCTGAAA 3'; r-*Thrsp*: 5' TATTTCGCGTCACCTCCTG 3') was measured relative to the 18S RNA (f-18S: 5' TTCCGATAACGAACGAGACTCT 3'; r-18S: 5' TGGCTGAACGCCACTTGTC 3') in the liver. Data was analyzed using the comparative  $2^{-\Delta\Delta Ct}$  method and normalized between vehicle and the highest dose of sobetirome. Individual data points are shown as normalized fold-change  $\pm$  SEM.  $EC_{50}$  values were calculated using a non-linear regression (GraphPad Prism 7 four-parameter model).

#### Statistical Analysis

Statistical significance was determined using one-way ANOVA (Fisher LSD) or multiple t-tests as indicated. All tests were two-tailed. Replicates in each experiment were as stated in the specific figure legend and in the corresponding methods. For animal groups, experimental numbers were informed by previous experience in the field in order to minimize total animal numbers as appropriate. Analysis was carried out in GraphPad Prism 7 and carried out without further modifications. Significance level ( $\alpha$ ) was set to  $<0.05$ . P-values are illustrated with the following symbols \*  $P < 0.05$ , \*\*  $P < 0.01$ , \*\*\*  $P < 0.001$ .

#### Supplementary Material

##### Supporting Information

[Click here to view.](#) <sup>(308K, pdf)</sup>

##### Abbreviations

BBB blood-brain barrier

FAAH fatty-acid amide hydrolyase

X-ALD X-linked adrenoleukodystrophy

MS multiple sclerosis  
TI therapeutic index  
AEA anandamide  
OEA oleamide  
AUC area-under-the-curve  
KO knock out  
VLCFA very long-chain fatty acids  
i.p. intraperitoneal  
i.v. intravenous

#### Supporting Information:

Hydrolysis rates of mock vs FAAH transfected COS-7 cell homogenate, extraction efficiency of arachidonic acid versus sobetirome, HPLC traces of novel compounds,  $^1\text{H}$  and  $^{13}\text{C}$  NMR spectra

#### Acknowledgements:

We thank Lisa Bleyle (OHSU Bioanalytical Shared Resource/Pharmacokinetics Core) for technical assistance with LC-MS/MS, Prof. Benjamin Cravatt (Scripps Research Institute) for the FAAH-KO mice, Prof. Martin Kaczocha (Stony Brook) for the pcDNA4-FAAH plasmid, and Prof. Michael Cohen (OHSU) for the COS-7 line.

#### Funding

This work was supported by the OHSU Laura Fund for Innovation in Multiple Sclerosis, the National Institutes of Health (DK 052798, T.S.S. & T32DK007680, support to S.J.F.), and the National Multiple Sclerosis Society (RG 5199A4/1 D.B.).

#### References:

1. Pangalos MN, Schechter LE, and Hurko O (2007) Drug development for CNS disorders: strategies for balancing risk and reducing attrition, *Nat. Rev. Drug Discov* 6, 521–532. [[PubMed](#)] [[Google Scholar](#)]

2. Abbott NJ, Ronnback L, and Hansson E (2006) Astrocyte-endothelial interactions at the blood-brain barrier, *Nat. Rev. Neurosci* 7, 41–53. [[PubMed](#)] [[Google Scholar](#)]
3. Abbott NJ (2013) Blood–brain barrier structure and function and the challenges for CNS drug delivery, *J. Inherit. Metab. Dis* 36, 437–449. [[PubMed](#)] [[Google Scholar](#)]
4. Weidle UH, Niewohner J, and Tiefenthaler G (2015) The Blood-Brain Barrier Challenge for the Treatment of Brain Cancer, Secondary Brain Metastases, and Neurological Diseases, *Cancer Genom. Proteom* 12, 167–177. [[PubMed](#)] [[Google Scholar](#)]
5. Varatharajan L, and Thomas SA (2009) The transport of anti-HIV drugs across blood–CNS interfaces: Summary of current knowledge and recommendations for further research, *Antiviral Res* 82, A99–A109. [[PMC free article](#)] [[PubMed](#)] [[Google Scholar](#)]
6. Hitchcock SA, and Pennington LD (2006) Structure–Brain Exposure Relationships, *J. Med. Chem* 49, 7559–7583. [[PubMed](#)] [[Google Scholar](#)]
7. Friesema EC, Visser WE, and Visser TJ (2010) Genetics and phenomics of thyroid hormone transport by MCT8, *Mol. Cell. Endocrinol* 322, 107–113. [[PubMed](#)] [[Google Scholar](#)]
8. Genin EC, Gondcaille C, Trompier D, and Savary S (2009) Induction of the adrenoleukodystrophy-related gene (ABCD2) by thyromimetics, *J. Steroid Biochem. Mol. Biol* 116, 37–43. [[PubMed](#)] [[Google Scholar](#)]
9. Hartley MD, Kirkemo LL, Banerji T, and Scanlan TS (2017) A Thyroid Hormone-Based Strategy for Correcting the Biochemical Abnormality in X-Linked Adrenoleukodystrophy, *Endocrinology* 158, 1328–1338. [[PMC free article](#)] [[PubMed](#)] [[Google Scholar](#)]
10. Compston A, and Coles A (2008) Multiple sclerosis, *Lancet* 372, 1502–1517. [[PubMed](#)] [[Google Scholar](#)]
11. Baxi EG, Schott JT, Fairchild AN, Kirby LA, Karani R, Uapinyoying P, Pardo-Villamizar C, Rothstein JR, Bergles DE, and Calabresi PA (2014) A selective thyroid hormone beta receptor agonist enhances human and rodent oligodendrocyte differentiation, *Glia* 62, 1513–1529. [[PMC free article](#)] [[PubMed](#)] [[Google Scholar](#)]
12. Baxter JD, and Webb P (2009) Thyroid hormone mimetics: potential applications in atherosclerosis, obesity and type 2 diabetes, *Nat. Rev. Drug Discov* 8, 308–320. [[PubMed](#)] [[Google Scholar](#)]
13. Scanlan TS (2010) Sobetirome: a case history of bench-to-clinic drug discovery and development, *Heart. Fail. Rev* 15, 177–182. [[PubMed](#)] [[Google Scholar](#)]
14. Trost SU, Swanson E, Gloss B, Wang-Iverson DB, Zhang H, Volodarsky T, Grover GJ, Baxter JD, Chiellini G, Scanlan TS, and Dillmann WH (2000) The Thyroid Hormone Receptor- $\beta$ -Selective Agonist GC-1 Differentially Affects Plasma Lipids and Cardiac Activity, *Endocrinology* 141, 3057–3064. [[PubMed](#)] [[Google Scholar](#)]
15. Takahashi N, Asano Y, Maeda K, and Watanabe N (2014) In vivo evaluation of 1-benzyl-4-aminoindole-based thyroid hormone receptor beta agonists: importance of liver selectivity in drug discovery, *Biol. Pharm. Bull* 37, 1103–1108. [[PubMed](#)] [[Google Scholar](#)]

16. Devereaux J, Ferrara SJ, Banerji T, Placzek AT, and Scanlan TS (2016) Increasing Thyromimetic Potency through Halogen Substitution, *ChemMedChem* 11, 2459–2465. [[PMC free article](#)] [[PubMed](#)] [[Google Scholar](#)]
17. Doran A, Obach RS, Smith BJ, Hosea NA, Becker S, Callegari E, Chen C, Chen X, Choo E, Cianfrogna J, Cox LM, Gibbs JP, Gibbs MA, Hatch H, Hop CECA, Kasman IN, LaPerle J, Liu J, Liu X, Logman M, Maclin D, Nedza FM, Nelson F, Olson E, Rahematpura S, Raunig D, Rogers S, Schmidt K, Spracklin DK, Szewc M, Troutman M, Tseng E, Tu M, Van Deusen JW, Venkatakrishnan K, Walens G, Wang EQ, Wong D, Yasgar AS, and Zhang C (2005) The impact of P-glycoprotein on the disposition of drugs targeted for indications of the central nervous system: evaluation using the MDR1A/1B knockout mouse model, *Drug Metab. Disposition* 33, 165–174. [[PubMed](#)] [[Google Scholar](#)]
18. Placzek AT, Ferrara SJ, Hartley MD, Sanford-Crane HS, Meinig JM, and Scanlan TS (2016) Sobetirome prodrug esters with enhanced blood–brain barrier permeability, *Bioorg. Med. Chem* 24, 5842–5854. [[PMC free article](#)] [[PubMed](#)] [[Google Scholar](#)]
19. Ferrara SJ, Meinig JM, Placzek AT, Banerji T, McTigue P, Hartley MD, Sanford-Crane HS, Banerji T, Bourdette D, and Scanlan TS (2017) Ester-to-amide rearrangement of ethanolamine-derived prodrugs of sobetirome with increased blood-brain barrier penetration, *Bioorg. Med. Chem* 25, 2743–2753. [[PMC free article](#)] [[PubMed](#)] [[Google Scholar](#)]
20. Egertová M, Cravatt BF, and Elphick MR (2003) Comparative analysis of fatty acid amide hydrolase and cb1 cannabinoid receptor expression in the mouse brain: evidence of a widespread role for fatty acid amide hydrolase in regulation of endocannabinoid signaling, *Neuroscience* 119, 481–496. [[PubMed](#)] [[Google Scholar](#)]
21. Cravatt BF, Giang DK, Mayfield SP, Boger DL, Lerner RA, and Gilula NB (1996) Molecular characterization of an enzyme that degrades neuromodulatory fatty-acid amides, *Nature* 384, 83–87. [[PubMed](#)] [[Google Scholar](#)]
22. Boger DL, Fecik RA, Patterson JE, Miyauchi H, Patricelli MP, and Cravatt BF (2000) Fatty acid amide hydrolase substrate specificity, *Bioorg. Med. Chem. Lett* 10, 2613–2616. [[PubMed](#)] [[Google Scholar](#)]
23. Lang W, Qin C, Lin S, Khanolkar AD, Goutopoulos A, Fan P, Abouzid K, Meng Z, Biegel D, and Makriyannis A (1999) Substrate Specificity and Stereoselectivity of Rat Brain Microsomal Anandamide Amidohydrolase, *J. Med. Chem* 42, 896–902. [[PubMed](#)] [[Google Scholar](#)]
24. Wyffels L, Muccioli GG, De Bruyne S, Moerman L, Sambre J, Lambert DM, and De Vos F (2009) Synthesis, In Vitro and In Vivo Evaluation, and Radiolabeling of Aryl Anandamide Analogues as Candidate Radioligands for In Vivo Imaging of Fatty Acid Amide Hydrolase in the Brain, *J. Med. Chem* 52, 4613–4622. [[PubMed](#)] [[Google Scholar](#)]
25. Mofford DM, Adams ST, Reddy GSKK, Reddy GR, and Miller SC (2015) Luciferin Amides Enable in Vivo Bioluminescence Detection of Endogenous Fatty Acid Amide Hydrolase Activity, *J. Am. Chem. Soc* 137, 8684–8687. [[PMC free article](#)] [[PubMed](#)] [[Google Scholar](#)]
26. Kaczocha M, Glaser ST, Chae J, Brown DA, and Deutsch DG (2010) Lipid droplets are novel sites of N-acyl ethanolamine inactivation by fatty acid amide hydrolase-2, *J. Biol. Chem* 285, 2796–2806. [[PMC free article](#)] [[PubMed](#)] [[Google Scholar](#)]

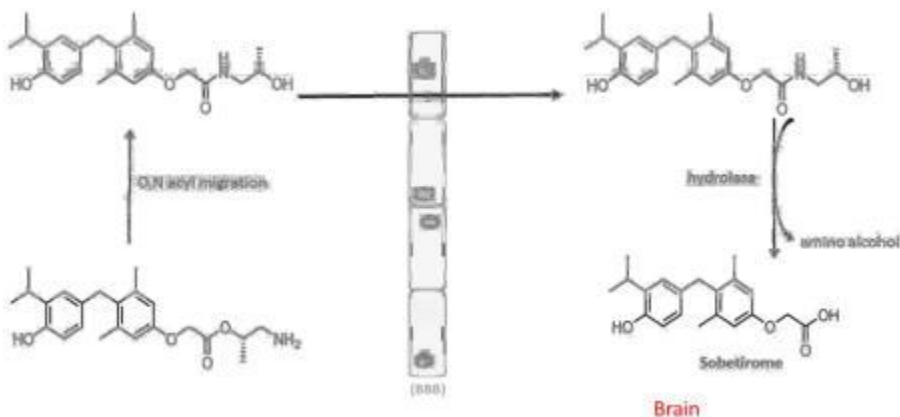
27. Kaczocha M, Glaser ST, and Deutsch DG (2009) Identification of intracellular carriers for the endocannabinoid anandamide, *Proc. Natl. Acad. Sci. U. S. A* 106, 6375–6380. [[PMC free article](#)] [[PubMed](#)] [[Google Scholar](#)]
28. Ahn K, Johnson DS, Mileni M, Beidler D, Long JZ, McKinney MK, Weerapana E, Sadagopan N, Liimatta M, Smith SE, Lazerwith S, Stiff C, Kamtekar S, Bhattacharya K, Zhang Y, Swaney S, Van Becelaere K, Stevens RC, and Cravatt BF (2009) Discovery and Characterization of a Highly Selective FAAH Inhibitor that Reduces Inflammatory Pain, *Chem. Biol* 16, 411–420. [[PMC free article](#)] [[PubMed](#)] [[Google Scholar](#)]
29. Sasso O, Bertorelli R, Bandiera T, Scarpelli R, Colombano G, Armirotti A, Moreno-Sanz G, Reggiani A, and Piomelli D (2012) Peripheral FAAH inhibition causes profound antinociception and protects against indomethacin-induced gastric lesions, *Pharmacol. Res* 65, 553–563. [[PMC free article](#)] [[PubMed](#)] [[Google Scholar](#)]
30. Cravatt BF, Demarest K, Patricelli MP, Bracey MH, Giang DK, Martin BR, and Lichtman AH (2001) Supersensitivity to anandamide and enhanced endogenous cannabinoid signaling in mice lacking fatty acid amide hydrolase, *Proc. Natl. Acad. Sci. U. S. A* 98, 9371–9376. [[PMC free article](#)] [[PubMed](#)] [[Google Scholar](#)]
31. Ohba K, Leow MK, Singh BK, Sinha RA, Lesmana R, Liao XH, Ghosh S, Refetoff S, Sng JC, and Yen PM (2016) Desensitization and Incomplete Recovery of Hepatic Target Genes After Chronic Thyroid Hormone Treatment and Withdrawal in Male Adult Mice, *Endocrinology* 157, 1660–1672. [[PMC free article](#)] [[PubMed](#)] [[Google Scholar](#)]
32. Thompson CC, and Bottcher MC (1997) The product of a thyroid hormone-responsive gene interacts with thyroid hormone receptors, *Proc. Natl. Acad. Sci. U. S. A* 94, 8527–8532. [[PMC free article](#)] [[PubMed](#)] [[Google Scholar](#)]
33. Schwartz CE, and Stevenson RE (2007) The MCT8 thyroid hormone transporter and Allan–Herndon–Dudley syndrome, *Best Pract. Res. Clin. Endocrinol. Metab* 21, 307–321. [[PMC free article](#)] [[PubMed](#)] [[Google Scholar](#)]
34. Kemp S, Huffnagel IC, Linthorst GE, Wanders RJ, and Engelen M (2016) Adrenoleukodystrophy - neuroendocrine pathogenesis and redefinition of natural history, *Nat. Rev. Endocrinol* 12, 606–615. [[PubMed](#)] [[Google Scholar](#)]
35. Ferrer I, Aubourg P, and Pujol A (2010) General aspects and neuropathology of X-linked adrenoleukodystrophy, *Brain Pathol* 20, 817–830. [[PubMed](#)] [[Google Scholar](#)]
36. Rautio J, Laine K, Gynther M, and Savolainen J (2008) Prodrug approaches for CNS delivery, *AAPS J* 10, 92–102. [[PMC free article](#)] [[PubMed](#)] [[Google Scholar](#)]
37. Liu X, Chen C, and Smith BJ (2008) Progress in brain penetration evaluation in drug discovery and development, *J. Pharmacol. Exp. Ther* 325, 349–356. [[PubMed](#)] [[Google Scholar](#)]
38. Mofford DM, and Miller SC (2015) Luciferins Behave Like Drugs, *ACS Chem. Neurosci* 6, 1273–1275. [[PubMed](#)] [[Google Scholar](#)]
39. Mao F, Ni W, Xu X, Wang H, Wang J, Ji M, and Li J (2016) Chemical Structure-Related Drug-Like Criteria of Global Approved Drugs, *Molecules* 21, 75. [[PMC free article](#)] [[PubMed](#)] [[Google Scholar](#)]

40. Chiellini G, Nguyen N-H, Yoshihara HAI, and Scanlan TS (2000) Improved synthesis of the iodine-free thyromimetic GC-1, *Bioorg. Med. Chem. Lett* 10, 2607–2611. [[PubMed](#)] [[Google Scholar](#)]
41. Placzek AT, and Scanlan TS (2015) New synthetic routes to thyroid hormone analogs: d6-sobetirome, 3H-sobetirome, and the antagonist NH-3, *Tetrahedron* 71, 5946–5951. [[PMC free article](#)] [[PubMed](#)] [[Google Scholar](#)]

Ferrara, S. J., Meinig J. M., Placzek, A. T., Banerji T., McTigue P., Hartley M.D., **Sanford-Crane H. S.**, Banerji T., Bourdette D., Scanlan T. S. *Ester-to-amide rearrangement of ethanolamine-derived prodrugs of sobetirome with increased blood-brain barrier penetration*. *Bioorganic & Medicinal Chemistry* 25, 2743-2753, 2017.

**Abstract:**

Current therapeutic options for treating demyelinating disorders such as multiple sclerosis (MS) do not stimulate myelin repair, thus creating a clinical need for therapeutic agents that address axonal remyelination. Thyroid hormone is known to play an important role in promoting developmental myelination and repair, and CNS permeable thyromimetic agents could offer an increased therapeutic index compared to endogenous thyroid hormone. Sobetirome is a clinical stage thyromimetic that has been shown to have promising activity in preclinical models related to MS and X-linked adrenoleukodystrophy (X-ALD), a genetic disease that involves demyelination. Here we report a new series of sobetirome prodrugs containing ethanolamine-based promoieties that were found to undergo an intramolecular O,N acyl migration to form the pharmacologically relevant amide species. Several of these systemically administered prodrugs deliver more sobetirome to the brain compared to unmodified sobetirome. Pharmacokinetic properties of the parent drug sobetirome and amidoalcohol prodrug **3** are described and prodrug **3** was found to be more potent than sobetirome in target engagement in the brain from systemic dosing.



**Personal contribution:**

HSC (also initialized as HSS) performed and optimized in vivo experiments.

**Introduction:**

Thyroid hormone is an essential regulatory molecule in vertebrate physiology and homeostasis. In the central nervous system (CNS) thyroid hormone plays an integral role in development and maintenance of brain function. Myelination of nerve fibers and neuronal and glial cell differentiation are processes in which thyroid hormone plays a key regulatory role.<sup>1</sup> Thyroid hormone prompts the maturation of oligodendrocytes (OLs) from oligodendrocyte progenitor cells (OPCs),<sup>2</sup> promotes the expression of oligodendrocyte-specific genes that activate the production of myelin,<sup>3</sup> and has been shown to play a role in stimulating myelin repair in response to demyelination.<sup>4-6</sup> Currently, the only treatment options for multiple sclerosis (MS), the most

prevalent demyelinating neurological disorder,<sup>7</sup> target the autoimmune inflammatory process of the disease that causes demyelination but do not address myelin repair.<sup>8-9</sup> The endogenous thyroid hormone is not a viable candidate for myelin repair as it lacks a therapeutic index (TI) separating desirable therapeutic effects from deleterious systemic thyrotoxic effects, particularly on heart, bone, and skeletal muscle.<sup>10</sup> The thyromimetic sobetirome (**1**, also known as GC-1) displays selective tissue action with a TI separating beneficial from adverse effects and has progressed to clinical studies in hyperlipidemia.<sup>11</sup> In terms of potential for CNS disorders, sobetirome has been studied in pre-clinical models of X-linked adrenoleukodystrophy (X-ALD), a lipid storage disease that produces severe neurological phenotypes involving demyelination.<sup>12</sup> In addition, sobetirome has been shown to promote oligodendrogenesis from human and rodent OPCs *in vitro*, and enhance oligodendrogenesis during development with attending increased production of myelin proteins *in vivo*, supporting the idea that thyromimetic agents that distribute to the central nervous system (CNS) may be useful candidates for treating demyelinating disorders.<sup>13</sup>

Most thyromimetics, including sobetirome, contain inner-ring, negatively charged carboxylate groups at physiological pH. These carboxylate groups are crucial for high affinity binding to the thyroid hormone receptor, but are a known liability for CNS drug distribution due to their inherent lipophobic character and electrostatic repulsion at negatively charged tight junctions of blood-brain barrier (BBB) endothelial cells.<sup>14, 15</sup> While sobetirome does distribute to the CNS,<sup>16, 17</sup> employing a prodrug strategy which masks these carboxylate groups should, in theory, provide greater access to the CNS and could potentially limit peripheral exposure of the parent drug. After crossing the BBB, these prodrugs can be hydrolyzed to the parent drug sobetirome. Recently, an *in vivo* study evaluating the brain exposure of ester-based prodrugs of sobetirome confirmed this strategy to be effective.<sup>18</sup> In this study, a particular ester derivative, an ethanolamino ester (**2**), was found to have the greatest CNS penetration with minimized peripheral exposure of the parent drug. Here we report a new series of prodrugs that feature improved CNS distribution compared to the originally reported ethanolamino ester and, in the process, it was discovered that these ester promoieties undergo an intramolecular rearrangement to form the corresponding amides, which were found to be the pharmacologically active forms of the prodrugs.

### **Animal studies**

Experimental protocols were in compliance with the National Institutes of Health Guide for the Care and Use of Laboratory Animals and approved by the Oregon Health & Science University Institutional Animal Care & Use Committee. Wild type male C57Bl/6 mice, aged 8–10 weeks, were housed in a climate-controlled room with a 12-hour light-dark cycle with ad libitum access to food and water. Mice were injected once intraperitoneally (ip) with sobetirome and prodrugs at 1.5  $\mu\text{mol} / \text{kg}$ . Oral gavage was performed with the use of plastic feeding tubes (20 ga  $\times$  38 mm, Instech Laboratories Inc., PA, USA) connected to 500  $\mu\text{L}$  insulin syringes (Covidien LLC MA, USA). Euthanasia was performed on three mice per time point at the following times: 0.25 h, 0.5 h, 1 h, 2 h, 4 h, and 8 h (except where noted otherwise) and the tissues and blood were harvested. Tissues were immediately frozen and blood was kept on ice for a minimum of 30 minutes and then spun down at  $7,500 \times G$  for 15 minutes. Serum (100  $\mu\text{L}$ ) was collected and was stored with tissues at  $-80^\circ\text{C}$  until samples were processed.

### **Serum processing**

The serum samples were warmed to rt and 10  $\mu\text{L}$  of 2.99  $\mu\text{M}$  internal standard ( $d_6$ -sobetirome<sup>38</sup>) was added to them. Acetonitrile (500  $\mu\text{L}$ ) was added and the sample was vortexed for 20 seconds. The sample was then centrifuged at  $10,000 \times G$  for 15 minutes at 4  $^\circ\text{C}$ . Next, 90% of the upper supernatant was transferred to a glass test tube and concentrated using a speedvac for 1.5 hours at 45  $^\circ\text{C}$ . The dried sample was then dissolved in 400  $\mu\text{L}$  of 50:50 ACN:H<sub>2</sub>O and vortexed for 20 seconds. The resulting mixture was transferred to an eppendorf and centrifuged at  $10,000 \times G$  for 15 minutes. The supernatant was filtered with 0.22  $\mu\text{m}$  centrifugal filters and submitted for LC-MS/MS analysis. The standard curve was made with 100  $\mu\text{L}$  of serum from an 8–10 week old mouse not injected with sobetirome or prodrug. The processing was performed exactly the same except after filtering the sample was split amongst 6 vials. To 5 out of the 6 vials was added sobetirome to make final concentrations in matrix of (0.1  $\text{pg}/\mu\text{L}$ , 1  $\text{pg}/\mu\text{L}$ , 10  $\text{pg}/\mu\text{L}$ , 100  $\text{pg}/\mu\text{L}$ , and 1000  $\text{pg}/\mu\text{L}$ ).

### **Brain processing**

The brain samples were warmed to r.t. and transferred to a homogenizer tube with 3 GoldSpec 1/8 chrome steel balls (Applied Industrial Technologies). The resulting tube was weighed and then 1 mL of H<sub>2</sub>O was added, followed by 10  $\mu\text{L}$  of 2.99  $\mu\text{M}$  internal standard ( $d_6$ -sobetirome<sup>38</sup>). The tube was homogenized with a Bead Bug for 30 seconds and then transferred to a falcon tube containing 3 mL of ACN. ACN (1 mL) was used to wash homogenizer tube and the solution was transferred back to the falcon tube. The sample was then processed using the same method for the serum processing except the sample was concentrated in a glass tube using a speed vac for 4 hours at 45  $^\circ\text{C}$ .

### **Liver processing**

The liver samples were warmed to rt and transferred to a homogenizer tube with 3 GoldSpec 1/8 chrome steel balls (Applied Industrial Technologies). The resulting tube was weighed and then 1 mL of H<sub>2</sub>O was added, followed by 10  $\mu\text{L}$  of 2.99  $\mu\text{M}$  internal standard ( $d_6$ -sobetirome). The tube was then homogenized with a Bead Bug for 30 s. A small sample (100  $\mu\text{L}$ ) was then taken from the homogenized mixture and processed. This was done because the liver levels found in some samples were too high for the LC—MS/MS instrument. The samples were then processed using the serum processing method.

### **Heart and kidney processing**

Heart and kidney samples were warmed to r.t. and transferred to a homogenizer tube (2 mL) with 3 GoldSpec 1/8 chrome steel balls (Applied Industrial Technologies). The resulting tube was weighed and then 400  $\mu\text{L}$  of H<sub>2</sub>O was added, followed by 10  $\mu\text{L}$  of 2.99  $\mu\text{M}$  internal standard ( $d_6$ -sobetirome<sup>38</sup>). The tube was homogenized with a Bead Bug for 120 s and then 1.2 mL acetonitrile was added and the tube vortexed for 20 s. The samples were then processed using the serum processing method.

### **LC-MS/MS analysis for sobetirome and prodrugs**

Sobetirome and  $d_6$ -sobetirome internal standard were analyzed using a QTRAP 4000 hybrid/triple quadrupole linear ion trap mass spectrometer (Applied biosystems) with electrospray ionization (ESI) in negative mode. The mass spectrometer was interfaced to a Shimadzu (Columbia, MD) SIL-20AC XR auto-sampler followed by 2 LC-20AD XR LC pumps and analysis on an Applied Biosystems/SCIEX QTRAP 4000 instrument (Foster City, CA). The instrument was operated

with the following settings: source voltage –4500 kV, GS1 50, GS2 60, CUR 15, TEM 650, and CAD MEDIUM. The scheduled multiple-reaction-monitoring (MRM) transitions are based on the precursor ion  $m/z$  and their corresponding diagnostic product ions. Compounds were infused individually and instrument parameters optimized for each MRM transition. MRM parameters are shown in the [supporting information](#). The gradient mobile phase was delivered at a flow rate of 0.5 mL/min, and consisted of two solvents, A: 10 mM ammonium formate in water and B: 10 mM ammonium formate in 90% acetonitrile, 10% water. An Imtakt Scherzo SS-C18 50 × 2mm 3 μm (prod# SS022) was used with an Imtakt Guard cartridge Scherzo SS-C18 5×2mm 3μm precolumn (prod# GCSS0S) and kept at 40 °C, and the autosampler was kept at 30 °C. Gradient was as follows, initial concentration of B was 10%, held for 0.5 min, followed by an increase to 98% B over 4.5 min, held for 0.9 min, dropping back to 10% B over 0.1 min, and held at 10% B for 2 min for a total run time of 8 min. Data were acquired using SCIEX Analyst 1.6.2 software (Framingham, MA, USA) and analyzed using Multiquant 3.0.2.

### Pharmacokinetics

To determine the oral bioavailability of **3**, orally (p.o.)- and intravenously (i.v.)-administered 8 h serum AUCs were obtained and compared as follows. An 8 h i.v. AUC was obtained by administering equimolar doses of **3** (3.05 μmol / kg) by tail vein injection to cohorts (n = 3) of age-matched c57bl/6 mice and collecting blood samples at spaced intervals post-injection (5 min, 10 min, 20 min, 1 h, 2 h, 4 h, 8 h). The blood was stored on ice for a minimum of 30 minutes and then spun down at 7,500 × G for 15 minutes. Serum (100 μL) was collected and stored at –80°C until samples were processed. Serum samples were processed according to the method described in the experimental of this paper (vida supra). An 8 h oral AUC was obtained by administering equimolar doses of **3** (30.5 μmol / kg) via oral gavage to cohorts (n = 3) of age-matched c57bl/6 mice and harvesting blood samples at spaced intervals post-gavage (10 min, 30 min, 45 min, 1 h, 2 h, 4 h, 8 h). The blood was stored on ice for a minimum of 30 minutes and then spun down at 7,500 × G for 15 minutes. Serum (100 μL) was collected and stored at –80°C until samples were processed. An identical standard curve as described for serum processing was generated for prodrug **3**. All serum samples were processed according to the method described in the experimental of this paper and the concentrations of both **3** and sobetirome (**1**) were quantified in each sample using the LC-MS/MS method also described in this paper's experimental section (vida supra). AUCs for both the i.v.-dosed and orally-dosed experiments were generated and oral bioavailability was calculated using the equation: % oral bioavailability (%F) = (AUC<sub>p.o.</sub>/AUC<sub>i.v.</sub>) • (dose<sub>i.v.</sub>/dose<sub>p.o.</sub>) • 100. The half-life of sobetirome and prodrug **3** was determined from the i.v.-administered serum AUCs described above. Data from the five latest time points, which approximate the elimination phase of the pharmacokinetic profile, was plotted as log (concentration in ng / g) vs time (h). The  $t_{1/2}$  values for sobetirome and **3** were calculated from the slopes of these plots. Clearance values were calculated from the AUC of the drug concentration vs. time plots.

### Quantitative PCR

Mice were injected once intraperitoneally (i.p.) with vehicle (1:1 saline/DMSO), sobetirome (6 doses; 30.5, 9.14, 6, 3.05, 1.22, and 0.305 μmol / kg), **3** (6 doses; 9.14, 3.05, 1.22, 0.305, 0.0914, and 0.00914 μmol / kg), and T3 (6 doses; 3.05, 0.305, 0.20, 0.12, 0.0914, and 0.00914 μmol / kg). Cohorts of 3 mice (n = 3) for each dose were used and tissues were collected 2 h post-injection. The brain tissues collected for qPCR analysis were processed according to a protocol for RNA extraction using Trizol reagent and the PureLink RNA mini kit, using a Qiagen RNase-free

DNase kit during the optional DNase treatment step. Extracted RNA (1  $\mu$ g) was used to synthesize cDNA via a reverse transcription (RT) reaction using the Qiagen QuantiTect Reverse Transcription kit. DNA contamination was controlled for by duplicating one sample without the addition of RT. Expression of the *Hairless* (*Hr*) gene was measured by qPCR using the QuantiTect SYBR green PCR kit from Qiagen. The primer sequences for hairless (Fwd: CCA AGT CTG GGC CAA GTT TG; Rev: TGT CCT TGG TCC GAT TGG AA) were previously described by Barca-Mayo et al.<sup>39</sup> The template cDNA was diluted two-fold to minimize the interference of RT reagents in the qPCR reaction. Glyceraldehyde-3-phosphate dehydrogenase (*GAPDH*) was the housekeeping gene used for normalizing between samples. Data analysis was performed using the comparative  $C_T$  method to monitor the relative differences in *Hr* gene expression, then a sigmoidal dose—response model to generate  $ED_{50}$  values  $\pm$  SEM was followed using GraphPad Prism v.4a. Experiments were performed in triplicate.

### Statistical analysis

Data are expressed as the mean  $\pm$  the standard error of the mean (SEM). Statistical analyses were done using Microsoft Excel and GraphPad Prism®. Differences between means were determined using multiple t-tests, and considered to be statistically significant  $p < 0.05$ .

### General Chemistry

$^1\text{H}$  NMR were recorded on a Bruker Avance 400 MHz nuclear magnetic resonance spectrometer. All  $^1\text{H}$  NMR spectra were calibrated to the NMR solvent reference peak ( $\delta$ ,  $d_6$ -DMSO,  $\text{CDCl}_3$ ,  $\text{CD}_3\text{OD}$ ) and are reported in parts per million (ppm). High-resolution mass spectrometry (HRMS) with electrospray ionization was performed by the Bioanalytical MS Facility at Portland State University. Inert atmosphere reactions were performed under argon gas passed through a small column of drierite and were conducted in flame-dried round-bottom flasks. Anhydrous tetrahydrofuran (THF), dichloromethane (DCM), and dimethylformamide (DMF) were obtained from a Seca Solvent System. All other solvents used were purchased from Sigma-Aldrich or Fisher. Purity analysis of final compounds was determined to be  $>95\%$  by HPLC. HPLC analysis was performed on a Varian ProStar HPLC with an Agilent Eclipse Plus C18 5  $\mu\text{m}$  column (4.6  $\times$  250 mm) with a gradient of 10% to 95% acetonitrile (0.1% TFA) over 30 minutes.

### Chemistry materials

Sobetirome (**1**), 2-(4-(4-(benzyloxy)-3-isopropylbenzyl)-3,5-dimethylphenoxy)acetic acid (benzyl protected (phenol) sobetirome, 2-(2-(4-(4-hydroxy-3-isopropylbenzyl)-3,5-dimethylphenoxy)acetoxy)ethan-1-amine (**2**) and the in situ generated acid chloride of benzyl protected sobetirome were synthesized as previously reported.<sup>18, 38</sup> 1-(dibenzylamino)-3-methylbutan-2-ol and 1-(benzyl(methyl)amino)-3-methylbutan-2-ol were synthesized according to a published procedure,<sup>22</sup> and 1-(isopropylamino)propan-2-ol was synthesized following a literature protocol.<sup>40</sup> Amino alcohols were N-Cbz protected according to standard procedures.<sup>41</sup>

### Representative procedure for preparation of acid chloride of benzyl protected sobetirome

A solution of oxalyl chloride (200  $\mu\text{L}$ , 2.33 mmol) in 2 mL of DCM was slowly added to a 0  $^\circ\text{C}$  solution of benzyl protected sobetirome (209 mg, 0.5 mmol) and DCM (4mL). DMF (2  $\mu\text{L}$ ) was then added and the reaction mixture was stirred at room temperature for 3 hours. The solution was then concentrated under reduced pressure. DCM (4mL) was added to the residue and the

solution was concentrated again, this process was repeated once more. The crude residue was of sufficient purity and was used immediately in the subsequent ester couplings.

(*S*)-1-aminopropan-2-yl 2-(4-(4-hydroxy-3-isopropylbenzyl)-3,5-dimethylphenoxy)acetate (3a)

To a 0° C solution of benzyl (*S*)-(2-hydroxypropyl)carbamate (262 mg, 1.25 mmol), DMAP (183 mg, 1.5 mmol), and THF (8 mL) was slowly added a solution of the acid chloride generated from benzyl protected sobetirome (vide supra, 0.5 mmol) in 4 mL THF. The reaction mixture was allowed to warm to room temperature, then heated to 50° C overnight with stirring. Filtration and evaporation of the resulting filtrate gave a light-yellow oil which was purified using flash chromatography (silica, 10% to 30% ethyl acetate/hexanes). The resulting ester (101 mg, 0.166 mmol, 33% yield) was dissolved in 5 mL of dry methanol with 1 mL THF and 10% Pd/C (80 mg) was added to generate a suspension. The reaction mixture was subjected to vacuum for approximately 1 min, then placed under argon for approximately 1 min. This process was repeated three times to ensure the mixture was properly degassed. Triethylsilane (0.82 mL, 5.15 mmol) was then added dropwise to the suspension and the reaction mixture was stirred for 4 h at room temperature. Filtration over a pad of celite with methanol and concentration *in vacuo* gave an oily residue which was precipitated with cold hexanes and washed with hexanes to give the desired product as a white solid (59 mg, 0.153 mmol, 90% yield, 30% overall yield). <sup>1</sup>H NMR (400 MHz, CD<sub>3</sub>OD): δ 6.77 (s, 1H), 6.61 (s, 2H), 6.54 (d, *J* = 8 Hz, 1H), 6.48 (d, *J* = 8.3 Hz, 1H), 5.19 (m, *J* = 3 Hz 1H), 4.70 (d, *J* = 4 Hz, 2H), 3.84 (s, 2H), 3.19 (m, 2H), 3.16 (sept, *J* = 6.8 Hz, 1H), 2.16 (s, 6H), 1.31 (d, *J* = 6.4 Hz, 3H), 1.09 (d, *J* = 6.9 Hz 6H). HRMS exact mass calcd for C<sub>23</sub>H<sub>32</sub>N<sub>1</sub>O<sub>4</sub> [M+H]<sup>+</sup>: *m/z* 386.23258. Found *m/z* 386.23287.

(*S*)-2-(4-(4-hydroxy-3-isopropylbenzyl)-3,5-dimethylphenoxy)-*N*-(2-hydroxypropyl)acetamide (3b)

To a solution of sobetirome (**1**, 203 mg, 0.618 mmol) in 3 mL dry methanol was added 1 drop of concentrated sulfuric acid and the mixture was heated to 65° C in a sealed reaction tube with stirring for 1 h. After cooling to r.t., TLC confirmed complete conversion to the sobetirome methyl ester. (*S*)-(+)-1-amino-2-propanol (279 mg, 3.71 mmol) in 2 mL methanol was added to the solution of sobetirome methyl ester and the reaction mixture was again heated to 65° C with stirring in a sealed reaction tube for 1h. The reaction mixture was then cooled to r.t., diluted with 50 mL of DCM, and added to 100 mL of 0.5 N aqueous NaOH. The product was extracted with 3 × 50 mL DCM, the organic layers were combined, dried with MgSO<sub>4</sub>, and evaporated to a crude product that was further purified on silica (10% MeOH in DCM) to give 185 mg of a colorless sticky solid (78% yield). <sup>1</sup>H NMR (400 MHz, CD<sub>3</sub>OD): δ 7.24 (br, 1H), 6.97 (s, 1H), 6.92 (s, 1H), 6.71 (s, 2H), 6.65 (d, *J* = 8.2 Hz, 1H), 6.56 (dd, *J* = 8.2, 2.3 Hz, 1H), 4.46 (s, 2H), 3.89 (s, 2H), 3.83–3.85 (m, 1H), 3.30–3.38 (m, 1H), 3.13–3.21 (m, 1H, overlapping), 2.21 (s, 6H), 1.15 (d, *J* = 6.9 Hz, 6H), 1.10 (d, *J* = 6.4 Hz, 3H). <sup>13</sup>C NMR (101 MHz, CD<sub>3</sub>CN): δ 169.02, 155.54, 151.92, 138.48, 134.49, 131.19, 125.92, 125.30, 117.38, 114.91, 114.05, 66.96, 66.20, 46.07, 33.19, 26.72, 21.93, 20.11, 19.65.

(*R*)-1-aminopropan-2-yl 2-(4-(4-hydroxy-3-isopropylbenzyl)-3,5-dimethylphenoxy)acetate (4)

To a 0° C solution of benzyl (*R*)-(2-hydroxypropyl)carbamate (262 mg, 1.25 mmol), DMAP (183 mg, 1.5 mmol), and THF (8 mL) was slowly added a solution of the acid chloride generated from benzyl protected sobetirome (0.5 mmol) in 4 mL THF. The reaction mixture was allowed to warm to room temperature, then heated to 50° C overnight with stirring. Filtration and

evaporation of the resulting filtrate gave a light-yellow oil which was purified using flash chromatography (silica, 10% to 30% ethyl acetate/hexanes). The resulting ester (50 mg, 0.082 mmol, 17% yield) was dissolved in 5 mL of dry methanol with 1 mL THF and 10% Pd/C (40 mg) was added to generate a suspension. The reaction mixture was subjected to vacuum for approximately 1 min, then placed under argon for approximately 1 min. This process was repeated three times to ensure the mixture was properly degassed. Triethylsilane (0.4 mL, 2.51 mmol) was then added dropwise to the suspension and the reaction mixture was stirred for 4 h at room temperature. Filtration over a pad of celite with methanol and concentration *in vacuo* gave an oily residue which was precipitated with cold hexanes and washed with hexanes to give the desired product as a white solid (22 mg, 0.057 mmol, 68% yield, 12% overall yield). <sup>1</sup>H NMR (400 MHz, CD<sub>3</sub>OD): δ 6.77 (s, 1H), 6.62 (s, 2 H), 6.55 (d, *J* = 8.1 Hz, 1H), 6.45 (d, *J* = 8.2 Hz, 1H), 5.20 (m, *J* = 3.0 Hz, 1H), 4.71 (d, *J* = 8.2 Hz, 2H), 3.84 (s, 2H), 3.21 (sept, *J* = 6.8 Hz, 1H), 3.18 (m, 2H), 2.16 (s, 6H), 1.31 (d, *J* = 6.5 Hz, 3H), 1.09 (d, *J* = 6.9 Hz, 6H). HRMS exact mass calcd for C<sub>23</sub>H<sub>32</sub>N<sub>1</sub>O<sub>4</sub> [M+H]<sup>+</sup>: m/z 386.23258. Found m/z 386.23349.

1-aminopropan-2-yl 2-(4-(4-hydroxy-3-isopropylbenzyl)-3,5-dimethylphenoxy)acetate (5)

This compound was synthesized followed the procedure described for the synthesis of (4) except with *N*-Cbz-1-amino-2-propanol and yielded an oil (2.2 mg, 0.0052 mmol, 2.1%): <sup>1</sup>H NMR (400 MHz, CD<sub>3</sub>OD) δ 6.75 (s, 1H), 6.54 (m, 3H), 6.47 (dd, *J* = 2.0, 6.0 Hz, 1H), 5.18 (m, 1H), 4.69 (d, *J* = 4.8 Hz, 2H), 3.84 (s, 2H), 3.15 (m, 3H), 2.15 (s, 6H), 1.30 (d, *J* = 6.4 Hz, 3H), 1.07 (d, *J* = 6.8 Hz, 6H). HRMS exact mass calcd for C<sub>23</sub>H<sub>32</sub>N<sub>1</sub>O<sub>4</sub> [M+H]<sup>+</sup>: m/z 386.23258. Found m/z 386.23308.

1-amino-2-methylpropan-2-yl 2-(4-(4-hydroxy-3-(propan-2-yl)phenyl)methyl-3,5-dimethylphenoxy)acetate (6)

To a 0 °C solution of *N*-Cbz-1-amino-2-methylpropan-2-ol (223 mg, 1 mmol), DMAP (92 mg, 0.75 mmol), and THF (3 mL) was added a solution of acid chloride of benzyl protected sobetirome (0.25 mmol) and THF (2 mL). The reaction mixture was allowed stir at 45 °C overnight. The reaction mixture was then concentrated, redissolved in a minimal amount of DCM, and purified using flash chromatography (silica, 20% to 50% ethyl acetate / hexanes) to yield the coupled *N*-Cbz ester (37 mg, 0.059 mmol). The resulting ester was dissolved in 2 mL MeOH and 2 mL of THF and purged with argon. 10% Pd/C (50mg) was added followed by the dropwise addition of triethylsilane (283 μL, 1.77 mmol). The reaction mixture was stirred at room temperature for 3 h and then filtered over a pad of celite with methanol. The solution was then concentrated under reduced pressure and precipitated with hexanes and ether to yield the product as an oily residue (5.6 mg, 5.6 % overall). <sup>1</sup>H NMR (400 MHz, CDCl<sub>3</sub>): δ 7.04 (m, 1 H), 6.94 (d, *J* = 2 Hz, 1H), 6.66 (s, 2 H), 6.62 (d, *J* = 8.08 Hz, 1H), 6.54 (dd, *J* = 8.08 Hz, 2.02 Hz, 1H), 4.55 (s, 2H), 3.92 (s, 2H), 3.38 (d, *J* = 6.32 Hz, 2H), 3.19 (sept, *J* = 6.82 Hz, 1H), 2.23 (s, 6H), 2.20 (br, 1H), 1.25 (s, 6H), 1.23 (d, *J* = 6.82 Hz, 6H). HRMS exact mass calcd for C<sub>24</sub>H<sub>34</sub>N<sub>1</sub>O<sub>4</sub> [M+H]<sup>+</sup>: m/z 400.24824. Found m/z 400.24765.

1-(methylamino) propan-2-yl 2-(4-(4-hydroxy-3-isopropylbenzyl)-3, 5-dimethylphenoxy) acetate (7)

This compound was synthesized followed the procedure described for the synthesis of (4) except with benzyl (2-hydroxypropyl)(methyl)carbamate to yield a white solid in 49 % yield. <sup>1</sup>H NMR (400 MHz, CDCl<sub>3</sub>): δ 6.92 (s, 1H), 6.64 (s, 2H), 6.60 (d, *J* = 8.1 Hz, 1H), 6.53 (d, *J* = 8.0 Hz, 1H),

4.70 (d,  $J = 8.2$  Hz, 2H), 4.08 (m, 1H), 3.88 (s, 2H), 3.54 (m, 1H), 3.30 (m, 1H), 3.18 (s, 3H), 3.02 (s, 1H), 2.19 (s, 6H), 1.22 (d,  $J = 6.9$  Hz, 6H), 1.18 (d,  $J = 6.4$  Hz, 3H). HRMS exact mass calcd for  $C_{24}H_{32}N_1O_4$   $[M-H]^+$ :  $m/z$  398.23258. Found  $m/z$  398.23336.

2-(isopropylamino) ethyl 2-(4-(4-hydroxy-3-isopropylbenzyl)-3,5-dimethylphenoxy)acetate (8)

This compound was synthesized followed the procedure described for the synthesis of (4) except with benzyl (2-hydroxypropyl)(isopropyl)carbamate to give a sticky residue in 24 % yield.

$^1H$ NMR (400 MHz,  $CDCl_3$ ):  $\delta$  6.93 (s, 1H), 6.68 (s, 2H), 6.53 (d,  $J = 8.0$  Hz, 1H), 6.49 (d,  $J = 8.0$  Hz, 1H), 4.74 (s, 2H), 4.60 (m, 1H), 4.23 (sep,  $J = 6.8$  Hz, 1H), 3.91 (s, 2H), 3.56 (dd,  $J = 14.6, 8.4$  Hz, 1H), 3.15 (sep,  $J = 7.0$  Hz, 1H), 3.09 (m, 1H), 2.22 (s, 6H), 1.21 (d,  $J = 6.8$  Hz, 6H), 1.15 (d,  $J = 6.9$  Hz, 6H), 1.08 (d,  $J = 6.5$  Hz, 3H). HRMS exact mass calcd for  $C_{26}H_{36}N_1O_4$   $[M-H]^+$ :  $m/z$  426.26389. Found  $m/z$  426.26464.

4-aminobutan-2-yl 2-(4-(4-hydroxy-3-isopropylbenzyl)-3, 5-dimethylphenoxy)acetate (9)

This compound was synthesized followed the procedure described for the synthesis of (4) except with benzyl (3-hydroxybutyl)(isopropyl)carbamate to yield the product as a white solid in 45% yield. The  $^1H$  NMR spectrum corresponds to the amide rearranged product.  $^1H$  NMR (400 MHz,  $CD_3CN$ ):  $\delta$  7.31 (m, 1H), 6.92 (s, 1H), 6.70 (s, 2H), 6.62 (d,  $J = 8.2$  Hz, 1H), 6.57 (dd,  $J = 8.1$  Hz, 2.04 Hz, 1H), 4.43 (s, 2H), 3.90 (s, 2H), 3.70–3.76 (m, 1H), 3.49 (m, 1H), 3.32–3.13 (m, 2H, overlapping), 2.22 (s, 6H), 1.61 (m, 1H), 1.46 (m, 1H), 1.13 (d,  $J = 7.0$  Hz, 6H), 1.11 (d,  $J = 6.6$  Hz, 3H). HRMS exact mass calcd for  $C_{24}H_{32}N_1O_4$   $[M-H]^+$ :  $m/z$  398.23258. Found  $m/z$  398.23335.

1-aminobutan-2-yl 2-(4-(4-hydroxy-3-isopropylbenzyl)-3,5-dimethylphenoxy)acetate (10)

To a 0° C solution of benzyl (2-hydroxybutyl)carbamate (587 mg, 2.63 mmol), DMAP (321 mg, 2.63 mmol), and THF (8 mL) was slowly added a solution of the acid chloride generated from benzyl protected sobetirome (0.66 mmol) in 4 mL THF. The reaction mixture was allowed to warm to room temperature, then heated to reflux overnight with stirring. Filtration and evaporation of the resulting filtrate gave a light-yellow oil which was purified using flash chromatography (silica, 10% to 50% ethyl acetate/hexanes). The resulting ester (236 mg, 0.378 mmol, 58% yield) was dissolved in 5 mL of dry methanol with 1 mL THF and 10% Pd/C (100 mg) was added to generate a suspension. The reaction mixture was subjected to vacuum for approximately 1 min, then placed under argon for approximately 1 min. This process was repeated three times to ensure the mixture was properly degassed. Triethylsilane (1.8 mL, 11.3 mmol) was then added dropwise to the suspension and the reaction mixture was stirred for 4 h at room temperature. Filtration over a pad of celite with methanol and concentration *in vacuo* gave an oily residue which was precipitated with cold hexanes and washed with hexanes. The desired product was obtained as a white solid after drying under high vacuum (87 mg, 0.217 mmol, 58% yield, 34% overall yield). The  $^1H$  NMR spectrum corresponds to the amide rearranged product.  $^1H$  NMR (400 MHz,  $CD_3CN$ ):  $\delta$  7.13 (m, 1H), 6.92 (s, 1H), 6.72 (s, 2H), 6.64 (d,  $J = 8.1$  Hz, 1H), 6.57 (dd,  $J = 7.9, 2.1$  Hz, 1H), 4.46 (s, 2H), 3.90 (s, 2H), 3.50–3.60 (m, 1H), 3.31–3.40 (m, 1H), 3.16–3.21 (m, 2H, overlapping), 2.22 (s, 6H), 1.30–1.49 (m, 2H), 1.15 (d,  $J = 7.1$  Hz, 6H), 0.93 (t,  $J = 6.7$  Hz, 3H). HRMS exact mass calcd for  $C_{24}H_{32}N_1O_4$   $[M-H]^+$ :  $m/z$  398.23258. Found  $m/z$  398.23331.

1-amino-3-methylbutan-2-yl 2-(4-(4-hydroxy-3-isopropylbenzyl)-3,5-dimethylphenoxy)acetate (11)

To a 0° C solution of 1-(dibenzylamino)-3-methylbutan-2-ol (745 mg, 2.63 mmol), DMAP (321 mg, 2.63 mmol), and THF (8 mL) was slowly added a solution of the acid chloride generated from benzyl protected sobetirome (0.66 mmol) in 4 mL THF. The reaction mixture was allowed to warm to room temperature, then heated to reflux overnight with stirring. Filtration and evaporation of the resulting filtrate gave a light-yellow oil which was purified using flash chromatography (silica, 10% to 50% ethyl acetate/hexanes). The resulting ester (128 mg, 0.187 mmol, 28% yield) was dissolved in 5 mL of dry methanol with 1 mL THF and 10% Pd/C (100 mg) was added to generate a suspension. The reaction mixture was subjected to vacuum for approximately 1 min, then placed under argon for approximately 1 min. This process was repeated three times to ensure the mixture was properly degassed. Triethylsilane (1.35 mL, 8.47 mmol) was then added dropwise to the suspension and the reaction mixture was stirred for 4 h at room temperature. Filtration over a pad of celite with methanol and concentration *in vacuo* gave an oily residue which was precipitated with cold hexanes and washed with hexanes. The desired product was obtained as a white solid after drying under high vacuum (69 mg, 0.167 mmol, 89% yield, 25% overall yield). <sup>1</sup>H NMR (400 MHz, CD<sub>3</sub>CN): δ 6.72 (s, 1H), 6.69 (s, 2H), 6.66 (d, *J* = 8.5 Hz, 1H), 6.53 (dd, *J* = 8.1 Hz, *J* = 2.5 Hz, 1H), 5.12 (m, 1H), 5.03 (d, *J* = 16.3 Hz, 1H), 4.75 (d, *J* = 16.5 Hz, 1H), 3.87 (s, 2H), 3.18 (m, 3H), 2.20 (s, 6H), 1.15 (d, *J* = 6.8 Hz, 6H), 0.92 (dd, *J* = 6.8, 1.7 Hz, 6H). HRMS exact mass calcd for C<sub>25</sub>H<sub>34</sub>N<sub>1</sub>O<sub>4</sub> [M-H]<sup>+</sup>: m/z 412.24824. Found m/z 412.24907.

3-methyl-1-(methylamino)butan-2-yl 2-(4-(4-hydroxy-3-isopropylbenzyl)-3,5-dimethylphenoxy)acetate (12)

To a 0° C solution of 1-(benzyl(methyl)amino)-3-methylbutan-2-ol (530 mg, 2.56 mmol), DMAP (312 mg, 2.55 mmol), and THF (8 mL) was slowly added a solution of the acid chloride generated from benzyl protected sobetirome (0.66 mmol) in 4 mL THF. The reaction mixture was allowed to warm to room temperature, then heated to reflux overnight with stirring. Filtration and evaporation of the resulting filtrate gave a light-yellow oil which was purified using flash chromatography (silica, 10% to 50% ethyl acetate/hexanes). The resulting ester (200 mg, 0.329 mmol, 50% yield) was dissolved in 5 mL of dry methanol with 1 mL THF and 10% Pd/C (100 mg) was added to generate a suspension. The reaction mixture was subjected to vacuum for approximately 1 min, then placed under argon for approximately 1 min. This process was repeated three times to ensure the mixture was properly degassed. Triethylsilane (1.6 mL, 10.04 mmol) was then added dropwise to the suspension and the reaction mixture was stirred for 4 h at room temperature. Filtration over a pad of celite with methanol and concentration *in vacuo* gave an oily residue which was precipitated with cold hexanes and washed with hexanes. The desired product was obtained as a white solid after drying under high vacuum (101 mg, 0.236 mmol, 72% yield, 36% overall yield). <sup>1</sup>H NMR (400 MHz, CD<sub>3</sub>CN): δ 6.93 (s, 1H), 6.71 (s, 2H), 6.69 (d, *J* = 8.6 Hz, 1H), 6.54 (dd, *J* = 8.3, 2.2 Hz, 1H), 5.22 (m, 1H), 5.12 (d, *J* = 16.5 Hz, 1H), 4.77 (d, *J* = 16.5 Hz, 1H), 3.88 (s, 2H), 3.18 (m, 3H), 2.62 (s, 3H), 2.20 (s, 6H), 1.15 (d, *J* = 6.8 Hz, 6H), 0.93 (dd, *J* = 7.0, 2.1 Hz, 6H). HRMS exact mass calcd for C<sub>26</sub>H<sub>36</sub>N<sub>1</sub>O<sub>4</sub> [M-H]<sup>+</sup>: m/z 426.26389. Found m/z 426.26456.

2-(methylamino)ethyl 2-(4-(4-hydroxy-3-methylbenzyl)-3,5-dimethylphenoxy)acetate (13)

To a 0° C solution of benzyl (2-hydroxyethyl)(methyl)carbamate (314 mg, 1.5 mmol), DMAP (183 mg, 1.5 mmol), and THF (8 mL) was slowly added a solution of the acid chloride generated from benzyl protected sobetirome (0.5 mmol) in 4 mL THF. The reaction mixture was allowed to warm to room temperature, then heated to 50° C overnight with stirring. Filtration and

evaporation of the resulting filtrate gave a light-yellow oil which was purified using flash chromatography (silica, 10% to 30% ethyl acetate/hexanes). The resulting ester (146 mg, 0.239 mmol, 48% yield) was dissolved in 5 mL of dry methanol with 1 mL THF and 10% Pd/C (100 mg) was added to generate a suspension. The reaction mixture was subjected to vacuum for approximately 1 min, then placed under argon for approximately 1 min. This process was repeated three times to ensure the mixture was properly degassed. Triethylsilane (1.2 mL, 7.53 mmol) was then added dropwise to the suspension and the reaction mixture was stirred for 4 h at room temperature. Filtration over a pad of celite with methanol and concentration *in vacuo* gave an oily residue which was precipitated with cold hexanes and washed with hexanes. The resulting residue was dissolved in 3 mL of ethyl acetate and 1 mL of 1 N HCl (ethyl acetate) was added and stirred 3 h. Evaporation of the solvent, followed by washing with hexanes gave the desired product as a white solid (37 mg, 0.088 mmol, 37% yield, 18% overall yield). <sup>1</sup>H NMR (400 MHz, CD<sub>3</sub>CN): δ 6.91 (s, 1H), 6.68 (s, 2H), 6.64 (d, *J* = 8.1 Hz, 1H), 6.53 (d, *J* = 7.8 Hz, 1H), 4.79 (s, 2H), 4.48 (m, 2H), 3.86 (s, 2H), 3.20 (m, 2H), 3.17 (sept, *J* = 6.9 Hz, 1H), 2.60 (s, 3H), 2.19 (s, 6H), 1.13 (d, *J* = 7.0 Hz, 6H). HRMS exact mass calcd for C<sub>23</sub>H<sub>32</sub>N<sub>1</sub>O<sub>4</sub> [M<sup>+</sup>H<sup>+</sup>]<sup>+</sup>: m/z 386.23258. Found m/z 386.23259.

3-amino-1,1,1-trifluoropropan-2-yl 2-(4-(4-hydroxy-3-isopropylbenzyl)-3,5-dimethylphenoxy)acetate (14)

To a 0° C solution of benzyl (3,3,3-trifluoro-2-hydroxypropyl)carbamate (207 mg, 0.786 mmol), DMAP (120 mg, 0.982 mmol), and chloroform (8 mL) was slowly added a solution of the acid chloride generated from benzyl protected sobetirome (0.392 mmol) in 4 mL chloroform. The reaction mixture was allowed to warm to room temperature, then heated to 50° C overnight with stirring. Evaporation of the product mixture gave a light-yellow oil which was purified using flash chromatography (silica, 10% to 30% ethyl acetate/hexanes). The resulting ester (79 mg, 0.119 mmol, 30% yield) was dissolved in 5 mL of dry methanol with 1 mL THF and 10% Pd/C (80 mg) was added to generate a suspension. The reaction mixture was subjected to vacuum for approximately 1 min, then placed under argon for approximately 1 min. This process was repeated three times to ensure the mixture was properly degassed. Triethylsilane (0.6 mL, 3.77 mmol) was then added dropwise to the suspension and the reaction mixture was stirred for 4 h at room temperature. Filtration over a pad of celite with methanol and concentration *in vacuo* gave an oily residue which was precipitated with cold hexanes and washed with hexanes to give the desired product as a white solid (39 mg, 0.089 mmol, 75% yield, 23% overall yield). <sup>1</sup>H NMR (400 MHz, CD<sub>3</sub>OD): δ 6.78 (s, 1H), 6.59 (s, 2H), 6.55 (d, *J* = 8.1 Hz, 1H), 6.48 (d, *J* = 8.4 Hz, 1H), 4.64 (s, 2H), 4.28 (m, 1H), 3.84 (s, 2H), 3.23 (dd, *J* = 13.1, 3.2 Hz, 1H), 3.17 (sept, *J* = 6.9 Hz, 1H), 3.04 (dd, *J* = 13.2, 9.5 Hz, 1H), 2.15 (s, 6H), 1.09 (d, *J* = 7.0 Hz, 6H). HRMS exact mass calcd for C<sub>23</sub>H<sub>29</sub>F<sub>3</sub>N<sub>1</sub>O<sub>4</sub> [M+H]<sup>+</sup>: m/z 440.20487. Found m/z 440.20412.

3-(trifluoromethyl)azetid-3-yl 2-(4-(4-hydroxy-3-(propan-2-yl)phenyl)methyl-3,5-dimethylphenoxy)acetate (15)

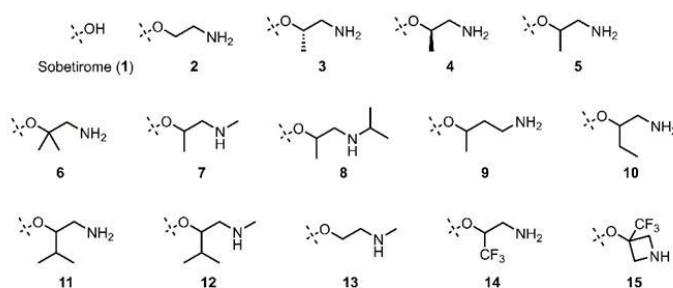
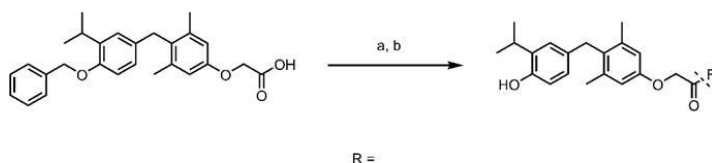
To a 0° C solution of *N*-Cbz-1-amino-3-hydroxy-3-(trifluoromethyl)-azetidine HCl (250 mg, 1.41 mmol), DMAP (122 mg, 1 mmol), and THF (3 mL) was added a solution of the acid chloride of benzyl protected sobetirome (0.25 mmol) and THF (2 mL). The reaction mixture was allowed stir at 45° C overnight. The reaction mixture was then concentrated, redissolved in a minimal amount of DCM, and purified using flash chromatography (silica, 20% to 50% ethyl acetate / hexanes) to yield the coupled *N*-Cbz ester (75 mg, 0.121 mmol). The resulting ester was dissolved in 2 mL MeOH and 2 mL of THF and purged with argon. 10% Pd/C (50mg) was added followed by the

dropwise addition of triethylsilane (484  $\mu\text{L}$ , 3.03 mmol). The reaction mixture was stirred at room temperature for 3 h and then filtered over a pad of celite with methanol. The solution was then concentrated under reduced pressure and precipitated with hexanes and ether to yield the product as an oily residue (6.8 mg, 6.0 % overall).  $^1\text{H NMR}$  (400 MHz,  $\text{CD}_3\text{OD}$ ):  $\delta$  6.82 (d,  $J = 2$  Hz, 1H), 6.67 (s, 2H), 6.59 (d,  $J = 8.08$  Hz, 1H), 6.52 (dd,  $J = 8.08, 2.02$  Hz, 1H), 4.78 (br s, 4H), 3.90 (s, 2H), 3.62 (t,  $J = 5.86$  Hz, 2H), 3.21 (sept,  $J = 7.02$  Hz, 1H), 2.21 (s, 6H), 1.23 (d,  $J = 7.02$  Hz, 6H). HRMS exact mass calcd for  $\text{C}_{24}\text{H}_{27}\text{F}_3\text{N}_1\text{O}_4$   $[\text{M}-\text{H}]^-$ :  $m/z$  450.18924. Found  $m/z$  450.18557.

## Results:

### Chemistry

In line with the recently reported successful application of an ethanolamine-based ester prodrug of sobetirome<sup>18</sup> and ethanolamine-based ester prodrugs of dexibuprofen,<sup>19, 20</sup> a drug with structural similarities to sobetirome, a new series of ethanolamine-derived prodrugs of sobetirome were synthesized in an effort to expand upon these findings and improve their pharmacokinetic properties regarding CNS distribution (Scheme 1). Derivatization of the ethanolamine moiety within the series explores varying aspects of steric and electronic parameters with subtle differences in lipophilicity. Branching at the alpha carbon adjacent to the ester group was examined in an effort to impede hydrolysis via steric hindrance of the ester carbonyl (3–12, 14–15). Electron withdrawing trifluoromethyl groups were incorporated to weaken the associated ester bonds (14–15), and alkylation of the amino group of the promo moiety (7–8, 12–13, 15) was implemented to modulate the amino group's pKa and deter potential interactions with monoamine oxidase (MAO).<sup>21</sup> Additionally, degrees of freedom about the promo moiety were altered by chain elongation (9) and incorporation of a heterocycle (15).



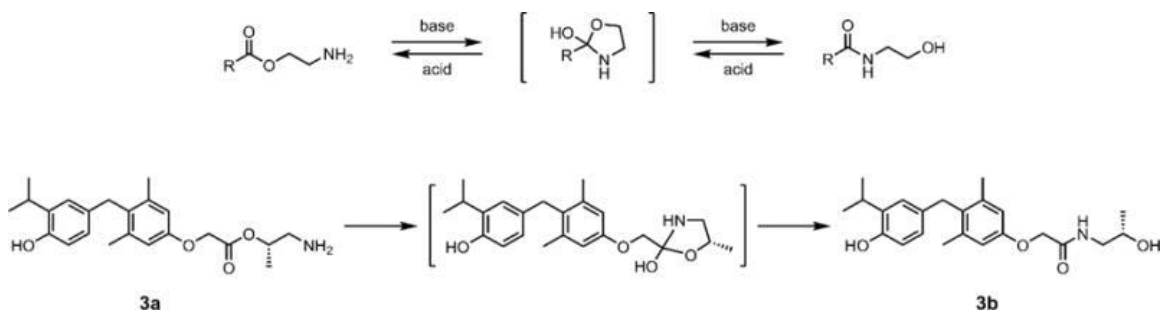
**Scheme 1**

*Synthesis and structures of sobetirome and sobetirome prodrugs. Reagents and conditions: (a) i) oxalyl chloride, DCM, DMF, (ii) N-Cbz amino alcohol or N-(di)benzyl amino alcohol, DMAP, THF (b) 10% Pd/C,  $\text{Et}_3\text{SiH}$ , MeOH/THF.*

Modular synthesis of the series of ethanolamine-based prodrugs was accomplished in two steps starting with coupling of a benzyl-protected sobetirome fragment to an N-Cbz or N-(di)benzyl protected amino alcohol, followed by parallel protecting group removal by hydrogenolysis to form the ester prodrugs in moderate-to-good yield (Scheme 1). To selectively form ester species of interest, the amino alcohol's amino group was protected with Cbz, which significantly alters the polarity of the promo moiety and provides for an easy separation and isolation of the N-protected amino alcohol. For amino alcohols that are not commercially available, zinc(II) perchlorate catalyzed nucleophilic attack of substituted epoxides by benzylated amines was employed according to a literature procedure.<sup>22</sup> Generation of the acid chloride of phenol-benzylated

sobetirome ([Scheme 1](#), left) is accomplished by treating phenol-benzylated sobetirome with oxalyl chloride in the presence of a catalytic amount of DMF.<sup>18, 23</sup> Coupling of the phenol-protected sobetirome acid chloride with *N*-protected amino alcohols occurs readily in the presence of DMAP in heated THF. Global deprotection of benzyl ether, *N*-Cbz, and *N*-benzyl protected fragments follows with treatment of the protected precursors with 10% Pd/C and triethylsilane in THF/MeOH.<sup>24</sup> Multiple precipitations of the resulting product from hexanes yields the desired ester derivatives in excellent purity.

All compounds in the series were characterized by <sup>1</sup>H NMR spectroscopy and assessed for purity by HPLC. While all isolated final compounds were spectroscopically determined to be the desired ester derivatives, it was discovered that by eluting some derivatives on silica led to the isolation of fractions that correspond to the promoiety-rearranged amide species ([Scheme 2](#)). Formally known as an O,N acyl migration, this intramolecular rearrangement proceeds with nucleophilic attack of the ester carbonyl by the promoiety's amino group lone pair leading to facile formation of a five-membered cyclic intermediate, followed by rearrangement to the thermodynamically favored amide. Intramolecular O,N acyl migrations have been well documented in organic synthesis, observed in a variety of natural products, and employed in medicinal chemistry as prodrug strategies.<sup>25, 26</sup> Characterization within the series regarding ester versus amide species is easily accomplished by <sup>1</sup>H NMR spectroscopy, where esters and amides can be distinguished on the basis of chemical shifts (see [Supporting Information](#)). Specifically, the proton attached to the oxygen-containing carbon within the promoiety displays a chemical shift around 5 ppm for esters, whereas this proton chemical shift is observed approximately 1 ppm upfield for the corresponding amide. Amide products also feature typical amide N-H peaks with chemical shifts occurring at 7.2 ppm in CD<sub>3</sub>CN or CD<sub>3</sub>OD within this series. Classically, this rearrangement is pH-controlled, favoring amide formation at neutral and alkaline pH ([Scheme 2](#)). The majority of deliberately prepared ester derivatives in this series readily rearrange to their amide counterparts in polar, protic solvents. HPLC analysis confirms the presence of both esters and amides, which can be distinguished on the basis of retention time and peak shape in each chromatogram. Both HPLC run conditions and sample preparation involve aqueous solutions, from which the majority of derivatives were shown to display only the amide product upon analysis by HPLC. Quick preparation and injection of ester derivative **3** (**3a**, [Scheme 2](#)) led to peaks in the chromatogram associated with both ester derivative and amide derivative by comparison to the chromatogram of the deliberately synthesized amide of **3** (**3b**, [Scheme 2](#)) under identical run conditions (see [Supporting Information](#)). Within 5 minutes of running approximately 25% of the ester had converted to the amide, and sampling the same solution in which ester **3a** was prepared for this run approximately 30 minutes later showed only the amide **3b** in the chromatogram. The only derivatives in this series which did not display rearrangement to the amide product were the derivatives which contained isopropyl groups next to the ester motif (**11** and **12**) and cyclic derivative **15**. Apparently, isopropyl groups represent the steric limit about the ester motif for which this rearrangement is inhibited. Interestingly, *N*-alkylated derivatives **7**, **8**, and **13** were observed to freely rearrange to their corresponding tertiary amides.



## Scheme 2

*O,N* and *N,O* acyl migration is an intramolecular rearrangement and is pH controlled (Top). Ester-to-amide rearrangement of lead prodrug **3** (Bottom).

## Biological Evaluation

To assess CNS penetration, a biodistribution study in mice was performed on each prodrug to determine brain concentrations and brain/serum ratios following systemic (i.p.) administration. Samples for this *in vivo* study and every subsequent *in vivo* study (i.p., p.o., and i.v.) were prepared in a vehicle consisting of 50% DMSO in saline, a solvent combination in which the prodrugs were found to rearrange to their amide conformation. Therefore, *all prodrugs tested were administered as their amide-rearranged isomers with the exception of esters 11, 12, and 15, which do not rearrange to amides*. Mouse cohorts received an equimolar dose (1.5  $\mu\text{mol} / \text{kg}$ ) of prodrug and one cohort received the same dose of sobetirome as a control. Whole brain and blood was collected 1 h after administration and the concentration of the parent drug sobetirome derived from each sample was quantified using LC-MS/MS. Most of the prodrugs produced increased brain sobetirome levels compared to the equimolar dose of sobetirome (Table 1). The highest sobetirome concentration in brain was delivered from prodrug **3**, which contains the (*S*) enantiomer of 1-amino-2-propanol as its promoity. Prodrug **3** delivers 3.6-fold more sobetirome to the brain than an equimolar dose of unmodified sobetirome, and its levels are 1.7-fold higher than the previously reported ethanolamine-derived prodrug of sobetirome **2** in a side-by-side comparison.<sup>18</sup> In addition to BBB penetration, an ideal prodrug would be stable in blood and limit exposure of the parent drug in peripheral tissues. Most prodrugs in this series displayed higher brain/serum ratios than the control dose of sobetirome. While prodrug **6** provided the greatest brain/serum ratio of 1.2, it was attended by very low brain levels which likely suggests that **6** hydrolyzes too slowly to be effective as a prodrug for delivering sobetirome to the CNS. Following prodrug **6**, the next highest brain/serum ratio is that for prodrug **3** with a value of 0.5, which is ~13-fold higher than the brain/serum ratio of sobetirome, and ~7-fold higher than previously reported **2**.<sup>18</sup> From this biodistribution study, it appears that the prodrugs which can undergo this intramolecular ester-to-amide rearrangement of their promoities display the desired PK-ADME properties for CNS distribution, suggesting that amide prodrugs of sobetirome are the pharmacologically active species of interest. This was confirmed by analyzing prodrug **3** synthesized as an ester (**3a**) side-by-side with the deliberately prepared amide of **3** (**3b**), which gave statistically identical brain levels and brain/serum ratios at equimolar doses (see Supporting Information). These findings suggest that a similar rearrangement may occur *in vivo* with the previously reported dexibuprofen ethanolamine prodrugs that inspired our efforts with sobetirome.<sup>19, 20</sup> This previous work reported an ethanolamino ester, *N*-alkyl ethanolamino ester,

and an *N,N*-dialkyl ethanolamino ester derivative, of which it seems likely that the former two could undergo a similar rearrangement to the corresponding amides. However, their results run counter to that which we observe, where the *bona fide* ester in their series (*N,N*-dialkyl ethanolamino derivative) displayed the best BBB permeability. Despite the structural similarities between the parent drugs, the CNS penetration mechanisms may be different; the dexibuprofen prodrugs may utilize a partial active transport process for derivatives containing promoieties that were not found to be effective for CNS penetration with sobetirome.

Table 1

Sobetirome concentrations (ng / g) in the brain and brain/serum ratios 1 h after administration of sobetirome (**1**, 1.5  $\mu\text{mol} / \text{kg}$ , i.p.) or prodrugs **2–15** (1.5  $\mu\text{mol} / \text{kg}$ , i.p.) in mice.<sup>a</sup>

Compound	Brain		Brain / Serum	
	[1] (ng/g)	SEM	Ratio	SEM
<b>1</b>	2.32	0.32	0.037	0.0044
<b>2</b>	4.92*	0.12	0.066	0.0011
<b>3</b>	8.26**	0.28	0.47	0.15
<b>4</b>	8.12**	0.31	0.19	0.062
<b>5</b>	5.92**	0.18	0.21	0.0062
<b>6</b>	0.40*	0.014	1.22	0.38
<b>7</b>	5.12	1.82	0.23	0.013
<b>8</b>	0.48	0.0031	0.23	0.0015
<b>9</b>	4.46	1.96	0.33	0.070
<b>10</b>	4.26	1.04	0.41	0.027
<b>11</b>	3.38	0.26	0.045	0.0027
<b>12</b>	1.79	0.71	0.024	0.0046
<b>13</b>	6.33*	0.64	0.21	0.026
<b>14</b>	5.23**	0.038	0.20	0.015
<b>15</b>	5.14**	0.21	0.13	0.027

Significance compared to sobetirome (**1**):

\* $p < 0.05$ ,

\*\* $p < 0.01$ ,

\*\*\* $p < 0.005$ .

<sup>a</sup>Values are reported as the mean ( $n = 3$  mice) with corresponding standard error of the mean (SEM).

Following the single time point study, an 8-hour time-course distribution study in mice was conducted to further understand the pharmacokinetic properties of prodrug **3** versus sobetirome. Analyzing for sobetirome concentration, pharmacokinetic time-course curves were generated, and area under the curve (AUC) values for brain, serum, liver, heart, and kidney were obtained (Figure 1, Table 2). Trends in the single point study are corroborated in the AUC analyses; prodrug **3** increases sobetirome exposure in brain (~2-fold) and significantly decreases sobetirome exposure in peripheral tissues compared to direct equimolar sobetirome administration. Although at earlier time points in this particular experiment the sobetirome brain levels generated from prodrug **3** are slightly lower than were found in the 1 h single time point study (*vide supra*), increased sobetirome brain levels are observed extending out to the 8 h time point. This is likely reflective of a slow hydrolysis rate for prodrug **3** once it has accessed the CNS. Prodrug **3** reduces peripheral exposure of the parent drug by ~3.5-fold in serum, ~2-fold in liver, ~3-fold in heart, and ~2-fold in kidney. The  $AUC_{\text{brain}}/AUC_{\text{serum}}$  ratio for sobetirome was found to be 0.02 consistent with our previous findings.<sup>18</sup> The  $AUC_{\text{brain}}/AUC_{\text{serum}}$  ratio for prodrug **3** was found to be 0.13 representing an approximate 3-fold improvement compared to the same previously reported ratio for prodrug **2**.<sup>18</sup> While both values lie on the low end of the range for approved CNS drugs,<sup>27,28</sup> prodrug **3** offers a significant improvement in CNS distribution. Clear  $C_{\text{max}}$  and  $T_{\text{max}}$  values were obscured by spread in the data, but occurred between the initial 15 and 30 min time points in all tissues analyzed for sobetirome and prodrug **3**, suggesting a rapid distribution phase for both in mice.

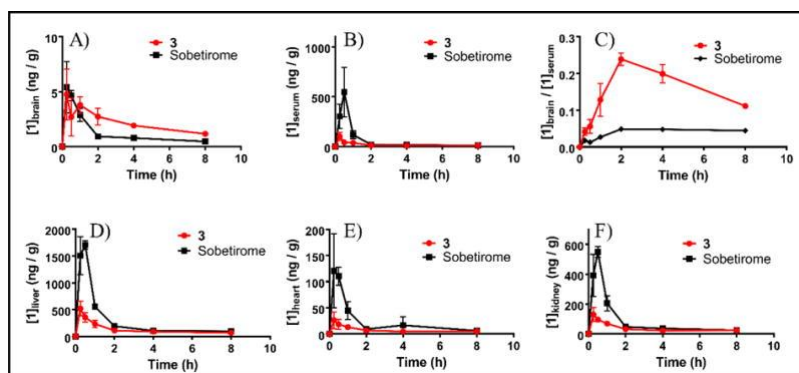


Figure 1

Sobetirome (black trace) and prodrug **3** (red trace) AUCs measuring parent drug sobetirome levels in brain (A), serum (B), brain/serum (C), liver (D),

heart (E), and kidney (F). Data are represented as the mean ( $n = 3$  mice) with corresponding standard error of the mean at time points (0.25 h, 0.5 h, 1 h, 2 h, 4 h, and 8 h) over an 8 h period.

Table 2

AUC values in  $\text{ng/g}\cdot\text{h}$  for sobetirome and **3** by tissue.

Sobetirome (1)     **3**

Tissue     $AUC_{0 \rightarrow t}$  ( $\text{ng/g}\cdot\text{h}$ )     $AUC_{0 \rightarrow t}$  ( $\text{ng/g}\cdot\text{h}$ )

## Sobetirome (1) 3

Tissue	AUC <sub>0→t</sub> (ng/g*h)	AUC <sub>0→t</sub> (ng/g*h)
Brain	9.9	17.2
Serum	472.6	136.5
Liver	2235	1017
Heart	180.3	57.2
Kidney	686.8	283.8

To further evaluate the PK-ADME properties of prodrug **3**, an oral bioavailability study was performed on **3** and the parent drug sobetirome for comparison. The pharmacokinetics for sobetirome described herein represent a re-evaluation of previously published data.<sup>18</sup> Triiodothyronine (T3) is known to participate in enterohepatic circulation (EHC),<sup>29, 30</sup> a process which recycles drugs or drug metabolites between the intestinal tract, portal circulation, and liver via the biliary tract and is characterized by multiple peaks in circulating drug concentration within the concentration-time profile from oral dosing, and often a long apparent drug half-life.<sup>31</sup> As a synthetic analog of T3, we questioned whether sobetirome and related prodrugs may also be subject to EHC. To evaluate the potential involvement in this process and obtain more accurate pharmacokinetic data, the serum concentration-time profiles were extended from 8-hours to 24-hours. Mouse cohorts were treated with a single dose of sobetirome or prodrug **3** administered by intravenous injection (i.v., 3.05  $\mu\text{mol} / \text{kg}$ ) and oral gavage (p.o., 30.5  $\mu\text{mol} / \text{kg}$ ) and drug blood levels were measured over a 24-hour time-course. Serum samples from each cohort were quantified using an LC-MS/MS method analyzing for both prodrug **3** and sobetirome (Fig. 2). Analysis of the data from sobetirome administration revealed a circulating half-life ( $t_{1/2}$ ) of approximately 7 h (Figure 2, D), a clearance of 8 mL / min / kg, and an oral bioavailability (%F) of 92%. In addition to its exceptional oral bioavailability, these data suggest that sobetirome has an unusually long half-life and correspondingly low clearance in mice.<sup>32</sup> Furthermore, the sobetirome concentration-time profile from oral dosing clearly displays a secondary peak in circulating drug concentration at around 8 h (Figure 2, C) which is distinct from  $C_{\text{max}}$  and is indicative of recycling of the bolus oral dose of sobetirome by EHC operating on the fraction of sobetirome subject to first-pass metabolism. The presence of EHC indicates that hepatic metabolism of sobetirome involves a reversible conjugation reaction such as glucuronidation which is the case with the fraction of T3 that is subject to EHC.<sup>30</sup>

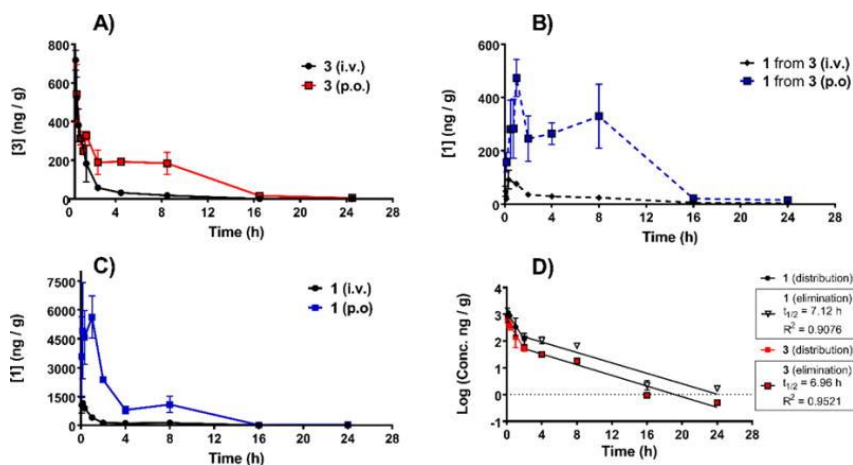


**Figure 2**

A) Serum [3] vs. time dosing prodrug 3 in mice. Intravenous dosing (black trace,  $3.05 \mu\text{mol} / \text{kg}$ ) and oral dosing (red trace,  $30.5 \mu\text{mol} / \text{kg}$ ). B) Serum [1] vs. time dosing prodrug 3 in mice. Intravenous dosing (black trace) and oral dosing (blue trace). C) Serum [1] vs. time dosing sobetirome in mice. Intravenous dosing (black trace,  $3.05 \mu\text{mol} / \text{kg}$ ) and oral dosing (blue trace,  $30.5 \mu\text{mol} / \text{kg}$ ). D) Semilog plot of serum [1] (black symbols) and [3] (red symbols) vs. time.

Prodrug **3** was also found to have a relatively long circulating half-life ( $t_{1/2}$ ) of approximately 7 h (Figure 2, D), a clearance of  $28 \text{ mL} / \text{min} / \text{kg}$ , and an oral bioavailability (%F) of 36% (Figure 2, A) in mice. Sobetirome concentration analyzed in these samples provided AUCs that correspond to the levels of parent drug liberated from **3** upon bolus intravenous or oral delivery into the mouse (Figure 2, B). The amount of sobetirome from cleavage of **3** in blood was found to be 2.4-fold greater from dosing **3** orally compared to intravenously. Total drug oral bioavailability (prodrug **3** + sobetirome **1**) can be estimated by adding the cleaved parent drug sobetirome AUCs (Figure 2, B) to the prodrug **3** AUCs (Figure 2, A) to give a value of %F = 56%. This %F corresponds to the calculated percent of combined prodrug and parent drug that make it into systemic circulation following an oral dose. A possible explanation for the reduced oral bioavailability of prodrug **3** may lie in the pH-controlled Scheme 2 for ester and amide interconversion. Upon dosing orally, the prodrug is placed in a low pH environment within the gut, which should effectively favor rearrangement to the ester, which is hydrolytically less stable. Differences in how sobetirome and prodrug **3** are metabolized following oral administration may account for the remainder of the discrepancy. Additionally, the second peak in the oral concentration-time profile of **3** around 8 h, along with its long half-life of 7 h, implicate the prodrug's involvement in EHC akin to the parent drug sobetirome. The recycling of prodrug **3** by virtue of EHC increases its time in and exposure to the gastrointestinal track likely increasing the fraction of prodrug cleavage to sobetirome before the prodrug reaches systemic circulation from an oral dose.

Having shown that prodrug **3** delivers more sobetirome to the CNS from a systemic dose compared to unmodified sobetirome, we next evaluated whether this translated into increased potency of target engagement in the brain. *Hairless (Hr)* is a gene that is positively regulated by thyroid hormone in the CNS, and is suggested to play a role in influencing the expression of downstream thyroid hormone-responsive genes.<sup>33, 34</sup> Upregulation of *Hr* was examined and dose-response data was collected and compared for prodrug **3**, sobetirome, and endogenous thyroid hormone (T3). Brains were collected from cohorts of mice ( $n = 3$ ) that received six different systemically administered doses of **3**, sobetirome, or T3 (i.p., once-daily, 7 days) and *Hr* expression was analyzed by qPCR (Fig. 3). ED<sub>50</sub> values obtained follow an expected trend in potency where T3 ( $0.09 \mu\text{mol} / \text{kg}$ ) > **3** ( $1.005 \mu\text{mol} / \text{kg}$ ) > sobetirome ( $1.8 \mu\text{mol} / \text{kg}$ ). The data

are in agreement with previously reported *Hr* activation by T3 in primary mouse cerebrocortical cell cultures,<sup>35</sup> and the observed ~20-fold difference in ED<sub>50</sub> values reported here between T3 and sobetirome parallels the approximate 20-fold difference in thyroid-stimulating hormone (TSH) levels in cholesterol-fed rats treated with T3 and sobetirome,<sup>36</sup> which is another direct readout of receptor activation in the CNS following peripheral dosing.<sup>37</sup> An approximate 2-fold increase in potency is observed for **3** compared to sobetirome, which can be fully accounted for by the increase in sobetirome brain exposure delivered by prodrug **3** (*vide supra*). Thus, prodrug **3** significantly improves the delivery and distribution of sobetirome in the CNS resulting in a formal increase in the CNS potency of sobetirome mediated TR activation with a concomitant decrease in peripheral sobetirome exposure.

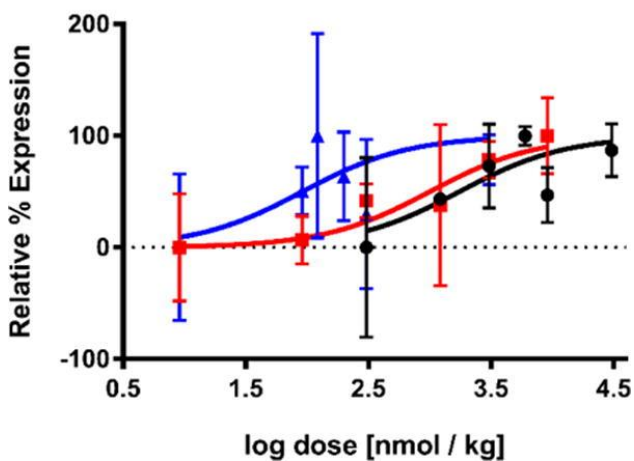


**Figure 3**

*Dose — response curves for relative brain expression of Hairless (*Hr*) gene following systemic administration (i.p.) of 3,3',5-triiodo-L-thyronine (T3, blue •), sobetirome (black •), and prodrug **3** (red •).*

#### Discussion:

A series of sobetirome ester prodrugs were synthesized that feature promoieties based on the ethanolamine motif. The majority of these derivatives were found to readily undergo intramolecular O,N acyl migration, isomerizing the esters to the corresponding amides, which were found to be the pharmacologically active species *in vivo*. Most derivatives analyzed delivered increased CNS exposure of sobetirome with prodrug **3** demonstrating superior properties including increased brain penetration and minimized peripheral exposure of the parent drug. Pharmacokinetic analysis revealed the likely involvement of both sobetirome and prodrug **3** in enterohepatic circulation. Systemic dosing of prodrug **3** was found to stimulate transcription of the TR target gene *Hr* in the brain with greater potency than unmodified sobetirome. Together, these results indicate that prodrug **3**, and more generally amide-based prodrugs of sobetirome, may offer advantages for thyromimetic targeting of the CNS.

#### Acknowledgements:

Research reported in this publication was supported by a grant from the National Institutes of Health ([DK052798](#), T.S.S.), the OHSU Laura Fund for Innovation in Multiple Sclerosis, and the National Institutes of Health under Award Number T32DK007680 (support to S.J.F.) and the National Multiple Sclerosis Society (FG 2023A1/2 M.D.H. and RG 5199A4/1 D.B.). Analytical support was provided by the Bioanalytical Shared Resource/Pharmacokinetics Core Facility, which is part of the University Shared Resource Program at Oregon Health & Sciences University. We thank L. Bleyle for her assistance with LC—MS/MS analysis. We would also like to thank Dr. Andrea DeBarber at the Portland State University BioAnalytical Mass Spectrometry Facility for HRMS.

## Abbreviations Used

ACN	acetonitrile
br	broad
Cbz	N-benzyloxycarbonyl
DMAP	4-dimethylaminopyridine
DMSO	dimethyl sulfoxide
ED <sub>50</sub>	median effective dose
HPLC	high performance liquid chromatography
LC-MS/MS	liquid chromatography tandem mass spectrometry
MeOH	methanol
MHz	megahertz
NMR	nuclear magnetic resonance spectroscopy
Pd/C	palladium on carbon
p.o	per os
r.t	room temperature
THF	tetrahydrofuran

## References:

1. Bernal J. Thyroid hormone receptors in brain development and function. *Nat Clin Pract Endocrinol Metab.* 2007;3:249–259. [[PubMed](#)] [[Google Scholar](#)]
2. Barres BA, Lazar MA, Raff MC. A novel role for thyroid hormone, glucocorticoids and retinoic acid in timing oligodendrocyte development. *Development.* 1994;120:1097–1108. [[PubMed](#)] [[Google Scholar](#)]
3. Dugas JC, Ibrahim A, Barres BA. The T3-induced gene KLF9 regulates oligodendrocyte differentiation and myelin regeneration. *Mol Cell Neurosci.* 2012;50:45–57. [[PMC free article](#)] [[PubMed](#)] [[Google Scholar](#)]
4. Harsan L-A, Steibel J, Zaremba A, Agin A, Sapin R, Poulet P, Guignard B, Parizel N, Grucker D, Boehm N, Miller RH, Ghandour MS. Recovery from chronic demyelination by thyroid hormone therapy: myelinogenesis induction and assessment by diffusion tensor magnetic resonance imaging. *J Neurosci.* 2008;28:14189–14201. [[PMC free article](#)] [[PubMed](#)] [[Google Scholar](#)]

5. Franco PG, Silvestroff L, Soto EF, Pasquini JM. Thyroid hormones promote differentiation of oligodendrocyte progenitor cells and improve remyelination after cuprizone-induced demyelination. *Exp Neurol*. 2008;212:458–467. [[PubMed](#)] [[Google Scholar](#)]
6. Zhang M, Zhan XL, Ma ZY, Chen XS, Cai QY, Yao ZX. Thyroid hormone alleviates demyelination induced by cuprizone through its role in remyelination during the remission period. *Exp Biol Med (Maywood)* 2015;240:1183–1196. [[PMC free article](#)] [[PubMed](#)] [[Google Scholar](#)]
7. Compston A, Coles A. Multiple sclerosis. *The Lancet*. 372:1502–1517. [[PubMed](#)] [[Google Scholar](#)]
8. Harlow DE, Honce JM, Miravalle AA. Remyelination therapy in multiple sclerosis. *Front Neurol*. 2015;6:257. [[PMC free article](#)] [[PubMed](#)] [[Google Scholar](#)]
9. Hartley MD, Altowajri G, Bourdette D. Remyelination and multiple sclerosis: therapeutic approaches and challenges. *Curr Neurol Neurosci Rep*. 2014;14:1–9. [[PubMed](#)] [[Google Scholar](#)]
10. Baxter JD, Webb P. Thyroid hormone mimetics: potential applications in atherosclerosis, obesity and type 2 diabetes. *Nat Rev Drug Discov*. 2009;8:308–320. [[PubMed](#)] [[Google Scholar](#)]
11. Scanlan TS. Sobetirome: a case history of bench-to-clinic drug discovery and development. *Heart Fail Rev*. 2010;15:177–182. [[PubMed](#)] [[Google Scholar](#)]
12. Genin EC, Gondcaille C, Tromprier D, Savary S. Induction of the adrenoleukodystrophy-related gene (ABCD2) by thyromimetics. *J Steroid Biochem Mol Bio*. 2009;116:37–43. [[PubMed](#)] [[Google Scholar](#)]
13. Baxi EG, Schott JT, Fairchild AN, Kirby LA, Karani R, Uapinyoying P, Pardo-Villamizar C, Rothstein JR, Bergles DE, Calabresi PA. A selective thyroid hormone beta receptor agonist enhances human and rodent oligodendrocyte differentiation. *Glia*. 2014;62:1513–1529. [[PMC free article](#)] [[PubMed](#)] [[Google Scholar](#)]
14. Hitchcock SA, Pennington LD. Structure-brain exposure relationships. *J Med Chem*. 2006;49:7559–7583. [[PubMed](#)] [[Google Scholar](#)]
15. Stella V, Borchardt R, Hageman M, Oliyai R, Maag H, Tilley J. *Prodrugs: Challenges and Rewards*. Springer; New York: 2007. [[Google Scholar](#)]
16. Trost SU, Swanson E, Gloss B, Wang-Iverson DB, Zhang H, Volodarsky T, Grover GJ, Baxter JD, Chiellini G, Scanlan TS, Dillmann WH. The thyroid hormone receptor-beta-selective agonist GC-1 differentially affects plasma lipids and cardiac activity. *Endocrinology*. 2000;141:3057–3064. [[PubMed](#)] [[Google Scholar](#)]
17. Takahashi N, Asano Y, Maeda K, Watanabe N. In vivo evaluation of 1-benzyl-4-aminoindole-based thyroid hormone receptor agonists: importance of liver selectivity in drug discovery. *Biol Pharm Bull*. 2014;37:1103–1108. [[PubMed](#)] [[Google Scholar](#)]
18. Placzek AT, Ferrara SJ, Hartley MD, Sanford-Crane HS, Meinig JM, Scanlan TS. Sobetirome prodrug esters with enhanced blood—brain barrier permeability. *Bioorg Med Chem*. 2016;24:5842–5854. [[PMC free article](#)] [[PubMed](#)] [[Google Scholar](#)]

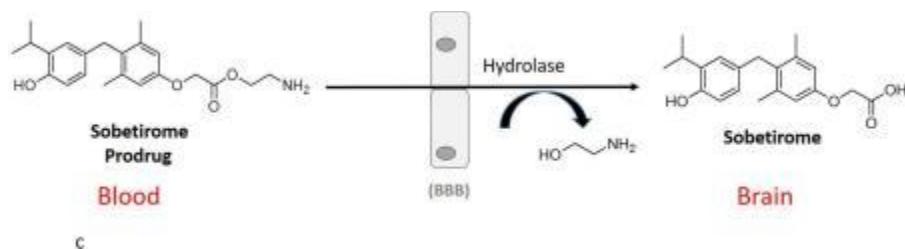
19. Zhang X, Liu X, Gong T, Sun X, Zhang ZR. In vitro and in vivo investigation of dexibuprofen derivatives for CNS delivery. *Acta Pharmacol Sin.* 2012;33:279–288. [[PMC free article](#)] [[PubMed](#)] [[Google Scholar](#)]
20. Li Y, Zhou Y, Jiang J, Wang X, Fu Y, Gong T, Sun X, Zhang Z. Mechanism of brain targeting by dexibuprofen prodrugs modified with ethanolamine-related structures. *J Cereb Blood Flow Metab.* 2015;35:1985–1994. [[PMC free article](#)] [[PubMed](#)] [[Google Scholar](#)]
21. Kalaria RN, Harik SI. Blood-brain barrier monoamine oxidase: enzyme characterization in cerebral microvessels and other tissues from six mammalian species, including human. *J Neurochem.* 1987;49:856–864. [[PubMed](#)] [[Google Scholar](#)]
22. Shivani, Pujala B, Chakraborti AK. Zinc(II) Perchlorate Hexahydrate Catalyzed Opening of Epoxide Ring by Amines:• Applications to synthesis of (RS)/(R)-propranolols and (RS)/(R)/(S)-naftopidils. *J Org Chem.* 2007;72:3713–3722. [[PubMed](#)] [[Google Scholar](#)]
23. Marson CM. Reactions of carbonyl compounds with (monohalo) methyleniminium salts (vilsmeier reagents) *Tetrahedron.* 1992;48:3659–3726. [[Google Scholar](#)]
24. Mandal PK, McMurray JS. Pd-C-induced catalytic transfer hydrogenation with triethylsilane. *J Org Chem.* 2007;72:6599–6601. [[PubMed](#)] [[Google Scholar](#)]
25. Mariusz S, Yoshiaki K. Application of the O-N intramolecular acyl migration reaction in medicinal chemistry. *Curr Med Chem.* 2007;14:2813–2823. [[PubMed](#)] [[Google Scholar](#)]
26. Markey SP, Dudding T, Wang T-CL. Base- and acid-catalyzed interconversions of O-acyl- and N-acyl-ethanolamines: a cautionary note for lipid analyses. *J Lipid Res.* 2000;41:657–662. [[PubMed](#)] [[Google Scholar](#)]
27. Doran A, Obach RS, Smith BJ, Hosea NA, Becker S, Callegari E, Chen C, Chen X, Choo E, Cianfroga J, Cox LM, Gibbs JP, Gibbs MA, Hatch H, Hop CE, Kasman IN, Laperle J, Liu J, Liu X, Logman M, Maclin D, Nedza FM, Nelson F, Olson E, Rahematpura S, Raunig D, Rogers S, Schmidt K, Spracklin DK, Szewc M, Troutman M, Tseng E, Tu M, Van Deusen JW, Venkatakrishnan K, Walens G, Wang EQ, Wong D, Yasgar AS, Zhang C. The impact of P-glycoprotein on the disposition of drugs targeted for indications of the central nervous system: evaluation using the MDR1A/1B knockout mouse model. *Drug Metab Dispos.* 2005;33:165–174. [[PubMed](#)] [[Google Scholar](#)]
28. Reichel A. The role of blood-brain barrier studies in the pharmaceutical industry. *Curr Drug Metab.* 2006;7:183–203. [[PubMed](#)] [[Google Scholar](#)]
29. DiStefano IJJ, Sternlicht M, Harris DR. Rat enterohepatic circulation and intestinal distribution of enterally infused thyroid hormones. *Endocrinology.* 1988;123:2526–2539. [[PubMed](#)] [[Google Scholar](#)]
30. Rutgers M, Heusdens FA, Bonthuis F, Herder WWD, Hazenberg MP, Visser TJ. Enterohepatic circulation of triiodothyronine (T3) in rats: importance of the microflora for the liberation and reabsorption of T3 from biliary T3 conjugates. *Endocrinology.* 1989;125:2822–2830. [[PubMed](#)] [[Google Scholar](#)]
31. Roberts MS, Magnusson BM, Burczynski FJ, Weiss M. Enterohepatic circulation. *Clin Pharmacokinet.* 2002;41:751–790. [[PubMed](#)] [[Google Scholar](#)]

32. Di L, Kerns EH. Drug-Like Properties: Concepts, Structure Design and Methods from ADME to Toxicity Optimization. Elsevier Science; 2015. [[Google Scholar](#)]
33. Thompson CC, Bottcher MC. The product of a thyroid hormone-responsive gene interacts with thyroid hormone receptors. Proc Natl Acad Sci USA. 1997;94:8527–8532. [[PMC free article](#)] [[PubMed](#)] [[Google Scholar](#)]
34. Thompson CC, Potter GB. Thyroid hormone action in neural development. Cereb Cortex. 2000;10:939–945. [[PubMed](#)] [[Google Scholar](#)]
35. Gil-Ibanez P, Bernal J, Morte B. Thyroid hormone regulation of gene expression in primary cerebrocortical cells: role of thyroid hormone receptor subtypes and interactions with retinoic acid and glucocorticoids. PLoS One. 2014;9:e91692. [[PMC free article](#)] [[PubMed](#)] [[Google Scholar](#)]
36. Grover GJ, Egan DM, Sleph PG, Beehler BC, Chiellini G, Nguyen NH, Baxter JD, Scanlan TS. Effects of the thyroid hormone receptor agonist GC-1 on metabolic rate and cholesterol in rats and primates: selective actions relative to 3,5,3'-triiodo-L-thyronine. Endocrinology. 2004;145:1656–1661. [[PubMed](#)] [[Google Scholar](#)]
37. Brent GA. Mechanisms of thyroid hormone action. J Clin Invest. 2012;122:3035–3043. [[PMC free article](#)] [[PubMed](#)] [[Google Scholar](#)]
38. Placzek AT, Scanlan TS. New synthetic routes to thyroid hormone analogs: d<sub>6</sub>-sobetirome, <sup>3</sup>H-sobetirome, and the antagonist NH-3. Tetrahedron. 2015;71:5946–5951. [[PMC free article](#)] [[PubMed](#)] [[Google Scholar](#)]
39. Barca-Mayo O, Liao X-H, Alonso M, Cosmo CD, Hernandez A, Refetoff S, Weiss RE. Thyroid hormone receptor and regulation of type 3 deiodinase. Mol Endocrinol. 2011;25:575–583. [[PMC free article](#)] [[PubMed](#)] [[Google Scholar](#)]
40. Saavedra JE. Reductive alkylation of beta.-alkanolamines with carbonyl compounds and sodium borohydride. J Org Chem. 1985;50:2271–2273. [[Google Scholar](#)]
41. Wünsch E, Graf W, Keller O, Keller W, Wersin G. On the synthesis of benzyloxycarbonyl amino acids. Synthesis. 1986;1986:958–960. [[Google Scholar](#)]

Placzek, A. T., Ferrara, S. J., Hartley M. D., **Sanford-Crane H. S.**, Meining J. M., & Scanlan, T. S. *Sobetirome prodrug esters with enhanced blood-brain barrier permeability*. *Bioorganic & Medicinal Chemistry*, 24(22), 5842-5854, 2016.

**Abstract:**

There is currently great interest in developing drugs that stimulate myelin repair for use in demyelinating diseases such as multiple sclerosis. Thyroid hormone plays a key role in stimulating myelination during development and also controls the expression of important genes involved in myelin repair in adults. Because endogenous thyroid hormone in excess lacks a generally useful therapeutic index, it is not used clinically for indications other than hormone replacement; however, selective thyromimetics such as sobetirome offer a therapeutic alternative. Sobetirome is the only clinical-stage thyromimetic that is known to cross the blood-brain-barrier (BBB) and we endeavored to increase the BBB permeability of sobetirome using a prodrug strategy. Ester prodrugs of sobetirome were prepared based on literature reports of improved BBB permeability with other carboxylic acid containing drugs and BBB permeability was assessed in vivo. One sobetirome prodrug, ethanolamine ester **11**, was found to distribute more sobetirome to the brain compared to an equimolar peripheral dose of unmodified sobetirome. In addition to enhanced brain levels, prodrug **11** displayed lower sobetirome blood levels and a brain/serum ratio that was larger than that of unmodified sobetirome. Thus, these data indicate that an ester prodrug strategy applied to sobetirome can deliver increased concentrations of the active drug to the central nervous system (CNS), which may prove useful in the treatment of CNS disorders.



**Personal contribution:**

HSC (also initialized as HSS) performed and optimized in vivo experiments.

**Introduction:**

Thyroid hormone is a principal regulator of essential processes in vertebrate development and homeostasis. In the central nervous system (CNS) these critical processes include myelination, and neuronal and glial cell differentiation and migration.<sup>1</sup> Thyroid hormone facilitates myelin development by driving the differentiation of oligodendrocyte progenitor cells (OPCs) into oligodendrocytes (OLs) as well as the control of specific genes expressed in mature OLs that stimulate the production of myelin.<sup>2-3</sup> In addition to its developmental function in initiating myelination, thyroid hormone plays a role in stimulating remyelination in response to demyelination.<sup>4-6</sup> Since thyroid hormone has no therapeutic window separating the desired therapeutic effects from thyrotoxic adverse effects, thyromimetics, small-molecules resembling thyroid hormone in structure and function, offer a potentially safer alternative therapy for the treatment of demyelinating neurological disorders such as x-linked adrenoleukodystrophy<sup>7</sup> and multiple sclerosis.<sup>8</sup>

Sobetirome (**1**, [Fig. 1a](#)), also known as GC-1, is a potent, orally active thyromimetic that displays selective tissue action, and is devoid of thyrotoxic adverse effects on the heart, bone, and skeletal muscle.<sup>9</sup> Sobetirome has been a useful chemical tool for studying the effects of thyroid hormone receptor (TR) isoform selectivity in both cellular and animal models. These earlier studies led to clinical trials of sobetirome as a cholesterol lowering agent where it was found to be effective at lowering cholesterol levels in human subjects.<sup>10</sup> Based on the promise of sobetirome as a treatment for demyelinating disorders and its ability to adequately cross the blood-brain-barrier (BBB) in murine models,<sup>11-12</sup> we sought to enhance the BBB penetration and CNS distribution of sobetirome through a prodrug strategy.

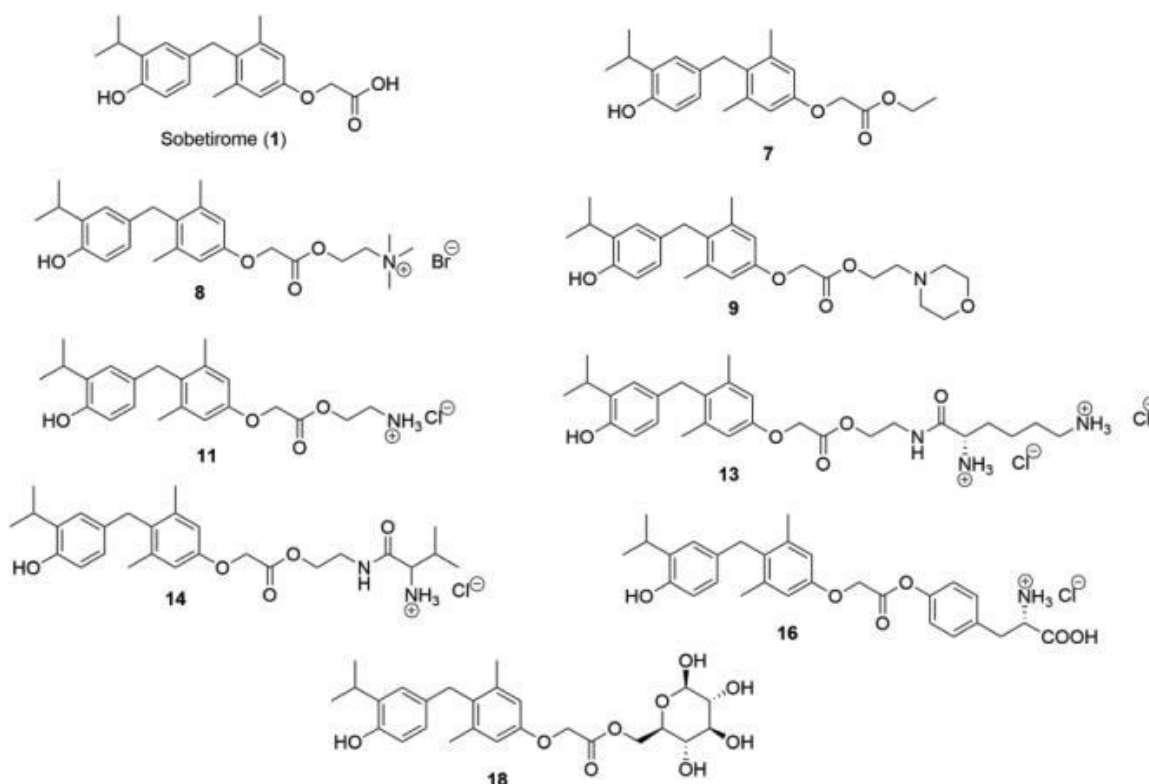


[Figure 1a](#)

*Structures of sobetirome (1) and sobetirome prodrugs synthesized in this study to evaluate a prodrug strategy for increasing brain distribution of sobetirome.*

Thyromimetics such as sobetirome have fairly restricted structure activity relations which limits efforts to create new entities with increased BBB penetration and complete retention of thyromimetic action.<sup>13</sup> Most, if not all thyromimetics, like sobetirome, contain an inner-ring carboxylic acid functional group, which is critical for high affinity binding to thyroid hormone receptors. The carboxylic acid is known to be a liability for CNS drug distribution, suggesting that carboxylate modification of sobetirome could enhance BBB permeability.<sup>14-15</sup> Ester and amide prodrugs of carboxylic acid containing drugs have been shown to increase CNS drug distribution following enzymatic hydrolysis in the CNS.<sup>15-16</sup> Esters are generally preferred to amides in this role, because they have a more ideal hydrolysis rate that provides maximal CNS drug distribution from a systemically administered dose.<sup>17</sup> Although systemically administered

sobetirome does distribute to the CNS,<sup>11-12</sup> we reasoned that esters of sobetirome would increase BBB permeability. To target the CNS, a prodrug strategy was devised in which the carboxylic acid moiety was esterified. Once across the BBB, the prodrug esters encounter endogenous, non-specific esterases that can cleave the prodrug ester liberating the active drug sobetirome in the CNS (Fig. 1b). This ester strategy has been used successfully to improve BBB penetration of other carboxylic acid containing drugs.<sup>18-19</sup> In addition to improving BBB penetration, ester prodrugs effectively mask sobetirome in circulation and peripheral organs potentially reducing the systemic exposure of the drug which may increase the therapeutic index.

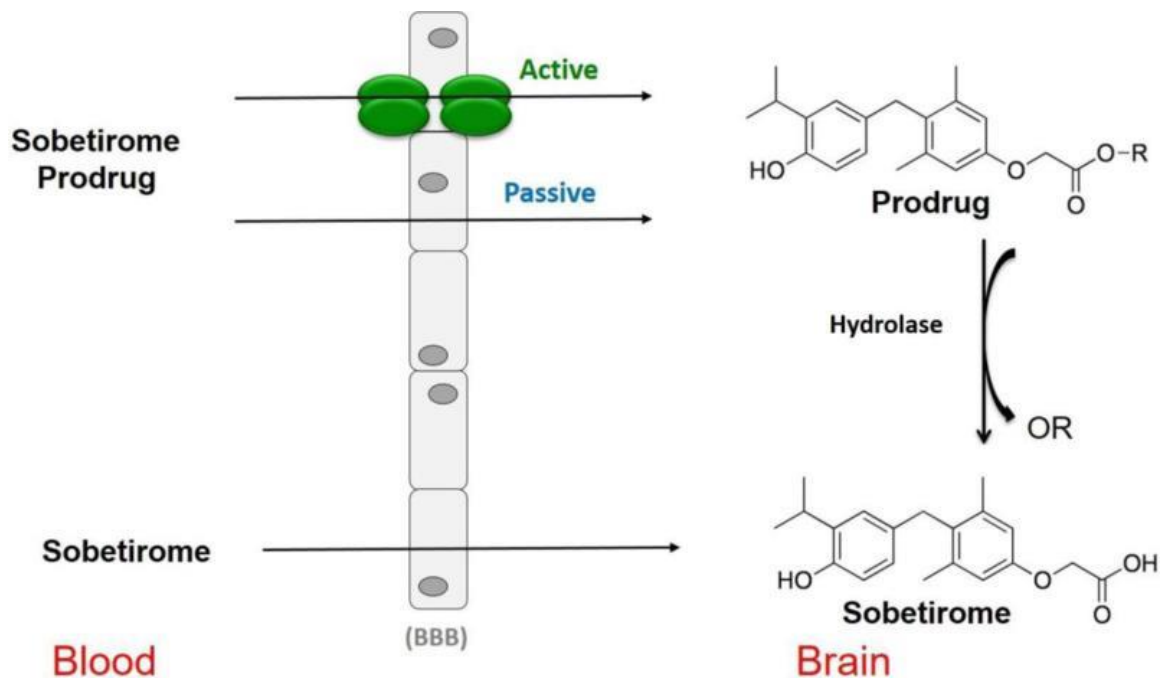


Figure 1b

*Prodrug strategy for enhanced brain uptake of sobetirome.*

In considering the nature of the alcohol portion of the sobetirome ester we elected to examine structures that would utilize both active and passive transport mechanisms (Fig. 1a). Variations of each of these esters have been used previously with carboxylate containing drugs to increase BBB permeability or oral bioavailability.<sup>15-16</sup> The active transport based prodrug esters were designed to take advantage of the presence of L-type amino acid, amino acid, glucose, or choline transporters expressed in the epithelial cells of the BBB.<sup>20</sup> Here again, each of these alcohols have been used to make a prodrug ester of an acidic drug that has increased CNS distribution compared to the parent drug presumably via association with specific small molecule transporters contained in the BBB.

## Materials and methods:

### Animal Studies

Experimental protocols were in compliance with the National Institutes of Health Guide for the Care and Use of Laboratory Animals and approved by the Oregon Health & Science University

Institutional Animal Care & Use Committee. Wild type male C57Bl/6 mice, aged 8–10 weeks, were housed in a climate controlled room with a 12hour light-dark cycle with ad libitum access to food and water. Mice were injected once intraperitoneally (IP) with sobetirome and prodrugs at 1.5  $\mu\text{mol} / \text{kg}$ . Euthanasia was performed on three mice per time point at the following times (0.15 h, 0.5 h, 1 h, 2 h, 4 h, and 8 h) and the tissues and blood were harvested. Tissues were immediately frozen and blood was kept on ice for a minimum of 30 minutes and then spun down at  $7,500 \times G$  for 15 minutes. Serum (100  $\mu\text{L}$ ) was collected and was stored with tissues at  $-80^\circ\text{C}$  until samples were processed.

### **Serum Processing**

The serum samples were warmed to r.t. and 10  $\mu\text{L}$  of 2.99  $\mu\text{M}$  internal standard ( $d_6$ -sobetirome<sup>45</sup>) was added to them. Acetonitrile (500  $\mu\text{L}$ ) was added and the sample was vortexed for 20 seconds. The sample was then centrifuged at  $10,000 \times G$  for 15 minutes at  $4^\circ\text{C}$ . Next, 90% of the upper supernatant was transferred to a glass test tube and concentrated using a speedvac for 1.5 hours at  $45^\circ\text{C}$ . The dried sample was then dissolved in 400  $\mu\text{L}$  of 50:50 ACN:H<sub>2</sub>O and vortexed for 20 seconds. The resulting mixture was transferred to an eppendorf and centrifuged at  $10,000 \times G$  for 15 minutes. The supernatant was filtered with 0.22  $\mu\text{m}$  centrifugal filters and submitted for LC-MS /MS analysis. The standard curve was made with 100  $\mu\text{L}$  of serum from a 8-10 week old mouse not injected with sobetirome or prodrug. The processing was performed exactly the same except after filtering the sample was split amongst 6 vials. To 5 out of the 6 vials was added Sobetirome to make final concentrations in matrix of (0.1  $\text{pg} / \mu\text{L}$ , 1  $\text{pg} / \mu\text{L}$ , 10  $\text{pg} / \mu\text{L}$ , 100  $\text{pg} / \mu\text{L}$ , and 1000  $\text{pg} / \mu\text{L}$ ).

### **Brain Processing**

The brain samples were warmed to r.t. and transferred to a homogenizer tube with 5 GoldSpec 1/8 chrome steel balls (Applied Industrial Technologies). The resulting tube was weighed and then 1 mL of H<sub>2</sub>O was added, followed by 10  $\mu\text{L}$  of 2.99  $\mu\text{M}$  internal standard ( $d_6$ -sobetirome<sup>45</sup>). The tube was homogenized with a Bead Bug for 30 seconds and then transferred to a falcon tube containing 3 mL of ACN. ACN (1 mL) was used to wash homogenizer tube and the solution was transferred back to the falcon tube. The sample was then processed using the same method for the serum processing except the sample was concentrated in a glass tube using a speed vac for 4 hours at  $45^\circ\text{C}$ .

### **Liver Processing**

The liver samples were warmed to r.t. and transferred to a homogenizer tube with 5 GoldSpec 1/8 chrome steel balls (Applied Industrial Technologies). The resulting tube was weighed and then 1 mL of H<sub>2</sub>O was added, followed by 10  $\mu\text{L}$  of 2.99  $\mu\text{M}$  internal standard ( $d_6$ -sobetirome<sup>45</sup>). The tube was then homogenized with a Bead Bug for 30 seconds. A small sample (100  $\mu\text{L}$ ) was then taken from the homogenized mixture and processed. This was done because the liver levels found in some samples were too high for the LC-MS/MS instrument. The samples were then processed using the serum processing method.

### **LC-MS/MS Analysis for Sobetirome and Prodrugs**

Sobetirome and  $d_6$ -sobetirome internal standard were analyzed using a QTRAP 4000 hybrid/triple quadrupole linear ion trap mass spectrometer (Applied biosystems) with electrospray ionization(ESI) in negative mode. The mass spectrometer was interfaced to a Shimadzu

(Columbia, MD) SIL-20AC XR auto-sampler followed by 2 LC-20AD XR LC pumps and analysis on an Applied Biosystems/SCIEX QTRAP 4000 instrument (Foster City, CA). The instrument was operated with the following settings: source voltage -4500 kV, GS1 50, GS2 60, CUR 15, TEM 650, and CAD MEDIUM. The scheduled multiple-reaction-monitoring (MRM) transitions are based on the precursor ion  $m/z$  and their corresponding diagnostic product ions. Compounds were infused individually and instrument parameters optimized for each MRM transition. MRM parameters are shown in the [supporting information](#). The gradient mobile phase was delivered at a flow rate of 0.5 ml/min, and consisted of two solvents, A: 10 mM ammonium formate in water and B: 10 mM ammonium formate in 90% acetonitrile, 10% water. A Hamilton PRP-C18 column: 5  $\mu$ m particle size (50 mm  $\times$  2.1 mm stainless steel) was used and kept at 40°C, and the autosampler was kept at 30°C. Gradient was as follows, initial concentration of B was 10%, held for 0.5 minutes, followed by an increase to 98% B over 4.5 minutes, held for 0.9 minutes, dropping back to 10% B over 0.1 minutes, and held at 10% B for 2 minutes for a total run time of 8 minutes. Data were acquired using SCIEX Analyst 1.6.2 software (Framingham, MA, USA) and analyzed using Multiquant 3.0.2.

### General Chemistry

$^1\text{H}$  NMR were recorded on a Bruker Advance 400 MHz nuclear magnetic resonance spectrometer. All  $^1\text{H}$  NMR spectra were calibrated to the NMR solvent reference peak ( $\text{D}_6$ -DMSO,  $\text{CDCl}_3$ ,  $\text{CD}_3\text{OD}$ ). High resolution mass spectrometry (HRMS) with electrospray ionization was performed by the Bioanalytical MS Facility at Portland State University. Inert atmosphere reactions were performed under argon gas passed through a small column of drierite and were conducted in flame-dried round-bottom flasks. Anhydrous tetrahydrofuran (THF), dichloromethane (DCM), and dimethylformamide (DMF) were obtained from a Seca Solvent System. All other solvents used were purchased from Sigma-Aldrich or Fisher. Purity analysis of final compounds was determined to be >95% by HPLC. HPLC analysis was performed on a Varian ProStar HPLC with an Agilent Eclipse Plus C18 5  $\mu$ m column (4.6  $\times$  250 mm) with a gradient of 10% to 95% acetonitrile (0.1% TFA) over 15 minutes.

### Statistical Analysis

Data are expressed as the mean  $\pm$  the standard deviation. Statistical analyses were done using Microsoft Excel and GraphPad Prism®. Differences between means were determined using multiple t-tests, and considered to be statistically significant  $p < 0.05$ .

### Chemistry Experimental

*tert*-butyl 2-(4-formyl-3,5-dimethylphenoxy)acetate (**3**)

To a solution of 4-hydroxy-2,6-dimethylphenol (**2**) (15.02 g, 100 mmol) and DMF (400 mL) was added  $\text{Cs}_2\text{CO}_3$  (65.2 g, 200 mmol). The resulting mixture was cooled to 0°C and *t*-butylchloroacetate (17.9 mL, 125 mmol) was slowly added. The reaction mixture was then stirred at rt for 3 hours and subsequently slowly poured into 800 mL  $\text{H}_2\text{O}$ . The resulting solution was stirred for 15 minutes at rt and then extracted with diethyl ether (3  $\times$  500 mL). The combined organic fractions were washed with water (3  $\times$  1 L), brine, dried with  $\text{MgSO}_4$  and concentrated. Recrystallization of the residue with hexanes gave **3** (23.6g, 89%).  $^1\text{H}$  NMR (400 MHz,  $\text{CD}_3\text{OD}$ ):  $\delta$  10.43 (s, 1 H), 6.65 (s, 2 H), 4.65 (s, 2 H), 2.58 (s, 6 H), 1.49 (s, 9 H). HRMS exact mass calcd for  $\text{C}_{15}\text{H}_{21}\text{O}_4$   $[\text{M}+\text{H}]^+$ : 265.14344. Found 265.14445

#### 1-(benzyloxy)-4-iodo-2-isopropylbenzene (5)

To a stirring solution of 2-isopropylphenol (**4**) (13.62 g, 100 mmol), sodium iodide (14.98 g, 100 mmol) and methanol (300 mL), was added 10 mL of a 10 M NaOH solution. The reaction mixture was then cooled to 4 °C and a solution of NaOCl (6% aq, 129 mL, 115 mmol) was slowly added dropwise over 18 hours. The reaction mixture was then allowed to stir at room temperature for 2 hours. A 10% Na<sub>2</sub>S<sub>2</sub>O<sub>3</sub> solution (300 mL) was added followed by acidification of the solution to neutral pH with conc. HCl. The solution was then extracted with diethyl ether (3 × 300 mL). The combined organic fractions were washed with brine, dried with MgSO<sub>4</sub> and concentrated. Purification of the residue with flash chromatography (silica, 0% to 75% dichloromethane / hexanes) gave 4-iodo-isopropylphenol (19.6g, 75%). <sup>1</sup>H NMR (400 MHz, CDCl<sub>3</sub>) δ (ppm): 7.45 (1H, d, J = 2.0 Hz), 7.35 (1H, dd, J = 8.4 Hz, 2Hz), 6.52 (1H, d, J = 8.4 Hz), 3.14 (1H, septet, J = 7.2 Hz), 1.23 (6H, d, J = 7.2 Hz). To a solution of 4-iodo-isopropylphenol (16.18 g, 61.73 mmol) in DMF (200 mL) was added K<sub>2</sub>CO<sub>3</sub> (25.6 g, 185.2 mmol) and benzyl bromide (92.6 mmol, 11 mL). The reaction mixture was then stirred at 75 °C for 16 hours. After cooling the solution to room temperature, the mixture was then slowly poured into 600 mL of H<sub>2</sub>O and subsequently stirred at r.t. for 15 min. The mixture was then extracted with hexanes (3 × 500 mL). The combined organic fractions were washed with water (3 × 500 mL), brine, dried with Mg<sub>2</sub>SO<sub>4</sub> and concentrated under reduced pressure. Purification of the residue with flash chromatography (silica, 0% to 2% ethyl acetate/hexanes) yielded **5** (16.7g, 77%). <sup>1</sup>H NMR (400 MHz, CDCl<sub>3</sub>): δ 7.50 (s, 2 H), 7.41 (m, 5 H), 6.67 (d, 2 H, J = 8.5 Hz), 5.05 (s, 2 H), 3.35 (sept, 1 H, J = 7.0 Hz), 1.22 (d, 6 H, J = 7.0 Hz).

#### 2-(4-(4-(benzyloxy)-3-isopropylbenzyl)-3,5-dimethylphenoxy)acetic acid (6)

A solution of **5** (16.2 g, 46 mmol), THF (180 mL), and 4 Å molecular sieves (3 g) was placed under reduced pressure for 1 minute and then placed under argon for 1 minute. This process was repeated three times to ensure a deoxygenated solution. The solution was then cooled to 0 °C and an <sup>i</sup>PrMgCl solution (2 M in THF, 34.5 mL, 69 mmol) was added. The reaction mixture was then stirred at r.t. for 2.5 hours where it was then cooled to -78 °C. A solution of **3** (9.36 g, 35.4 mmol) and THF (20 mL) was then added and the reaction mixture was stirred at -78 °C for 1 h and at room temperature for 1 hr. The reaction was quenched with a 10% NH<sub>4</sub>Cl(aq) solution (200 mL) and extracted with ethyl acetate (3 × 200 mL). The combined organic fractions were washed with brine, dried with Mg<sub>2</sub>SO<sub>4</sub>, and concentrated under reduced pressure. A <sup>1</sup>H NMR was taken to confirm consumption of **5** and the resulting crude residue was then utilized in the subsequent reaction. The crude residue was dissolved in DCM (200 mL) and cooled to 0 °C. Triethylsilane (28.3 mL, 177 mmol) was added followed by the slow addition of trifluoroacetic acid (40.7 mL, 531 mmol). The reaction mixture was then stirred at room temperature for 3 hours and then concentrated with reduced pressure. DCM (100 mL) was added and the solution was concentrated again with reduced pressure. This process was repeated two more times to remove the remaining TFA. Hexanes was added and the resulting mixture was cooled to 0 °C to precipitate the desired product (**6**) as a white solid (8.15g, 55% (over two steps)). <sup>1</sup>H NMR (400 MHz, CD<sub>3</sub>OD): δ 7.41-7.24 (m, 5 H), 6.91 (d, 1 H, J = 2 Hz), 6.76 (d, 1 H, J = 8.4 Hz), 6.63 (m, 3 H), 4.97 (s, 2 H), 4.58 (s, 2 H), 3.89 (s, 2 H), 3.30 (sept, 1 H, J = 7.1 Hz), 2.17 (s, 6 H), 1.14 (d, 6 H, J = 7.1 Hz). HRMS exact mass calcd for C<sub>27</sub>H<sub>30</sub>O<sub>4</sub>Na[M+Na<sup>+</sup>]<sup>+</sup>: m/z 441.20363. Found m/z 441.20463.

#### Ethyl 2-(4-(4-hydroxy-3-(propan-2-yl)phenyl)methyl)-3,5-dimethylphenoxy) acetate (7)

To a stirred solution of **6** (209 mg, 0.5 mmol) in 2 mL ethanol was added 1 M HCl (ethanol) (15mL, 15mmol). The reaction mixture was stirred at room temperature for 24 h. The solution was then dried with MgSO<sub>4</sub> and concentrated under reduced pressure. The resulting residue was then dissolved in 5 mL of methanol and purged with argon. 10% Pd/C (50mg) was added followed by the dropwise addition of triethylsilane (1.01 mL, 6.33 mmol). The reaction mixture was stirred at room temperature for 3 h and then filtered over a pad of celite with methanol. The solution was then concentrated under reduced pressure and purified with flash chromatography (silica, 0% to 2% ethyl acetate/hexanes) to yield **7** as an oil (113 mg, 62%). <sup>1</sup>H NMR (400 MHz, CDCl<sub>3</sub>): δ 6.91 (d, 1 H, J = 2.0 Hz), 6.62 (s, 2 H), 6.60-6.54 (m, 2 H), 4.60 (s, 2 H), 4.59 (s, 1H), 4.29 (q, 2 H, J = 7.2 Hz), 3.89 (s, 2 H), 3.15 (sept, 1H, J = 7.1 Hz), 2.20 (s, 6 H), 1.30 (t, 3 H, J = 7.2 Hz), 1.21 (d, 6 H, J = 7.1 Hz). HRMS exact mass calcd for C<sub>22</sub>H<sub>28</sub>O<sub>4</sub>Na [M+Na<sup>+</sup>]<sup>+</sup>: m/z 379.18798. Found m/z 379.18823.

2-(trimethylamino)ethyl 2-(4-(4-hydroxy-3-(propan-2-yl)phenyl)methyl-3,5-dimethylphenoxy)acetate hydrobromide (**8**)

To a solution of **6** (209 mg, 0.5 mmol) dissolved in DMF (5 mL) was added K<sub>2</sub>CO<sub>3</sub> (138 mg, 1.0 mmol) followed by (2-bromoethyl) trimethylammonium bromide (309mg, 1.25 mmol). The reaction mixture was then stirred at r.t. for 72 hours and then filtered. The mixture was then directly purified with flash chromatography (silica, 0%, 5%, 10%, 20%, 30% methanol / DCM) to yield the desired product (121 mg). The residue was then dissolved in MeOH (4 mL) and purged with argon. 10% Pd/C (60mg) was added followed by the dropwise addition of triethylsilane (479 μL, 3 mmol). The reaction mixture was stirred at room temperature for 4 h and then filtered over a pad of celite with methanol. The solution was then concentrated under reduced pressure and the resulting solid was isolated with ether to yield **8** (97mg, 39% (two steps)). <sup>1</sup>H NMR (400 MHz, CD<sub>3</sub>OD): δ 6.82 (d, 1 H, J = 2Hz), 6.67 (s, 2H), 6.60 (d, 1 H, J = 8.2 Hz), 6.54 (dd, 1 H, J = 8.2 Hz, 2 Hz), 4.77 (s, 2H), 4.46 (m, 2 H), 3.90 (s, 2 H), 3.31 (m, 2 H), 3.21 (sept, 1 H, J = 7.0 Hz), 2.22 (s, 6H), 1.14 (d, 6 H, J = 7.0 Hz). LRMS (ESI<sup>+</sup>). Found 414.3 (M-Br)<sup>+</sup>

Representative procedure for preparation of acid chloride (**6a**)

A solution of oxalyl chloride (200 μL, 2.33 mmol) in 2 mL of DCM was slowly added to a 0 °C solution of **6** (209 mg, 0.5 mmol) and DCM (4 mL). DMF (2 μL) was then added and the reaction mixture was stirred at room temperature for 3 hours. The solution was then concentrated under reduced pressure. DCM (4 mL) was added to the residue and the solution was concentrated again, this process was repeated once more. The crude residue was of sufficient purity and was used immediately in the subsequent ester couplings.

2-(morpholin-4-yl)ethyl 2-(4-(4-hydroxy-3-(propan-2-yl)phenyl)methyl-3,5-dimethylphenoxy)acetate (**9**)

To a 0 °C solution of 4-(2-hydroxyethyl)morpholine (182 μL, 1.5 mmol), DMAP (122mg, 1.0 mmol), and DCM(5 mL) was added a solution of **6a** (0.5 mmol) and DCM (2 mL). The reaction mixture was allowed to warm to r.t. overnight. The reaction mixture was then concentrated, redissolved in a minimal amount of DCM, and purified using flash chromatography (silica, 0% to 4% MeOH / DCM). The resulting ester was then dissolved in 5 mL MeOH and purged with argon. 10% Pd/C (50 mg) was added followed by the dropwise addition of triethylsilane (799 μL, 5 mmol). The reaction mixture was stirred at room temperature for 4 h and then filtered over a pad of celite with methanol. The solution was then concentrated under reduced pressure and

purified using flash chromatography (silica, 0% to 5% MeOH / DCM) to yield **9** as an oil (107 mg, 48% over two steps). <sup>1</sup>H NMR (400 MHz, CDCl<sub>3</sub>): δ 6.92 (d, 1 H, J = 2.0 Hz), 6.55(m, 4 H), 4.55 (s, 2 H), 4.36 (t, 2 H, J = 5.7 Hz), 3.87 (s, 2 H), 3.70 (t, 4 H, J = 4.6 Hz), 3.19 (sept, 1 H, J = 7.0 Hz), 2.67 (t, 2 H, J = 5.7 Hz), 2.51 (t, 4 H, J = 4.6 Hz), 2.18 (s, 6 H), 1.20 (d, 6 H, J = 7.0 Hz). HRMS exact mass calcd for C<sub>26</sub>H<sub>36</sub>N<sub>1</sub>O<sub>5</sub> [M+H]<sup>+</sup> : m/z 442.25880. Found m/z 442.25979.

2-(2-(4-(4-hydroxy-3-isopropylbenzyl)-3,5-dimethylphenoxy)acetoxy)ethan-1-aminium chloride (11)

To a 0 °C solution of N-Boc-ethanolamine (161 mg, 1.0 mmol), DMAP (183mg, 1.5 mmol), and DCM (5 mL) was added a solution of **6a** (0.5 mmol) and DCM (2 mL). The reaction mixture was allowed to warm to r.t. overnight. The reaction mixture was then concentrated, redissolved in a minimal amount of DCM, and purified using flash chromatography (silica, 10% to 20% ethyl acetate / hexanes) to yield **10** (72%, 0.36 mmol). The resulting ester (**10**) (200 mg, 0.36 mmol) was dissolved in 4 mL MeOH and purged with argon. 10% Pd/C (40mg) was added followed by the dropwise addition of triethylsilane (569 μL, 3.56 mmol). The reaction mixture was stirred at room temperature for 4 h and then filtered over a pad of celite with methanol. The solution was then concentrated under reduced pressure and purified using flash chromatography (silica, 10% to 30% ethyl acetate / hexanes) to the debenzylated product as an oil (112 mg). The resulting oil (112 mg, 0.237 mmol) was dissolved in ethyl acetate (2 mL) and 3 mL of 1 M HCl (ethyl acetate) was added. The reaction mixture was then stirred at room temperature overnight, concentrated under reduced pressure, and resulting solid **11** was collected with diethyl ether (75 mg, 51% (over two steps)). <sup>1</sup>H NMR (400 MHz, CD<sub>3</sub>OD): δ 6.82 (d, 1 H, J = 2.0 Hz), 6.67 (s, 2H), 6.60 (d, 1 H, J = 8.2 Hz), 6.54 (dd, 1 H, J = 8.2 Hz, 2 Hz), 4.77 (s, 2H), 4.46 (m, 2 H), 3.90 (s, 2 H), 3.31 (m, 2 H), 3.21 (sept, 1 H, J = 7.0 Hz), 2.22 (s, 6H), 1.14 (d, 6 H, J = 7.0 Hz). HRMS exact mass calcd for C<sub>22</sub>H<sub>30</sub>N<sub>1</sub>O<sub>4</sub> [M-Cl]<sup>+</sup> : m/z 372.21693. Found m/z 372.21807.

2-(2-(4-(4-(benzyloxy)-3-isopropylbenzyl)-3,5-dimethylphenoxy)acetoxy)ethan-1-aminium chloride (12)

To a solution of **10** (200 mg, 0.356 mmol) in ethyl acetate (2 mL) was added 10 mL of 1 M HCl (ethyl acetate). The reaction mixture was then stirred at room temperature overnight, concentrated under reduced pressure, and resulting white solid (**12**) was collected with diethyl ether (143 mg, 81%). <sup>1</sup>H NMR (400 MHz, CD<sub>3</sub>OD): δ 7.45 – 7.29 (m, 5H), 6.92 (d, 1 H, J = 2.0 Hz), 6.83 (d, 1 H, J = 8.4 Hz), 6.71 – 6.65 (m, 3 H), 5.03 (s, 2 H), 4.78 (s, 2H), 4.47(t, 2 H, J = 5.0 Hz), 3.94 (s, 2H), 3.33 (m, 3H), 2.21 (s, 6H), 1.16 (d, 6 H, J = 7.1 Hz). HRMS exact mass calcd for C<sub>22</sub>H<sub>30</sub>N<sub>1</sub>O<sub>4</sub> [M-Cl]<sup>+</sup> : m/z 462.26389. Found m/z 462.26450.

2-(2,6-diaminohexanamido)ethyl 2-(4-(4-(benzyloxy)-3-(propan-2-yl)phenyl)methyl-3,5-dimethylphenoxy)acetate (13)

To a solution of Boc-Lys(Boc)-OH (106 mg, 0.2 mmol) and DMF (2 mL) was added EDCI-HCl (38 mg, 0.2 mmol) and HOBt-H<sub>2</sub>O (31 mg, 0.2 mmol). The reaction mixture was stirred at room temperature for 30 min. DIEA (87 μL, 0.5 mmol) was added to the reaction mixture followed by **11** (50 mg, 0.1 mmol) and the reaction mixture was stirred at r.t. overnight. The mixture was then poured into H<sub>2</sub>O (20 mL) and extracted with ethyl acetate (3 × 20 mL). The combined organic layers were then washed with sat. NaHCO<sub>3</sub>, 1M HCl, and brine. After drying the organic layer with MgSO<sub>4</sub>, the organic layer was concentrated using reduced pressure and purified via flash chromatography (silica, 0% to 2.5% DCM / MeOH). The residue was dissolved in 4 mL MeOH

and purged with argon. 10% Pd/C (100mg) was added followed by the dropwise addition of triethylsilane (320  $\mu$ L, 2 mmol). The reaction mixture was stirred at room temperature for 4 h and then filtered over a pad of celite with methanol. The methanol solution was then concentrated and hexanes was added to the round-bottom flask. A white solid appeared on the walls of the round-bottom flask, and the resulting hexanes layer was decanted. This process was repeated two more times. The resulting solid was dissolved in 1 mL of ethyl acetate and to this solution was added 4 mL of 1M HCl (ethyl acetate). The reaction mixture was stirred at r.t. overnight and then concentrated using reduced pressure. Diethyl ether was added and the resulting solid was collected to give **13** (23 mg, 40%).  $^1\text{H NMR}$  (400 MHz,  $\text{CD}_3\text{OD}$ ):  $\delta$  6.81 (d, 1 H,  $J = 2$  Hz), 6.67 (s, 2 H), 6.60 (d, 1 H,  $J = 8.2$  Hz), 6.52 (dd, 1H,  $J = 8.2$  Hz, 2.0 Hz), 4.73 (s, 2 H), 4.41 (m, 1H), 4.30 (m, 1 H), 3.89 (m, 3H), 3.62 (m, 3H), 3.20 (sept, 1 H,  $J = 6.70$  Hz), 2.96 (t, 2 H,  $J = 7.2$  Hz), 2.21 (s, 6 H), 1.90 (m, 2H), 1.73 (m, 2H), 1.51 (m, 2H), 1.13 (d, 6 H,  $J = 6.70$  Hz). HRMS exact mass calcd for  $\text{C}_{28}\text{H}_{42}\text{N}_3\text{O}_5$  [ $\text{M} - 2\text{Cl}^- - \text{H}^+$ ] $^+$ :  $m/z$  500.31190. Found  $m/z$  500.31243.

2-(2-amino-4-methylpentanamido)ethyl 2-(2-(4-(benzyloxy)-3-(propan-2-yl)phenyl)methyl-3,5-dimethylphenoxy)acetate (**14**)

To a solution of (Boc)-Valine-OH (60 mg, 0.274 mmol) and DMF (5 mL) was added EDCI-HCl (53 mg, 0.274 mmol) and HOBt-H<sub>2</sub>O (42 mg, 0.274 mmol). The reaction mixture was stirred at room temperature for 30 min. DIEA (119  $\mu$ L, 0.685 mmol) was added to the reaction mixture followed by **11** (68 mg, 0.137 mmol) and the reaction mixture was stirred at r.t. overnight. The mixture was then poured into H<sub>2</sub>O (30 mL) and extracted with ethyl acetate (3  $\times$  30 mL). The combined organic layers were then washed with sat. NaHCO<sub>3</sub>, 1M HCl, and brine. After drying the organic layer with MgSO<sub>4</sub>, the ethyl acetate was concentrated using reduced pressure and purified via flash chromatography (silica, 50% ethyl acetate/hexanes). The residue was dissolved in 3 mL MeOH and purged with argon. 10% Pd/C (30mg) was added followed by the dropwise addition of triethylsilane (320  $\mu$ L, 2 mmol). The reaction mixture was stirred at room temperature for 4 h and then filtered over a pad of celite with methanol. The methanol solution was then concentrated and purified with flash chromatography (silica, 30% to 50% ethyl acetate/hexanes). The resulting residue was dissolved in 1 mL of ethyl acetate and to this solution was added 4 mL of 1M HCl (ethyl acetate). The reaction mixture was stirred at r.t. overnight and then concentrated using reduced pressure. Diethyl ether was added and the resulting solid was collected to give **14** (24mg, 32% overall yield).  $^1\text{H NMR}$  (400 MHz,  $\text{CD}_3\text{OD}$ ):  $\delta$  8.58 (m, 1 H), 7.92 (s, 1H), 6.82 (d, 1 H,  $J = 2.0$  Hz), 6.66 (s, 2 H), 6.60 (d, 1 H,  $J = 8.2$  Hz), 6.54 (dd, 1H,  $J = 8.2$  Hz, 2.0 Hz), 4.70 (s, 2 H), 4.33 (m, 2 H), 3.90 (s, 2H), 3.66 (m, 2H), 3.50 (m, 2H), 3.20(sept, 1 H,  $J = 6.70$  Hz), 2.21 (s, 6 H), 1.14 (d, 6 H,  $J = 6.70$  Hz), 1.07 ( m, 6 H). HRMS exact mass calcd for  $\text{C}_{27}\text{H}_{39}\text{N}_2\text{O}_5$  [ $\text{M} + \text{H}^+$ ] $^+$  :  $m/z$  471.28535. Found  $m/z$  471.28686.

azetidin-3-yl 2-(4-(4-hydroxy-3-(propan-2-yl)phenyl)methyl-3,5-dimethylphenoxy)acetate (**15**)

To a 0  $^\circ\text{C}$  solution of 1-(tert-butylcarbonyl)-3-hydroxyazetidine (**15a**, 260 mg, 1.5 mmol), DMAP (183mg, 1.5 mmol), and DCM(5 mL) was added a solution of the acid chloride generated from **6** (0.5 mmol) and DCM (2 mL). The reaction mixture was allowed to warm to r.t. overnight. The reaction mixture was then concentrated, redissolved in a minimal amount of DCM, and purified using flash chromatography (silica, 10% to 30% ethyl acetate/hexanes). The resulting ester (242 mg, 0.422 mmol) was dissolved in 5 mL MeOH and purged with argon. 10% Pd/C (90mg) was added followed by the dropwise addition of triethylsilane (1.01 mL, 6.33 mmol). The reaction mixture was stirred at room temperature for 4 h and then filtered over a pad of celite with methanol. The solution was then concentrated under reduced pressure and purified using flash

chromatography (silica, 10% to 30% ethyl acetate / hexanes) to yield the desired product as an oil (106 mg, 51% over two steps). The resulting residue was dissolved in ethyl acetate (3 mL) and 5 mL of 1 M HCl (ethyl acetate) was added. The reaction mixture was then stirred at room temperature overnight, concentrated under reduced pressure, and resulting solid was collected with hexanes. The solid was then purified using flash chromatography (silica, 0% to 10% methanol / (DCM + 1% isopropylamine)) to yield **15** (101 mg, 45% overall yield). <sup>1</sup>H NMR (400 MHz, CD<sub>3</sub>OD): δ 6.80 (d, 1 H, J = 2.0 Hz), 6.65 (s, 2 H), 6.60 (d, 1 H, J = 8.2 Hz), 6.52 (dd, 1H, J = 8.2 Hz, 2 Hz), 5.44 (m, 1H), 4.78 (s, 2 H), 4.45 (m, 2 H), 4.18 (m, 2H), 3.88 (s, 2H), 3.20(sept, 1 H, J = 6.95 Hz), 2.20 (s, 6 H), 1.13 (d, 6 H, J = 6.95 Hz). HRMS exact mass calcd for C<sub>23</sub>H<sub>30</sub>N<sub>1</sub>O<sub>4</sub> [M+H]<sup>+</sup>: m/z 384.21693. Found m/z 384.21735.

2-amino-3-(4-(2-(4-(4-hydroxy-3-(propan-2-yl)phenyl)methyl-3,5-dimethylphenoxy)acetyl)oxy-phenyl)propanoic acid (**16**)

To a solution of N-t-Boc-L-tyrosine (281 mg, 1 mmol) and acetone (4 mL) was added 1 N NaOH (aq) (2 mL, 2 mmol). This reaction mixture was then cooled to 0 °C and a solution of the acid chloride generated from (**6**) (0.5 mmol) and acetone (2 mL) was added dropwise. The reaction mixture was allowed to warm to r.t. overnight. To the reaction mixture was added 30 mL of 1 M HCl and the mixture was extracted with ethyl acetate (3 × 30 mL). The combined organic layers were then washed with brine, dried, and concentrated under reduced pressure. The crude residue was then purified with flash chromatography (silica, 0% to 5% methanol/DCM + 1% acetic acid). The residue was dissolved in 4 mL MeOH and purged with argon. 10% Pd/C (40mg) was added followed by the dropwise addition of triethylsilane (479 μL, 3 mmol). The reaction mixture was stirred at room temperature for 4 h and then filtered over a pad of celite with methanol. The methanol solution was then concentrated and purified with flash chromatography (silica, 0% to 5% methanol /DCM + 1% acetic acid). The resulting residue was dissolved in 2 mL of ethyl acetate and to this solution was added 3 mL of 1M HCl (ethyl acetate). The reaction mixture was stirred at r.t. overnight and then concentrated using reduced pressure. Diethyl ether was added and the resulting solid was collected to give **16** (33 mg, 12.5% (overall for three steps)). <sup>1</sup>H NMR (400 MHz, DMSO-D<sub>6</sub>): δ 7.32 (d, 2 H, J = 8.5 Hz), 7.14 (d, 2 H, J = 8.5 Hz), 6.83 (d, 1 H, j = 2.0 Hz), 6.71 (s, 2 H), 6.61 (d, 1 H, J = 8.2 Hz), 6.46 (dd, 1 H, J = 8.2, 2 Hz), 5.01 (s, 2 H), 4.17 (t, 1 H, J = 6.5 Hz), 3.8 (s, 2 H), 3.11 (m, 3 H), 2.18 (s, 6 H), 1.08 (d, 6 H, J = 6.8 Hz). HRMS exact mass calcd for C<sub>29</sub>H<sub>34</sub>N<sub>1</sub>O<sub>6</sub> [M-Cl]<sup>+</sup>: m/z 492.23806. Found m/z 492.23738.

((2R,3S,4S,5R,6R)-3,4,5,6-tetrahydroxoxan-2-yl)methyl 2-(4-(4-hydroxy-3-(propan-2-yl)phenyl)methyl-3,5-dimethylphenoxy)acetate (**18**)

To a 0 °C solution of **17** (306 mg, 0.566 mmol), DMAP (175 mg, 1.43 mmol), and DCM (4 mL) was added a solution of the acid chloride generated from **6** (0.714 mmol) and DCM (3 mL). The reaction mixture was allowed to warm to r.t. overnight. The reaction mixture was then concentrated under reduced pressure and purified with flash chromatography (silica, 10% to 30% ethyl acetate/ hexanes) to yield 377 mg of purified product. This product (279 mg, 0.296 mmol) was then dissolved in acetic acid (10 mL) and THF (5 mL) and purged with argon. 10% Pd/C (300 mg) was added followed by the dropwise addition of triethylsilane (2.84 mL, 17.8 mmol). The reaction mixture was stirred at room temperature for 40 h and then filtered over a pad of celite with methanol. The methanol solution was then concentrated under reduced pressure. To this solution (acetic acid remained) was added hexanes and concentrated again under reduced pressure, this was repeated five more times. Lastly, the white solid was collected with hexanes to yield **18** (123 mg, 85% (44% overall yield)). <sup>1</sup>H NMR (400 MHz, CD<sub>3</sub>OD) δ: 6.82 (d, 1 H, J = 2.0

Hz), 6.64 (s, 2 H), 6.58 (d, 1 H, J = 8.2 Hz), 6.52 (dd, 1 H, J = 8.2, 2 Hz), 5.10 (d, 1 H, J = 3.8 Hz), 4.68 (m, 2H), 4.50 (m, 2H), 4.33 (m, 1H), 4.00 (m, 1H), 3.88 (s, 2H), 3.65 (m, 1H), 3.20 (m, 2H), 2.19 (s, 6 H), 1.29 (d, 2H, J = 6.6 Hz), 1.08 (d, 6 H, J = 6.9 Hz). HRMS exact mass calcd for C<sub>26</sub>H<sub>35</sub>N<sub>1</sub>O<sub>9</sub> [M+H]<sup>+</sup>: m/z 491.22756. Found m/z 491.22775.

2-(dimethylamino)ethyl 2-(4-(4-hydroxy-3-isopropylbenzyl)-3,5-dimethylphenoxy)acetate (19)

To a 0 °C solution of *N,N*-dimethylethanolamine (**19a**, 150 μL, 1.5 mmol), DMAP (92 mg, 0.5 mmol), NEt<sub>3</sub>(208 μL, 1.5 mmol) and DCM (4 mL) was added a solution of the acid chloride generated from **6** (0.5 mmol) and DCM (5 mL). The reaction mixture was allowed to warm to r.t. overnight. The reaction mixture was then concentrated under reduced pressure and purified with flash chromatography (silica, 0% to 5% MeOH/DCM) to yield 40 mg of purified product. This product (279mg, 0.296 mmol) was then dissolved in acetic acid (750 μL) and THF (375 mL) and purged with argon. 10% Pd/C (40mg) was added followed by the dropwise addition of triethylsilane (253 mL, 1.59 mmol). The reaction mixture was stirred at room temperature for 4 h and then filtered over a pad of celite. The solution was then concentrated under reduced pressure. To this solution (acetic acid remained) was added hexanes and concentrated again under reduced pressure, this was repeated five more times. Lastly, the white solid was collected with hexanes to yield **19** (21 mg, (11% overall yield)). <sup>1</sup>H NMR (400 MHz, CDCl<sub>3</sub>) δ: 6.94 (d, 1 H, J = 2.0 Hz), 6.61 (s, 2 H), 6.58 (m, 2 H), 4.62 (s, 2 H), 4.35 (t, 2H, J = 5.6 Hz), 3.90 (s, 2H), 3.20 (sept, 1H, J = 6.8 Hz), 2.66 (t, 2 H, J = 5.6 Hz), 2.32 (s, 6 H), 2.21 (s, 6 H), 1.23 (d, 2H, J = 6.8 Hz). HRMS exact mass calcd for C<sub>24</sub>H<sub>31</sub>N<sub>1</sub>O<sub>4</sub> [M+H]<sup>+</sup>: m/z 400.24824. Found m/z 400.24905.

1-methylazetididin-3-yl 2-(4-(4-hydroxy-3-isopropylbenzyl)-3,5-dimethylphenoxy)acetate (20)

To a 0 °C solution of 1-(tert-butylcarbonyl)-3-hydroxyazetididine (**20a**, 260 mg, 1.5 mmol), DMAP (183mg, 1.5 mmol), and DCM(5 mL) was added a solution of the acid chloride generated from **6** (0.5 mmol) and DCM (2 mL). The reaction mixture was allowed to warm to r.t. overnight. The reaction mixture was then concentrated, redissolved in a minimal amount of DCM, and purified using flash chromatography (silica, 10% to 30% ethyl acetate/hexanes). The resulting ester was dissolved in DCM (5 mL) and Et<sub>3</sub>SiH (80 μL) was added. The solution was then cooled to 0°C and treated with TFA (574 μL, 7.5 mmol) and stirred at room temperature for 2 hours. The solution was then concentrated under reduced pressure and the product was precipitated from the solution with diethyl ether to yield the product as a white solid (177mg, 60%). The isolated benzyl-protected intermediate (40 mg, 0.0681 mmol) was dissolved in AcOH (1 mL) and paraformaldehyde (41 mg, 1.36 mmol) was added followed by 10% Pd/C (40 mg). To this solution was added Et<sub>3</sub>SiH (325 μL, 2.04 mmol) dropwise and the reaction mixture was stirred at room temperature for 4 hours and filtered over a pad of celite. Ethyl acetate was added to the solution and the resulting organic layer was washed 2x with sat. NaHCO<sub>3</sub>, and 1x with water, followed by Brine. The organic layer was then dried with MgSO<sub>4</sub> and concentrated under reduced pressure. The product was isolated as a white solid with hexanes (12 mg, 44%). <sup>1</sup>H NMR (400 MHz, CDCl<sub>3</sub>): δ 6.94 (d, 1 H, J = 2.0 Hz), 6.62 (s, 2 H), 6.56 (m, 2H) 5.18 (m, 1H), 4.63 (s, 2 H), 3.90 (s, 2 H), 3.76 (m, 2 H), 3.20(m, 3 H), 2.41 (s, 3 H), 2.22 (s, 6 H), 1.23 (d, 6 H, J = 7.1 Hz). HRMS exact mass calcd for C<sub>24</sub>H<sub>32</sub>N<sub>1</sub>O<sub>4</sub> [M+H]<sup>+</sup>: m/z 398.23258. Found m/z 398.23307.

(R)-pyrrolidin-2-ylmethyl 2-(4-(4-hydroxy-3-isopropylbenzyl)-3,5-dimethylphenoxy)acetate (21)

To a 0 °C solution of *N*-Boc-*L*-prolinol (**21a**, 252 mg, 1.25 mmol), DMAP (183mg, 1.5 mmol), and DCM (3 mL) was added a solution of **6a** (0.25 mmol) and DCM (2 mL). The reaction

mixture was allowed to warm to r.t. overnight. The reaction mixture was then concentrated, redissolved in a minimal amount of DCM, and purified using flash chromatography (silica, 10% to 20% ethyl acetate / hexanes) to yield the coupled N-Boc ester. The resulting ester was dissolved in 4 mL MeOH and purged with argon. 10% Pd/C (50mg) was added followed by the dropwise addition of triethylsilane (599  $\mu$ L, 3.75 mmol). The reaction mixture was stirred at room temperature for 4 h and then filtered over a pad of celite with methanol. The solution was then concentrated under reduced pressure and purified using flash chromatography (silica, 10% to 30% ethyl acetate / hexanes) to yield the debenzylated product as an oil. The resulting oil was dissolved in ethyl acetate (2 mL) and Et<sub>3</sub>SiH (0.25 mmol, 40  $\mu$ L) was added followed by 1 M HCl (ethyl acetate, 4 mL). The reaction mixture was then stirred at room temperature overnight, concentrated under reduced pressure, and resulting solid **11** was collected with diethyl ether (52 mg, 47% (over three steps)). <sup>1</sup>H NMR (400 MHz, CDCl<sub>3</sub>):  $\delta$  6.94 (d, 1 H, J = 2.0 Hz), 6.62 (s, 2 H), 6.61 (d, 1 H, J = 8.1 Hz), 6.55 (dd, 1 H, J = 8.1 Hz, 2.0 Hz), 4.66 (m, 2 H), 4.27 (m, 1H), 3.91 (s, 2 H), 3.76-3.50 (m, 4 H), 3.19 (sept, 1 H, J = 6.8 Hz), 2.23 (s, 6 H), 2.11-1.86 (m, 3 H), 1.65 (m, 1 H), 1.23 (d, 6 H, J = 6.8Hz). HRMS exact mass calcd for C<sub>25</sub>H<sub>34</sub>N<sub>1</sub>O<sub>4</sub> [M+H]<sup>+</sup>: m/z 412.24824. Found 412.24878 m/z.

3-methylazetididin-3-yl 2-(4-(4-hydroxy-3-isopropylbenzyl)-3,5-dimethylphenoxy)acetate (22)

Followed procedure for the synthesis of (**21**) except with 1-Boc-3-Hydroxy-3-methylazetididine (**22a**), THF, and heating during the coupling step (45°C) yielded a white solid (22 mg, 22% overall yield). <sup>1</sup>H NMR (400 MHz, CDCl<sub>3</sub>):  $\delta$  6.94 (d, 1 H, J = 2.0 Hz), 6.62 (m, 3 H), 6.51 (dd, 1 H, J = 8.1 Hz, 2.0 Hz), 4.64 (m, 2 H), 4.35 (br, 2H), 4.10 (br, 2H), 3.90 (s, 2 H), 3.18 (sept, 1 H, J = 7.1 Hz), 2.22 (s, 6 H), 1.81 (s, 3 H), 1.22 (d, 6 H, J = 6.8 Hz). HRMS exact mass calcd for C<sub>24</sub>H<sub>32</sub>N<sub>1</sub>O<sub>4</sub> [M+H]<sup>+</sup>: m/z 398. 23258. Found m/z 398. 23363.

piperidin-4-yl 2-(4-(4-hydroxy-3-isopropylbenzyl)-3,5-dimethylphenoxy)acetate (23)

Followed procedure for the synthesis of (**21**) except with 1-Boc-4-hydroxypiperidine (**23a**) and yielded a white solid (52 mg, 50% overall yield). <sup>1</sup>H NMR (400 MHz, CDCl<sub>3</sub>):  $\delta$  6.94 (d, 1 H, J = 2.0 Hz), 6.62 (s, 2 H), 6.55 (d, 1 H, J = 8.1 Hz), 6.52 (dd, 1 H, J = 8.1Hz, 2.0 Hz), 5.03 (sept, 1 H, J = 4.4 Hz), 4.62 (s, 2 H), 3.90 (s, 2 H), 3.21 (sept, 1 H, J = 6.8 Hz), 3.05 (m, 2 H), 2.74 (m, 2 H), 2.22 (s, 6 H), 1.94 (m, 2 H), 1.62 (m, 2 H), 1.23 (d, 6 H, J = 6.8 Hz). HRMS exact mass calcd for C<sub>25</sub>H<sub>34</sub>N<sub>1</sub>O<sub>4</sub> [M+H]<sup>+</sup>: m/z 412.24824. Found m/z 412.24886.

piperidin-3-yl 2-(4-(4-hydroxy-3-isopropylbenzyl)-3,5-dimethylphenoxy)acetate (24)

Followed procedure for the synthesis of (**21**) except with 1-Boc-3-hydroxypiperidine (**24a**) and yielded a white solid (37 mg, 36% overall yield). <sup>1</sup>H NMR (400 MHz, CDCl<sub>3</sub>):  $\delta$  6.94 (d, 1 H, J = 2.0 Hz), 6.61 (s, 2 H), 6.52 (d, 1 H, J = 8.1 Hz), 6.49 (dd, 1 H, J = 8.1 Hz, 2.02 Hz), 4.95 (m, 1 H), 4.60 (d, 2 H, J = 1.5 Hz), 3.87 (s, 2 H), 3.22 (sept, 1 H, J = 7.1 Hz), 3.02 (dd, 1 H, J = 13 Hz, 2.8 Hz), 2.87 (dd, 1 H, J = 13.1 Hz, 5.8 Hz), 2.80 (t, 2 H, J = 5.1 Hz), 2.20 (s, 6 H), 1.88 (m, 1 H), 1.81-1.68 (m, 2 H), 1.51 (m, 1 H), 1.21 (d, 6 H, J = 6.8 Hz). HRMS exact mass calcd for C<sub>25</sub>H<sub>34</sub>N<sub>1</sub>O<sub>4</sub> [M+H]<sup>+</sup>: m/z 412.24824. Found m/z 412.24845.

piperidin-2-ylmethyl 2-(4-(4-hydroxy-3-isopropylbenzyl)-3,5-dimethylphenoxy)acetate (25)

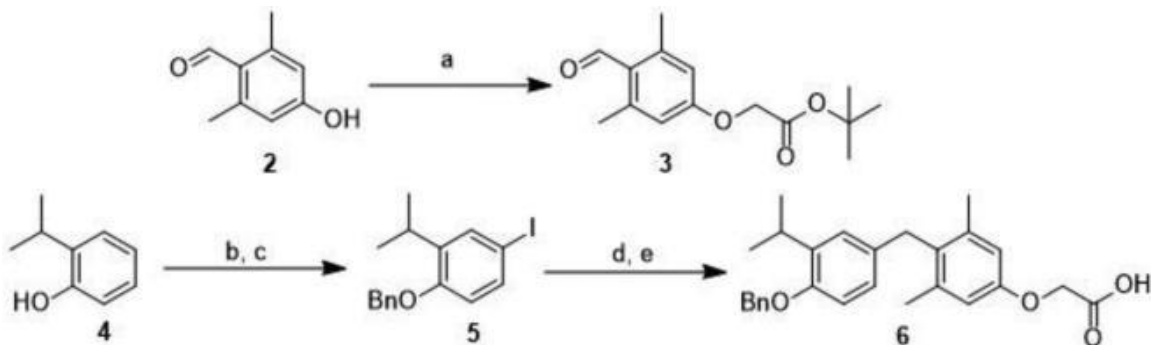
To a 0° C solution of 1-(*tert*-butylcarbonyl)-2-(hydroxymethyl)piperidine (**25a**, 296 mg, 1.25 mmol), DMAP (183 mg, 1.5 mmol), and DCM (6 mL) was slowly added a solution of the acid chloride generated from **6** (0.5 mmol) in 4 mL DCM. The reaction mixture was allowed to warm

to room temperature overnight with stirring. Evaporation of the resulting mixture gave a light-yellow oil which was purified using flash chromatography (silica, 10% to 30% ethyl acetate/hexanes). The resulting ester (288 mg, 0.468 mmol, 94% yield) was dissolved in 5 mL of dry methanol with 1 mL THF and 10% Pd/C (100 mg) was added to generate a suspension. The reaction mixture was subjected to vacuum for approximately 1 min, then placed under argon for approximately 1 min. This process was repeated three times to ensure the mixture was properly degassed. Triethylsilane (1.2 mL, 7.53 mmol) was then added dropwise to the suspension and the reaction mixture was stirred for 4 h at room temperature. Filtration over a pad of celite with methanol, concentration *in vacuo*, and purification via flash chromatography (silica, 10% to 30% ethyl acetate/hexanes) gave the desired product as an oil (129 mg, 0.245 mmol, 52% yield). The product oil (129 mg, 0.245 mmol) was dissolved in 5 mL ethyl acetate and 3 mL of 1 M HCl in ethyl acetate was added, followed by the addition of triethylsilane (39  $\mu$ L, 0.245 mmol). The reaction mixture was stirred overnight at room temperature, concentrated under vacuum, and precipitated with hexanes to give the product as a white solid (92 mg, 0.199 mmol, 81% yield, 40% overall yield).  $^1\text{H NMR}$  (400 MHz,  $\text{CD}_3\text{OD}$ ):  $\delta$  6.76 (s, 1 H), 6.61 (s, 2 H), 6.53 (d, 1 H,  $J = 8.6$  Hz), 6.48 (d, 1 H,  $J = 7.6$  Hz), 4.74 (s, 2 H), 4.38 (dd, 1 H,  $J = 12.4$  Hz,  $J = 3.2$  Hz), 4.25 (dd, 1H,  $J = 12.1$  Hz,  $J = 1.7$  Hz), 3.84 (s, 2 H), 3.41 (m, 1 H), 3.16 (m, 2 H), 2.99 (sept, 1 H,  $J = 6.8$  Hz), 2.16 (s, 6 H), 1.89 (m, 2 H), 1.56 (m, 2 H), 1.08 (d, 6 H,  $J = 6.6$  Hz). HRMS exact mass calcd for  $\text{C}_{26}\text{H}_{36}\text{N}_1\text{O}_4$   $[\text{M}+\text{H}^+]^+$ :  $m/z$  426.26389. Found  $m/z$  426.26465.

## Results:

### Chemistry

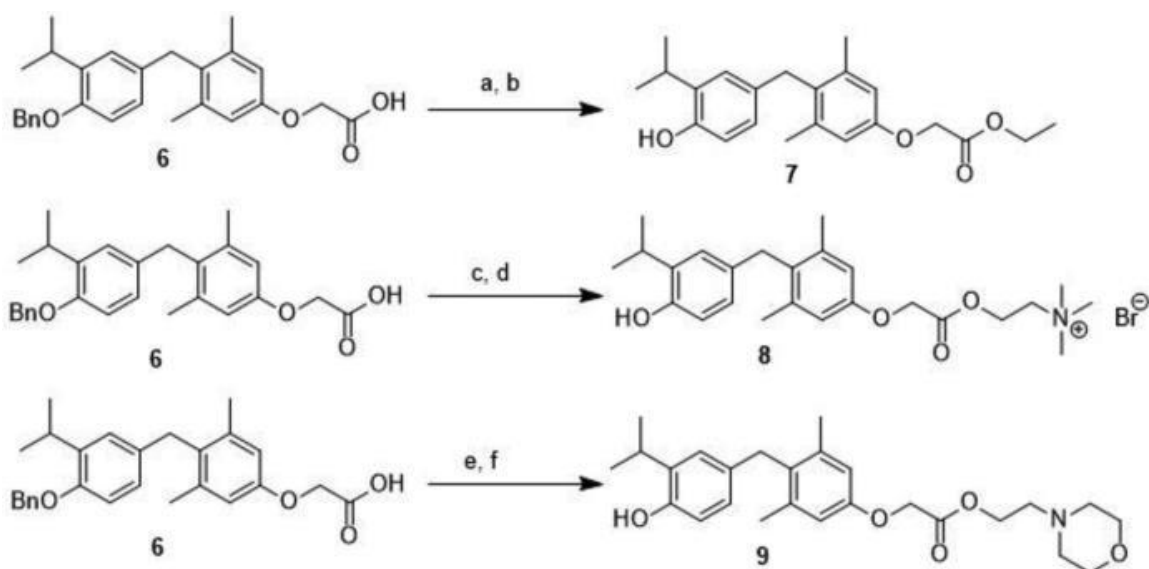
Synthesis of the sobetirome prodrugs was achieved in 5 linear steps starting from 2-isopropylphenol and 2,6-dimethyl-4-hydroxybenzaldehyde ([Scheme 1](#)). The inner-ring carboxylate portion of sobetirome (**1**) was synthesized by alkylating 2,6-dimethyl-4-hydroxybenzaldehyde (**2**) with tert-butyl chloroacetate resulting in **3**. The phenolic portion of sobetirome (**1**) was prepared by first iodinating 2-isopropylphenol (**4**) at the para position using NaI and NaOCl.<sup>22</sup> The phenol was then alkylated with benzyl bromide resulting in the benzyl protected phenol (**5**). The coupling of **5** and **3** proceeded by first generating the aryl Grignard reagent of **5** via the Knochel procedure<sup>21</sup> with  $^i\text{PrMgCl}$  followed by addition of aldehyde **3**. This resulted in the corresponding coupled product containing a carbinol in the methylene bridge connecting the two fragments. The carbinol and t-butyl ester were then removed by treating with TFA and triethylsilane<sup>23</sup> resulting in the key intermediate **6** in gram quantities and a 55% overall yield for the two steps.



### [Scheme 1](#)

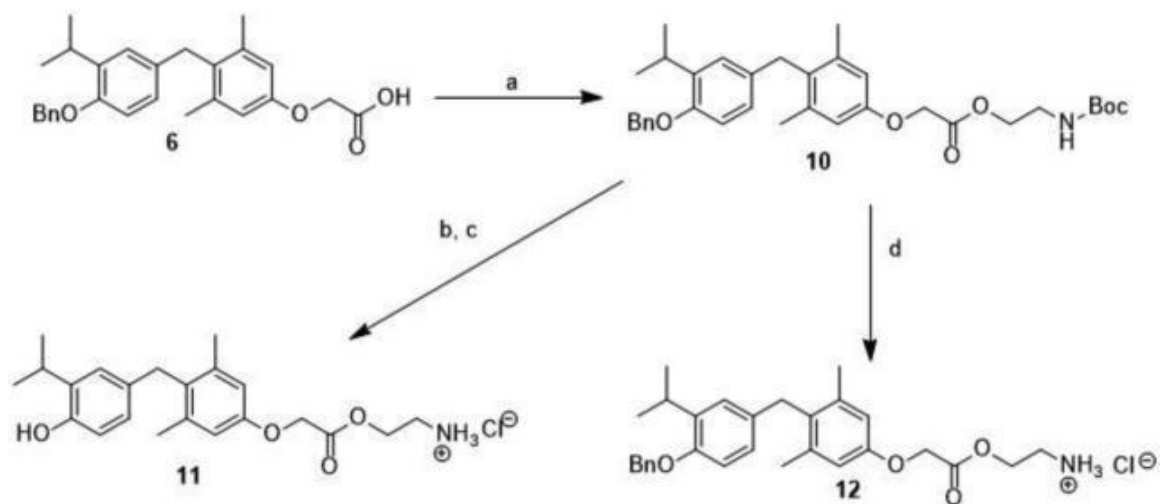
*Synthesis of benzyl-protected sobetirome 6. Reagents and conditions: (a) DMF, Cs<sub>2</sub>CO<sub>3</sub>, t-butyl chloroacetate, 89%; (b) NaI, NaOCl, NaOH, MeOH, H<sub>2</sub>O, 75%; (c) K<sub>2</sub>CO<sub>3</sub>, benzyl bromide, DMF, 75 °C, 77%; (d) (i) <sup>i</sup>PrMgCl, THF, 4 Å MS, (ii) **3**, THF, -78 °C; (e) DCM, Et<sub>3</sub>SiH, TFA, 55% (two steps).*

With the phenol-protected sobetirome (**6**) in esterification followed by protecting group removal treating **6** with acidic ethanol and then deprotecting the choline prodrug (**8**) was next synthesized because of a levels of a COX inhibitor when the carboxylic acid hand, ester prodrugs could be synthesized by simple ([Scheme 2](#)). The ethyl ester (**7**) was synthesized by benzyl ether with 10% Pd/C and triethylsilane<sup>24</sup> The previous report showing an increase in brain exposure portion of the molecule was converted into a choline ester.<sup>25</sup> After a few unsuccessful attempts at esterification of **6** with choline chloride and the acid chloride of **6**, an alkylation of **6** with (2-bromoethyl) trimethylammonium bromide and K<sub>2</sub>CO<sub>3</sub> was attempted. This resulted in the generation of the corresponding benzyl-protected ester which was then deprotected with the same 10% Pd/C and triethylsilane conditions giving the choline-sobetirome prodrug (**8**) in 39% overall yield. The 4-(2-hydroxyethyl)morpholine sobetirome prodrug (**9**) was synthesized by treating a cooled solution of 4-(2-hydroxyethyl)morpholine, DMAP, and DCM with a solution of the acid chloride (**6a**) and DCM. Following the same benzyl deprotection method, this resulted in the morpholino prodrug (**9**) in a 48% yield. The next set of sobetirome prodrugs synthesized contained an ethanolamine sidechain for increasing the logP and adding a positive charge to sobetirome, or for acting as a linker to amino acids. Ethanolamine moieties, when attached to carboxylic acids, have been shown previously to enhance the brain/serum ratios of dexibuprofen.<sup>26-27</sup> The ethanolamine sobetirome prodrug synthesis was started in a similar manner to **9** except Boc-ethanolamine (Boc = *tert*-butyloxycarbonyl) was used ([Scheme 3](#)). The protected ethanolamine intermediate (**10**) was then subjected to benzyl deprotection conditions, followed by HCl (ethyl acetate) to remove the Boc residue resulting in **11** in a 37% overall yield for the three steps. The lysine and valine sobetirome prodrugs were synthesized by first deprotecting the Boc residue of **10** resulting in the primary amine salt (**12**). The primary amine of **12** was then coupled with the carboxylic acid of Boc-lysine(Boc)-OH and Boc-valine using EDCI, HOBt, DIEA and DMF. Following the standard benzyl ether deprotection and Boc deprotection conditions yielded the sobetirome-lysine (**13**) and sobetirome-valine (**14**) ([Scheme 4](#)).



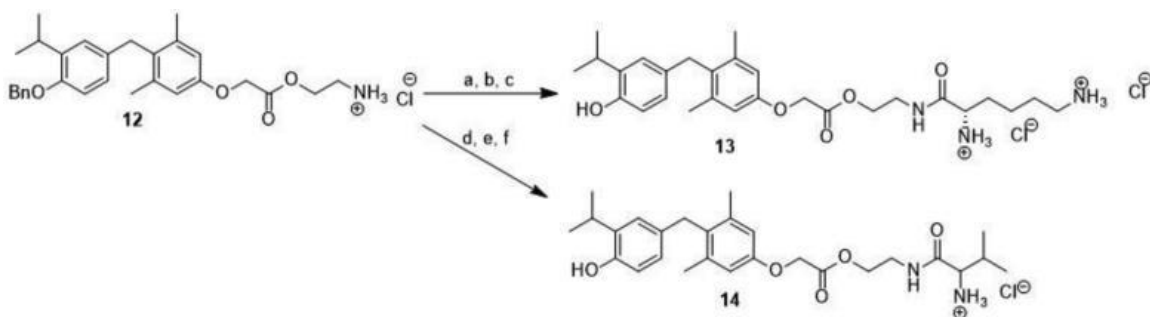
**Scheme 2**

Synthesis of sobetirome prodrugs **7**, **8**, and **9**. Reagents and conditions: (a) 1M HCl (ethanol); (b) 10% Pd/C,  $\text{Et}_3\text{SiH}$ , MeOH, 62% (two steps); (c)  $\text{K}_2\text{CO}_3$ , DMF, (2-Bromoethyl) trimethylammonium bromide; (d) 10% Pd/C,  $\text{Et}_3\text{SiH}$ , MeOH, 39% (two steps); (e) (i) oxalyl chloride, DCM, DMF, (ii) 4-(2-hydroxyethyl)morpholine, DMAP, DCM; (f) 10% Pd/C,  $\text{Et}_3\text{SiH}$ , MeOH, 48% (two steps)



**Scheme 3**

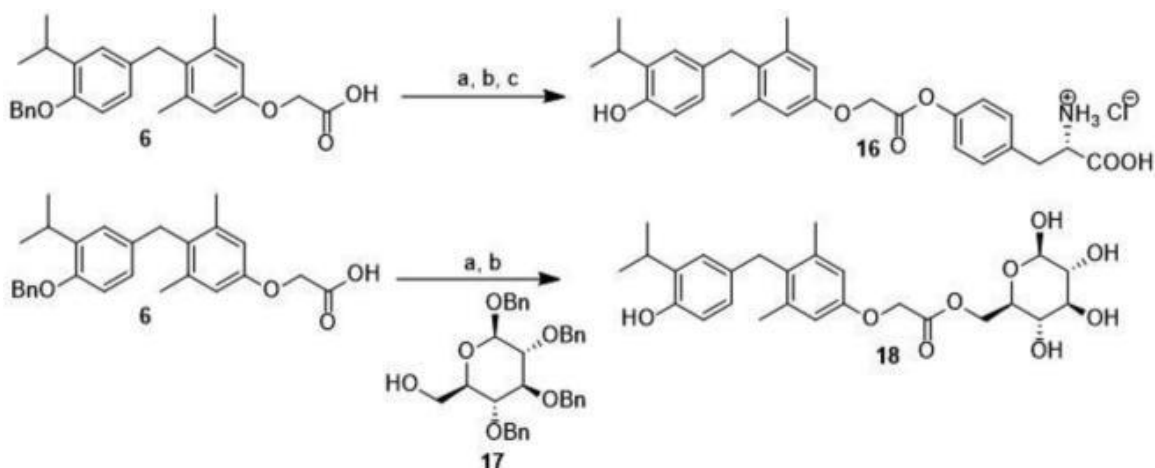
Synthesis of sobetirome prodrug **11** and intermediate **12**. Reagents and conditions: (a) (i) oxalyl chloride, DCM, DMF, (ii) *N*-Boc-ethanolamine, DMAP, DCM, 72%; (b) 10% Pd/C,  $\text{Et}_3\text{SiH}$ , MeOH; (c) 1 M HCl (ethyl acetate), 51%. (d) 1 M HCl (ethyl acetate), 81%.



[Scheme 4](#)

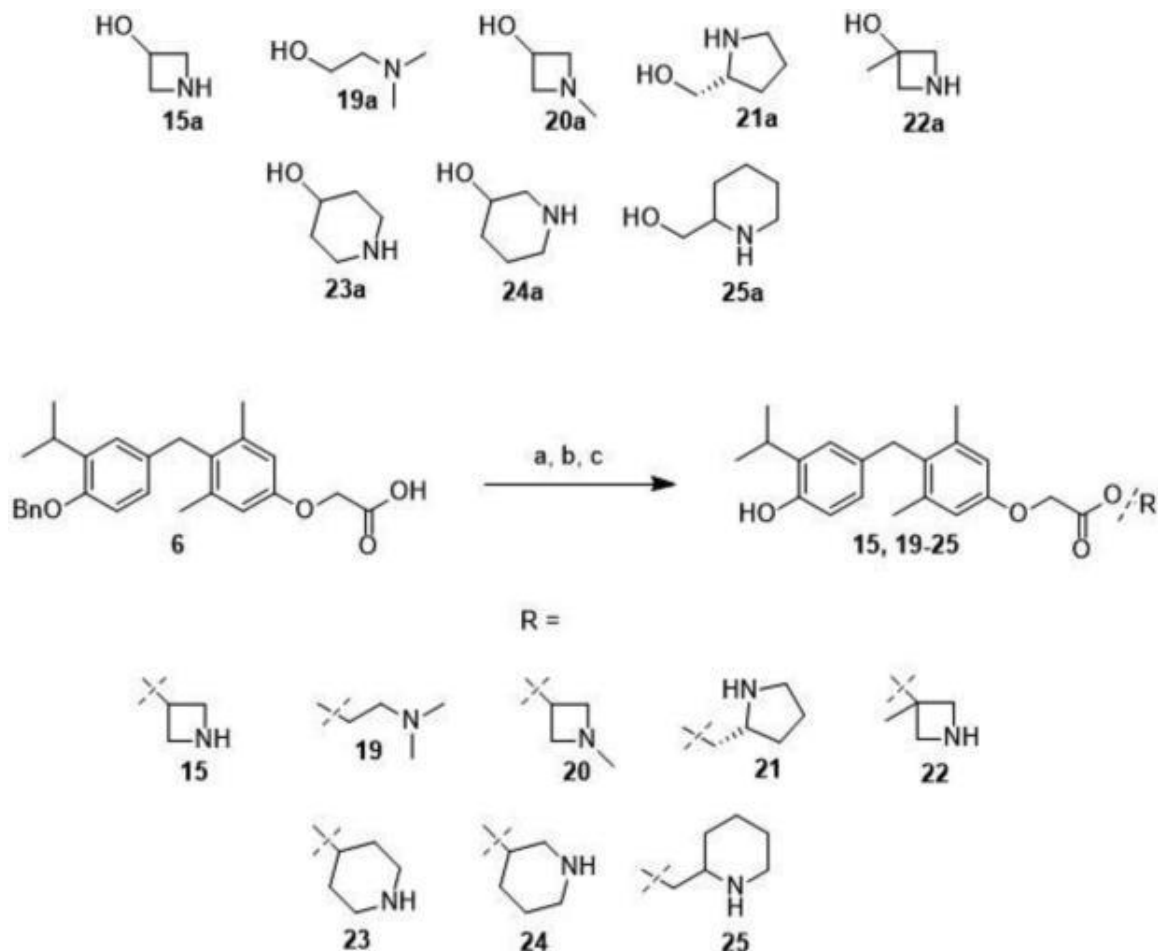
*Synthesis of sobetirome prodrugs 13 and 14. Reagents and conditions: (a) Boc-Lys(Boc)-OH, EDCI-HCl, HoBt-H<sub>2</sub>O, DMF, DIEA; (b) 10% Pd/C, Et<sub>3</sub>SiH, MeOH; (c) 1 M HCl (ethyl acetate), 40%; (d) Boc-Valine-OH, EDCI-HCl, HoBt-H<sub>2</sub>O, DMF, DIEA; (e) 10% Pd/C, Et<sub>3</sub>SiH, MeOH; (f) 1 M HCl (ethyl acetate), 32%.*

Two sobetirome prodrugs were designed to utilize tyrosine and glucose specific active transport mechanisms to gain access to the CNS ([Scheme 5](#)). The sobetirome-tyrosine prodrug was synthesized using Schotten-Baumann conditions as described by Millar and Hare.<sup>28</sup> The acid chloride of **6** was treated with Boc-tyrosine, and the resulting phenolic ester was then subjected to benzyl ether and Boc deprotection yielding **16**. The sobetirome-glucose prodrug was prepared by first synthesizing benzyl 2,3,4-tri-O-benzyl-beta-D-glucopyranoside (**17**) according to Lu and colleagues.<sup>29</sup> The ester was formed by reacting **17** with the acid chloride generated from **6**. With the ester in hand, the five benzyl ethers were deprotected using 100 mol% of 10% Pd/C and 60 eq. of triethylsilane yielding **18** in a 44% overall yield. In an effort to expand upon the enhanced CNS-distribution properties of prodrug **11**, a series of prodrugs (**15**, **19-25**) were synthesized in which the promoieties were variations of the ethanolamine motif ([Scheme 6](#)). This series included alkylation of the promoiety amino group and altered steric profiles and degrees of freedom by the incorporation of heterocycles of varying size. A similar synthetic sequence to that for **11** was used to generate prodrugs **15** and **19-25**.



[Scheme 5](#)

Synthesis of sobetirome prodrugs **16** and **18**. Reagents and conditions: (a) i) oxalyl chloride, DCM, DMF, (ii) *N*-*t*-Boc-*L*-Tyrosine, NaOH, Acetone; (b) 10% Pd/C, Et<sub>3</sub>SiH, MeOH, 51% (two steps); (c) 1 M HCl (ethyl acetate), 12.5% (three steps); (d) i) oxalyl chloride, DCM, DMF, (ii) **17**, DMAP, DCM; (e) 10% Pd/C, Et<sub>3</sub>SiH, Acetic Acid, THF, 44% (two steps).



[Scheme 6](#)

Synthesis of second generation sobetirome prodrugs **15**, **19-25**. Reagents and conditions: (a) i) oxalyl chloride, DCM, DMF, (ii) *N*-Boc-amino alcohol, DMAP, DCM or THF (b) 10% Pd/C, Et<sub>3</sub>SiH, MeOH, THF; (c) 1 M HCl (ethyl acetate).

### Biological Studies

A biodistribution study in mice was performed on each prodrug to determine the brain, liver, and serum concentrations of sobetirome following systemic (i.p.) administration. The mice cohorts received an equimolar dose (1.5  $\mu\text{mol}$  / kg) of each prodrug and one cohort received the same dose of sobetirome as a control. Tissue and blood were collected 30 minutes post-injection (the time corresponding to C<sub>max</sub> of sobetirome in the brain, liver, and serum) and the concentration of sobetirome was determined using an LC-MS/MS method containing D<sub>6</sub>-Sobetirome as an internal standard. The first generation sobetirome prodrugs (**7**, **8**, **9**, **13**, **14**, **16**, **18**) did not show increased

brain sobetirome levels compared to the equimolar systemic injection of sobetirome (Fig. 2a). However, a significant (~2-fold) brain sobetirome level increase was observed with ethanolamine ester prodrug **11**. In addition to increased brain sobetirome levels, this ester showed significantly lower liver and serum sobetirome levels compared to the direct sobetirome injection leading to a 7-fold increase compared to sobetirome in the brain/serum sobetirome ratio for **11** (Fig. 2b). Moreover, the brain/liver sobetirome ratio was increased compared to sobetirome injection by 4-fold for **11** (Fig. 2c). Of the series of tested prodrugs, ethanolamine derivative **11** outperformed all other derivatives with respect to both increased brain exposure and minimized peripheral exposure of the active drug component sobetirome.

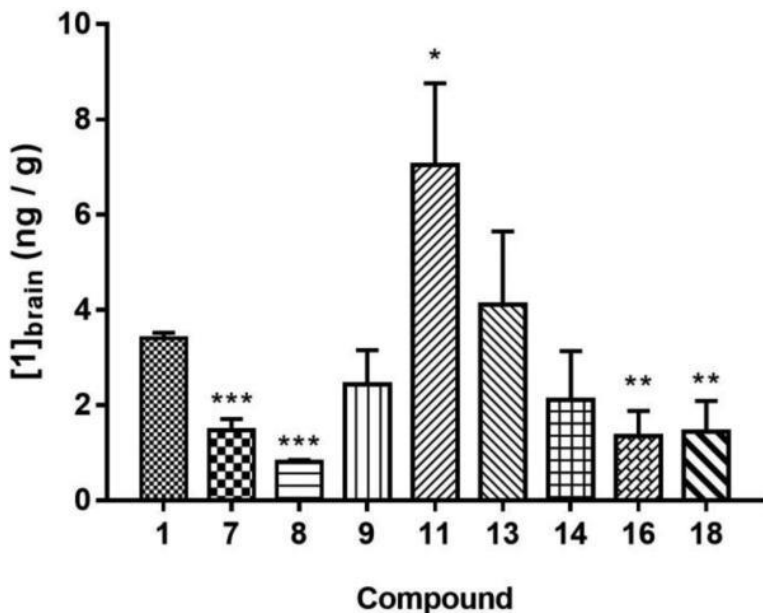


[Figure 2a](#)

Sobetirome concentrations (ng / g) in the brain 30 minutes after ip administration of sobetirome (1.5 μmol / kg) or prodrugs **7, 8, 9, 11, 13, 14, 16, 18** (1.5 μmol / kg) in mice. Significance compared to sobetirome (**1**): \* =  $p < 0.05$ , \*\* =  $p < 0.01$ , \*\*\* =  $p < 0.005$ .

[Figure 2b](#)

Sobetirome (brain / serum) ratios of sobetirome (**1**) or prodrugs following ip administration of sobetirome (1.5 μmol / kg) or prodrugs **7, 8, 9, 11, 13, 14, 16, 18** (1.5 μmol / kg) in mice. Significance compared to sobetirome (**1**): \* =  $p < 0.05$ , \*\* =  $p < 0.01$ , \*\*\* =  $p < 0.005$ .

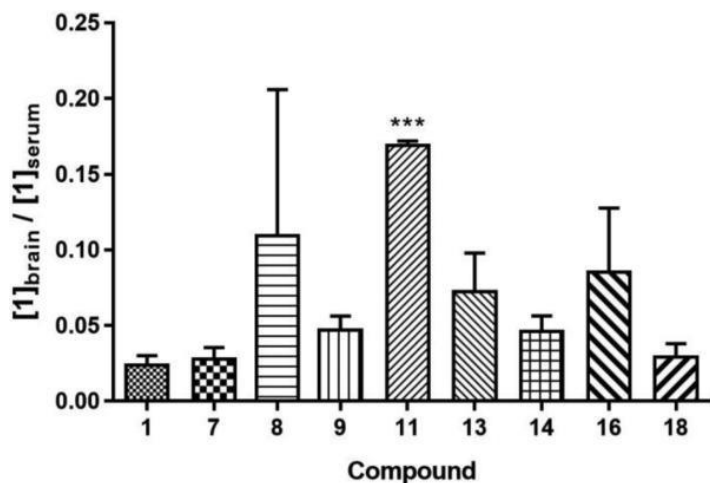
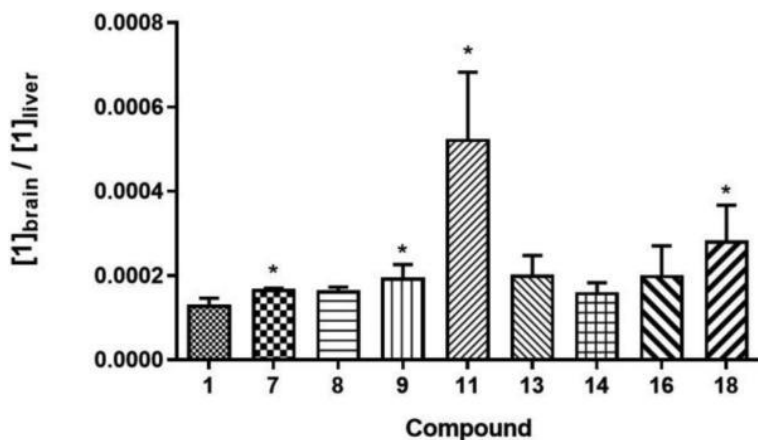


[Figure 2c](#)



*Sobetirome (brain / liver) ratios of Sobetirome (1) or prodrugs following ip administration of sobetirome (1.5  $\mu\text{mol} / \text{kg}$ ) or prodrugs 7, 8, 9, 11, 13, 14, 16, 18 (1.5  $\mu\text{mol} / \text{kg}$ ) in mice. Significance compared to sobetirome (1): \* =  $p < 0.05$ , \*\* =  $p < 0.01$ , \*\*\* =  $p < 0.005$ .*

The single time point pilot study was followed up for **11**

vs. sobetirome with an 8-hour time course distribution study in mice. A pharmacokinetic study showed that the  $t_{1/2}$  of sobetirome in mice is approximately 1.3 h indicating that an 8 h study would be sufficient to quantify >99% of the sobetirome exposure vs. time from a single dose ([Supplementary Material](#)). Analyzing for sobetirome concentration, pharmacokinetic time-course curves were generated, and AUC (Area Under the Curve) values in brain, liver and serum resulting from systemic administration of sobetirome and **11** were obtained (Fig. 3, [Table 1](#)). The results show that the trend observed in the single time point study parallels the full time course experiments; prodrug **11** generates increased sobetirome exposure (compared to direct sobetirome injection) in brain and decreased sobetirome exposure in liver and serum ([Fig. 3a,b,b](#)). The brain/serum ratio based on AUC values was found to be 0.02 for sobetirome compared to 0.05 for **11** ([Table 2](#)). In addition to improved sobetirome brain/serum ratios, prodrug **11** also displayed a 2.4-fold increase in sobetirome  $\text{AUC}_{(\text{brain})} / \text{AUC}_{(\text{liver})}$  relative to sobetirome ([Fig. 3c](#), and [Table 2](#)). Clear  $C_{\text{max}}$  and  $T_{\text{max}}$  values were difficult to obtain, as maximal sobetirome concentrations were recorded roughly at the initial (15 min) time points in brain, liver, and serum for both sobetirome and **11**, suggesting a rapid distribution phase for both drug and prodrug.

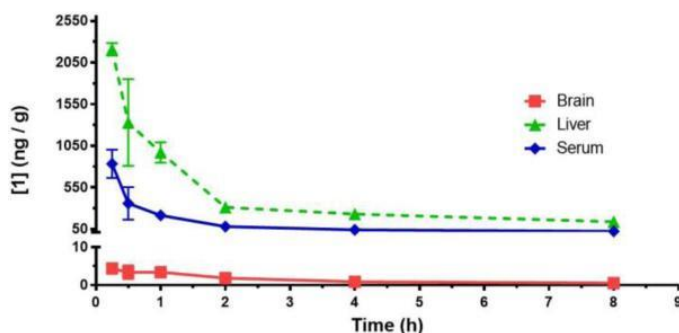


[Figure 3a](#)

*Sobetirome concentrations in the brain, liver, and serum (ng / g) vs time (h) after ip administration of sobetirome (1.5  $\mu\text{mol} / \text{kg}$ ).*

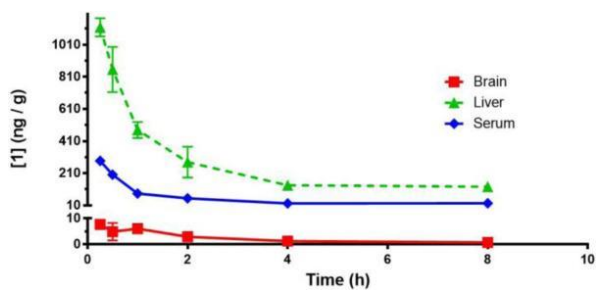


Figure 3b

Sobetirome concentrations in the brain, liver, and serum (ng / g) vs time (h) after ip administration of prodrug **11** (1.5 μmol / kg).

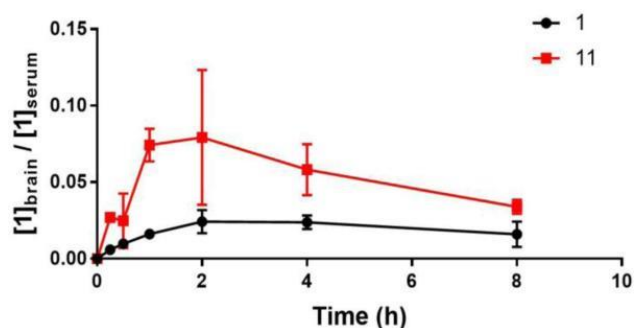


Figure 3c

Sobetirome brain / serum ratios following ip administration of sobetirome **1** (1.5 μmol / kg) or prodrug **11** (1.5 μmol / kg) in mice vs time (h).

Table 1

Pharmacokinetic parameters ( $AUC_{0 \rightarrow t}$  and  $T_{max}$ ) of sobetirome in mouse serum, brain, and liver tissues after ip administration of sobetirome (**1**) (1.5 μmol / kg) or prodrug **11** (1.5 μmol / kg).

Sobetirome (**1**)    **11**

Tissue  $AUC_{0 \rightarrow t}$  (ng/g\*h)     $AUC_{0 \rightarrow t}$  (ng/g\*h)

Serum 681.7                      367.8

Brain 10.8                        17.1

Liver 2933                        1897

Table 2

Sobetirome tissue distribution values ( $AUC_{brain} / AUC_{serum}$ ) and ( $AUC_{brain} / AUC_{liver}$ ) after ip administration of sobetirome or prodrug **11**.

## Sobetirome Distribution

Compound	AUC <sub>brain</sub> / AUC <sub>serum</sub>	AUC <sub>brain</sub> / AUC <sub>liver</sub>
1	0.02	0.004
11	0.05	0.009

Based on the finding that of all the esters tested ethanolamine **11** showed the most promise as sobetirome prodrug for enhancing CNS exposure and BBB permeability, a series of additional sobetirome amino esters was prepared ([Scheme 6](#)) and tested. An equimolar dose (1.5  $\mu\text{mol} / \text{kg}$ ), single time point experiment analogous to that which was previously described ([Fig. 2a](#)) was performed to measure the brain exposure of sobetirome by this new series of prodrugs ([Fig. 3d](#)). None of the additional amino esters were found to deliver more sobetirome to the brain compared to the parent compound, ethanolamine **11**.

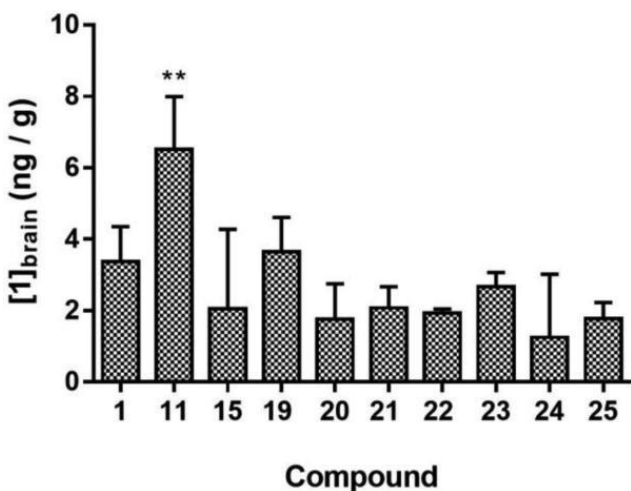


[Figure 3d](#)

*Sobetirome concentrations (ng / g) in the brain 30 minutes after ip administration of sobetirome (1.5  $\mu\text{mol} / \text{kg}$ ) or prodrugs 11, 15, 19, 20, 21, 22, 23, 24, and 25 (1.5  $\mu\text{mol} / \text{kg}$ ) in mice. Significance compared to sobetirome (1): \* =  $p < 0.05$ , \*\* =  $p < 0.01$ , \*\*\* =  $p < 0.005$ .*

### Discussion:

There is increasing interest in activating specific thyroid hormone signaling pathways in the brain for the treatment of certain CNS diseases, in particular those that involve defects in myelin repair.<sup>30-31</sup> Thyroid hormones T4 and T3 are not suitable as therapeutics for these diseases, as there is no therapeutic index for T4 and T3 separating the desired therapeutic effect of myelin repair from adverse effects associated with hyperthyroidism such as tachycardia, muscle wasting, and osteoporosis.<sup>32-35</sup> This issue is potentially addressed by selective thyromimetics, which are synthetic T3 agonists that show tissue selective thyroid hormone action.<sup>36</sup> Sobetirome is a thyromimetic that has been studied extensively over the past 15 years.<sup>9,37</sup> Similar to T3, sobetirome affects LDL cholesterol lowering by stimulating hepatic cholesterol clearance mechanisms, but unlike T3, does so at doses that have no deleterious effect on heart, muscle, or bone.<sup>38-40</sup> Distribution to the CNS is an essential property for such a thyromimetic to be useful as a therapeutic agent that stimulates myelin repair, and sobetirome is unique among thyromimetics in that it is the only compound reported in the class that distributes significantly to the CNS from a systemically administered dose.<sup>11-12</sup> In addition, quantitative data from this study using mice confirmed that with a brain/serum ratio of 0.02 ([Table 2](#)), a ratio lower than was found in rats

(*vide supra*), sobetirome distributes to the CNS from systemic circulation with an efficiency that lies at the lower end of the range for approved CNS drugs.<sup>41-42</sup> However, we felt the CNS distribution of sobetirome could be increased using a prodrug strategy that would mask the carboxylic acid, a functional group known to impede BBB penetration.<sup>14</sup> A prodrug variant of sobetirome that increased CNS distribution with a concomitant decrease in systemic exposure would be a beneficial profile in principle for a remyelinating agent.

We approached this problem by preparing ester derivatives of sobetirome comprised of promoieties designed to increase BBB permeability of the sobetirome ester. Promoiety alcohols were selected based on precedent from the prodrug literature and contained functionality that either enhanced passive diffusion across the BBB or facilitated active transport. With test compounds in hand, we began biological studies by testing two different previously reported cell culture models to evaluate BBB permeability, MDCK II and hCMEC/D3 cell lines, but found that neither of these models faithfully replicated the *in vivo* derived BBB permeability across our series of compounds (data not shown).<sup>43-44</sup> As such, we performed all BBB permeability analyses in mice by dosing systemically (i.p.) with the test compound and quantifying liberated sobetirome in brain extract and plasma using LC-MS/MS. Despite the reported success of these alcohols for enhancing CNS distribution of prodrug esters of carboxylic acid drugs, only the ethanolamine ester **11** showed a significant increase in sobetirome brain levels or the sobetirome brain/serum ratio compared to an equimolar systemic dose of sobetirome (Fig. 2a++b,b, Fig. 3d). The failure of all of the other alcohols to facilitate CNS distribution of sobetirome indicates that transport of these esters across the BBB depends on the carboxylic acid containing drug and not solely on the alcohol moiety, thus limiting the generality of these modifications as an approach to increasing CNS distribution of carboxylate containing drugs.

Based on the promising enhanced CNS distribution of ethanolamine **11**, a series of aminoesters were prepared and their ability to distribute sobetirome to the brain from a systemic dose was analyzed (Scheme 6 and Fig. 3d). Unlike ethanolamine **11**, none of these additional analogs were capable of delivering more sobetirome to the brain compared to a systemic dose of sobetirome itself (Fig. 3d), although some of these modifications decreased blood levels of sobetirome resulting in an increased brain/blood ratio (data not shown). The dimethylethanolamine (**19a**) was previously shown to be more effective than ethanolamine<sup>26</sup> at increasing BBB permeability when esterified to dexibuprofen,<sup>27</sup> a different carboxylic acid containing drug, but in the context of sobetirome **19** is significantly less effective than **11** and offers no BBB permeability enhancement over sobetirome itself. Likewise, the 2-morpholinoethyl ester **9** that contains a tertiary ethanolamine did not significantly increase sobetirome brain levels (Fig. 2a) or the brain/serum ratio (Fig. 2b) indicating that the more highly substituted tertiary ethanolamine esters are either not as efficient at traversing the BBB or are less hydrolytically stable in the periphery than the ethanolamine ester. Similar results were also observed in the ethanolamine-derived prodrug series, where all prodrugs contained secondary or tertiary amino motifs and did not increase brain exposure. Moreover, the structurally related quaternary ammonium choline ester **8** did not improve CNS distribution of sobetirome despite reports of its successful use in promoting CNS distribution of a carboxylate containing COX inhibitor.<sup>25</sup> This suggests the requirement for an amino group that can shuttle between neutral and cationic forms for the mechanism involved in the BBB transport of the sobetirome-aminoethyl ester prodrug.

The structural characteristics of prodrug **11** that may contribute to its ability to increase brain concentration of sobetirome are unclear. Prodrug **11** (clogP: 4.62) maintains similar lipophilicity

compared to sobetirome (clogP: 4.87) and at the same time eliminates the negative charge on sobetirome that predominates at physiological pH. The flexibility associated with the ethanolamine motif provides a scenario in which intramolecular interactions between the amino group and ester carbonyl may play a role in BBB permeability or hydrolytic stability. Acyl migration of the promoiety from oxygen to nitrogen is conceivable, and this augmented stability upon rearrangement to the amide species could possibly account for the improved delivery of **11** to the CNS. However, the prodrugs were prepared and administered as esters in accord with the previous work that demonstrated increased BBB permeability with ethanolamine esters of carboxylate drugs.<sup>26,27</sup> Future mechanistic studies to elucidate how prodrug **11** accesses the CNS *in vivo* are warranted.

The 8 h time-course study comparing brain, liver, and serum sobetirome levels from an equimolar systemic dose of either sobetirome or **11** suggests that the prodrug preferentially delivers sobetirome into the brain, as brain levels increase and peripheral exposure decreases compared to sobetirome injection. Prodrug **11** showed roughly the same kinetic profile for sobetirome delivery in the three compartments as sobetirome, albeit with lower absolute peripheral values (Fig. 3a+b). The data indicates that the prodrug limits sobetirome exposure in circulation while increasing exposure in the brain, which should lead to an increase in CNS thyromimetic actions with a concomitant decrease in peripheral actions compared to the profile of the parent drug sobetirome. Such a profile should in theory be desirable for a thyromimetic used to treat CNS indications.

#### **Acknowledgements:**

Research reported in this publication was supported by a grant from the National Institutes of Health (DK 052798, T.S.S.), the OHSU Laura Fund for Innovation in Multiple Sclerosis, and the National Institutes of Health under Award Number T32DK007680 (support to S.J.F.). Analytical support was provided by the Bioanalytical Shared Resource/Pharmacokinetics Core Facility, which is part of the University Shared Resource Program at Oregon Health & Sciences University. We thank L. Bleye for her assistance with LC-MS/MS analysis. We would also like to thank Dr. Andrea DeBarber at the Portland State University BioAnalytical Mass Spectrometry Facility for HRMS.

#### **References:**

1. Bernal J. Thyroid hormone receptors in brain development and function. *Nat Clin Pract Endocrinol Metab.* 2007;3(3):249–59. [[PubMed](#)] [[Google Scholar](#)]
2. Barres BA, Lazar MA, Raff MC. A novel role for thyroid hormone, glucocorticoids and retinoic acid in timing oligodendrocyte development. *Development.* 1994;120(5):1097–108. [[PubMed](#)] [[Google Scholar](#)]
3. Dugas JC, Ibrahim A, Barres BA. The T3-induced gene KLF9 regulates oligodendrocyte differentiation and myelin regeneration. *Mol Cell Neurosci.* 2012;50(1):45–57. [[PMC free article](#)] [[PubMed](#)] [[Google Scholar](#)]
4. Harsan L-A, Steibel J, Zaremba A, Agin A, Sapin R, Poulet P, Guignard B, Parizel N, Grucker D, Boehm N, Miller RH, Ghandour MS. Recovery from Chronic Demyelination by Thyroid Hormone Therapy: Myelinogenesis Induction and Assessment by Diffusion Tensor Magnetic

- Resonance Imaging. *J Neurosci*. 2008;28(52):14189–14201. [[PMC free article](#)] [[PubMed](#)] [[Google Scholar](#)]
5. Franco PG, Silvestroff L, Soto EF, Pasquini JM. Thyroid hormones promote differentiation of oligodendrocyte progenitor cells and improve remyelination after cuprizone-induced demyelination. *Exp Neurol*. 2008;212(2):458–467. [[PubMed](#)] [[Google Scholar](#)]
  6. Zhang M, Zhan XL, Ma ZY, Chen XS, Cai QY, Yao ZX. Thyroid hormone alleviates demyelination induced by cuprizone through its role in remyelination during the remission period. *Exp Biol Med (Maywood)* 2015;240(9):1183–96. [[PMC free article](#)] [[PubMed](#)] [[Google Scholar](#)]
  7. Genin EC, Gondcaille C, Trompier D, Savary S. Induction of the adrenoleukodystrophy-related gene (ABCD2) by thyromimetics. *J Steroid Biochem Mol Biol*. 2009;116(1-2):37–43. [[PubMed](#)] [[Google Scholar](#)]
  8. Baxi EG, Schott JT, Fairchild AN, Kirby LA, Karani R, Uapinyoying P, Pardo-Villamizar C, Rothstein JR, Bergles DE, Calabresi PA. A selective thyroid hormone beta receptor agonist enhances human and rodent oligodendrocyte differentiation. *Glia*. 2014;62(9):1513–29. [[PMC free article](#)] [[PubMed](#)] [[Google Scholar](#)]
  9. Scanlan TS. Sobetirome: a case history of bench-to-clinic drug discovery and development. *Heart Fail Rev*. 2010;15(2):177–82. [[PubMed](#)] [[Google Scholar](#)]
  10. Lin V, Klepp H, Hanley R. Sobetirome as a thyroid hormone receptor[beta]- and liver-selective thyromimetic that can effect substantial LDL-C lowering without significant changes in heart rate or the thyroid axis in euthyroid men. 90th Annual Meeting Of the Endocrine Society. 2008:OR36. [[Google Scholar](#)]
  11. Trost SU, Swanson E, Gloss B, Wang-Iverson DB, Zhang H, Volodarsky T, Grover GJ, Baxter JD, Chiellini G, Scanlan TS, Dillmann WH. The thyroid hormone receptor-beta-selective agonist GC-1 differentially affects plasma lipids and cardiac activity. *Endocrinology*. 2000;141(9):3057–64. [[PubMed](#)] [[Google Scholar](#)]
  12. Takahashi N, Asano Y, Maeda K, Watanabe N. In vivo evaluation of 1-benzyl-4-aminoindole-based thyroid hormone receptor  $\beta$  agonists: importance of liver selectivity in drug discovery. *Biol Pharm Bull*. 2014;37(7):1103–8. [[PubMed](#)] [[Google Scholar](#)]
  13. Hirano T, Kagechika H. Thyromimetics: a review of recent reports and patents (2004 - 2009). *Expert Opin Ther Pat*. 2010;20(2):213–28. [[PubMed](#)] [[Google Scholar](#)]
  14. Hitchcock SA, Pennington LD. Structure-brain exposure relationships. *J Med Chem*. 2006;49(26):7559–83. [[PubMed](#)] [[Google Scholar](#)]
  15. Stella V, Borchardt R, Hageman M, Oliyai R, Maag H, Tilley J. *Prodrugs: Challenges and Rewards*. Springer; New York: 2007. [[Google Scholar](#)]
  16. Pavan B, Dalpiaz A, Ciliberti N, Biondi C, Manfredini S, Vertuani S. Progress in drug delivery to the central nervous system by the prodrug approach. *Molecules*. 2008;13(5):1035–65. [[PMC free article](#)] [[PubMed](#)] [[Google Scholar](#)]

17. Rautio J, Kumpulainen H, Heimbach T, Oliyai R, Oh D, Järvinen T, Savolainen J. Prodrugs: design and clinical applications. *Nat Rev Drug Discov.* 2008;7(3):255–70. [[PubMed](#)] [[Google Scholar](#)]
18. Jana S, Mandlekar S, Marathe P. Prodrug design to improve pharmacokinetic and drug delivery properties: challenges to the discovery scientists. *Curr Med Chem.* 2010;17(32):3874–908. [[PubMed](#)] [[Google Scholar](#)]
19. Rautio J, Laine K, Gynther M, Savolainen J. Prodrug approaches for CNS delivery. *AAPS J.* 2008;10(1):92–102. [[PMC free article](#)] [[PubMed](#)] [[Google Scholar](#)]
20. Lee G, Dallas S, Hong M, Bendayan R. Drug transporters in the central nervous system: brain barriers and brain parenchyma considerations. *Pharmacol Rev.* 2001;53(4):569–96. [[PubMed](#)] [[Google Scholar](#)]
21. Boymond L, Rottländer M, Cahiez G, Knochel P. Preparation of Highly Functionalized Grignard Reagents by an Iodine–Magnesium Exchange Reaction and its Application in Solid-Phase Synthesis. *Angew. Chem. Int. Ed.* 1998;37:1701–1703. [[PubMed](#)] [[Google Scholar](#)]
22. Edgar KJ, Falling SN. An efficient and selective method for the preparation of iodophenols. *J Org Chem.* 1990;55(18):5287–5291. [[Google Scholar](#)]
23. Penning TD, Chandrakumar NS, Chen BB, Chen HY, Desai BN, Djuric SW, Docter SH, Gasiiecki AF, Haack RA, Miyashiro JM, Russell MA, Yu SS, Corley DG, Durley RC, Kilpatrick BF, Parnas BL, Askonas LJ, Gierse JK, Harding EI, Highkin MK, Kachur JF, Kim SH, Krivi GG, Villani-Price D, Pyla EY, Smith WG, Ghoreishi-Haack NS. Structure—Activity Relationship Studies on 1-[2-(4-Phenylphenoxy)ethyl]pyrrolidine (SC-22716), a Potent Inhibitor of Leukotriene A4 (LTA4) Hydrolase. *J Med Chem.* 2000;43(4):721–735. [[PubMed](#)] [[Google Scholar](#)]
24. Mandal PK, McMurray JS. Pd-C-induced catalytic transfer hydrogenation with triethylsilane. *J Org Chem.* 2007;72(17):6599–601. [[PubMed](#)] [[Google Scholar](#)]
25. Smith ND, Reger TS, Payne J, Zunic J, Lorrain D, Correa L, Stock N, Cramer M, Chen W, Yang J, Prasit P, Munoz B. Water soluble prodrug of a COX-2 selective inhibitor suitable for intravenous administration in models of cerebral ischemia. *Bioorg Med Chem Lett.* 2005;15(13):3197–200. [[PubMed](#)] [[Google Scholar](#)]
26. Zhang X, Liu X, Gong T, Sun X, Zhang ZR. In vitro and in vivo investigation of dexibuprofen derivatives for CNS delivery. *Acta Pharmacol Sin.* 2012;33(2):279–88. [[PMC free article](#)] [[PubMed](#)] [[Google Scholar](#)]
27. Li Y, Zhou Y, Jiang J, Wang X, Fu Y, Gong T, Sun X, Zhang Z. Mechanism of brain targeting by dexibuprofen prodrugs modified with ethanolamine-related structures. *J Cereb Blood Flow Metab.* 2015;35(12):1985–94. [[PMC free article](#)] [[PubMed](#)] [[Google Scholar](#)]
28. Millar JG, Hare JD. Identification and synthesis of a kairomone inducing oviposition by parasitoid *Aphytis melinus* from California red scale covers. *J Chem Ecol.* 1993;19(8):1721–36. [[PubMed](#)] [[Google Scholar](#)]

29. Lu W, Navidpour L, Taylor SD. An expedient synthesis of benzyl 2,3,4-tri-O-benzyl-beta-D-glucopyranoside and benzyl 2,3,4-tri-O-benzyl-beta-D-mannopyranoside. *Carbohydr Res*. 2005;340(6):1213–7. [[PubMed](#)] [[Google Scholar](#)]
30. Calza L, Fernandez M, Giardino L. Cellular approaches to central nervous system remyelination stimulation: thyroid hormone to promote myelin repair via endogenous stem and precursor cells. *J Mol Endocrinol*. 2010;44(1):13–23. [[PubMed](#)] [[Google Scholar](#)]
31. Taveggia C, Feltri ML, Wrabetz L. Signals to promote myelin formation and repair. *Nat Rev Neurol*. 2010;6(5):276–287. [[PMC free article](#)] [[PubMed](#)] [[Google Scholar](#)]
32. Biondi B, Klein I. Hypothyroidism as a risk factor for cardiovascular disease. *Endocrine*. 2004;24(1):1–13. [[PubMed](#)] [[Google Scholar](#)]
33. Klein I, Ojamaa K. Thyrotoxicosis and the heart. *Endocrinol Metab Clin North Am*. 1998;27(1):51–62. [[PubMed](#)] [[Google Scholar](#)]
34. O'Neal P, Alamdari N, Smith I, Poylin V, Menconi M, Hasselgren P-O. Experimental hyperthyroidism in rats increases the expression of the ubiquitin ligases atrogin-1 and MuRF1 and stimulates multiple proteolytic pathways in skeletal muscle. *J Cell Biochem*. 2009;108(4):963–973. [[PubMed](#)] [[Google Scholar](#)]
35. Williams GR. Thyroid Hormone Actions in Cartilage and Bone. *Eur Thyroid J*. 2013;2(1):3–13. [[PMC free article](#)] [[PubMed](#)] [[Google Scholar](#)]
36. Scanlan TS, Yoshihara HA, Nguyen NH, Chiellini G. Selective thyromimetics: tissue-selective thyroid hormone analogs. *Current opinion in drug discovery & development*. 2001;4(5):614–22. [[PubMed](#)] [[Google Scholar](#)]
37. Lammel Lindemann J, Webb P. Sobetirome: the past, present and questions about the future. *Expert Opin Ther Targets*. 2016;20(2):145–9. [[PubMed](#)] [[Google Scholar](#)]
38. Grover GJ, Egan DM, Sleph PG, Beehler BC, Chiellini G, Nguyen NH, Baxter JD, Scanlan TS. Effects of the thyroid hormone receptor agonist GC-1 on metabolic rate and cholesterol in rats and primates: selective actions relative to 3,5,3'-triiodo-L-thyronine. *Endocrinology*. 2004;145(4):1656–61. [[PubMed](#)] [[Google Scholar](#)]
39. Freitas FRS, Moriscot AS, Jorgetti V, Soares AG, Passarelli M, Scanlan TS, Brent GA, Bianco AC, Gouveia CHA. Spared bone mass in rats treated with thyroid hormone receptor TR $\beta$ -selective compound GC-1. *Am J Physiol Endocrinol Metab*. 2003;285(5):E1135–E1141. [[PubMed](#)] [[Google Scholar](#)]
40. Grover GJ. Selective thyroid hormone receptor-[beta] activation: a strategy for reduction of weight, cholesterol, and lipoprotein (a) with reduced cardiovascular liability. *Proc Natl Acad Sci USA*. 2003;100:10067–10072. [[PMC free article](#)] [[PubMed](#)] [[Google Scholar](#)]
41. Doran A, Obach RS, Smith BJ, Hosea NA, Becker S, Callegari E, Chen C, Chen X, Choo E, Cianfroga J, Cox LM, Gibbs JP, Gibbs MA, Hatch H, Hop CE, Kasman IN, Laperle J, Liu J, Liu X, Logman M, Maclin D, Nedza FM, Nelson F, Olson E, Rahematpura S, Raunig D, Rogers S, Schmidt K, Spracklin DK, Szewc M, Troutman M, Tseng E, Tu M, Van Deusen JW, Venkatakrishnan K, Walens G, Wang EQ, Wong D, Yasgar AS, Zhang C. The impact of P-glycoprotein on the disposition of drugs targeted for indications of the central nervous system:

- evaluation using the MDR1A/1B knockout mouse model. *Drug Metab Dispos.* 2005;33(1):165–74. [[PubMed](#)] [[Google Scholar](#)]
42. Reichel A. The role of blood-brain barrier studies in the pharmaceutical industry. *Curr Drug Metab.* 2006;7(2):183–203. [[PubMed](#)] [[Google Scholar](#)]
43. Gumbleton M, Audus KL. Progress and limitations in the use of in vitro cell cultures to serve as a permeability screen for the blood-brain barrier. *J Pharm Sci.* 2001;90(11):1681–98. [[PubMed](#)] [[Google Scholar](#)]
44. Poller B, Gutmann H, Krahenbuhl S, Weksler B, Romero I, Couraud PO, Tuffin G, Drewe J, Huwyler J. The human brain endothelial cell line hCMEC/D3 as a human blood-brain barrier model for drug transport studies. *J Neurochem.* 2008;107(5):1358–68. [[PubMed](#)] [[Google Scholar](#)]
45. Placzek AT, Scanlan TS. New synthetic routes to thyroid hormone analogs: d6-sobetirome, 3H-sobetirome, and the antagonist NH-3. *Tetrahedron.* 2015;71(35):5946–5951. [[PMC free article](#)] [[PubMed](#)] [[Google Scholar](#)]

## **Biographical Sketch:**

OMB No. 0925-0001 and 0925-0002 (Rev. 09/17 Approved Through 03/31/2020)

### BIOGRAPHICAL SKETCH

Provide the following information for the Senior/key personnel and other significant contributors. Follow this format for each person. **DO NOT EXCEED FIVE PAGES.**

NAME: Sanford-Crane, Hannah

eRA COMMONS USER NAME (credential, e.g., agency login):

POSITION TITLE: Ph.D. candidate

EDUCATION/TRAINING (*Begin with baccalaureate or other initial professional education, such as nursing, include postdoctoral training and residency training if applicable. Add/delete rows as necessary.*)

INSTITUTION AND LOCATION	DEGREE (if applicable)	Completion Date MM/YYYY	FIELD OF STUDY
University of Maryland, College Park, MD.	B.S.	05/2012	Animal Sciences
The Johns Hopkins University, Baltimore, MD.	M.S.	05/2014	Biotechnology
Oregon Health & Science University, Portland, OR.	Ph.D.	01/2021	Cancer Biology

#### **A. Personal Statement**

**Connecting the finer details of biological pathways to downstream system-wide biological signaling responses is key to taking a phenotype from proteins in a tube, to pathways *in vitro*, to biological relevance *in vivo*, and ultimately to applications in human medicine and disease. My long-term goal is to better understand the relationship between cellular pathways and their interactions with systemic responses, including the development of the TME in cancer and immune response. I am passionate and committed to understanding the world better by studying the minute details in seemingly disparate pathways and connecting these pathways to a larger context in the field of cancer. For example, the secreted factors of a tumor causes the activation of stellate cells, which in turn release factors that cause cancer cells to change their metabolism, thus secreting new factors that once again impact their environment – thus creating a cycle of feedback loops between cancer cells and their environment. Being a Ph.D. candidate of the Knight Cancer Institute at Oregon Health & Science University, surrounded by highly motivated and innovative mentors with state-of-the-art laboratories, provides me an ideal setting to investigate the development of the pancreatic tumor microenvironment and an opportunity to grow as an individual and scientist.**

#### **B. Positions and Honors**

### Positions and Employment

- 2010 Undergraduate Research Assistant. Gudelskey Veterinary Center, College Park, MD.
- 2011 Advanced Research Intern. DOW Electronic Materials, Newark, DE.
- 2012-2015 Contract Laboratory Operations Manager. Sigmovir Biosystems Inc., Rockville, MD.

### Other Experience and Professional Memberships

- 2009 Northeast Regional Junior President: Collegiate 4-H.
- 2010 Northeast Regional President: Collegiate 4-H.
- 2015-2016 Chemistry Lab Volunteer at OMSI, Portland, OR.
- 2015- Member, American Association for the Advancement of Science.

### Honors

- 2006 7<sup>th</sup> Place National Egg and Poultry Competition: Maryland 4-H Egg Preparation Competitor.
- 2007 Agriculture Ambassador, Cecil County, Maryland.
- 2007 7<sup>th</sup> Place National Egg and Poultry Competition: Maryland 4-H Judging Team Member.
- 2008 National Honors Society Member.
- 2008 Northrup Grumman Engineering Scholarship recipient.
- 2008 Maryland 4-H Diamond Clover Award recipient.
- 2008 Maryland 4-H Foundation Scholarship recipient.
- 2008 Cecil County VFW Democracy Scholarship recipient.
- 2009 Cecil County Commissioners Award for community service recipient.
- 2009 Outstanding Achievement Environmental Services: EPA certificate of recognition recipient.
- 2008-2012 Kinghorne Poultry Scholarship recipient.
- 2008-2012 Maryland Senatorial Scholarship recipient.

### C. Contributions to Science

**I identified and created an equation to calculate the ratio of groove design to slicing material required for the effective removal of polishing biproducts while maintaining the lowest amount of non-reacted waste products. Through my experiments in groove design and tracking waste material removal, I was able to work with my mentor to create equations to calculate ideal planarization pad design to optimize reagent usage. This project will save the company millions of dollars in expensive polishing regents over the years.**

McCormick, John, **Sanford-Crane, Hannah**. Impact of Groove Design on Transportative Properties of Chemical Mechanical Planarization Pads. *Department of Research and Development*, DOW Electronic Materials. Corporate Research Report. 2011.

**During my time at Sigmovir Biosystems Inc.**, I was Project Leader in two research projects: HSV-1 hormonal mucosal defense regulation; and, FI-RSV vaccine enhancement of disease. The results from my HSV-1 study showed that progesterone levels had a direct impact on the infectivity of HSV-1. This data could then be matched with the increasing HSV-1 rates in women and the observed epidemiological changes that have been found. The data from this single study can be carried over and applied to hormonal regulation of defense mechanisms across the immune system. It suggests that the efficacy of mucosal targeting vaccines could be dependent upon the hormonal state of the individual and makes a strong case for not only the inclusion of females in pre-vaccine approval studies, but in the inclusion of female reproductive cycles as a key part of mucosal targeting vaccine research.

Boukhvalova, M., McKay, J., Mbaye, A., **Sanford-Crane, H.**, Blanco, J. C., Huber, A., & Herold, B.C. Efficacy of the Herpes Simplex Virus 2 (HSV-2) Glycoprotein D/AS04 Vaccine against Genital HSV-2 and HSV-1 Infection and Disease in the Cotton Rat *Sigmodon hispidus* Model. *Journal of Virology*, 89(19), 9825-9840, 2015

**In addition to the contributions described above, I collaborated with the Scanlan lab at OHSU to document *in vivo* impacts of sobetirome prodrugs on the blood-brain barrier. As an expert in *in vivo* technical skills and study design, I was able to provide the Scanlan lab with the knowledge and skills they need to take their pro-drug design to various *in vivo* models. These studies are showing that the prodrugs have made promising improvements to sobetirome for the treatment of MS with marked reduction of off-target side effects.**

Placzek, A. T., Ferrara, S. J., Hartley M. D., Sanford-Crane H. S., Meinig J. M., & Scanlan, T. S. Sobetirome prodrug esters with enhanced blood-brain barrier permeability. *Bioorganic & Medicinal Chemistry*, 24(22), 5842-5854, 2016.

Ferrara, S. J., Meinig J. M., Placzek, A. T., Banerji T., McTigue P., Hartley M.D., Sanford-Crane H. S., Banerji T., Bourdette D., Scanlan T. S. Ester-to-amide rearrangement of ethanolamine-derived prodrugs of sobetirome with increased blood-brain barrier penetration. *Bioorganic & Medicinal Chemistry* 25, 2743-2753, 2017.

J. Matthew Meinig, Skylar J. Ferrara, Tania Banerji, Tapasree Banerji, Hannah S. Sanford-Crane, Dennis Bourdette, and Thomas S. Scanlan. Targeting Fatty-Acid Amide Hydrolase with Prodrugs for CNS-Selective Therapy. *ACS Chemical Neuroscience*, 8(11), 2468-2476, 2017.

J. Matthew Meinig, Skylar J. Ferrara, Tapasree Banerji, Tania Banerji, Hannah S. Sanford-Crane, Dennis Bourdette, Thomas S. Scanlan. Structure-Activity Relationships

of Central Nervous System Penetration by Fatty Acid Amide Hydrolase (FAAH)-Targeted Thyromimetic Prodrugs. *ACS Med. Chem. Lett.*, 10(1) 111-116, 2019.

**My work in the Sherman lab is based on the lab's discovery of a novel lipid-based mechanism for tumor-stroma crosstalk that promotes pancreatic cancer progression. As stellate cells activate, they lose their cytoplasmic lipid droplets. The fate of these lipid droplets was previously unknown, however, Dr. Sherman showed that lysophosphatidylcholine secreted by activated stellate cells supports pancreatic cancer cell proliferation by providing an extracellular source of lipids. My project has been on characterizing the role of fatty acid transporter GOT2/FABPpm in pancreatic cancer, and if this upregulated fatty acid transporter plays a key role behind how lipid droplets from activated stellate cells are used by pancreatic cancer for growth and proliferation. We showed that GOT2 is at a novel location in the nucleus of PDAC cells and plays a role in the development of the immune suppressive TME of PDAC through a novel GOT2-PPAR $\delta$  axis. We also showed that GOT2 directly binds fatty acids, including arachidonic acid and oleic acid, and loss of GOT2 decreases the uptake of arachidonic acid of nuclear lysates. This suggests that GOT2 plays a role in the transport of key ligands for nuclear receptor activation, and likely affects the TME signaling of tumor cells in this manner.**

Hannah Sanford-Crane, Jaime Abrego, Mara Sherman. Fibroblasts as modulators of local and systemic cancer metabolism. *Cancers* 11(5), 619, 2019.

Hannah Sanford-Crane, Jaime Abrego, Chet Oon, Xu Xiao, Shanthi Nagarajan, Sohinee Bhattacharyya, Peter Tontonoz, Mara H. Sherman. A cancer cell-intrinsic GOT2-PPAR $\delta$  axis suppresses antitumor immunity. *Nature* Jan 2021, sent for review.

#### **Platform and Poster Presentations:**

Delmarva Poultry Association National Conference, 2012. Attendee.

Sanford-Crane, H.S., Li, B., Xiao, X. "Role of Lamin B1 in DNA DSB repair." OHSU Chemical Biology & Physiology conference. 2017. Poster.

Sanford-Crane, H.S. "Role of Lamin B1 in DNA DSB repair." OHSU Research Week, 2018. Presentation.

Pacific Northwest Science and Communication Conference, 2018. Attendee.

Sanford-Crane, H.S. "Role of Lamin B1 in DNA DSB repair." North West Volcano Conference, 2018. Presentation.

Sanford-Crane, H.S. "Role of Lamin B1 in DNA DSB repair." OHSU Physiology & Pharmacology Department Seminars, 2017, 2018. Presentation.

Sanford-Crane, H.S. "Role of Lamin B1 in DNA DSB repair." OHSU Program in Cellular and Molecular biology retreat. Fall 2018. Poster & Presentation.

Sanford-Crane, H.S. "A novel GOT2- PPAR $\delta$  axis regulates the PDAC immune microenvironment and tumor growth." OHSU Cell and Developmental Biology & Cancer Biology annual retreat, 2019. Presentation.

Sanford-Crane, H.S. “A novel GOT2- PPAR $\delta$  axis regulates the PDAC immune microenvironment and tumor growth.” OHSU Cell and Developmental Biology & Cancer Biology annual retreat, 2020. Presentation.

**D. Additional Information: Research Support and/or Scholastic Performance**

2020 graduate student fellowship from the Knight Cancer Institute Cancer Center Support Grant P30 CA069533.